

# **CONTINUUM ROBOTIC SYSTEMS FOR INTRA-OPERATIVE MRI-GUIDED INTERVENTIONS**

by

**Lee Kit Hang**

A thesis submitted in partial fulfilment of the requirements of  
the Degree of Doctor of Philosophy  
at The University of Hong Kong

May 2019





Abstract of thesis entitled

**"Continuum Robotic Systems for Intra-operative MRI-Guided Interventions"**

Submitted by

**Lee Kit Hang**

for the degree of Doctor of Philosophy  
at The University of Hong Kong  
in May 2019

Recent advancement in interventional Magnetic Resonance Imaging (MRI) has opened a new realm in image-guided surgery. Although MRI offers possibilities to visualize the confined anatomy through high contrast volumetric scan, the limited bore size and extreme magnetic field physically hinder the surgeon from sufficiently accessing the patient. To this end, much research effort has been expended to the development of robotic systems that can operate under MRI environments. It enables surgeons to perform intervention remotely even when imaging is performed, demonstrating remarkable improvements in surgical precision and safety. However, due to the absence of appropriate tools, its clinical potential only prevails for needle-based interventions such as soft tissue biopsy, which require a straight entry pathway to the surgical site.

The overall goal of this thesis is to propose a generic hardware and software framework that integrates intra-op MRI, continuum robot and enhanced human-robot interface to overcome the navigation problem in complex environments. Inspired by biological trunks and snakes, continuum robot designs offer possibilities to traverse confined anatomy and hence enable flexible access routes to surgical sites, e.g. through natural orifices like transoral approach. The design challenge of such a miniaturized, MR Safe, yet dexterous manipulator is addressed by employing advanced Finite Element Analysis (FEA) formulation. To achieve precise robot control in confined surgical site, a novel control framework based on non-parametric localized online learning is proposed. Such technique can learn the inverse model directly without prior knowledge of the robot's structural parameters while adapting to unknown soft tissue interactions. Furthermore,



parallel processing of real-time MRI data based on Graphical Processing Unit (GPU) is also investigated to enhance the human-robot control interface, providing instant and clear pathologic indication and detailed structural information. All in all, these proposed techniques have contributed to the development of an integrated robotic catheter platform for MRI environments. Low-friction Hydraulics actuation based on rolling diaphragm sealing is incorporated to provide high performance actuation with negligible influence to MRI quality. To demonstrate its clinical potential, detailed quantitative validations were conducted on groups of subjects. Finally, the thesis concludes by highlighting the future work and potential improvements of proposed techniques.

(Word count: 351 words)

### Declaration

I declare that this thesis represents my own work, except where due acknowledgement is made, and that it has not been previously included in a thesis, dissertation or report submitted to this University or to any other institution for a degree, diploma or other qualifications.

Signed \_\_\_\_\_ Lee Kit Hang

*"Praise be to the God and Father of our Lord Jesus Christ,  
who has blessed us in the heavenly realms  
with every spiritual blessing in Christ.", Ephesians 1:3*

## **DEDICATION**

To the God Almighty  
The true light.  
The source of all wisdom.  
The hand behind of all creations.  
All the achievements and Glory belongs to him.

To my mother  
A strong and gentle soul  
who always gifts the best to my brother and me  
even at the toughest moment of life.

To my brother  
My companion and buddy,  
who taught me how to share and be considerate.

To my fiancée  
My beloved one and best friend  
who never cease to support me and those in need.

To the Croucher Foundation  
for their most generous support  
so that I can be the helping hand for others.

# Acknowledgements

*"The reasonable man adapts himself to the world;  
the unreasonable one persists in trying to adapt the world to himself.  
Therefore all progress depends on the unreasonable man."*

George Bernard Shaw

*"Man and Superman"*

1903

I consider myself fortunate indeed to have had the opportunity to pursue research work toward the PhD with Dr Ka-Wai Kwok, who might not be the most *"reasonable"* supervisor in the world, yet his burning passion has motivated me to push myself beyond the limit and strive for perfection. When I look back to my PhD journey, though it was full of sweat and tears, I feel grateful to have gone through this wonderful life-changing experience. Dr Kwok's emphasis on comprehensive training reminds me that research excellence cannot be achieved by technical skills alone, but also requires effective communication, leadership and most importantly, a sincere mind.

I am also thankful to my co-supervisor Prof. K. Y. Sze for his thoughtful insight in soft robot design and his fruitful input to my study in continuum mechanics. I want to extend my sincere gratitude to Prof. Wayne Luk and Mr Gary C. C. Chow for their brilliant guidance on the development of high performance computing techniques. My gratitude also goes to Prof. Kaspar Althoefer for his overhead support and invaluable advice that makes my development on soft robotics possible.

I am also grateful to all my excellent fellows in the IRIS lab. It was an honour to work with such a persistent and thoughtful team. Never would I forget those stimulating discussion and sleepless nights before deadlines.



I must also pay tribute to the most generous support of the Croucher Foundation. Not only did it lighten my financial burden, but also granted me the opportunities to participate in numerous international academic events.

Nobody has been more important to me in the pursuit of PhD than my family. I want to thank you my mother, who has provided me with unlimited support. Were your warm glances that told me always to look ahead firmly, and never give up when stumbling. I also wish to thanks my beloved and supportive fiancée



# Contents

<b>Abstract</b>	<b>1</b>
<b>Acknowledgements</b>	<b>5</b>
<b>List of Figures</b>	<b>11</b>
<b>List of Tables</b>	<b>24</b>
<b>List of Algorithms</b>	<b>25</b>
<b>Nomenclature</b>	<b>27</b>
<b>1 Introduction</b>	<b>29</b>
1.1 Motivation and Objectives . . . . .	29
1.2 Thesis Organization and Main Technical Contributions . . . . .	33
1.3 Publications for the Work Presented in this Report . . . . .	35
<b>2 MRI-guided Robot-assisted Interventions</b>	<b>39</b>
2.1 Introduction . . . . .	39
2.2 Recent Advances in Interventional MRI Technology . . . . .	40
2.3 Robotic System for MRI-guided Surgery . . . . .	42
2.3.1 MRI Safety Classification . . . . .	43
2.3.2 Neurosurgery . . . . .	45
2.3.3 Prostate Interventions . . . . .	48
2.3.4 Breast Biopsy . . . . .	51
2.4 Clinical Considerations and Technical Challenges of MRI-guided Robotic Intervention . . . . .	53
2.4.1 Tissue Deformation and Intra-operative Update of Surgical Map . .	54
2.4.2 Confined Space and Endoluminal Entry . . . . .	55
2.4.3 Teleoperation of Flexible Instruments . . . . .	56
2.5 Soft Continuum Robotic System . . . . .	56
2.5.1 Actuation Design . . . . .	56



2.5.2	Modelling and Control . . . . .	58
2.6	Current Trends and Perspectives of MRI-guided Intervention . . . . .	60
2.6.1	High-Performance Image Processing for <i>in situ</i> Guidance . . . . .	60
2.6.2	MR Safe Continuum Manipulator and Actuation . . . . .	62
2.6.3	Integrated Navigation and Control Interface for Continuum Robot . . . . .	64
2.7	Conclusion . . . . .	65
<b>3</b>	<b>High Performance Image Processing for MRI-guided Navigation</b>	<b>67</b>
3.1	Introduction . . . . .	67
3.2	Performance-aware Programming for Deformable Image Registration . . . . .	68
3.2.1	Diffeomorphic Demons Registration for Large Tissue Deformation . . . . .	69
3.2.2	Acceleration Scheme based on Novel Computing Architecture . . . . .	70
3.2.3	Experimental Results . . . . .	72
3.3	Fast Proximity Query with Graphical Processing Unit . . . . .	73
3.3.1	Previous Work . . . . .	74
3.3.2	Problem Definition . . . . .	75
3.3.3	Proximity Queries for Irregular Mesh Model . . . . .	78
3.3.3.1	Analytical Formulation of Edge-Segment Point Pairs . . . . .	78
3.3.3.2	Optimization-based Closest Point Pair Estimation . . . . .	79
3.3.3.3	Identification of Shortest Distance . . . . .	82
3.3.4	Experimental Results . . . . .	84
3.3.4.1	Fast Triangular Proximity Query . . . . .	84
3.3.4.2	Broad-phase Culling with Level of Detail Techniques . . . . .	84
3.3.5	Applications and Implementations . . . . .	87
3.3.5.1	MRI-guided Catheter Navigation . . . . .	87
3.3.5.2	Collision Detection for Robot-assisted Laparoscopy . . . . .	87
3.3.5.3	Motion Planning for Anthropomorphic Manipulator . . . . .	89
3.3.5.4	Collision-free Trajectory Planning for Human-Robot Collaborative Tasks . . . . .	90
3.4	Discussion and Conclusion . . . . .	94
<b>4</b>	<b>MR Safe Actuation and Control of Robotic Catheter System</b>	<b>95</b>
4.1	Introduction . . . . .	95
4.2	Clinical Motivation . . . . .	96
4.3	MR Safe Robotic Catheter based on Hydraulic Actuation . . . . .	97
4.3.1	State-of-the-art . . . . .	97
4.3.2	Hydraulic Actuation for Robotic Teleoperation . . . . .	98
4.3.3	Novel Design for MR Safe Robotic Catheter Manipulator . . . . .	102

4.4	Experimental Evaluation . . . . .	105
4.4.1	MR-compatibility Test . . . . .	105
4.4.2	Performance of Hydraulic Actuation . . . . .	108
4.4.2.1	Force Transmission . . . . .	108
4.4.2.2	Hysteresis . . . . .	108
4.4.2.3	Dynamic Response . . . . .	109
4.4.3	Catheter Manipulation for Cardiovascular Interventions . . . . .	112
4.5	Human-Robot Control Interface . . . . .	113
4.5.1	Visual Guidance with Intra-operative MRI . . . . .	113
4.5.1.1	Virtual Endoscopic View . . . . .	115
4.5.2	Closed-loop Control for Catheter Manipulation . . . . .	116
4.5.2.1	Model-based Control Approach . . . . .	117
4.5.2.2	Model-free Control Approach . . . . .	119
4.5.3	Experimental Results . . . . .	120
4.5.3.1	Experimental Setup . . . . .	120
4.5.3.2	Subject Test . . . . .	122
4.6	Towards Clinical Validation of MRI-Guided and Robot-assisted Cardiac Electrophysiology . . . . .	125
4.6.1	Real-time Tracking Techniques for MRI-guided Catheter . . . . .	127
4.6.1.1	Passive MR Fiducials/Markers . . . . .	127
4.6.1.2	Real-time Active Tracking Coil . . . . .	128
4.6.1.3	Semi-active tracking . . . . .	129
4.6.2	Fast Multi-phase Cardiac Image Registration . . . . .	129
4.6.2.1	Diffeomorphic Demons Approach . . . . .	130
4.6.2.2	Integration into Surgical Workflow . . . . .	131
4.7	Conclusion . . . . .	132
<b>5</b>	<b>Soft Robot Design and Control for Flexible Access MRI-guided Surgery</b>	<b>135</b>
5.1	Introduction . . . . .	135
5.2	Clinical Motivation . . . . .	136
5.3	Soft Robotic Manipulator . . . . .	139
5.3.1	Design of Hyper-elastic Actuator . . . . .	140
5.3.2	Kinematic Modeling with Finite Element Analysis . . . . .	141
5.4	FEA-based Kinematics Control for Image Space Navigation . . . . .	144
5.4.1	Characterization of Robot Kinematics . . . . .	145
5.4.2	Local Linearization of Kinematics Model . . . . .	146
5.4.3	Optimization-based Inverse Kinematics Solver . . . . .	148
5.4.4	Experiments Results . . . . .	149

5.4.4.1	Experimental Setup . . . . .	150
5.4.4.2	Performance Evaluation . . . . .	152
5.5	Nonparametric Online Learning for Soft Robot Control . . . . .	154
5.5.1	Characterization of Robot Motion Transition . . . . .	155
5.5.2	Inverse Problem for Online Learning Task Space Control . . . . .	156
5.5.3	Inverse Model Learning with Multiple Local Controllers . . . . .	157
5.5.4	Online Learning of the Global Controller . . . . .	158
5.5.4.1	Pre-processing of Training Dataset with Redundancy . . . . .	160
5.5.4.2	Constrained Optimization to Resolve Redundancy . . . . .	160
5.5.5	Experimental Results . . . . .	163
5.5.5.1	Initialization of Online Learning by FEA-based Model . . . . .	163
5.5.5.2	Experimental Setup . . . . .	163
5.5.5.3	Performance Evaluation . . . . .	165
5.6	Conclusion . . . . .	174
<b>6</b>	<b>Conclusions and Future Work</b>	<b>175</b>
6.1	Achievements of this Thesis . . . . .	175
6.2	Ongoing Research and Future Directions . . . . .	177
	<b>References</b>	<b>181</b>
<b>A</b>	<b>Overview of the MR Safe Catheter Robot Control System</b>	<b>205</b>
A.1	System Architecture . . . . .	205
A.2	Communication Protocol . . . . .	207
<b>B</b>	<b>Technical Details of Soft Robotics Actuator</b>	<b>209</b>
B.1	Pneumatic Static Mixing Dispenser for Silicone Rubber Molding . . . . .	209
B.2	Individually Constrained Design . . . . .	210
B.3	Overall Constrained Design . . . . .	211
B.3.1	Mechanical Structure . . . . .	211
B.3.2	Design Optimization with Finite Element Analysis . . . . .	213
B.3.3	Fabrication . . . . .	216

# List of Figures

1.1	(a) MrBot: an MR-conditional robot actuated by pneumatic step motor for image-guided access of the prostate gland; (b) Virtual robotic manipulator and corresponding safety operation region augmented on MR image; (c) Motion input interface incorporated with force-feedback that resists the instrument deviated from the safety region defined along the luminal structure. . . . .	30
1.2	Integrated robotic framework comprising the high performance image processing, teleoperation control interface, MR Safe actuation and continuum surgical instrument. . . . .	32
2.1	(a) Complete MR angiography (MRA) of the aortic arch extended to the vertex in frontal view; (b) Functional MRI (fMRI) denoting the activation of brain region responsible for phonological processing. <b>Image Source:</b> [1, 2]	41
2.2	(a) Example surgery in a GE Signa SP 0.5T intra-op MRI. The surgeon can stand between the two magenets and perform surgery during MRI acquisition. (b) IMRIS operating suite equipped with a ceiling mounted MRI scanner, which can be moved in-and-out to accomodate the surgical workflow. <b>Image Source:</b> [3], IMRIS . . . . .	41
2.3	AMIGO multimodal image-guided operating suite at the Brigham and Women’s Hospital (BHW) and Harvard Medical School. <b>Image Source:</b> [4] . . . . .	42
2.4	The first MRI compatible robotic needle manipulator for neurosurgery. A later upgrade of the system has incoported 2 micro-grasping forceps for endoscopic microsurgery. (The University of Tokyo, Tokyo, Japan) <b>Image Source:</b> [5, 6] . . . . .	47
2.5	(Left) NeuroArm/SYMBIS surgical system consisted of two 7 DoF MR conditional teleoperated robotic arms; (Right) MRI-guided robotic stereotaxy system actudated by low-noise piezoelectric drives (Worcester Polytechnic Institute, Worcester, MA, USA). <b>Image Source:</b> [7, 8] . . . . .	47

- 2.6 **(Left)** Multi-imager compatible and MR Safe needle guiding robot that utilize remote center of motion mechanism for manipulation (Johns Hopkins University, Baltimore, MD, USA); **(Right)** Concentric tube ablation probe that allows transforaminal access to hippocampus without the need for a burr hole on the patient skull. **Image Source:** [9, 10] . . . . . 48
- 2.7 **(a)** MR compatible robotic needle manipulator for TRUS prostate interventions developed in The Johns Hopkins University, Baltimore, MD, USA; **(b)** MrBot, the pneumatic-driven MR Safe robot for prostate biopsy and patient in the MRI scanner; **(c)** PneuStep, the pneumatic step motor providing precise actuation for MrBot. **Image Source:** [11–13] . . . . . 49
- 2.8 Innomotion™ robot-assisted system and Innomotion™ AMO biopsy needle guide for percutaneous intervention under CT/MRI. **Image Source:** INNOMEDIC . . . . . 50
- 2.9 **(a)** MRI-guided needle placement robot integrated with fiber optic force sensing developed in Worcester Polytechnic Institute, Worcester, MA, USA; **(b)** Motorized needle guide template for MRI-guided transperineal prostate biopsy. **Image source:** [14–16] . . . . . 51
- 2.10 **(a)** MRI-guided robotic breast biopsy system equipped with telescoping shafts for motion transmission (University of Minnesota, Minneapolis, MN, USA); **(b)** Another MRI-compatible Cartesian manipulator for breast biopsy under open type MRI, developed by the Chinese University of Hong Kong, Hong Kong, China. **Image source:** [17, 18] . . . . . 52
- 2.11 **(a)** Master-slave robot platform with pneumatic transmission for MRI-guided breast biopsy, developed by University of Maryland, College Park, MD, USA; **(b)** Sunram 5: An MR Safe robotic system for breast biopsy driven by 3D-printed pneumatic stepper motors. **Image source:** [19, 20] . . . . . 53
- 2.12 Brain MRI illustrating the "brain shift" effect before and after the craniotomy. **Image Source:** [21] . . . . . 54
- 2.13 Artificial ablation landmarks (denoted by yellow arrows) inside the atrium wall created by injecting gadolinium contrast via thin tubes. . . . . 55
- 2.14 **(a-b)** Early design of soft robot mechanisms with elastomeric chamber that can actuated by inflating pressurized gas/liquid; **(c)** Tendon-driven soft continuum robot capable of dexterous manipulation under water; **(d-e)** STIFF-FLOP soft robot equipped with active stiffing mechanism to change to overall robot body rigidity during keyhole surgery; **(f)** Endotics soft robotic colonoscope. **Image Source:** [22–25] and Endotics Inc. . . . . 57

- 2.15 List of common model-based approach for soft continuum robot kinematics/dynamics modelling. **Image Source:** [26–28] . . . . . 58
- 2.16 (a) Sample of pre-op high resolution Cine image acquired during diastole phase; (b) Intra-op low-resolution images captured at systole phase; (c) Registration result of pre-op and intra-op image sets. The high definition pre-op anatomy information is realigned to compensate the deformation due to cardiac motion; (d) Transformation grid showing the deformation field in image domain. . . . . 61
- 2.17 MRI scan of a MR Conditional pneumatic step motor, using two typical imaging sequences: turbo spin echo (TSE) and gradient echo (GRE). No obvious artefact is observed when in motion or rest. **Image source:** [29] . . . . . 63
- 2.18 (Left) Motor maximum output torque correlated with various operation speed and air supply pressure; (Right) Plot of positioning error against nominal motor speed of pneumatic motor **Image source:** [29] . . . . . 64
- 3.1 Schematic diagram of the CUDA hardware and software architecture. (a) Model CUDA GPU enable parallel processing of large amount of data by distributing the load to thousands of computation units, known as streaming multiprocessors. The streaming multiprocessors can read from/write to the off-chip graphics memory through a heavily cached data bus. (b) To execute kernel processes, the GPU will instantiate a grid of thread blocks composed of numerous threads. . . . . 71
- 3.2 Two-dimensional view of the left atrium on the transverse plane. (a) *Fixed image*; (b) *Moving image*; (c) Non-rigidly registered image using the GPU-accelerated diffeomorphic demons registration algorithm; (d) Projected deformation field onto the transverse plane. . . . . 73
- 3.3 Computation performance of *Diffeomorphic Demons* registration algorithm evaluated on CPU and two different GPUs using our proposed framework. Around 30 iterations is required for the registration to converge. . . . . 74
- 3.4 (a) CAD model of the ATLAS robot arm and the Sandia Robotic Hand; (b) Volumetric pathways comprising segments (in green) tightly enclosing along the arm and four fingers; (c) The corresponding twenty series of segments, of which the contours can be posed flexibly along with the subsequentially updated robot configuration; (d) Collision model approximated by the union of same number of standard bounding cylinders; (e) Such collision model fails to fully enclose the robot arm under alternative configuration. . . . . 76

- 3.5 (a) Basic structure of a single segment enclosed by two adjacent circular contours. Mathematics variables introduced for geometric analysis; (b) New variables are estimated after the previous iterative result. . . . . 77
- 3.6 Example configuration showing the temporary closest point pairs of each step processed by the optimization-based estimation. This configuration can be considered as an more extreme case requiring for more number of steps to reach convergence. . . . . 80
- 3.7 (a) Portion of cross-sectional region extracted from a single segment. It passes through the corresponding contour centers  $P_j$  and  $P_{j+1}$ . The potential closest points  $x_{0...3}$  always lay inside the Voronoi Region of the corresponding closest feature  $F_Y$ ; (b) Voronoi Regions of a triangle in 2D space. . . . . 83
- 3.8 (a) Illustration of GPU and CPU computational performance of PQ process with 30 segments and millions of meshes; (b) Speedup of GPU-based PQ computation with respect to CPU . . . . . 85
- 3.9 Segmented sub-mesh of the left atrium model with (a) 8 segments (b) 4 segments for broad-phase culling . . . . . 86
- 3.10 (a-b) Two catheter configurations with different degree of steering curvature. The catheter (with 7 segments) is advanced inside the left atrium model (with 10,658 mesh) for radiofrequency ablation during the cardiovascular electrophysiology procedure. The PQ sampling rate is maintained at rate of 1kHz. . . . . 88
- 3.11 Time lapse illustration of the fast PQ computation between the surgical instrument and live anatomical structure during a robot-assisted minimally-invasive prostatectomy. The warm color on the mesh surface depicts the separation from the robot. The white line reveals the shortest distance. . . . . 89
- 3.12 (a) ATLAS reaching the valve wheel through a hole created previously by the hand-held cutting tool; (b) PQ processed between the robot hand (with 39 segments) and the wall with hole (with 4,308 meshes). An optimal collision-free trajectory is estimated online with the aim to grasp the wheel. The warmer the colour on wall indicates, the closer distance to the robot arm and fingers is. . . . . 90
- 3.13 Color mesh illustrating the PQ computational result as overlayed on the 3D wall geomtry. The updating frequency can be maintained above 30Hz throughout the entire manipulation with various configurations of the ATLAS robot arm. . . . . 91



- 3.14 **(a)** CAD models of the Baxter robot arm; **(b)** Volumetric pathways comprising twenty segments (in green) tightly enclosing along the corresponding arm; **(c)** Circular contours attached flexibly along with their kinematic configurations updated. . . . . 91
- 3.15 **(a)** Schematic diagram showing an example control workflow of using the proposed PQ for a human-robot collaborative task. . . . . 92
- 3.16 **(a)** Example industrial product assemble process that requires intimate human-robot collaborations. The Baxter industrial robot is integrated with depth sensing unit to identify humans and other objects within its workspace; **(b)** Graphic result of GPU-based PQ implemented on ROS. The warmer the color on the mesh surface, the closer the separation from the robot. . . . . 93
- 4.1 **(a)** Pneumatic motor composing of seven 3D-printed components; **(b)** Motor after handy assembly; **(c)** Linear correlation between power and speed holding below 60 rpm. High speed and power are achieved. . . . . 99
- 4.2 Three basic manipulation DoFs of a catheter, namely translation, rotation and steering. All the DoFs have to be precisely controlled with sufficient range in order to perform an intra-cardiac ablation targeting task. . . . . 99
- 4.3 Overview of the MR Safe hydraulic catheter robotic manipulator showing the allocation of master-slave actuation in MRI room setting; **(a)** Two small active tracking coils wired along the catheter for real-time positional MR-tracking of its tip; **(b)** MR Safe robotic platform plugged-in with a standard EP catheter for RF ablation. The master-slave actuation units provide rotation, bending, coarse and fine insertion of the catheter; **(c)** Bending actuation unit that transmits the linear hydraulic actuation of rolling diaphragm into rotary motion. All hydraulic actuation units and the robot body are made of MR Safe materials; **(d)** Master electric motor units located in the control room serving as the source of hydraulics. The hydraulic fluid is transmitted to the slave catheter robot platform in MRI room via long ( $\approx 10\text{m}$ ) hydraulics pipelines. These hydraulics tubes can be channeled through the waveguide. . . . . 101
- 4.4 **(a)** Conceptual design of master-slave hydraulic transmission to ensure MR-compatibility of robot actuation. The contact between the gear teeth can be maintained by preloading fluid pressure, thus minimizing backlash. Rolling diaphragms are adopted to tightly sealed the pressurized fluid. **(b)** Conventional sealing using O-rings may induce significant sliding friction inside the cylinders. . . . . 102

- 4.5 (a) Main components of the MR Safe robotic manipulator (the slave system) which operates in the MRI room. A clinically used EP catheter can be tightly mounted on a tailor-made catheter holder. (b) and (c): Actuation units providing steering, rotation, coarse and fine translation of the catheter. 103
- 4.6 (a) Experimental setup of MR-compatibility test for the presented robot. Key components are connected between the MRI and the control rooms via the wave guide. The operator can tele-manipulate the catheter using the catheter navigation interface. (b) MR images of an MRI phantom placed aside the robot indicate the negligible EM interference in four different operating conditions. . . . . 107
- 4.7 Hysteresis of the master-slave actuation unit at different preload fluid pressure. The average values of hysteresis were 0.88mm, 0.93mm, 1.02mm, 1.29mm for preloaded pressure 0.05 MPa, 0.1 MPa, 0.15 MPa and 0.2 MPa, respectively. . . . . 109
- 4.8 Periodic motion of master-slave actuation unit pre-loaded with 0.1 MPa of fluid pressure. The slave position (a, dash line) could precisely follow the sinusoidal reference trajectory (a, concrete line) of the master unit at 0.1 Hz. The absolute error (b) has a maximum of 0.67 mm. . . . . 110
- 4.9 Bode plot showing torque transmission response of the master-slave hydraulic actuation unit at four different levels of preloaded fluid pressure. The magnitude (a) and phase shift (b) are shown. The data were collected from 10 cycles at the steady state. . . . . 111
- 4.10 Experiment settings of the PVI task. (a) EP catheter tele-manipulated by the proposed robot to perform "ablation" on the left atrium (LA) phantom model; (b) Locations of the ablations (127 points) on the interior surface . 112
- 4.11 (a) Left atrial EP roadmap showing the virtual lesion targets defined close to the pulmonary vein ostia: Yellow for ablated regions; red for incomplete ones. The virtual endoscopic view is rendered from the catheter tip point of view. (b) Schematic diagram showing the movement of the catheter tip at time step  $k$  and step  $(k + 1)$ , along with its endoscopic image plane. . . . . 115
- 4.12 Schematic diagram of a typical catheter mechanism. (a) Constant curvature geometry of the distal section of the catheter. (b) Geometry of steering knob on the catheter handle indicated with its insertion distance  $d$ , twisting angle  $\phi$ , and rotating angle  $\alpha$ . . . . . 118

- 4.13 Experimental setup: **(a)** Left atrial phantom model and the EP ablation catheter. **(b)** Robot control interface providing the operator with simulated cardiac roadmap displayed in three different camera perspectives, including the virtual endoscopic view. . . . . 121
- 4.14 Two major performance indices, namely accuracy and efficiency defined based on **(a)** proximity distance measured from tip to lesion target around the pulmonary vein ostia and **(b)** total length of incomplete lesion segments (red). . . . . 123
- 4.15 Trajectory of the catheter tip in the LA phantom model. . . . . 123
- 4.16 Schematic diagram of the MRI-guided robot-assisted catheterization. The operator can perform robotic EP catheterization in a closed-loop manner. . . 126
- 4.17 **(a)** 3-D EP roadmap of left ventricle segmented and rendered based on pre-op MR images; **(b)** Significant disparity (indicated by orange arrows) between the roadmap and intra-op images during the diastole; **(c)** Ablation landmarks selected on a slice of 2D intra-op MR images. Yellow flow arrows are shown as the deformation field estimated by the Demons-based registration method; **(d)** Landmarks re-aligned appropriately on the 3D roadmap based on the deformation field. . . . . 130
- 5.1 The head and neck anatomy denoted with the actual tumor mass from nasopharynx and oropharynx cavity. **Image Source: [30, 31] and NIH National Cancer Institute** . . . . . 137
- 5.2 MR and PET-CT images of oropharyngeal cancer in axial plane. White arrow locates the primary tonsillar lesion. Yellow arrows indicate the critical neurovascular structures. Parotid glands are denoted by the green allows. **Image Source: [32]** . . . . . 138
- 5.3 **(a)** Soft robotic endoscope prototype made of silicone rubber. The robot dimension is compatible with the insertion tube of conventional endoscope; **(b)** CAD/CAM model of the soft manipulator showing the simulated helical strain-wrapping constrains around its individual actuation chamber using linear truss, where the anisotropic expansion can be achieved; **(c)** Finite element model tessellated with 12,000 linear hexahedron elements. A total of 2,214 truss elements are defined to emulate the effect of strain-wrapping constraint; **(d)** Cross-sectional area tessellated by hexahedron meshing. . . 140
- 5.4 Bending angle of the soft actuator with individual fiber constraints under various inflation volume. . . . . 141

- 5.5 (a) Three dimensional quadratic tetrahedral elements with 10 nodes (C3D10); (b) Hexahedral elements with 8 nodes (C3D8); (c) Cross-section of the individually constrained soft robot FEA model tessellated by C3D10 elements. Automatic mesh generation function of Abaqus was employed; (d) Same soft robot FEA model tessellated by C3D8 elements using the Abaqus automatic mesh generation. Less elements (203) are required for hexahedral elements to fully cover the same cross-section as compared to tetrahedral elements (616). However, the automatic meshing quality is not satisfactory, the nodes distribution is highly irregular; (e) FEA model obtained by custom-designed protrusions. The overall meshing quality is restored while similar number of elements are employed. 142
- 5.6 FEA models (Left) simulated with 7 levels of inflation pressure in a single chamber. Similar deformation characteristics are exhibited in actual configurations of the soft manipulator (Right) under the same corresponding pressure levels. . . . . 143
- 5.7 FEA results showing (a) correlation of the bending angle and (b) steering angle of the soft robot with pneumatic pressure (0-0.7 bar) applied on any two of the three actuation chambers. . . . . 144
- 5.8 FEA-simulated kinematics data covering the entire workspace of the soft robot. The arrows illustrate the predicted movement of the robot tip when an arbitrary pressure change  $\Delta u_k$  is applied. These data enable pre-training of a reasonable initial control policy before the online learning begins, without the need for undesired random movement (babbling). . . . . 145
- 5.9 Soft robot configurations under various inflation pressure simulated by FEA. The corresponding targeting point  ${}^w s_i$  on intracavity surface  $S$  (yellow) is the extension of the manipulator end-effector at  ${}^w p_i$  along the normal  ${}^w n_i$ . . . . . 146
- 5.10 (a) Illustration of the "virtual camera view" provided to the operators during tele-operative navigation. The Jacobian matrix of motion mapping is estimated w.r.t. this image coordinate, hence aligned with the visual guidance. (b) Neighbor targeting points ( ${}^w s_2, {}^w s_3, {}^w s_4$ ) projected from intracavity surface  $S$  (yellow) to the camera coordinate  $L$  (red) as  ${}^w y_i$ . These points are used for local kinematics linearization. Others targeting points ( ${}^w s_1, {}^w s_5$ ) are neglect as they are out of the kinematics FOV. . . . . 147

- 5.11 System architecture of the experimental setup illustrating the interconnection of the primary components: the human-machine interface, the process core that implement our proposed soft robot control framework and the robot control system. . . . . 151
- 5.12 The desired trajectory is pre-registered on the intracavity surface (transparent sphere shell) by using EM position tracking system. The soft manipulator is controlled by operator's joystick input to trace the trajectory in virtual camera perspective. The position of the end-effector is also monitored by the same EM system throughout the experiment to validate the trajectory tracking accuracy of the proposed control framework. . . . . 152
- 5.13 Results from the trajectory tracking experiment. Blue line represents the pre-defined target trajectory. Red line represents the resultant trajectory of the targeting point of manipulator end-effector projected on the spherical intracavity surface. . . . . 153
- 5.14 Absolute error of the tracking result in millimeters. . . . . 153
- 5.15 Three robot configurations illustrating the example of localized inverse models. Assume that their tip directions  $\mathbf{s}_i$  will undergo the same rotation  $\Delta\mathbf{s}_{ref}$  (blue arrow) with the proper pressure changes  $\Delta\mathbf{u}_i$  applied, where  $i = 1 \dots 3$ . **(a)** In the case of configurations 1 and 2, the average of their control inputs  $\Delta\mathbf{u}_1$  and  $\Delta\mathbf{u}_2$  would still lead to a consistent  $\Delta\mathbf{s}_{avg}$  (red arrow); **(b)** While two configurations, such as 1 and 3, are vastly different, this average of inputs  $\Delta\mathbf{u}_1$  and  $\Delta\mathbf{u}_3$  may lead to two dramatically different rotations  $\Delta\mathbf{s}_{avg}$ , leading to undesired movement. Therefore, learning the inverse model directly with a global function approximator may lead to invalid solutions and unstable robot performance. . . . . 156
- 5.16 Schematic diagram of the robot control routine. The measured value of task space coordinate  $\mathbf{s}_k$  and actuation input  $\mathbf{u}_k$  provide localized information for the inverse estimation. . . . . 157
- 5.17 Example set of localized linear controllers that approximate the nonlinear inverse mapping  $\Phi$  of a 1-D actuation  $\Delta\mathbf{u}$ . The valid region of each spatially localized controller is centered at  $\mathbf{c}_i$  (denoted by plus sign), with their range parameterized by  $\mathbf{D}_i$  (colored ellipse) in the robot state space. The warm color depicts the actuation  $\Delta\mathbf{u}$  predicted by the linear control law  $\beta_i$ , in order to achieve a particular movement  $\Delta\mathbf{s}^*$  in task space. . . . . 159

- 5.18 System architecture of the proposed control framework depicting interconnection of the key components. The processing core is responsible for fast computation of inverse solution. The inverse model is also updated continuously by incorporating the online data in real time. The operator can specify the reference input  $\mathbf{s}_k^{ref}$  via a motion input device for effective endoscopic navigation. In our experiments, this input is replaced by a pre-defined reference trajectory to evaluate the online learning performance of the inverse mapping. . . . . 164
- 5.19 (a) Registration process of the predefine trajectory using an EM position tracking system. Blue line on the transparent sphere illustrates the tracking trajectory on the task space; (b) Soft manipulator is commanded to follow the desired trajectory automatically. Its end-effector position is also measured by the tracking system to close the feedback loop under online learning control policy. Plastic rod actuated by a stepping motor pushes against the soft robot, generating the external constrains. The contact force is monitored by a force/torque sensor. . . . . 166
- 5.20 Learning curve of the nonparametric method approximating the inverse motion transition model  $\Delta \mathbf{u} = \Phi(\Delta \mathbf{s}^*, \mathbf{s}, \mathbf{u})$  for each of the three soft actuators A, B and C. Nonparametric method offers fast learning convergence as shown by the test error curve (nMSE) that rapidly descent within the first few epochs. The number of localized model and the complementary receptive fields increase over training epochs to achieve more accurate approximation of the inverse model. . . . . 169
- 5.21 Plot of (Left) tracked trajectory and (Right) corresponding tracking error in time domain. In the control experiment, the robot is allowed to move freely without any constraint. Control performance of the online learning controllers trained by three different data source is validated: (a) Pre-trained by FEA without using online data; (b) Pure online learning initialized by random exploration; (c) Pre-trained by FEA data and updated by online data. The online learning initialized by FEA data approach (c) combines the advantage of (a) and (b), in which random exploration (Green path in (b)) in not required, but its tracking error converge to similar accuracy as in pure online learning. . . . . 172

- 5.22 Plot of **(Left)** tracked trajectory and **(Right)** corresponding tracking error in time domain under external interactions. Control performance is validated in the three different conditions as in Fig. 5.21. It can be observed that the online learning for **(b)** and **(c)** is capable of compensating the external interaction with the tracking error reduced, as compared to the controller without using online data **(a)**. . . . . 173
- A.1 Schematic diagram of the catheter robot control electronic system. The low-level tasks related to motor control (e.g. step counting and pulse generation) are off loaded to the PIC chipKIT™ uC32™ microcontrollers. Each motor is equipped with its dedicated microcontroller to ensure consistent generation of high frequency motor stepping pulse. Such design paradigm also favour system scalability for others potential applications. . . . . 206
- A.2 **(a)** PIC chipKIT™ uC32™ microcontrollers with 32-bit MIPS processor core running at 80MHz; **(b)** High power stepper motor and driver set with a maximum output torque of 4Nm. The proximal end of motor shaft is connected to an encoder to measure the exact motor rotation. It allows compensation of skipping step and hence robust motor positioning. . . . . 207
- B.1 **(a)** Typical stir-mixing of 2-components RTV Silicone Rubber. The mixing process will induce a significant amount of micro-bubbles in the silicone fluid mixture, deteriorating the outcome quality of workpiece; **(b)** Pneumatic mixing and dispenser system for silicone fluid. The 2 components of silicone fluid are first de-gassed and then pumped out of the chamber by pressured air. The AB components are forced through the sealed static mixer nozzle and hence thoroughly combined. This approach could prevent the formation of micro-bubbles during the mixing process. . . . . 209
- B.2 Fabrication procedure of the individually constrained soft robotic actuator. **(a)** Assembly of 3D-printed mold for inner chamber walls; **(b)** Deposit of RTV silicone with automatic mixing dispenser; **(c)** Wrapping of fiber constraints to the inner chamber walls; **(d)** Assembly of inner chamber wall with the mold of outer wall; **(e)** Deposit of RTV silicone to form outer wall; **(f)** Demolding, trimming and addition of silicone tubes to attain final product. . . . . 210

- B.3 **(a)** CAD/CAM model of the soft actuator internal structure with overall constraint. The air chamber can expand when being pressurized. Both the bellow sheath and close-coiled spring act as physical constraint of the air chambers, forcing them to expand in axial direction, which leads to bending motion; **(b)** Illustration of the cross-sectional design and dimensions; **(c)** Soft robotic actuator with overall constraints; **(d)** The bellow sheath constraint obtained by compressing a braided fiber mesh. The constraint sheath with bellow structure restricts radial expansion of the actuator during chamber inflation but allows elongation to permit bending. . . . . 212
- B.4 Experimental result of the actuator stiffness analysis. The robot stiffness is measured by pushing its tip in lateral direction with a stepping motor. The contact force is measured by an industrial grade-force sensor. The soft actuation integrated with metal spring reinforce exhibit a significant improvement in stiffness, facilitate high actuation force and fast dynamic response. . . . . 213
- B.5 **(a)** FEA simulation result of an overall constrained soft actuation when one chamber is pressurized. Without any support, the instrument channel will collapse due to the internal expansion of fluidic chamber, hindering the movement of any instrument passing-through; **(b)** Closed-coil spring is integrated as a central channel to reinforce the integrity of the instrument channel, acting against the internal expansion pressure. . . . . 214
- B.6 **(a)** FEA model of the overall constrained soft actuation generated by Abaqus automatic meshing of C3D8; **(b)** Same robot FEA obtained by a well-structured manual mesh design; **(c)** FEA plot showing the high strain areas (red area) was observed at the corner and the outer surface of the bendable section, when one actuation chambers was inflated; **(d)** Revised cross-section design of the bendable section. The high strain areas found in previous FEA plot were reinforced with chamfered corners and thicker outer wall. . . . . 215



- B.7 (a) Fabrication procedure of the soft robotic actuator with overall constrained design. The soft body is molded with silicone rubber in 3D-printed mold. The cross-sectional geometry of the inflatable chamber shape is determined by the inner mold; (b) Exploded-view drawing of the actuation with closed-coil spring backbone, soft body and bellow sheath. The combined effect of these components allows much higher actuation pressures without rupture or bulging, while also enhancing the actuator's stiffness with the closed-coil spring; (c) Final assembly of the actuator. Two rigid fixtures are adhered to both ends, connecting silicone tubes and reinforcing the sealing at the typically weak end connections of soft actuators. . . . . 217

# List of Tables

2.1	Markings of ASTM F2503-13 MR environment classification . . . . .	44
3.1	Computation time of PQs on 1 million of mesh with different levels of bisections culling. . . . .	86
4.1	Specification of the MR Safe manipulator . . . . .	104
4.2	Measured performance indices averaged across 10 subjects in performing the robotic catheterization of the phantom model . . . . .	124
4.3	Latest technologies for MRI-based positional tracking . . . . .	127
5.1	Trajectory tracking performance under freely moveable environment . . . .	171
5.2	Trajectory tracking performance under constrained environment . . . . .	171
A.1	Communication protocol of motor control command and response between the central PC and microcontroller for motor control . . . . .	207
A.2	Sample message type of the communication protocol . . . . .	208

# List of Algorithms

3.1	General diffeomorphic demons framework . . . . .	69
5.1	Pseudocode of the training dataset pre-processing scheme. Input variable $\mathbf{Q}$ denotes the arbitrary training dataset obtained from experiment, and output variable $\mathbf{R}$ refers to the pre-processed training dataset. . . . .	160
5.2	Nonparametric online learning of inverse mapping. . . . .	162

# Nomenclature

## Acronyms

DBS	Deep Brain Stimulation
DD	Diffeomorphic Demons
DoF	Degree of Freedom
EM	Electromagnetic
EP	Electrophysiology
FOV	Field of View
FPGA	Field Programmable Gate Array
FPU	Floating Point Unit
GPU	Graphical Processing Unit
IK	Inverse Kinematics
Intra-op	Intra-Operative
LWPR	Locally Weighted Projection Regression
MIS	Minimally Invasive Surgery
MRI	Magnetic Resonance Imaging
PQ	Proximity Query
Pre-op	Pre-Operative
RCM	Remote Center of Motion
RF	Radiofrequency
RFA	Radiofrequency Ablation

RoI            Region of Interest

RTV Silicone   Room-Temperature-Vulcanizing Silicone



# Chapter 1

## Introduction

### 1.1 Motivation and Objectives

Magnetic resonance imaging (MRI)-guided robotics offers possibilities for physicians to perform interventions remotely on confined anatomy that could be visualized by high contrast volumetric scan during the procedure. MRI provides several unique modality properties for interventional operations: **i)** rapid assessment of tissue deformation, **ii)** clear detection of pathological and physiological changes of targeted anatomy (e.g. scars and edema created by tissue ablation), and **iii)** no ionizing and harmful radiation emitted throughout the scan. However, the enclosed environment of the magnetic bore physically hinders surgeons from adequate access to the patient while imaging is performed.

Large amount of MRI data will also have to be processed instantly to provide surgeons with clear pathologic indication and detailed structural information for enhanced interventional guidance. These strongly drive the demand of developing an MRI-guided robotic system integrated with intra-operative (op) MRI data. Computational complexity of processing such volumetric Magnetic Resonance (MR) scan still poses an unmet technical requirement for providing smooth and consistent operation workflow.

While the majority of research focused on navigation with a linear entry pathway, e.g. tissue biopsy [12] or placement of brachytherapy seed [33] with straight needles, MRI-guided intervention is still only relevant to a small fraction of all surgeries. Many interventions do not have the viable MRI conditional instrument to reach the surgical sites.

These sites may only be reached through narrow and twisted entry pathways. Moreover, the instrument should also provide sufficient articulation after reaching the site. All of these technical challenges drive the demand for enhanced design and control scheme for continuum robotic tools.

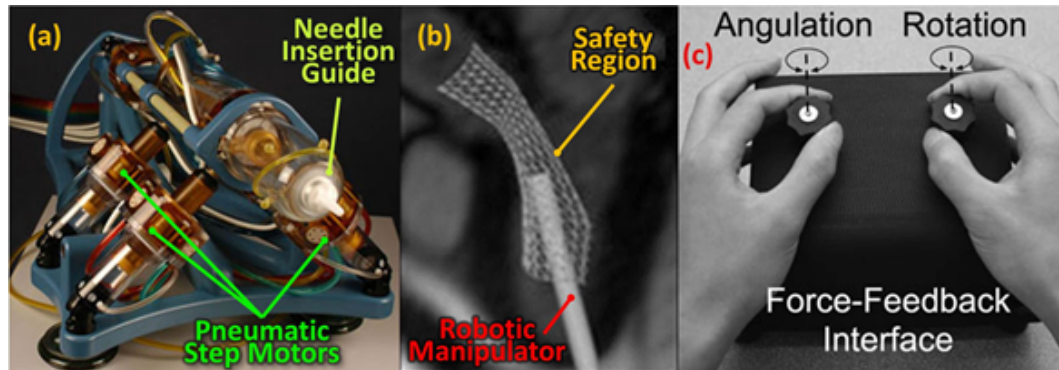


**Figure 1.1:** (a) MrBot: an MR-conditional robot actuated by pneumatic step motor for image-guided access of the prostate gland; (b) Virtual robotic manipulator and corresponding safety operation region augmented on MR image; (c) Motion input interface incorporated with force-feedback that resists the instrument deviated from the safety region defined along the luminal structure.

Furthermore, there are very few research efforts on investigation of novel robotic control approaches (e.g. [34], Fig. 1.1a) which facilitate visual and haptic guidance (Fig. 1.1b) using the teleoperated interface (Fig. 1.1c) through direct interfacing with MR scanners. Such approach involves real-time scanning mode in compensation of image quality, whereas rapid recovery of tissue morphology inevitably leads to great computation challenges. Another primary focus is also to pursue safe actuation under MRI circumstance, where ferromagnetic material and electromagnetic (EM) interference are ought to be avoided. The current advances of MR conditional motors (e.g. [13]) still have not fulfilled the standard of natural, delicate robotic instrument control regarding output speed, torque and accuracy, akin to the manually manoeuvring of a handheld instrument. The above unresolved technical challenges make the existing platforms clinically impractical, and also not being tested in real clinical trials.

The ultimate goal of my study is to develop a generic hardware and software framework that integrates intra-op MRI, continuum robotic instrument and enhanced visual guidance to improve outcomes of various therapeutic interventions in terms of surgical safety, accuracy and effectiveness. (Fig. 1.2) The main objectives of this thesis include:

1. To enable a real-time, large-scale proximity query (PQ) scheme for computing the relative configurations or potential collision between robotic manipulators and



- surgical environments by utilizing novel computational architecture;
2. To accelerate non-rigid intensity-based image registration for updating and re-align the high-quality anatomical model acquired pre-operatively to the intra-operative images, facilitating surgical planning and navigation during procedures;
  3. To propose MR Safe actuation and control techniques for a robotic catheter platform that incorporates real-time image registration, high performance hydraulic actuation, MR-based tracking and enhanced human-robot control interface.
  4. To investigate the use of model-free control method for enhancing human-robot interface of robotic catheter.
  5. To propose a flexible design scheme for optimization of soft and flexible robotic manipulator based on finite element analysis (FEA);
  6. To exploit online nonparametric local learning and FEA technique with the aim of directly approximating the inverse kinematics of a redundantly actuated flexible manipulator, thus to achieve precise feedback control even under dynamic external disturbance.

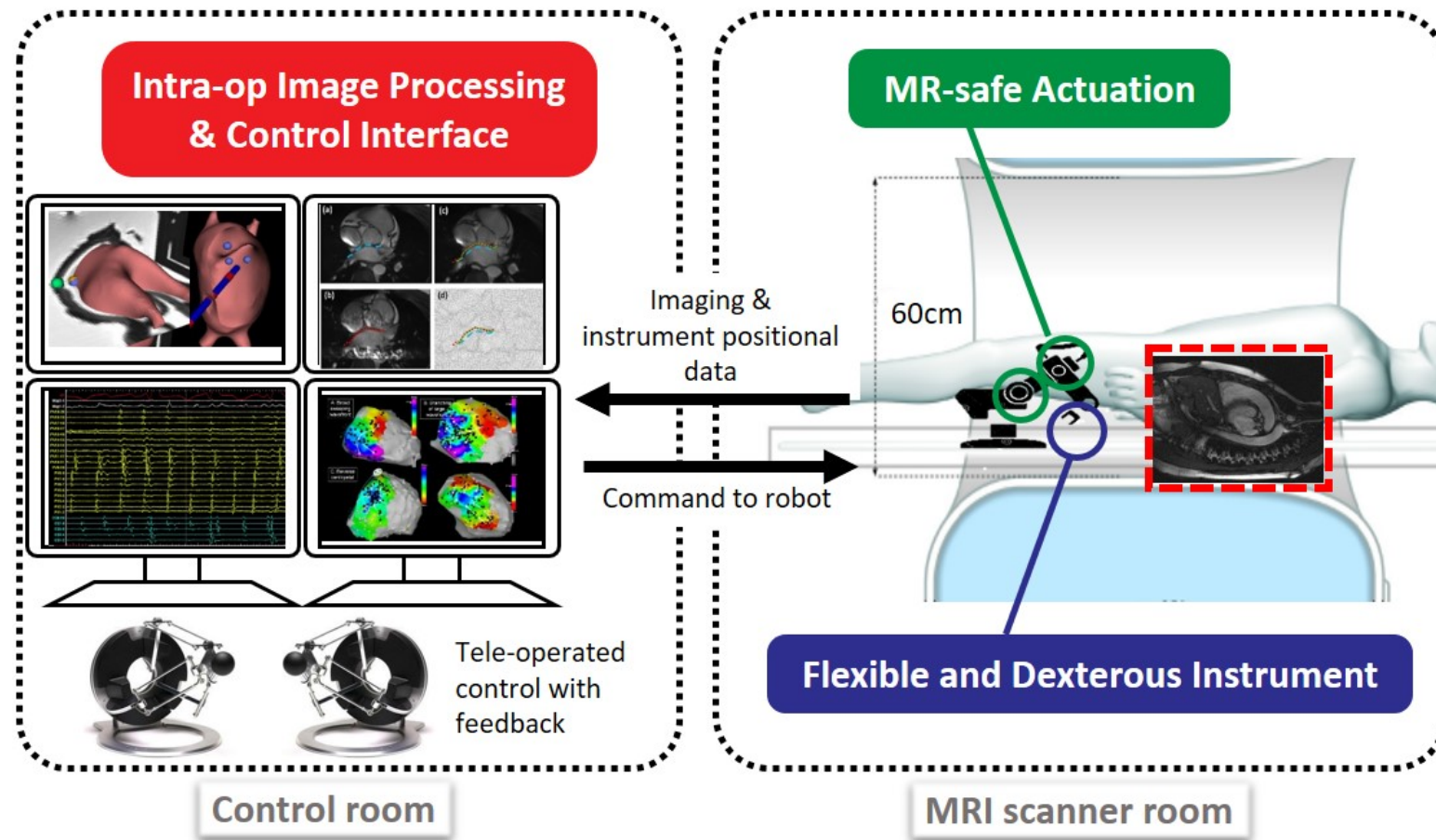


**Figure 1.2:** Integrated robotic framework comprising the high performance image processing, teleoperation control interface, MR Safe actuation and continuum surgical instrument.

## 1.2 Thesis Organization and Main Technical Contributions

**Chapter 2** provides an overview of the current robot-assisted MRI-guided interventions. The latest advancement in interventional MRI system and associated techniques have been introduced. The safety classification for MRI devices is also highlighted. This chapter presents the previous work on MRI-guided robotic systems from a historical perspective in three major types of interventions, namely neurosurgery, prostate intervention and breast biopsy. Their clinical considerations and key technical challenges are also discussed in detail. In this chapter, the design and control for soft robot are also reviewed, with the aim of exploring their potential applications in MRI-guided interventions. Finally, this chapter concludes by highlighting some of the current trends and future development directions of robot-assisted MRI-guided interventions.

In **Chapter 3**, novel high performance computation schemes for solving large scale data processing problem, namely intensity-based deformable image registration and proximity query are introduced. Fast deformable registration is a prerequisite to intra-op update of surgical plans. The initial 3-D navigation anatomical “roadmap”, used for guidance during interventions, is computed and acquired pre-operatively from high-quality MR images. This chapter presents the incorporation of novel computational architecture that could register/update the high-quality anatomical model obtained pre-operatively for intra-op robotic surgical planning. It involves real-time deformable co-registration between pre- and intra-op MR images, which is a well-known challenge. Furthermore, a novel type of fast Proximity Query (PQ) based on high performance computing is also proposed to impose a safety boundary that is synchronized to tissue deformation. Hence, operators can intuitively navigate with this online guidance and appropriately react to dynamic soft tissue environments throughout the surgery.

**Chapter 4** presents timely and key enabling techniques that could realize the robotic catheter platform under magnetic resonance imaging (MRI). The proposed robotic catheterization system integrates the enhanced monitoring of lesions creation using MRI, with the aim of improving procedural safety, accuracy and effectiveness. These aspects are of paramount importance to cardiac electrophysiological intervention, which is the effective treatment of arrhythmia. The relevant technical challenges are reviewed. This chapter presents the first MR Safe robot for intra-cardiac electrophysiology (EP) intervention. Its robot actuation features small hysteresis, effective force transmission and quick response, which has been experimentally verified for its capability to precisely tele-manipulate a standard EP catheter. Moreover, this chapter also reviews the timely

techniques for real-time positional tracking in MRI and intra-operative image registration, which can be integrated with the presented robotic catheter platform to improve the surgical outcome. The proposed system is also validated with a series of subject tests.

**Chapter 5** describes the design of an MR Safe soft robotics actuator and its closed-loop control scheme to fulfil high-precision, -compliance and -dexterity of robotic interventional tools, but also without deteriorating MRI quality. The pneumatic/hydraulic driven actuators made of soft materials are inherently compatible with the strong magnetic field of MRI. This chapter also proposes a model-free control framework which adopts online nonparametric local learning technique to enable precise manipulation of the soft actuators, even in the presence of dynamic external disturbance. Advanced formulation of finite element analysis (FEA) is also employed to initialize the control policy, hence eliminating the need for random exploration in the robot's workspace. This closed-loop controlled continuum robot can traverse confined environments and provide effective manipulation in many robot-assisted interventions.

Finally, **Chapter 6** summarises this thesis by highlighting the technical merits and potential pitfalls of the proposed MRI-guided intervention approach with continuum robotic techniques. A detailed discussion concerning the possible future research directions is also provided.

The original technical innovations and contributions of this thesis include:

- Development of a high performance, large deformation non-rigid image registration scheme based on novel computational architecture to achieve 60 times speed up;
- Design and implementation of a versatile, fast PQ formulation by exploiting the parallelism of Graphical Processing Unit (GPU), in which the unstructured environment involved in robotic tasks can be flexibly represented by irregular triangular meshes, without having to preprocess the input geometric data;
- Development of an MR Safe robotic catheter platform, which is the first of its kind that offers sufficient degrees of freedom (DoFs) to tele-manipulate a standard catheter under intra-op MRI guidance.
- Experimental validation and quantitative evaluation of model-based and model-free control methods for robotic catheter navigation with subject tests.
- Design optimization of fluid-driven soft robotic actuators with individual constraints via advanced Finite Element Analysis (FEA) formulation;

- Development of an online nonparametric local learning technique with the aim to directly approximate the inverse kinematics of a redundantly-actuated, fluid-driven endoscope prototype for soft robot control in 3-D space;
- Development and integration of an FEA model into the online learning method, providing a reliable initialization of the inverse model before deployment of the proposed controller in practical scenarios;

### 1.3 Publications for the Work Presented in this Report

The work conducted in my study period has resulted in the following publications in peer-reviewed international journals and conference proceedings, as well as patents:

- [1] **K. H. Lee**, D. K. Fu, M. C. Leong, M. Chow, H. C. Fu, K. Althoefer, K. Y. Sze, C. K. Yeung, and K. W. Kwok, “Nonparametric online learning control for soft continuum robot: An enabling technique for effective endoscopic navigation,” *Soft Robotics*, vol. 4, no. 4, pp. 324–337, 2017.
- [2] **K. H. Lee\***, D. K. C. Fu\*, Z. Guo, Z. Dong, M. C. W. Leong, C. L. Cheung, A. P. W. Lee, and K. W. Kwok, “MR safe robotic manipulator for MRI-guided intracardiac catheterization,” *IEEE/ASME Transactions on Mechatronics*, vol. 23, no. 2, pp. 586–595, 2018. (\* indicate co-first author).
- [3] **K. H. Lee**, M. C. Leong, M. C. Chow, H. C. Fu, W. Luk, K. Y. Sze, C. K. Yeung, and K. W. Kwok, “FEM-based soft robotic control framework for intracavitary navigation,” in *Proceedings of IEEE International Conference on Real-time Computing and Robotics (RCAR)*, 2017. (Received the best conference paper award).
- [4] **K. H. Lee**, Z. Guo, G. C. Chow, Y. Chen, W. Luk, and K. W. Kwok, “GPU-based proximity query processing on unstructured triangular mesh model,” in *Proceedings of IEEE International Conference on Robotics and Automation (ICRA)*, pp. 4405–4411, IEEE, 2015.
- [5] Z. Guo, Z. Dong, **K. H. Lee**, C. L. Cheung, H. C. Fu, J. D. L. Ho, H. He, W. S. Poon, D. T. M. Chan, and K. W. Kwok, “Compact design of a hydraulic driving robot for intraoperative MRI-guided bilateral stereotactic neurosurgery,” *IEEE Robotics and*

- Automation Letters*, vol. 3, pp. 2515–2522, July 2018. (Received the best conference paper award of ICRA2018).
- [6] X. Wang, **K. H. Lee**, D. K. C. Fu, Z. Dong, K. Wang, G. Fang, S. L. Lee, A. P. W. Lee, and K. W. Kwok, “Experimental validation of robot-assisted cardiovascular catheterization: model-based versus model-free control,” *International journal of computer assisted radiology and surgery*, pp. 1–8, 2018.
- [7] J. D. L. Ho, **K. H. Lee**, W. L. Tang, K. M. Hui, K. Althoefer, J. Lam, and K. W. Kwok, “Localized online learning-based control of a soft redundant manipulator under variable loading,” *Advanced Robotics*, pp. 1–16, 2018.
- [8] Z. Dong, Z. Guo, **K. H. Lee**, G. Fang, W. L. Tang, H. C. Chang, D. T. M. Chan, and K. W. Kwok, “High-performance continuous hydraulic motor for MR safe robotic teleoperation,” *IEEE Robotics and Automation Letters*, vol. 4, no. 2, pp. 1964–1971, 2019.
- [9] G. Fang, X. Wang, K. Wang, **K. H. Lee**, J. D. Ho, H. C. Fu, D. K. C. Fu, and K. W. Kwok, “Vision-based online learning kinematic control for soft robots using local gaussian process regression,” *IEEE Robotics and Automation Letters*, vol. 4, no. 2, pp. 1194–1201, 2019.
- [10] T. L. T. Lun, K. Wang, J. D. Ho, **K. H. Lee**, K. Y. Sze, and K. W. Kwok, “Real-time surface shape sensing for soft and flexible structures using fiber bragg gratings,” *IEEE Robotics and Automation Letters*, vol. 4, no. 2, pp. 1454–1461, 2019.
- [11] Z. Zhang, Y. Xin, B. Liu, W. X. Li, **K. H. Lee**, C. F. Ng, D. Stoyanov, R. C. Cheung, and K. W. Kwok, “FPGA-based high-performance collision detection: an enabling technique for image-guided robotic surgery,” *Frontiers in Robotics and AI*, vol. 3, p. 51, 2016.
- [12] M. Yin, Y. Chen, **K. H. Lee**, D. K. Fu, Z. T. H. Tse, and K. W. Kwok, “Dynamic modeling and characterization of the core-xycartesian motion system,” in *2018 IEEE International Conference on Real-time Computing and Robotics (RCAR)*, pp. 206–211, IEEE, 2018.
- [13] C. L. Cheung, **K. H. Lee**, Z. Guo, Z. Dong, C. W. M. Leong, A. P. W. Lee, K. W. Kwok, and Y. Chen, “Kinematic-model-free positional control for robot-assisted cardiac catheterization,” in *Proceedings of The Hamlyn Symposium on Medical Robotics*, Imperial College London, 2016.

- [14] J. Li, T. Kong, J. Yu, **K. H. Lee**, Y. H. Tang, J. T. KIM, H. C. Shum, *et al.*, “Electrocoiling-guided printing of multiscale architectures at single-wavelength resolution,” *Lab on a Chip*, 2019, (Pre-print).
- [15] V. Vardhanabhuti, Z. Liu, W. Jiang, **K. H. Lee**, S. Zhang, and K. W. Kwok, “Transfer learning application to prostate magnetic resonance imaging in detecting clinically significant prostate cancer,” *ECR, Abstract book*, 2019, (Accepted).
- [16] H. C. Fu, J. D. L. Ho, **K. H. Lee**, Y. C. Hu, S. K. Au, S. K. Y. Cho, Kyu Jin, and K. W. Kwok, “Interfacing soft and hard: a spring reinforced actuator,” *Soft Robotics*, (Under review).
- [17] K. W. Kwok, Z. Dong, Z. Guo, K. C. D. Fu, **K. H. Lee**, and C. L. Cheung, “Robotic catheter system for MRI-guided cardiovascular interventions,” Dec. 28 2017. US Patent App. 15/630,406.
- [18] Z. Guo, K. W. Kwok, Z. Dong, **K. H. Lee**, H. C. Fu, and C. L. Cheung, “Robotic stereotactic system for MRI-guided neurosurgery.” US Prov. Patent: US62/623,280.
- [19] Z. Dong, K. W. Kwok, Z. Guo, and **K. H. Lee**, “Fluid powered master-slave actuation for MRI-guided interventions.” US Prov. Patent: US62/640,3029.





## Chapter 2

# MRI-guided Robot-assisted Interventions

### 2.1 Introduction

The first robotic system for MRI environment dates back to 20 years ago. In 1995, Masamune *et al.* [5] reported the first MRI-compatible needle manipulator designed for stereotactic neurosurgery. Since then, extensive effort has been devoted to developing numerous teleoperated systems for various MRI-guided interventions, including prostate, breast or liver biopsy. Clinical/ Pre-clinical validations have demonstrated their unprecedented navigation accuracy and safety, accredited to the teleoperated manipulation and real-time MR imaging. Intra-op MRI enables reliable monitoring and compensation of soft tissue deformation. It also allows surgeons to determine if the surgical goals have been met, then to react upon that information as necessary. Despite all these unique advantages, MRI-guided robotics system has yet entered the mainstream of clinical practice, and commercialized systems are yet available. The extreme magnetic field, restricted workspace and constraints on EM interference impose significant challenges on the effectiveness and safety of robotic devices in MRI environments. With the increasing maturity of MR Conditional robotics techniques, there is new hope for accelerating the developing trend of MRI-guided robot-assisted system and compact manipulator can be realized by piezoelectric motors that generate motion by applying EM field on magnetism-free piezoelectric crystals. Novel high performance pneumatic/hydraulic actuation that is inherently MR Safe are also developed, enabling manipulation that is free

from EM interference [35]. Advances in MR-based tracking also provide 3D positional tracking of surgical instruments within the imaging coordinates, making task-space feedback control of robotic devices possible even under MR environments.

This chapter will provide an overview of the state-of-the-art interventional MRI systems and the development of MRI-guided robotic intervention from a historical perspective. It will also cover the latest development in soft continuum robotics and discuss its potential applications in image-guided surgery. Furthermore, the clinical motivations of employing continuum robotic system in MRI-guided interventions will also be highlighted. This chapter will establish the basis for the technical issues to be addressed in this thesis.

## 2.2 Recent Advances in Interventional MRI Technology

In modern medicine, Magnetic Resonance Imaging (MRI) is an indispensable imaging modality for diagnosis and pre-operative planning. MRI is also a versatile tool for a wide variety of clinical and basic science research, as it offers intrinsically three-dimensional (3D) scanning without emitting ionizing radiation. One unique feature of MRI is that it offers high contrast imaging of soft tissue, allowing visualization of morphology and anatomical structure of the patient's inner cavity. The morphology details can be further enhanced by incorporating MR contrast agents. Magnetic resonance angiography (MRA) [36] is one example that gives rise to high-quality imaging of blood vessel and blood flow (Fig. 2.1a). For the assessment of anatomical function, a new technique called functional MRI (fMRI) has also been discovered (Fig. 2.1b). This technique can access the brain activities by measuring the hemodynamics (e.g. tissue perfusion and blood oxygen level-dependent (BOLD)) inside different brain regions, and thus to associate a functional mapping to mental operations. fMRI soon becomes a key imaging technique for neuroscience research and also studies on neurobiology change occurred during rehabilitation.

Recent advancement in MRI technology has broadened its usage from medical diagnosis to image-guided interventions. Substantial effort has been devoted to the development of various intra-op MRI scanner systems and new surgical devices dedicated to operating under MR environments. This section will provide a summary of the latest innovations in intra-op MRI.

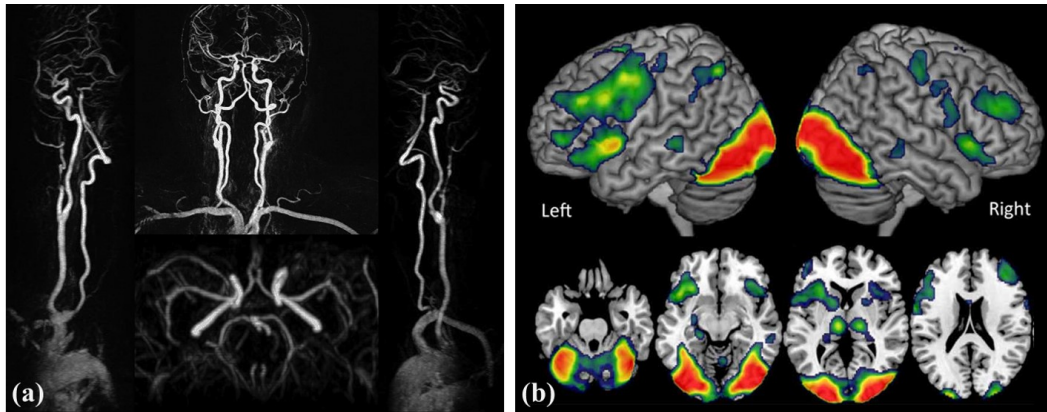


**Figure 2.1:** (a) Complete MR angiography (MRA) of the aortic arch extended to the vertex in frontal view; (b) Functional MRI (fMRI) denoting the activation of brain region responsible for phonological processing. **Image Source:** [1, 2]

To leverage the prevailing benefit of MRI-guided interventions, a number of intra-op MRI systems have been developed. The *Signa SP* was the first of its kind introduced by General Electric (GE) Healthcare in 1991 [37]. The open MRI design (also called "double doughnut" design) comprises of two magnetics on each side of the patient table, providing surgeons sufficient space to directly access the patient inside the scanner (Fig. 2.2a). However, such open-type scanners can only generate a relatively low magnetic field (0.02-0.7 Tesla) when compared to conventional scanners (1.5-3 Tesla), resulting in a reduced image resolution and also prolonged image acquisition time.

Another intra-op MRI system was developed by IMRIS Inc. in Manitoba, Canada (Fig. 2.2). The IMRIS suite features a high-field MR scanner with a close-bore design. The scanner can be moved "in-and-out" of an operating theatre with a ceiling-mounted rail. The system gives rise to improved patient safety and surgical-workflow, because the MRI

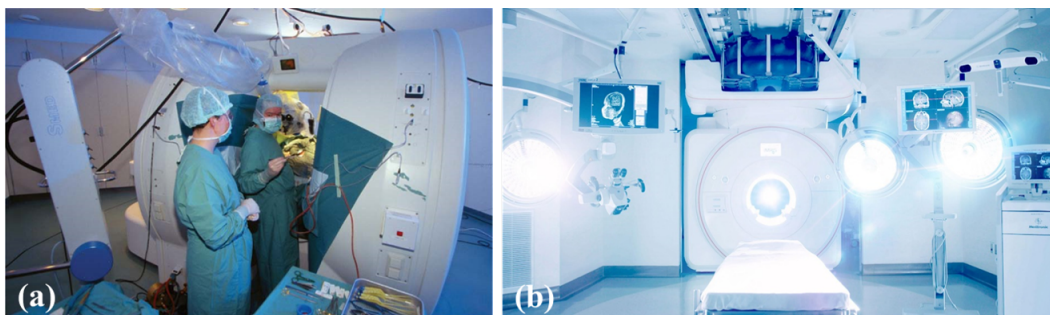


**Figure 2.2:** (a) Example surgery in a GE Signa SP 0.5T intra-op MRI. The surgeon can stand between the two magenets and perform surgery during MRI acquisition. (b) IMRIS operating suite equipped with a ceiling mounted MRI scanner, which can be moved in-and-out to accomodate the surgical workflow. **Image Source:** [3], IMRIS

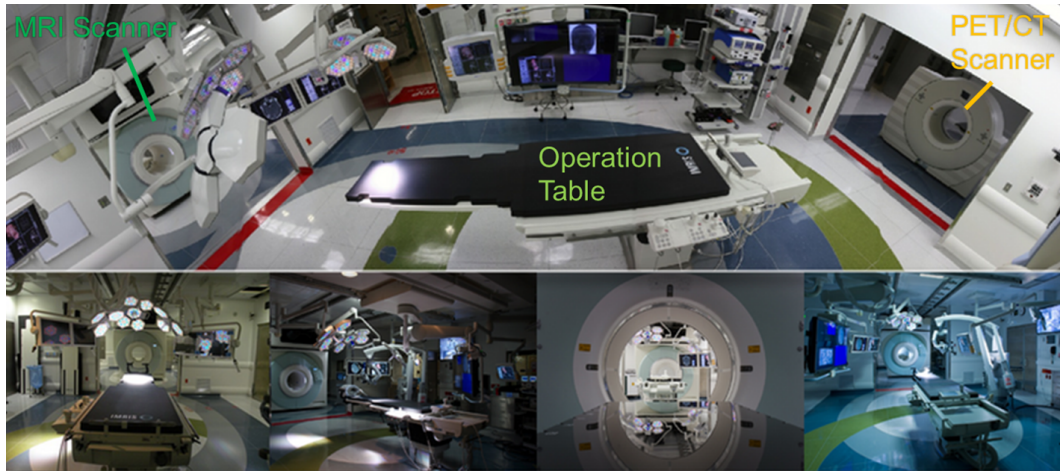


**Figure 2.3:** AMIGO multimodal image-guided operating suite at the Brigham and Women’s Hospital (BWH) and Harvard Medical School. **Image Source:** [4]

magnet can be brought in only when scanning is required, then move-out to give space for surgeons to continue the procedures. The system also possesses an MRI room that is separated from the operating theatre. The sliding doors in-between the two rooms are responsible for shielding radiofrequency (RF) and sound, so that the scanner can be used for diagnostic purpose when not used in surgical operations. Until 2018, over 60 IMRIS systems have been installed in hospitals worldwide (e.g. U.S., Germany, China, and Japan), indicating a growing trend of intra-op MRI-guided interventions. For the latest development, the Advanced Multimodality Image-Guided Operating (AMIGO) suite was introduced by the Brigham and Women’s Hospital (BWH) and Harvard Medical School in 2011 (Fig. 2.3). AMIGO was one of the first multimodality image-guided operating suite that offers immediate access to MRI, CT, ultrasound, X-ray and PET scan. The 5,700 square feet suite is divided into three separated procedural rooms, namely MRI room, operating room, and PET/CT room. The patient can be rapidly transferred between rooms on-demand throughout the procedure.

### 2.3 Robotic System for MRI-guided Surgery

Although MRI possesses many unique advantages, it presents a critical burden in image-guided interventions: limited access to the patient. For a typical closed MR scanners, the size of the cylindrical bore is only around 60cm in diameter and 1.2m to 2m in length, while new commercial systems offer 70cm diameter. This type of scanners can generate magnetic field strength of 1.5T to 3T, which enables high signal response and

generates decent homogeneity of magnetic field. Since the patient must stay at the isocenter to acquire best image quality, the enclosed environment of the magnetic bore physically hinders the surgeon from sufficient access to the patient. The open-type scanner (e.g. *GE Signa SP*) is not an ideal choice of intra-op image guidance because of its limited magnetic field strength (0.02-0.7T), leading to lower image quality and longer image acquisition time. As a result, the closed-type, cylindrical scanners are still the mainstream for the practice of intra-op MRI-guided procedures. Yet, the patient is required to be removed from the scanner after image acquisition, so that surgeons can gain access and carry on the procedure. Then the patient is often reinserted to the scanner to reassure the accurate placement of surgical tools. These steps might need to be repeated until the correct tool placement is verified with intra-op scans. This moving in-and-out paradigm inevitably leads to a complicated surgical workflow, causing prolonged surgical time and additional discomfort to patients. To pursue a seamless workflow of MRI-guided interventions, various robotics systems have been developed and validated clinically throughout the last decade. The primary goal of these studies is to develop fully teleoperated platforms that can work inside the scanner even when scanning is performed. Thus, the patients can remain unmoved in the scanner throughout the surgery.




This section gives an overview of the development of robotic platforms for MRI-guided interventions. It will briefly introduce the safety requirement for instruments to be used under MRI environments, then followed by a detailed review on the current development trend of MRI-guided robotic systems in three major surgical domains, namely neurosurgery, prostate interventions and breast biopsy.

### 2.3.1 MRI Safety Classification

MRI scanner performs imaging by incorporating high-intensity primary magnetic fields, rapidly modulated magnetic field gradients, and excitation RF pulse. Such characteristics prohibit the use of standard robotic or mechatronic setup, which often comprise of metallic components and electromagnetic (EM) actuation. As a result, this discrepancy drives the development of a new generation of devices: the MR-compatible systems.

In 1993, devices for the MR environment was only classified by MRI Compatible or Incompatible [38]. Despite the wide acceptance of this classification, its formal definition is still unclear, lacking descriptive information for system designer [39, 40]. This has led to the introduction of new standards such as the American Society for Testing and Materials

**Table 2.1:** Markings of ASTM F2503-13 MR environment classification

<p>MR Safe</p> 	<p>An item that poses no known hazards resulting from exposure to any MR environments. MR Safe items are composed of materials that are electrically nonconductive, nonmetallic, and nonmagnetic.</p> <p>An item composed entirely of electrically nonconductive, nonmetallic and nonmagnetic materials may be determined to be MR Safe by providing a scientifically based rationale rather than test data. Examples of MR Safe items are a cotton blanket or a silicone catheter.</p>
<p>MR Conditional</p> 	<p>An item with demonstrated safety in the MR environment within defined conditions. At a minimum, address the conditions of the static magnetic field, the switched gradient magnetic field and the radiofrequency fields. Additional conditions, including specific configurations of the item, may be required.</p> <p>Supplementary Marking - Additional information that, in association with a marking as "MR Conditional," states via additional language the conditions in which an item can be used safely within the MR environment.</p>
<p>MR Unsafe</p> 	<p>An item which poses unacceptable risks to the patient, medical staff or other persons within the MR environment.</p>

(ASTM), which aims to provide a meticulous classification (ASTM F2503) for devices that work under MR environment (Table 2.1). The devices are also required to meet a series of test standard (ASTM F2052, F2213, F2182, F2119). Moreover, Food and Drug Administration (FDA) also demand that all clinically used device in the United States must fulfill these standards.

The ASTM standards offer a comprehensive definition and specification on the MR devices design requirements. First of all, it detailed a rational guideline that devices solely made of nonconductive, nonmetallic, and nonmagnetic materials pose no known hazards in the MR environment. Device that fulfills the definition can be claimed "MR Safe". Further, it also lays the regulatory foundation for the definition of MRI safety based on a scientific rationale.

Due to the safety concerns of testing a device in actual MR environments, any device that uses electricity is not qualified to be claimed MR Safe. This gives rise to the "MR

Conditional" category to distinguish electrical devices that can operate safely inside MRI environments. [41, 42] The test procedure for an MR Conditional device is usually more complicated, as proper test must be performed in all MR environments associated with the specific procedure. In contrast, MR Safe devices can circumvent such testing requirements and be applied to a broader range of applications. Thus, it is generally preferable to design a device to meet the MR Safe standard. Another key incentive is that it can simplify the clinical translation as governed by the regulatory protocol and to wider dissemination.

There is still a technical gap for the development of clinical instruments that are capable of operating accurately and safely inside an MRI, without deteriorating the imaging quality [43]. Furthermore, most of the pioneering research on MRI guided interventions were relying on direct manual operation in clinical trials[44–46]. The pursue of teleoperated and robotic devices is then followed, with the aim of enhancing the surgical outcome. However, the migration of robotic devices will require innovations in MRI Conditional version of many essential components, such as sensing and actuation. It is because most of these robotic components (e.g. EM motors) are typically not safe in MR environments. The following of this chapter will highlight the key research achievements in the previous development of MRI-guided interventional devices.

### 2.3.2 Neurosurgery

Neurosurgery is one of the earliest domains that adopt robotic tools in MRI-guided interventions. Stereotactic is typical neurosurgical approach that involves high precision device positioning techniques. With the aims of locating 3D targets within the brain, stereotactic technique is widely used in various procedures, e.g. biopsy, needle placement, catheter placement or deep brain stimulation (DBS).

Although the standard workflow has been well-established and practiced for many decades, stereotactic is still considered a challenging procedure due to the high demand for accuracy and minimal invasiveness. DBS is an example stereotactic procedure designed to treat debilitating motor symptoms of Parkinson's disease (PD) and dystonia. In the procedure, the surgeon has to insert two long needles of 300mm length into the patient's skull via burr holes ( $\leq 14$ mm). Each needle is embedded with a stimulation electrode that will hence be implanted to the deep brain region of interest, delivering electrical impulses. The needle placement requires high surgical accuracy, in which an average acceptable error is only 2-3mm [47]. In conventional fluoroscopy/computed tomography (CT) guided

DBS, the pre-op MRI will be fused with intra-op CT for surgical planning and navigation guidance. Yet, the reliability of the fused roadmap is often deteriorated by deformation of brain tissue, namely "Brain shift" effect. Such shift is a result of the gravity and also leakage of cerebrospinal fluid (CSF) after a burr hole is opened, causing a misalignment up to 10-30mm [48] from the pre-op roadmap. Therefore, microelectrode recording (MER) is frequently adopted to assure proper placement of electrodes in conventional DBS procedures that utilize fluoroscopy/computed tomography (CT) as image guidance. However, the MER can only access the corresponding symptoms while the patient is awake under local anesthesia, which further convolute the stereotactic navigation and lead to prolonged surgery time (3-6 hours).

These obstacles have drawn increasing attention to intra-op MRI-guided stereotaxy. MRI is advantageous in high-contrast visualization of soft tissue anatomies in the deep brain region, such as the subthalamic nucleus (STN), globus pallidus interna (GPi) or ventral intermediate nucleus. Furthermore, MRI also allows intraoperative monitoring and refinement of the instrument placement, without emitting ionizing radiation.

The first MR conditional robots that can perform neurosurgery inside a closed scanner was developed by Masamune *et al.* [5] in Tokyo University, 1995 (Fig. 2.4). The robot is actuated by ultrasonic motors and primarily constructed by polyethylene terephthalate (PET). Optical encoders provide accurate position feedback of motor shafts movements. The robot can manipulate a needle inserter with 6-DoF, targeting the needle with an accuracy of approximately 3mm. Following that, Miyata *et al.* [6] developed an endoscopic micro-grasping forceps manipulator to perform more complicated neurosurgical procedures. The system comprises two micro-manipulator with 5DoF, each has a diameter of 3.2mm. Grasping and movement of tissue are achieved by the cam cylinder mechanism. The robot also contains a neuro-endoscope, an irrigation tube and a suction tube. These tools can all enter the burr hole with an insertion tube of 10mm (Fig. 2.4). Chizei *et al.* [49] also developed a surgical assistive robot platform designed to work inside a low-field interventional scanner (i.e., Signa SP 0.5T [GE Medical Systems, Boston, Massachusetts, USA]). The navigation can be realized with an external optical tracking system [50], without the need for a stereotactic frame. Limited by the size of MRI bore, the piezoelectric actuators are forced to be installed on the top of the scanner, far from the actual operation site. Two long titanium arms are responsible for transmitting the manipulation to the end effectors. One major drawback of the design is that the surgeons can only operate within the confined space between the two imaging magnets. Such arrangement hinders their performance when complicated operation is required. The image



quality is also deteriorated by the metallic components of the robot.

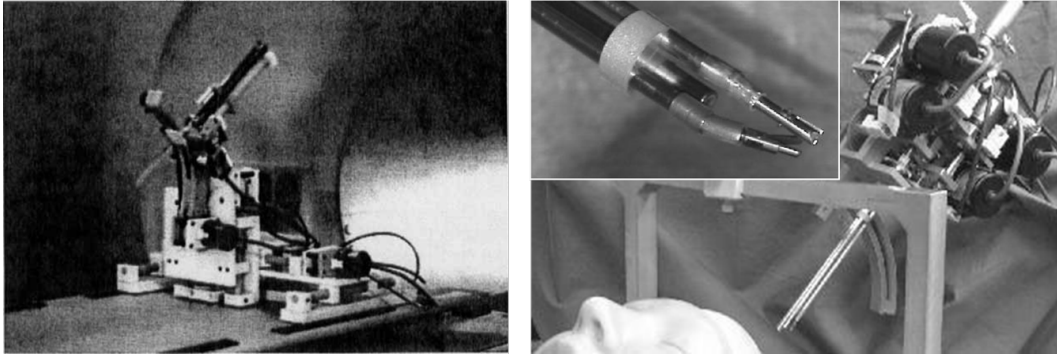


**Figure 2.4:** The first MRI compatible robotic needle manipulator for neurosurgery. A later upgrade of the system has incorporated 2 micro-grasping forceps for endoscopic microsurgery. (The University of Tokyo, Tokyo, Japan) **Image Source:** [5, 6]

Following that, an MR conditional robotic platform for teleoperated microsurgery and stereotactic brain biopsy, *NeuroArm/SYMBIS surgical system* (Fig. 2.5), is developed by Deerfield Imaging, Minnetonka, Minnesota, USA [7, 51, 52]. Integrated with two 7 DoF arms, the robotic system is capable of teleoperation via a remote console. It also provides many assistive features for surgeons, such as motion scaling, force feedback augmentation, as well as tremor filtering. A clinical study demonstrated that the system was successful in the treatment of 18 patients with glioma [53]. It became the first FDA approved MRI-guided neurosurgery robot. With the advance of low-noise piezoelectric drive and EM shielding, Li *et al.* developed a robotic stereotaxy system that allows simultaneous actuation and imaging [8, 54] (Fig. 2.5). The 7-DoF needle driver can attain high targeting accuracy of 1.38mm. The drivers can also maintain a low signal-to-noise ratio (SNR) variation of less than 15% even when ultrasonic motor is active.

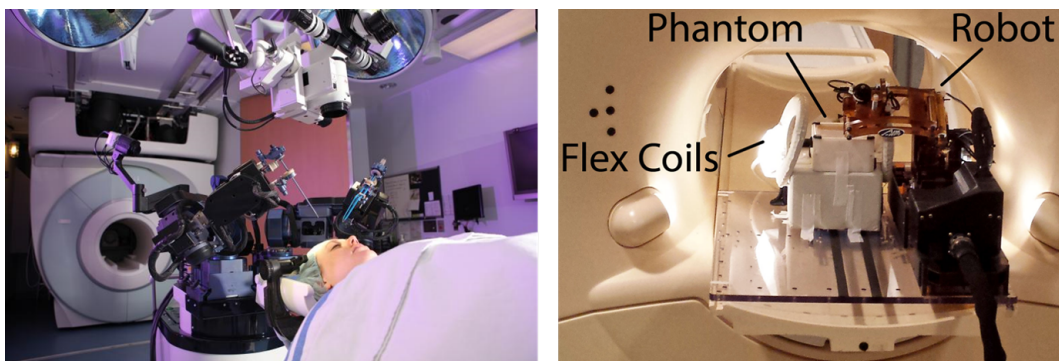


**Figure 2.5:** (Left) NeuroArm/SYMBIS surgical system consisted of two 7 DoF MR conditional teleoperated robotic arms; (Right) MRI-guided robotic stereotaxy system actuated by low-noise piezoelectric drives (Worcester Polytechnic Institute, Worcester, MA, USA). **Image Source:** [7, 8]

To further mitigate the EM interference emitted by piezoelectric drives, Ho *et al.* [55, 56] proposed a robot named *Mesoscale*, which is powered by shape-memory alloy

(SMA). The serially-linked robot arm is actuated by the contraction of SMA spring when heated with electric current. The actuator adopts a water-cooling system to enhance the response time of SMA spring [57], yet the robot still requires 6-10 sec to bend for 10°. Pneumatic/Hydraulics actuation is another form of energy source that does not involve EM interference. In 2008, Raoufi *et al.* developed a 6-DoF manipulator for MRI-guided neurosurgery [58]. The parallel mechanism manipulates the instrument using 6 pneumatic/hydraulic cylinders. However, precise and continuous motion control of pneumatic cylinders is a well-known challenge due to the friction of rubber O-ring sealing. The metallic materials of cylinders also affect the image quality. To enable needle manipulation with inherently MR Safe components, Stoianovici *et al.* [9] has developed a Remote Center of Motion (RCM) mechanism that is entirely made of electrically nonconductive, nonmetallic, and nonmagnetic materials (Fig. 2.6). Precise targeting of needle is thus realized by pneumatic stepping motors. Comber *et al.* [10, 59] has also explored a concentric tube robot for hippocampectomy by ablation (Fig. 2.6). The curved, nonlinear robot probe can traverse through the natural pathway to the hippocampus with a transforaminal approach. It provides access to deep brain region without the need for a burr hole opening on the skull.

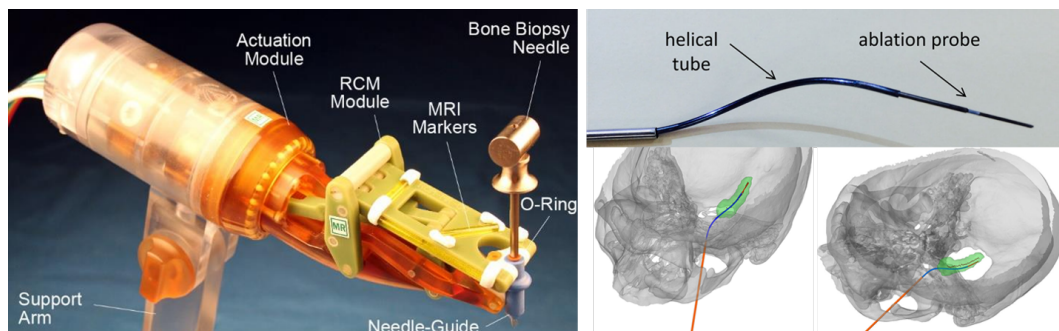


**Figure 2.6:** (Left) Multi-imager compatible and MR Safe needle guiding robot that utilize remote center of motion mechanism for manipulation (Johns Hopkins University, Baltimore, MD, USA); (Right) Concentric tube ablation probe that allows transforaminal access to hippocampus without the need for a burr hole on the patient skull. **Image Source:** [9, 10]

### 2.3.3 Prostate Interventions

Prostate cancer is known as the most common noncutaneous cancer in American male. In 2017, it has been predicted that there will be 161,360 new cases of prostate cancer in the United States, with a mortality rate up to 16.5% [60]. Conventional screening methods for prostate cancer include prostate-specific antigen test (PSA) and digital rectal exam (DRE) [61]. If these tests indicate abnormal results, needle biopsy will normally be recommended

to determine the existence of tumor and also whether the tumor is malignant or benign. Transrectal ultrasound (TRUS) guided biopsy is the current standard procedure to diagnose prostate cancer. In the procedure, 6-18 tissue samples will be taken from various locations (upper, mid, lower areas of the left and right side) of the gland to determine the region affected by the tumor cell.

However, the diagnostic accuracy of TRUS is limited by the poor image resolution of ultrasound. Accurate tumor localization is not feasible, therefore hinder its reliability in identifying and sampling from cancerous target sites [62]. As pointed out by [62], TRUS biopsy could only achieve sensitivity between 60% to 85% [63, 64]. MRI provides a new alternative for high precision guided biopsy. Its superior imaging capability in discriminating soft tissue enables accurate detection and localization of prostate lesions. With intra-op MRI-guidance, there is an increasing trend of targetted biopsy procedures that only take a few samples from the cancerous site of prostate gland. This approach can increase the targeting accuracy and also reduce the number of necessary biopsy samples as in TRUS, thus reducing patient discomfort.

To perform needle insertion under MRI environment, it requires a compact, MR-conditional manipulator that can fit inside the scanner bore, along with the patient. Various research prototypes have been developed in the last decade. An MR Conditional manipulator robot for transrectal prostate intervention was developed by Susil *et al.* in 2003 (Fig. 2.7a) [11, 65]. This work was the first of its kind to incorporate an imaging coil

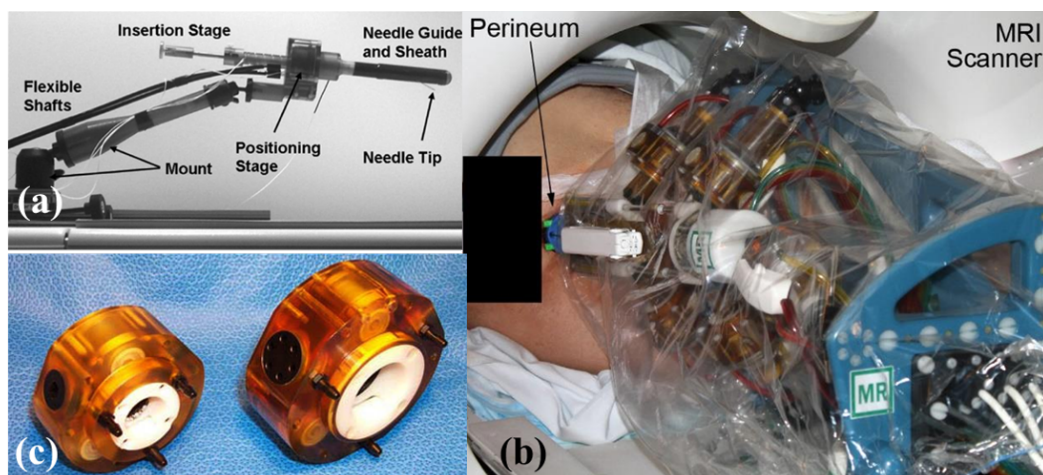


**Figure 2.7:** (a) MR compatible robotic needle manipulator for TRUS prostate interventions developed in The Johns Hopkins University, Baltimore, MD, USA; (b) MrBot, the pneumatic-driven MR Safe robot for prostate biopsy and patient in the MRI scanner; (c) PneuStep, the pneumatic step motor providing precise actuation for MrBot. **Image Source:** [11–13]

within the rectal sheath. Three active tracking coils and the needle guide were also integrated into the rectal sheath, achieving precision targeting with positional feedback. However, due to the limited length of the flexible transmission shafts, the surgeon had to operate the robot via the shafts while standing next to the bore of MR scanner. Stoianovici *et al.* developed a compact needle insertion robot, called *MrBot* (Fig. 2.7b) [12]. This robot enables complete teleoperation. The 6-DoF robot is actuated by a new type of pneumatic stepping motor (Fig. 2.7c) [13] that is made of nonmagnetic and dielectric materials, including plastics, ceramics, and rubbers. Recently, the latest version of *MrBot* has obtained FDA clearance and performed five successful clinical trials of transperineal needle targeting [66]. Similar MRI-guided needle targeting robotic system with pneumatic actuation was also demonstrated, including *Utrecht* robot developed by Van *et al.* [67] and the system designed by Yakar *et al.* [68].

In 2011, the first commercialized robot-assisted system for percutaneous intervention, *Innomotion* was introduced. The robotics system was designed to work inside both MRI and CT scanners [69]. The robot arm is equipped with pneumatic actuation and MRI-conditional optical encoder to fulfill the MRI safety requirements. Twenty successful clinical trials have been reported, but the product was eventually discontinued.



**Figure 2.8:** Innomotion™ robot-assisted system and Innomotion™ AMO biopsy needle guide for percutaneous intervention under CT/MRI. **Image Source:** INNOMEDIC

Besides pneumatic actuation, several piezoelectric driven platforms were also developed to achieve MRI-guided prostate interventions. Su *et al.* [14, 70] proposed the first piezoelectrically actuated robot (Fig. 2.9a) that integrates fiber optics sensor for MRI-guided prostate brachytherapy. The fiber optics sensor provides high-resolution force sensing of the needle insertion force. Song *et al.* [15, 16] developed a robotic platform that aims to enhance the resolution and workflow of traditional templated based needle placement, by incorporating high precision piezoelectric motor drive (Fig. 2.9b).

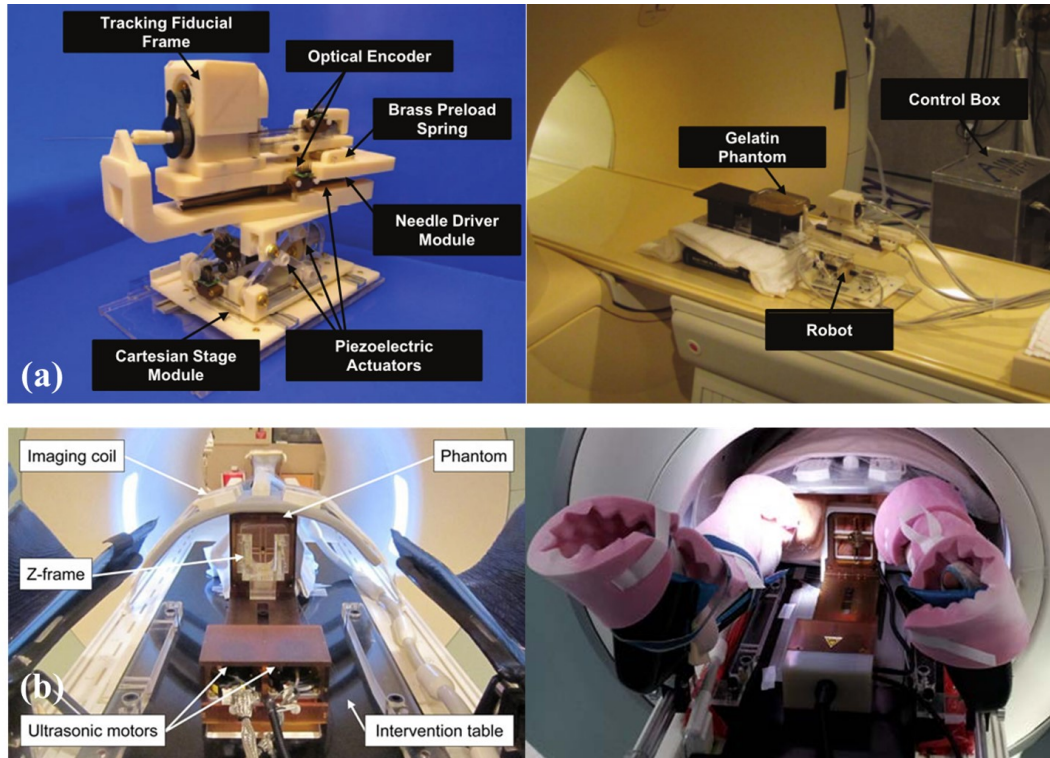


**Figure 2.9:** (a) MRI-guided needle placement robot integrated with fiber optic force sensing developed in Worcester Polytechnic Institute, Worcester, MA, USA; (b) Motorized needle guide template for MRI-guided transperineal prostate biopsy. **Image source:** [14–16]

### 2.3.4 Breast Biopsy

Breast cancer is one of the most common cancer worldwide. In 2012, there are an estimated 1.67 million new breast cancer cases, which is also the leading cause of cancer-related mortality [71]. Needle biopsy is currently the standard approach for breast cancer screening, in which a small tissue sample from suspicious lesions will be obtained through biopsy surgery for pathological diagnosis. Magnetic Resonance Mammography (MRM) is a favorable imaging modality for surgical navigation because it can visualize some abnormalities that are otherwise not observable on X-ray mammography nor ultrasound inspections. The sensitivity of MRM in breast cancer detection can reach 97% to 100% [72].

However, due to the size constraint of MRI bore ( $\varnothing 55\text{-}70\text{cm}$ ), the patient must be moved in and out of the MRI bore for multiple times to allow the needle to be inserted manually [73, 74]. Such an iterative process of position adjustment and verification led to prolonged surgical time and also patient discomfort. To enhance the surgical workflow, many robot-assisted systems are developed to enable tele-manipulation of biopsy needle within MRI bore.

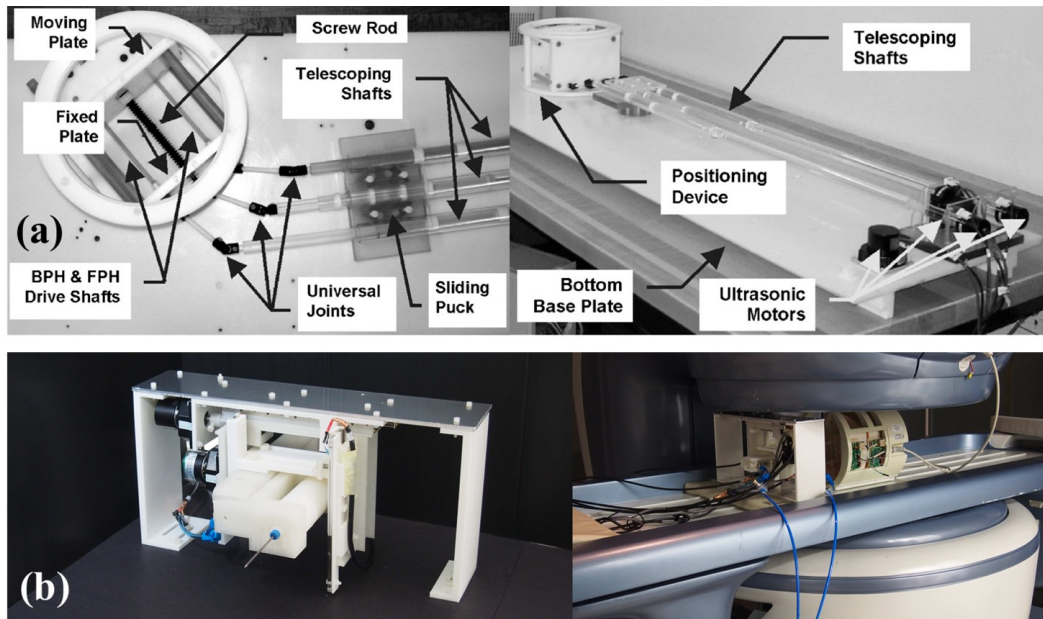


**Figure 2.10:** (a) MRI-guided robotic breast biopsy system equipped with telescoping shafts for motion transmission (University of Minnesota, Minneapolis, MN, USA); (b) Another MRI-compatible Cartesian manipulator for breast biopsy under open type MRI, developed by the Chinese University of Hong Kong, Hong Kong, China. **Image source:** [17, 18]

The *ROBITOM* (Robotic system for Biopsy and Interventional Therapy of Mammary lesions) system was the first MRI-conditional breast biopsy robot introduced by Kaiser *et al.* in 2001 [75, 76]. The system enabled simultaneous MR imaging and needle insertion inside the bore of a 1.5T scanner, without the need of moving the patient. Piezoelectric motors were employed. The newer version of *ROBITOM II* is also equipped with a high-speed trocar setting unit, which aims to reduce the breast deformation after manual insertion of needles. In 2004, Larson *et al.* proposed another MRI-guided robot-assisted breast biopsy system with a 5-DoF manipulator [17]. When compared with the previous design, this system can perform needle insertion from any desired orientations. Such improvement can be accredited to the rotating base mechanism with two compression plates, which is designed to compress the breast in the desired angle, facilitating fixture of needle insertion axis. The MRI-conditional actuation is achieved by ultrasound motors that drives multiple telescopic rotating shafts and universal joints (Fig. 2.10a).

Another robotics needle driver that allows insertion from both frontal and lateral directions in an open MRI scanner was developed by Navarro-Alarcon *et al.* [18]. The robot consists of a compact Cartesian mechanism that combines piezoelectric and pneumatic actuators. (Fig. 2.10b) To facilitate force control during needle insertion, Kokes *et al.* developed a 1-DoF needle driver for Radiofrequency ablation (RFA) of breast tumors [77]. It was achieved by adopting a 6-axis force sensor and a SensAble Phantom<sup>®</sup> to

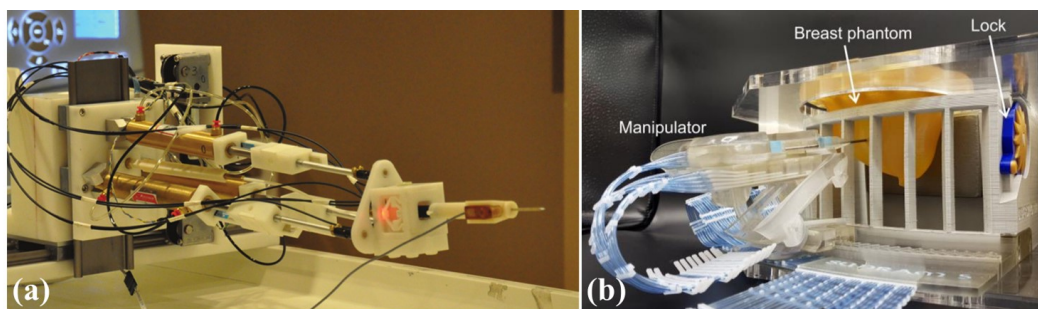


**Figure 2.11:** (a) Master-slave robot platform with pneumatic transmission for MRI-guided breast biopsy, developed by University of Maryland, College Park, MD, USA; (b) Sunram 5: An MR Safe robotic system for breast biopsy driven by 3D-printed pneumatic stepper motors. **Image source:** [19, 20]

provide real-time force feedback to the operator. A fully articulate version of the system with a 4-DoF manipulator was later developed by Yang *et al.* [19]. (Fig. 2.11a) The master-slave needle driving platform is positioned with parallel mechanism consisted of MR-compatible pneumatic cylinders. Although the parallel mechanism can attain high target accuracy, its large footprint hinders its deployment in clinical workflow. An MR Safe miniaturized system, *Sunram 5*, was developed by Groenhuis *et al.* in 2018[20, 78]. The system is mainly constructed by 3D-printed polymeric components and has a small footprint of  $72 \times 51 \times 40\text{mm}$ . The newly designed pneumatic stepper mechanism can achieve needle targeting with a mean positioning error of 0.7mm and repeatability of 0.1mm. (Fig. 2.11b)

## 2.4 Clinical Considerations and Technical Challenges of MRI-guided Robotic Intervention

Despite the tremendous effort on the abovementioned research and development trend, MRI-guided robotic intervention has yet enter the main stream of clinical practice. The large soft tissue deformation, limited space in MRI bore and lack of steerable tool make it a challenging task to perform surgery under MRI. This section will highlight the key clinical considerations that still await new pragmatic solutions driven by technological breakthrough.

### 2.4.1 Tissue Deformation and Intra-operative Update of Surgical Map

In proceeding of surgery, pre-op imaging data may lose the validity during the procedure due to the large-scale deformation of soft tissues. For example, "brain shift" (Fig. 2.12) is commonly observable in neurosurgery. The other physiological movements, for instance, respiratory and cardiac motion, are also the major causes of tissue deformation in image-guided intervention. High-resolution MR images with a large number of slices require long scanning time. This may not be clinically practical to perform such imaging intra-operatively, particularly for cardiac interventions. Full electrocardiography (ECG)-gated Cine imaging requires long scanning time (>4 min) to capture a whole set of images throughout all phases of the cardiac cycle.

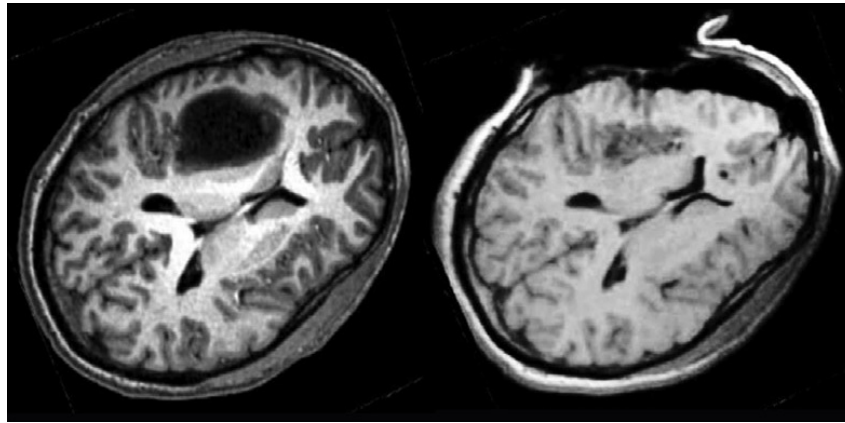


**Figure 2.12:** Brain MRI illustrating the "brain shift" effect before and after the craniotomy.  
**Image Source:** [21]

Current advances of real-time MRI allow fast scan at <1Hz with low latency, of which the images help instantly visualize the actual morphology of tissue, but may not be sufficiently detailed to delineate the physiological features right after the treatment, such as ablation; therefore, deformable image registration [79] is the pre-requisite to continuously updating the pre-op imaging model with both physiological (Fig. 2.13) and morphological (Fig. 2.16a-c) changes based on the intra-op images. Further, the registration should accommodate pre-op and intra-op image sets in different resolutions, dimensions and scanning directions [80]. However, the intensive computation of processing such deformable registrations is the current bottleneck hampering its real clinical application.



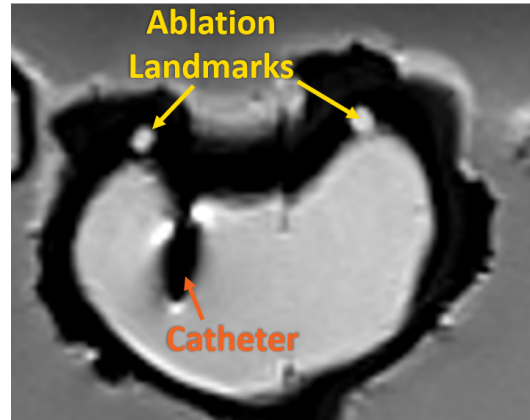


**Figure 2.13:** Artificial ablation landmarks (denoted by yellow arrows) inside the atrium wall created by injecting gadolinium contrast via thin tubes.

### 2.4.2 Confined Space and Endoluminal Entry

MRI-guided robotic interventions have enabled new opportunities for minimally invasive surgery (MIS) with reliable intra-op 3D guidance and reduced trauma and speeding healing. However, after decades of extensive work, MRI-guided intervention remains applicable to only a small fraction of all procedures. One major hamper is that many intervention sites lack a viable tool to reach them, especially those lay deep inside the patient cavity. These sites may only be accessed by navigating through narrow pathways and complicated winding in 3D, requiring the surgical tools to turn corners. Moreover, upon reaching the surgical site, the surgical tool must also provide dexterous manipulation inside the tightly confined space. These constraints make confined surgical sites a forbidden zone for the current MRI-guided approaches, which heavily rely on straight and rigid tools. For incidence, head and neck surgery is still a less explored area in MRI-guided interventions. Standard surgical treatment of various head and neck lesions involves traumatic dissections. Layers of tissue structures, including skin, muscle, bone have to be temporally removed to create access to the lesions. Furthermore, the surgeon must also open sufficient space to allow complex surgical maneuvers, which leads to substantial damage to patients and extended recovery period. These clinical concerns have motivated the growing trend of less invasive approaches, such as endoluminal surgery and natural orifice transluminal endoscopic surgery (NOTES). Such experimental approaches aim to reduce unnecessary trauma by performing operations with an endoscopic tool that passes through a small incision or even natural orifice. Flexible endoscopic devices with acute bending capabilities are mandatory to navigate the curved entry pathways. Yet, MR-compatible tools that can provide comparable flexibility and dexterity for the endoluminal approach is still not available.

### 2.4.3 Teleoperation of Flexible Instruments

To enable master-slave control of robotic flexible tools, a new tele-operation control interface must be considered, in order to accommodate their unique characteristics. Flexible tools can often be characterized by their thin and long body, with a large number of DoFs. Catheters and endoscopes are two great examples. These devices excel in traversing a single small incision and then conducting treatments in distal locations inside the confined cavity. However, their high kinematic redundancy poses a great challenge for the operator to handle such a large number of DoFs. As for conventional flexible endoscope, the learning curve is considerably long to "master" the control and perform complicated maneuver using the turning knobs handle. This scenario quickly exaggerates when the robot DoF increases. It drives the demand for novel control interface for MRI-guided therapy, with the following considerations: 1) the long and flexible instruments have to be maneuvered to reach the small target precisely in confined space surrounded by highly deformable soft tissue; 2) the 3-D position of target lesions or even the instrument end-effector may not be readily measured and tracked in the same coordinates. Cardiac electrophysiology (EP) is a typically challenging example of image-guided therapy. A flexible catheter has to navigate and perform ablations in the left atrium (LA) or left ventricle (LV) under the interference of strong blood flow and heartbeat.

## 2.5 Soft Continuum Robotic System

Design of nature-inspired manipulators actuated based on soft material properties has become one of the most engaged research areas in robotics [23, 81]. Soft robots (Fig. 2.14a-c) embedded with delicate chambers can be driven by fluidic input [22, 81–83], resulting in functional deformations such as bending and elongation/shortening [84]. This section introduces the latest trend of soft robot design and control, as well as its potential applications in MIS.

### 2.5.1 Actuation Design

Accredited to the limber robotic structure, soft actuator assures high compliance within a confined region, facilitating versatile interaction with surrounding objects [85, 86]. These

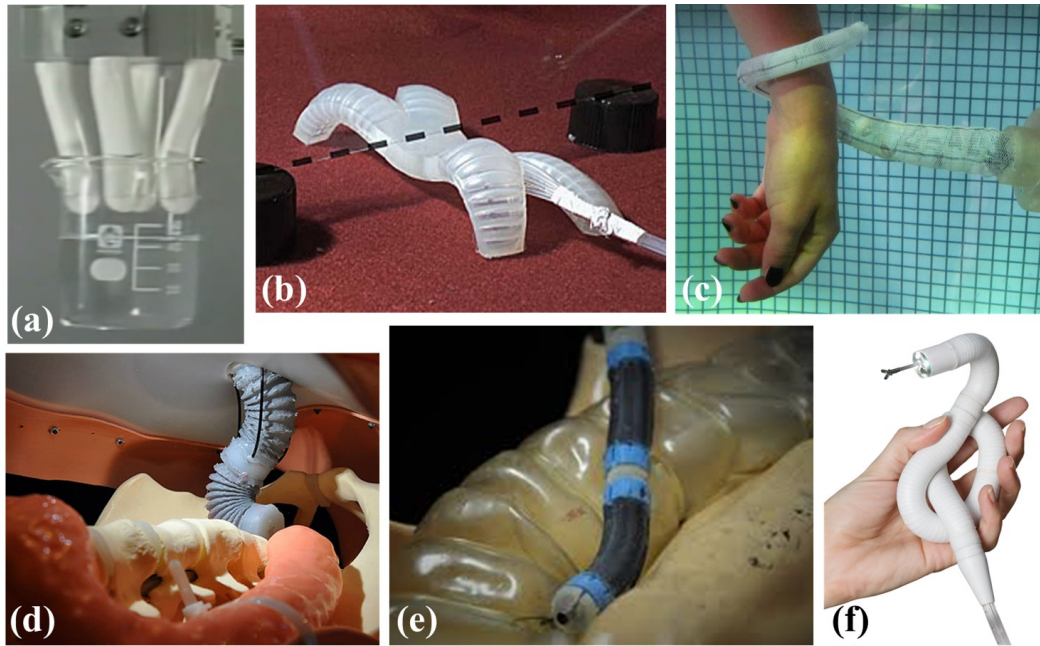
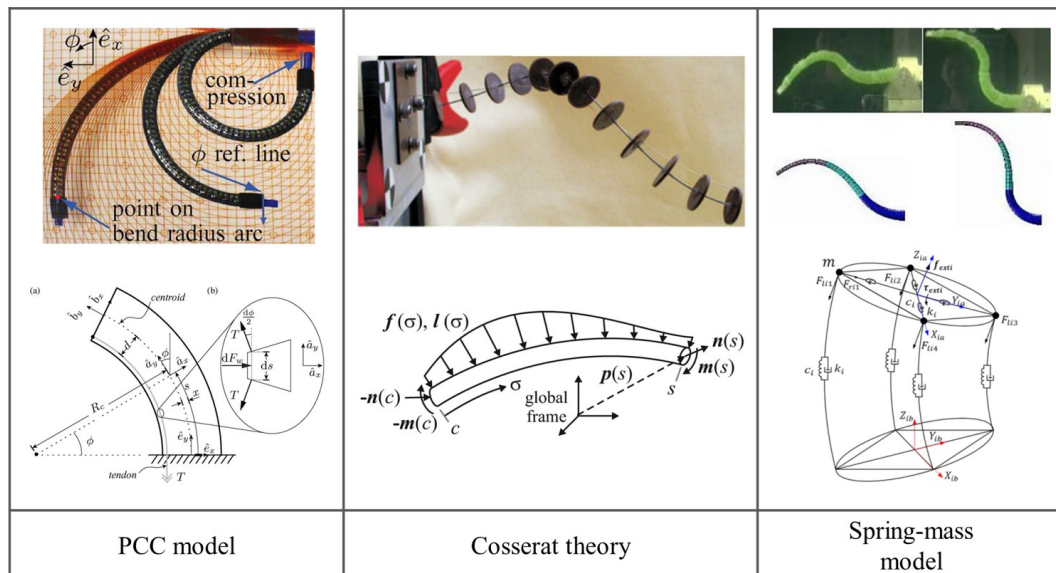


**Figure 2.14:** (a-b) Early design of soft robot mechanisms with elastomeric chamber that can be actuated by inflating pressurized gas/fluid; (c) Tendon-driven soft continuum robot capable of dexterous manipulation under water; (d-e) STIFF-FLOP soft robot equipped with active stiffening mechanism to change to overall robot body rigidity during keyhole surgery; (f) Endotics soft robotic colonoscope. **Image Source:** [22–25] and Endotics Inc.

features introduce a potential impact on many robotic applications demanding safe interaction within a dynamic environment, such as soft tissue in MIS [24, 87]. Therefore, endoscopy is one of the timely applications. Conventional endoscopes predominately comprise of metallic skeleton-driven by steel cables, governing the kinematics of a series of bending mechanisms. It inevitably induces high friction and is susceptible to fatigue failure upon prolonged duration of service. These metallic structures also come with a high rigidity at the scope tip, which may increase the risk of causing trauma or even perforation when the scope is forcefully pushed against the wall of a confined lumen or cavity [88]. Moreover, the metallic components of conventional endoscopy hinder their applications in MRI environments. These challenges have motivated the development of soft robotic instruments for surgical interventions [25, 89–91] which can also be disposable to ensure zero risk of endoscopy-related infection transmission. Endotics (Fig. 2.14f) [89, 90] was the first system developed for the purpose of pain-free colonoscopy. Its novel locomotion scheme attempted to prevent the formation of complex looping at the sigmoid/descending colon. As a result, its single-segment bending is capable of omnidirectional endoscopic exploration along the colon. Aer-O-Scope [91] was another commercial colonoscope relying on a simple approach making use of single-segment bending which is combined with effective locomotion. The STIFF-FLOP soft robot (Fig. 2.14d-e) [24, 25] was another milestone in keyhole surgery to offer intra-cavitary exploration using a soft-material robot,

validated in a cadaveric trial for the first time.

Soft robotic endoscopes have brought a few branches of research directions in the limelight. Various control approaches have also been developed to master the dexterity of such manipulators, giving rise to agile and responsive tele-manipulation. Paramount to surgical safety, having a decent control performance in the presence of a confined and dynamic environment is also essential. Therefore, much research effort [26, 92–94] has been paid for deriving analytical models with the aim to describe or predict the robot kinematic/dynamic behavior [95], akin to controlling conventional rigid-link robots. However, these analytical models are complicated due to the intrinsic non-linear hyper-elastic property of the soft elastomeric materials, which constitute the robot body. Any additional control dimensionality of the soft robot would further exacerbate the complexity of such kinematic equations [92].



without taking the PCC assumption, such as the approximation of trunk-like structures to infinite degree-of-freedom (DoF) system [102], and modeling spring-mass modeling techniques [28, 103, 104] which can be incorporated in a hierarchical controller for generating stereotyped motions of an octopus-like manipulator [103]. Recently, the Cosserat theory [27, 105] of elasticity has been used to predict the underwater motion of a cable-driven, octopus-like soft robot [106] by deducing its geometrically exact formulations. Yet, external disturbance to the robot, such as gravity, payload and external interaction, can promptly invalidate those assumptions. These over-simplified assumptions would substantially degrade the model's reliability in real applications. Moreover, structural parameters in the kinematics have to be determined prior to the modeling process. The search for these invariant coefficients is a heuristic process. This might induce further complications when mapping the robot motion analytically. In addition, such invariant can only hold upon slight modification of the robot, as they possess strong correlation with the robot's mechanical structure. Inevitably, the analytical model has to be revisited after any major change to the robot structure, further diminishing the effectiveness of such an approach.

With the foreseen difficulty of developing the analytical/kinematic model, research attempts were made to control the soft, pliable robot using non-parametric, learning-based approaches. The idea is to obtain forward/inverse mappings for kinematics/dynamics robot control based on measurement data only. Model-free control methods can also be developed based on direct modeling architecture [107], where the inverse mapping is directly obtained. This mapping depicts the inverse transition model of the robot, which could be a changing function due to the contact between the robot and the environments, such as soft tissue. The use of Neural Networks (NNs) has been proposed to globally approximate the inverse mapping between end-effector and robot actuation [108, 109]. Such an approach can compensate for uncertainties in robot dynamics [108], and has been demonstrated to yield even more reliable solutions when compared to using an analytical model of a cable-driven soft robot [109]. Previous studies of NNs mostly consider simplified scenarios, such as a non-redundant manipulator and contact-free situation [108, 109]. Although redundantly actuated robotic systems can be controlled in lower dimensionality in a hierarchical manner, it may require pre-defined movement patterns (primitives) for specific task goals [103]. Moreover, there has been a great demand on using machine learning approaches to address the change in inverse mapping of the hyper-elastic robot upon contact [81]. A Jacobian-based model-free controller has shown its capabilities to manipulate a planar cable-driven continuum robot in an environment with static constraints [110]. However, there is still no example that demonstrates

manipulation of redundantly-actuated soft continuum robot in three-dimensional space, and is adaptive to unknown external disturbance.

## 2.6 Current Trends and Perspectives of MRI-guided Intervention

With the evolve of flexible and continuum robotics tools, it is anticipated that a new generation of MRI-guided robots with smaller size, higher precision, and improved dexterity will emerge. Such robotic platform, featuring small incision and dexterous maneuver, will also favor more sophisticated operation at the surgical site deep inside patient's body. Surgeons will be able to teleoperate the robot with a control interface that can directly interface with MRI scanner. All the images obtained by MRI, including underlying tissue anatomy, tissue physiological features, and thermal map, can all be visualized and processed on a single control interface, enabling a smooth procedural workflow. The following sections will introduce the current trend and future perspectives initiated by the use of articulated continuum robotic device under MRI environments. They also represent the main focus of this thesis.

### 2.6.1 High-Performance Image Processing for *in situ* Guidance

In MRI-guided interventions, *in situ* guidance endows access routes to the target anatomy. The imaging data also render a distinct awareness of surgical tools configuration relative to the patient anatomy. Therefore, such image-guided robotic platform will heavily rely on 1) online co-registration and update of the surgical plan with the real-time imaging data captured during the intervention; 2) fast proximity query (PQ) between the robotic tools and cluttered anatomy in the confined surgical site. The surgical plan, and subsequently the anatomical roadmap must be updated frequently with minimal delay using reliable image registration techniques, based on the intra-op image. Real-time PQ is also mandatory for online generation of haptic feedback and collision-free trajectory. However, the slow computational process is still the major bottleneck in the practical implementation of many image-guided interventions; advanced computing technique is required to enable instant and accurate image processing.

Intensity-based deformable co-registration approach, which is relatively immune to

image artifacts, require processing of large amounts of voxels in order to recover the changes in image morphology. A nonparametric deformation field (Fig. 2.16d) needs to be found to describe the transformation between pre- and intra-op images. Such registration involves iterative computation of voxel gradient and relative intensity difference between the two image sets. Thus, the process induces complicated memory access which has not been well-resolved even using state-of-the-art parallel computing units, such as graphics processing units (GPUs) [111]. Moreover, the latest development adopts diffeomorphic demons method [112] to ensure inevitability and smoothness of deformation field. This implementation inevitably further increases the computation complexity due to a large amount of iterative gradient and composition/interpolation operations.

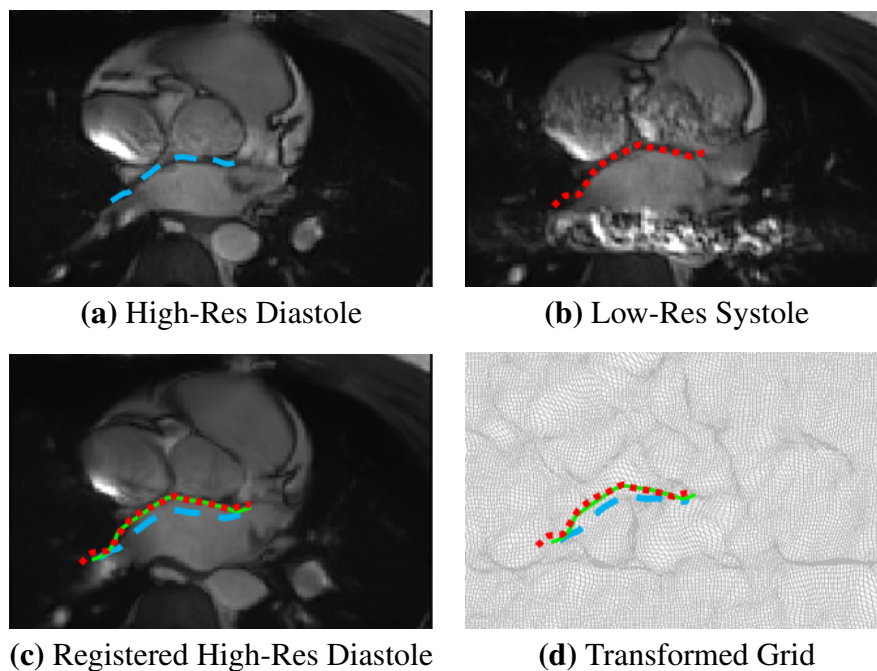


**Figure 2.16:** (a) Sample of pre-op high resolution Cine image acquired during diastole phase; (b) Intra-op low-resolution images captured at systole phase; (c) Registration result of pre-op and intra-op image sets. The high definition pre-op anatomy information is realigned to compensate the deformation due to cardiac motion; (d) Transformation grid showing the deformation field in image domain.

To facilitate safe interaction between the robot and the surgical environment, Proximity Query (PQ) is a crucial computational process to render haptic force feedback and update the potential trajectories to account for the rapidly changing environment. PQ is a process to compute the relative geometric configurations between objects, for instance, the shortest distance between the robot and the internal cavity of surgical site. A fast and efficient PQ comprises many computationally intensive tasks, with the aim of processing the high-quality 3D representation of soft tissue acquired by intra-op MRI. By exploiting the computational flexibility and parallelism of new computation architecture (e.g. GPU),

there are high hopes to resolve the computation barrier in real-time. This computation scheme requires flexible adjustment of the parameters controlling the parallelism, allowing it to accommodate various manipulation scenarios. For instance, multiple levels of computational precision can be processed in a pipeline: 1) high precision for delicate manipulation planning within the region of interest (RoI), such as object targeting; 2) reduced precision for obstacle avoidance outside the RoI. The overall PQ process can hence be accelerated since the reduced-precision PQ consumes significantly less computational resources. Such reduce precision scheme is applicable to obstacles or target objects that are located far away from the operating area.

### 2.6.2 MR Safe Continuum Manipulator and Actuation

Hyper-elastic and soft continuum robot made of biocompatible elastomer compose a new research trend in minimally invasive surgery. It facilitates luminal exploration while still guarantee the diagnostic and therapeutic capabilities. With the compact and dexterous design, as well as the enhanced control framework, continuum robot would act as the next-generation of MRI-guided interventional tools in the new standards of less pain, low cost, single use and zero chance of cross infection. In contrast, the current mainstream of MRI-guided therapy still relies on linear entry pathway, which possesses several drawbacks and limitations. For neurosurgery, the use of straight and rigid tools requires twist-drill entry into the skull and potentially longer approaches traversing healthy brain tissue. With the use of continuum robotic tools, it has the potential to reduce procedure invasiveness by navigating the transluminal trajectories to access the target structure, enabling entry through natural orifices. Flexible tools also excel in reaching target sites via a curved trajectory, in order to avoid delicate anatomical structures or vessels, which will be otherwise damaged if a linear entry path is taken. Furthermore, flexible robotic tools also feature better maneuverability than rigid-link tools in cluttered or unstructured environments.

High-performance actuation units for MR environments is another prerequisite to fulfilling various precise and effective manipulation of flexible surgical tools. Acting as the source of energy, such actuators need to be safely operated under MRI without adversely affecting the MR image quality. Conventional actuators driven by EM force are not permitted under the strong magnetic field of MRI. Piezoelectric motor is, hitherto, the most prevalent choice for the design of MRI Conditional robotic system, since the motion is driven by magnetism-free piezoelectric crystals. However, its excitation current inevitably



produces EM interferences, particularly when both the driving and encoding signals are required to maintain the motor performance. It is technically challenging to filter such high-frequency signals, without degrading the motor performance.

As a result, this limitation in EM driven system shifts the research focuses to intrinsically MR Safe actuation. Other energy sources such as pressured fluid have demonstrated a couple of advantages over the convention EM-based actuation. First, pneumatic cylinders driven by compressed air do not contain any ferromagnetic materials. Second, the components used to regulate the air supply (piezoelectric valve) are readily MR Conditional, hence to minimize the influence on MR image quality (Fig. Fig. 2.17). Finally, the source of energy - pressurized air supply (30-55 psi) is commonly available in MRI rooms through the medical piped gas system in hospitals. Such design ensures power efficiency as it only consists of small moving parts, but possesses extra challenges in precise control, which hinder the widespread deployment of pneumatic actuators.

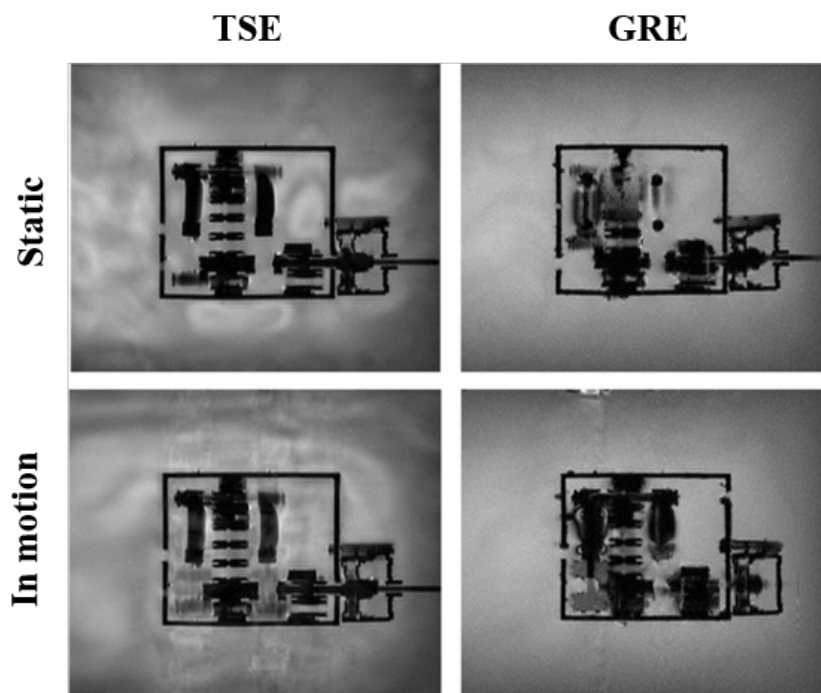


**Figure 2.17:** MRI scan of a MR Conditional pneumatic step motor, using two typical imaging sequences: turbo spin echo (TSE) and gradient echo (GRE). No obvious artefact is observed when in motion or rest. **Image source:** [29]

First of all, modern linear control methods (such as state-space approaches) are insufficient to handle pneumatic servo system because of their intrinsic nonlinearity, including hysteresis associated to the compressibility of air, as well as Coulomb friction of piston seal. Previous work in pneumatic actuation, such as Chen *et al.* [29] and Stoianovici *et al.* [13], bypass this burden by using pneumatic stepping motor. These motors transfer

piston stroke into rotary motion through crankshaft or planetary gear, which inevitably induce fluctuation of transmission efficiency coupled to stroke phase. Consequently, the inconsistency of output torque over revolution cycle will result in large position error as shown in (Fig. 2.18a). It may also deteriorate the power efficiency from transferring the air pressure to output torque and speed (Fig. 2.18b).

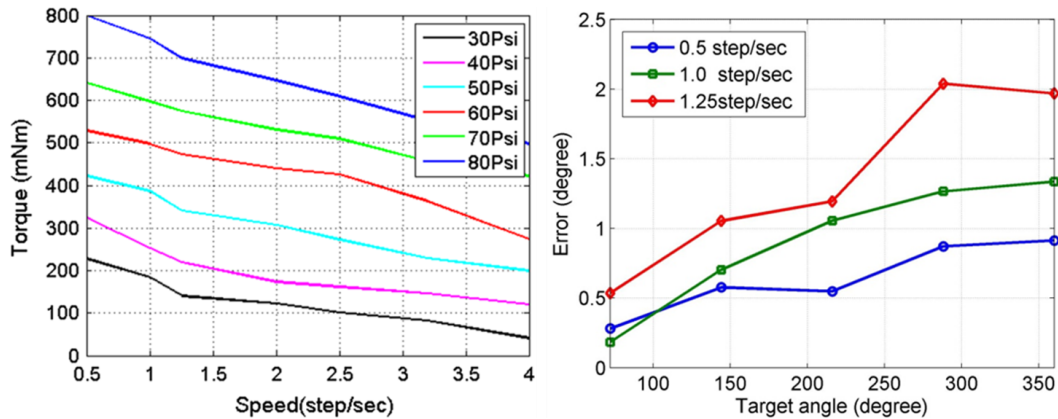


**Figure 2.18:** (Left) Motor maximum output torque correlated with various operation speed and air supply pressure; (Right) Plot of positioning error against nominal motor speed of pneumatic motor **Image source:** [29]

### 2.6.3 Integrated Navigation and Control Interface for Continuum Robot

The ultimate goal of a human-robot collaborative control framework is to seamlessly combine the strength of both robot and clinicians for improved teleoperated manipulation. The clinical impact and considerations of such control framework were first explored in 1998 [113]. After that, much research effort has been focused on enhancing human performance via intuitive robot manipulation, while enforcing surgical safety and precision at the same time, even under complex environment. Virtual-fixture is one of the well-known software frameworks that aims to augment the user's input by interactive force feedback. Many functional force interaction models were proposed to supplement the image-based navigation, enabling intuitive guidance to follow a designated trajectory or to prevent them from entering a safety region. [114] However, the clinical impact of these human-robot collaboration techniques is only well established for serially-linked robot comprised of rigid body. The underlying assumptions include a fixed robot geometry, well-defined kinematics model and also reliable sensing of robot configurations.

However, these features are usually not available for flexible robots because their continuum body can undergo large deformation during actuation. Kinematics modeling is not always a reliable way to represent the material and geometric nonlinearity of the

compliance body. The hyper-redundancy of the continuum robot also impose substantial challenges on task space control, especially for thin and long manipulators with many actuators. To this end, there is a need for new data-driven motion parameterization scheme that enables the operator to ergonomically maneuver high DoF "slave" flexible manipulator using an intuitive lower dimensional "master" input device, but without encountering the side effects of solving complicated inverse kinematics. Also, a generic interface that could incorporate MRI-based tracking of instruments with the frequently-registered model is also required. Such positional tracking should always take place in the same coordinates with the MR image domain, thus avoiding significant offset due to the coordinate misalignment between the instrument and the target anatomy. Visual navigation guidance in the 3D virtual environment is also required, which account for directing the instrument manipulation within a safe region of surgical interest, thus reducing the chance of inadvertent damage on delicate tissue, e.g. atrial wall.

## 2.7 Conclusion

This chapter highlights the current state-of-art techniques for MRI-guided interventions and robotic systems. It is followed by a brief introduction to the latest trend in design and control of soft continuum robot. This chapter aims to identify the motivations and rationale of my proposed work on continuum robotic system to enhance MRI-guided interventions. This review offers profound insight into the investigation of necessary techniques, namely, fast image processing, MR Safe continuum manipulator design and control, and integrated human-robot interface for navigation. Currently, there is no existing commercial robotic platform is MR Conditional, that is also integrated with flexible manipulator and real-time MR image registration. It is anticipated that the proposed study will increase confidence to perform image-guided surgery, while improving the safety of instrument navigation.

The proposed innovations will be introduced in detail in the following chapters. In [Chapter 3](#), the development of the high-performance image process technique by using novel computational architecture is addressed. The enabling techniques for developing the MR Safe robotic platform for MRI-guide catheterization is presented in [Chapter 4](#). The design of a fluidic-driven soft robot and its learning-based control strategy are described in [Chapter 5](#). Finally, this thesis concludes with the future research direction and potential improvements to the proposed studies in [Chapter 6](#).



## Chapter 3

# High Performance Image Processing for MRI-guided Navigation

### 3.1 Introduction

MRI offers superior image contrast for delineating and distinguishing soft tissue, allowing surgeons to identify tumors margins and critical neurovascular and muscular structures. By rapid acquisition of intra-op MR images, 3-D important regions that details the physiological changes of tissue can be monitored. In MIS, such *in situ* guidance can provide access routes to the target anatomy, as well as enable a distinct awareness between the configuration of robotic instrument relative to the anatomy of surgical interest. To allow seamless integration of intra-op image guidance without disrupting the fast-paced surgical workflow, large amount of MRI voxel data will also have to be processed instantly to provide surgeons with clear pathologic illustration and detailed structural information.

There are two major image processing techniques that require rapid, frequent update to generate reliable image guidance: **1)** Deformable image co-registration between pre- and intra-op MR images, with the aim of updating the pre-op anatomical roadmap; **2)** Real-time Proximity Query (PQ), which is crucial in rendering haptic force feedback and updating the potential trajectories in account for rapidly changing environment. This slow process is still the major bottleneck in real implementation on many image-guided interventions.

Much effort has been devoted to relief the computational bottleneck by algorithmic

optimization. This approach aims at reducing Big-O complexity of the computation problem by applying various assumptions and complicated pruning logic. Although central processing units (CPU) are "fast" to deal with these heterogeneous tasks due to their high clock rate, it lacks scalability to cope with problems that involve large amount of data like MR image in 3D. With the widespread popularity of an affordable application accelerator, namely the graphics processing unit (GPU), there were high hopes in leveraging the GPU's parallel processing power to enhance such computation. GPUs are specialized hardware originally being developed for rendering images for display output. To this end, the GPU possess numerous processing cores to render images in a highly parallelized manner. The recent development of general-purpose GPUs also leverages GPU's parallel processing capability to support many performance-demanding applications such as computer vision and artificial intelligence.

This chapter will highlight the major computation bottleneck and optimized implementation of intensity-based image registration and real-time PQ. The customization and parallelization for efficient GPU processing will also be described in details.

## 3.2 Performance-aware Programming for Deformable Image Registration

Advances in image registrations facilities safer, more precise and effective intervention guided by intra-operative (intra-op) images [115]. ItCo-registration of the detailed physiological features acquired by pre-operative (pre-op) imaging (e.g. fMRI, DT-MRI) with the intra-op images can help surgeons to identify the critical regions of interest, as well as determine the surgical plan during the procedure. However, large-scale morphological change caused by tissue deformation would cause severe misalignment between two image sets, making such co-registration very challenging. To this end, non-rigid image registration is required to deduce the non-linear transformation among the image sets.

As intra-op scans sacrifice image quality for temporal resolution, intensity-based registration schemes (such as the "*Demons Algorithm*" [79]) is superior to its feature-based counterpart in the intra-op scenario, as it is relatively immune to image artifacts and noise. However, intensity-based registrations are well known as computationally intensive, due to its complicated memory access for pixel/voxel-wise correspondence search. Long

processing time (>10min) poses a major bottleneck to be applicable in real practice of image-guided intervention, in which the navigation of instrument may have to be adjusted responsively in a minute.

Previous research attempts [111, 116] have demonstrated fast demons image registration based on Graphical Processing Units (GPUs). In this work, we explore the potential intra-operational applications of a more recent approach, *Diffeomorphic Demons (DD)* [112]. *DD* can handle large deformation and possess many beneficial properties, but it involves a series of complex computation that hinders its potential for application in intra-op scenarios. In the light of this complexity, we develop a computing framework capable to resolve the computation bottleneck effectively using GPUs, which will be open sourced to various practical implementation.

### 3.2.1 Diffeomorphic Demons Registration for Large Tissue Deformation

*DD* is a non-parametric image registration framework that uses a Lie group structure [112]. In contrast to the additive model accepted by Thirion's approach [79], *DD* adopts a compositive deformation model to ensure continuity and prevent folding of deformation field. Under the diffeomorphic framework, the registration can be considered as an optimization problem to maximize the similarity between a fixed and a moving image within the Lie group structure. The cost function, known as the harmonic energy ( $E$ ), measures the similarity ( $Sim$ ) between fixed image ( $F$ ) and moving image ( $M$ ), as well as the likelihood ( $Reg$ ) of deformation field [112]:

$$E = \frac{1}{\sigma_i^2} Sim(F, M \circ \exp(v)) + \frac{1}{\sigma_T^2} Reg(\exp(v)) \quad (3.1)$$

where  $\sigma_i$  and  $\sigma_T$  are the regularization terms for the registration. The optimal diffeomorphic transformation  $\Phi^* = \exp(v|_{E=E^*})$  can therefore be found by maximizing of the energy term using iterative approaches, such as Newton's method.

---

#### Algorithm 3.1 General diffeomorphic demons framework

---

- 1 **Input:** Fixed image  $F$  and moving Image  $M$
  - 2 **repeat until converge:**
  - 3     Compute update field  $u$  based on  $F$  and  $M \circ \exp(v)$
  - 4     Apply fluid-like regularization  $u \leftarrow K_{fluid} * u$
  - 5     Update velocity field  $v \leftarrow \log(\exp(v) \circ \exp(u))$
  - 6     Apply diffusion-like regularization  $v \leftarrow K_{diffusion} * v$
  - 7 **Output:** Transformation  $\phi = \exp(v)$  from  $F$  to  $M$
-

### 3.2.2 Acceleration Scheme based on Novel Computing Architecture

It is worth noting that the major computational burden resides in the regularization (also known as “smoothing”) of displacement field. Such regularization is usually performed by 3D-convolution with a Gaussian kernel on every voxel. Although the convolution operation can be distributed to the thousands of processing unit on GPU, the memory bandwidth will eventually hinder the total throughput. It is because each convolution involves accessing the intensity value of adjacent pixels. This random pattern of memory access aggravates the memory transfer latency between the processing unit and the global memory in GPU. In our proposed GPU-based framework, 3D images are divided into smaller segments and hence can be pre-fetched into the local memory (or shared memory in CUDA) which is ~20x faster than global memory. Such memory organization paradigm enabling fast access to adjacent pixel values and as a result improve the overall computation time.

*DD* possess several unique operations, thereby imposing extra computational load as compared to the conventional additive approach. For instance, it utilizes compositive update rule (denoted as “ $\circ$ ”, as shown in [Algorithm 3.1](#), Line 5) to satisfy the requirement of Lie group operation. For a non-parametric form of deformation field, the composition has to be done by interpolating one deformation field by another. Moreover, the newly computed update step will have to go through an exponential mapping into Lie group. Vercauteren *et al.* [112] proposed a recursive “scaling and squaring” method to approximate such mapping.

In order to optimize these operations, we integrated 3 computing techniques for CUDA GPUs: **1)** optimization of parallel pipeline; **2)** efficient memory management via the user-managed cache; and **3)** utilization of dedicated texture hardware. CUDA GPUs can manage a large number of computing pipelines by taking advantages of the dedicated microarchitecture of streaming multiprocessor (SM) which executes the threads in a highly parallel manner. With the Single Instruction, Multiple Threads (SIMT) architecture, each CUDA cores can execute warps of 32 threads at the same time under a single fetch-decode instruction cycle. However, warps can be bottlenecked (“stalled”) if there are insufficient warps for the SM to “process”, especially when high latency operations or synchronization barriers are involved [117]. Therefore, SM is prone to latency bottlenecks when there are no eligible warps. While each SM possess limited computation resources, the maximum number of warps executable, so-called occupancy, is heavy influenced by the kernel’s requirement on computation resources, including registers and shared memory. As a result, it is critical to optimize the SM’s occupancy by effectively managing the kernel resources. At optimal occupancy, each SM can execute 2048 threads (64 warps) in parallel. With an



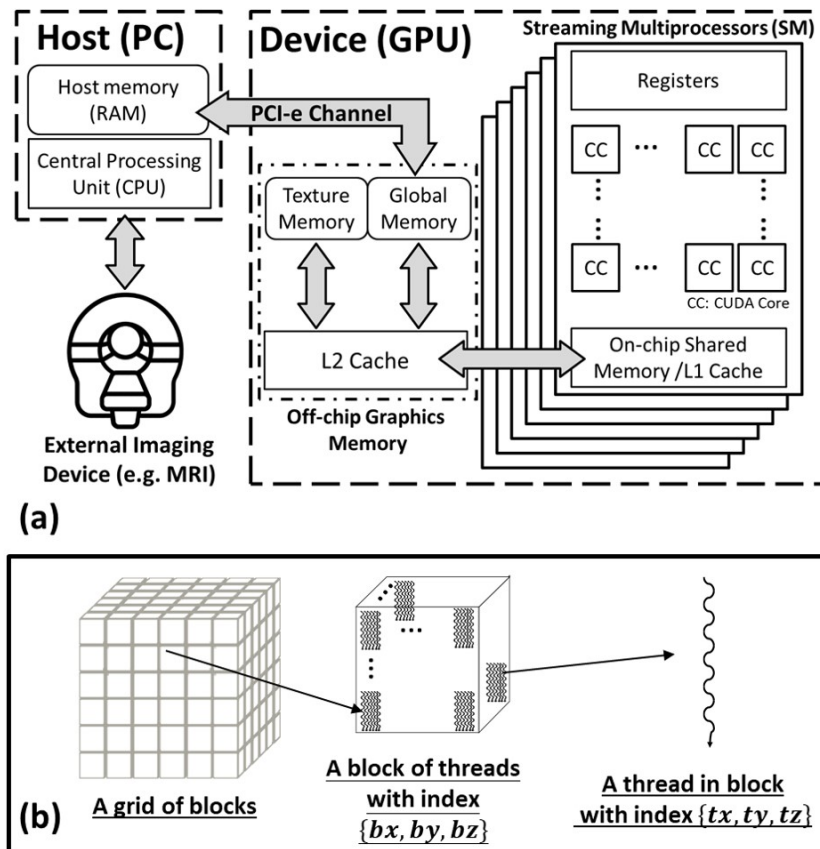


**Figure 3.1:** Schematic diagram of the CUDA hardware and software architecture. **(a)** Model CUDA GPU enable parallel processing of large amount of data by distributing the load to thousands of computation units, known as streaming multiprocessors. The streaming multiprocessors can read from/write to the off-chip graphics memory through a heavily cached data bus. **(b)** To execute kernel processes, the GPU will instantiate a grid of thread blocks composed of numerous threads.

increasing number of SMs ( $>10$ ) available in modern GPUs, a CUDA device is capable of providing the necessary computation throughput to acceleration the registration process.

Efficient memory management on a CUDA device requires delicate usage and allocation of the on-board memory, also known as "shared memory" on each SM. Due to the fact that the shared memory has a much ( $> 80\times$ ) faster accessing speed than the global memory, the shared memory can serve as an low-latency, user-managed memory to cache any data for localized computation. Adding shared memory to the computation pipeline can significantly lower the requirement on both global memory bandwidth and register [118]. One way to incorporate shared memory is to prefetch data onto it before the computation begin, as optimally reuse the data, hence minimize the redundant access to the global memory. However, the memory access patterns must be properly managed, in order to achieve this data pre-fetching technique efficiently. Moreover, the shared memory can also store any intermediate results generated by the kernel, which can then quickly access

by other threads in the SM. After the computation is completed, the cached data on shared memory can be transferred back to the global memory in a batched manner.

The dedicated texture filtering hardware on CUDA GPU can also benefit the interpolation process. While CPU-based 3D interpolation is an arithmetic and memory intensive operation, texture hardware on GPU is designed to resolve this computational bottleneck with its dedicated hardwired data channels. The memory that details the data points are designate to the texture memory/cache for read access only. The memory access is performed with the help of hardware-managed 3D "pitched" memory pointers, which provide spatial locality for the processors to rapidly access all the essential data for interpolation. Futheternore, the subsequent 3D interpolation are also accelerated by the hardwired digital units within the texture filtering hardware, which enable trade-off between high speed interpolation and reduced interpolant precision.

Besides, vectorized data type (e.g. float4) are adopted to increase memory bandwidth while reducing the number of executed instructions by cascading the data into the 128-bit memory bus. Both vectorized memory access and arithmetic instructions enable to load, store and batch processing multiple primitive data (e.g. 32-bit float) with a single instruction. This vectorized memory access scheme is particularly suitable for 3D image registration because the 3D deformation field data can be cascaded into a vectorized variable and hence processed efficiently.

### 3.2.3 Experimental Results

The proposed framework has been evaluated using five sets of ECG gated cardiac MR images in different cardiac phase. The registration accuracy and computation speed are validated. In all test case, the registration converged within 30 iteration cycles, and the tissue deformation due to the cardiac motion was recovered as presented in [Fig. 3.2](#).

The proposed GPU framework can effectively register the moving image to the fixed image even under the large tissue deformation. The computation time was reduced from 18-25 min to <25 sec, indicating that the GPU-based framework has achieved at least 60 times speed up as compared to a CPU running single-threaded. This framework is also at least 8 times faster even the CPU is running 8-threaded. Detailed computation performance is presented in [Fig. 3.3](#). It demonstrated the potential acceleration by the ensemble of the 3 computing techniques for CUDA GPUs: **1)** optimization of parallel pipeline; **2)** efficient

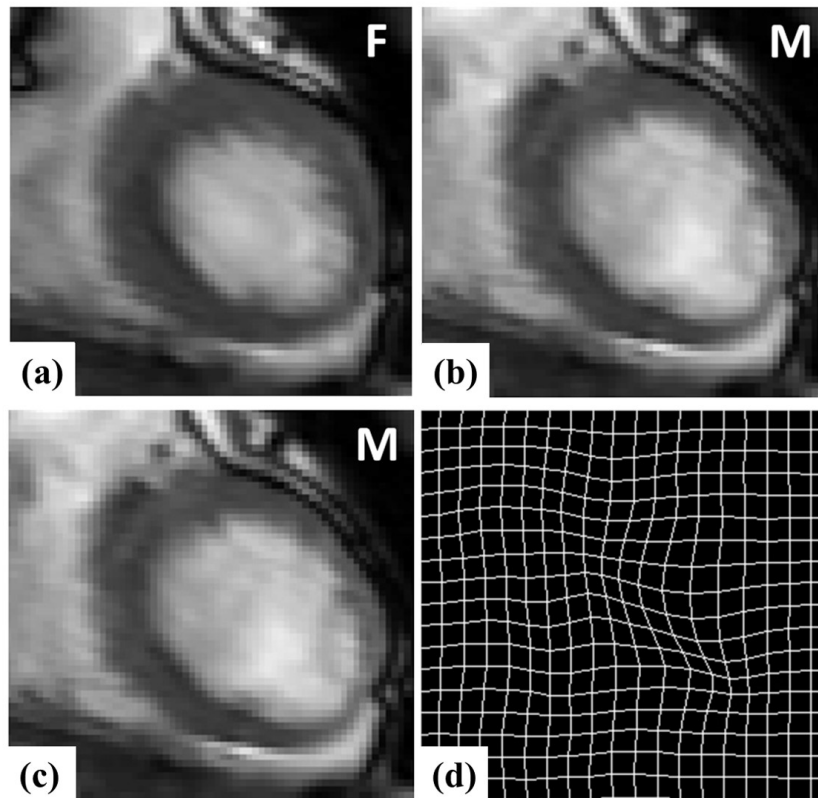


**Figure 3.2:** Two-dimensional view of the left atrium on the transverse plane. (a) *Fixed image*; (b) *Moving image*; (c) Non-rigidly registered image using the GPU-accelerated diffeomorphic demons registration algorithm; (d) Projected deformation field onto the transverse plane.

memory management via the user-managed cache; and 3) utilization of dedicated texture hardware.

### 3.3 Fast Proximity Query with Graphical Processing Unit

Proximity Query (PQ) is a process to request for the relative configuration or placement among 3D objects. This PQ computational problem has been widely investigated and is fundamental to many applications in the fields of robot motion planning, virtual prototyping, haptics rendering, computer graphics and animation. The demand for efficient and fast PQ is mainly driven by the trend to having online simulations of high-fidelity haptic feedback at rate of  $>1\text{kHz}$  [119], or real-time generation of continuous and collision-free trajectory for safe robotic manipulation [120]. Poor PQ performance can be the major bottleneck for developing various robotic control schemes even with sufficient sensing data available [121]. One of the typical examples can be found in image-guided surgical robotics, e.g.

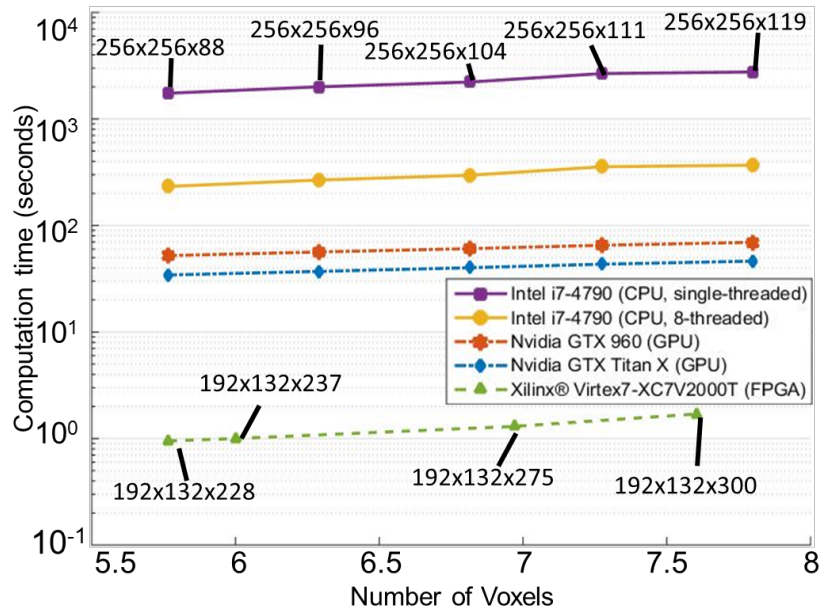


**Figure 3.3:** Computation performance of *Diffeomorphic Demons* registration algorithm evaluated on CPU and two different GPUs using our proposed framework. Around 30 iterations is required for the registration to converge.

Virtual Fixtures [122] and Active Constraints [123, 124], of which the control concept is to impose force feedback based on the anatomical model acquired by imaging data.

### 3.3.1 Previous Work

Broad-phase PQ involves checking whether two objects are potentially touched or collided with each other. Bounding volumes in primitive shapes, such as box (e.g. AABB [125] or OBB), sphere [126] and torus [127], are commonly used to tightly enclose the object for further detection of object collision. These techniques have been extended to narrow-phase PQ, which refers computation of the minimal Euclidean separation or penetration depth when they are intersected; however, the non-convex objects that are complex in shape may neither readily be bounded nor partitioned by the boxes and spheres. Convex decomposition of the non-convex object is not efficient and also known as an NP-hard problem [128].

Triangular mesh is commonly used in representing 3D objects. Lin-Canny [129, 130] and Voronoi-Clip (V-Clip) [131] algorithms are typical narrow-phase PQ approaches. They exploited Voronoi regions to determine the closest features pair such as vertices, edges and faces between two convex polyhedral meshes. The generation of Voronoi regions of both object features is computationally expensive process due to the complex data structure required. These approaches are particularly not appropriate for objects of

which their geometric structure is rapidly changed or deformed time-by-time. Gilbert-Johnson-Keerthi Algorithm (GJK) [132, 133] is a rather efficient method without having to perform any data pre-processing. The overall real-time computational performance of this iterative minimization method is sensitive to the initial guess of the closest feature pair. Chakraborty *et al.* [134] adopted Interior Point Algorithm [135] of which the iterative process is sufficiently fast and efficient for providing high-frequent PQs; however, it required the objects to be represented by implicit surface functions that act as a set of inequality constraints subject to the minimization search.

To guarantee the global convergence, the approaches mentioned above can only be applied to convex objects, thus hampering their practical values in dynamic scenarios where unstructured and irregular geometry details are involved. Although some of these approaches (e.g. [131–134]) may ensure low Big-O complexity in coping with large sampling, their computational parallelism is forgone in the algorithmic design. The inherent limitation is that these iterative minimization approaches (e.g. GJK) cannot take advantage of using parallel computing architecture which has become a trending solution to processing large and complicated dataset [120]. In our previous work, we have demonstrated the superior computational performance of PQ on a large amount of cloud points using GPU [114] and FPGA [80, 136].

In this study, we derive a PQ formulation which allows for real-time computation of the shortest distance between contour segment and irregular-shape mesh model. We suggest that multiple series of contour segments enclosing the robotic manipulator can be readily updated and moved based on its kinematics chain. Moreover, the form of triangular meshes modeling the unstructured and dynamic environment can still be preserved. We exploit GPU-based parallel computing techniques to support high-frequency and low-latency PQ processing, thereby fulfilling many standard real-time requirement (>1kHz). Detailed validation is conducted on two scenarios of robotic tasks in extremely different natures of application.

### 3.3.2 Problem Definition

The motivation of addressing the aforementioned technical challenges has led to the development of novel PQ algorithm, which aims to determine the shortest distance between the robot manipulator and its surrounding environment constraints with high speed and efficiency. This algorithm is the logical progression based on the work proposed

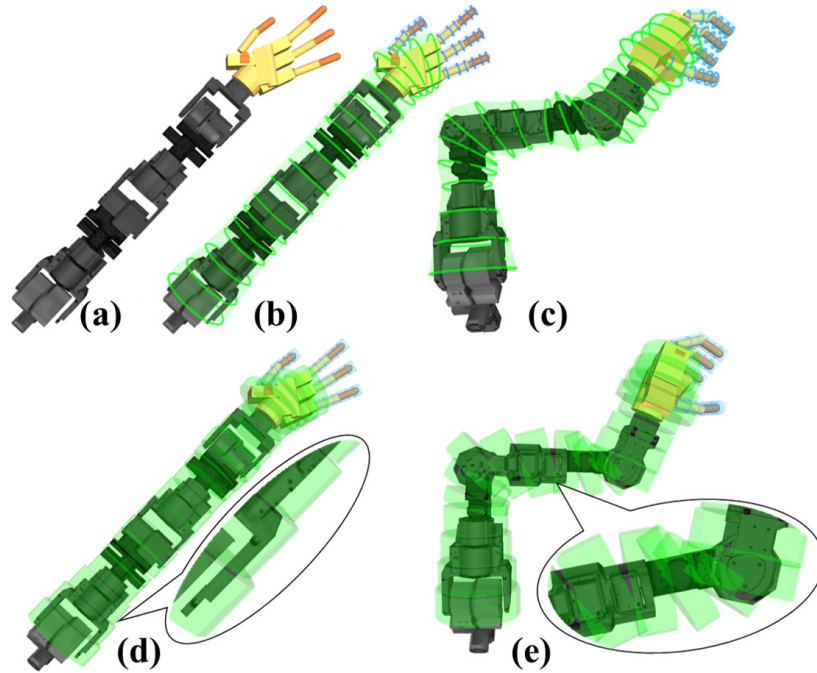


**Figure 3.4:** (a) CAD model of the ATLAS robot arm and the Sandia Robotic Hand; (b) Volumetric pathways comprising segments (in green) tightly enclosing along the arm and four fingers; (c) The corresponding twenty series of segments, of which the contours can be posed flexibly along with the subsequently updated robot configuration; (d) Collision model approximated by the union of same number of standard bounding cylinders; (e) Such collision model fails to fully enclose the robot arm under alternative configuration.

by Kwok *et al* [114], which calculates the shortest distance between an arbitrary point  $x \in \mathbb{R}^{3 \times 1}$  and the enclosing segment. In this study, the PQ formulation for analytical calculation of the shortest distance between contour segments (robot) and triangular meshes (environment) is explored.

Instead of performing PQ with an exact robot model (Fig. 3.4a), our approach can greatly improve computational efficiency by establishing the tight enclosure [137] as Fig. 3.4b-c as compared to the standard bound cylinders (Figure 3.4d-e). Such approach also enables parallelization by discretizing robot segment and mesh. The pathway of robot segment, which has been applied to various robotic kinematic configurations, can be approximately defined as a centerline along the manipulator consisting of a finite chain of line segments  $\overrightarrow{P_j P_{j+1}}$  ( $j = 1, 2, \dots, N_c - 1$ ),  $N_c$  is the total number of nodes) with their node at point  $P_j$  and tangent of  $M_j$ . A single enclosing segment  $\Omega_j$  (Fig. 3.5a) of the pathway comprises two adjacent circles  $C_j$  and  $C_{j+1}$ . Each circle  $C_j$  has its center at point  $P_j$  and lies on the plane normal to tangent  $M_j$ . The radius  $R_j$  of circle  $C_j$  is chosen such that the segments can be tightly fitted along the model of robotic segments. The resolution of segments is related to the interval of nodes  $\Delta$ , where  $\Delta = |\overrightarrow{P_j P_{j+1}}|$ . The lower the interval  $\Delta$

is, the higher the resolution increases with the expense of extra computation effort.

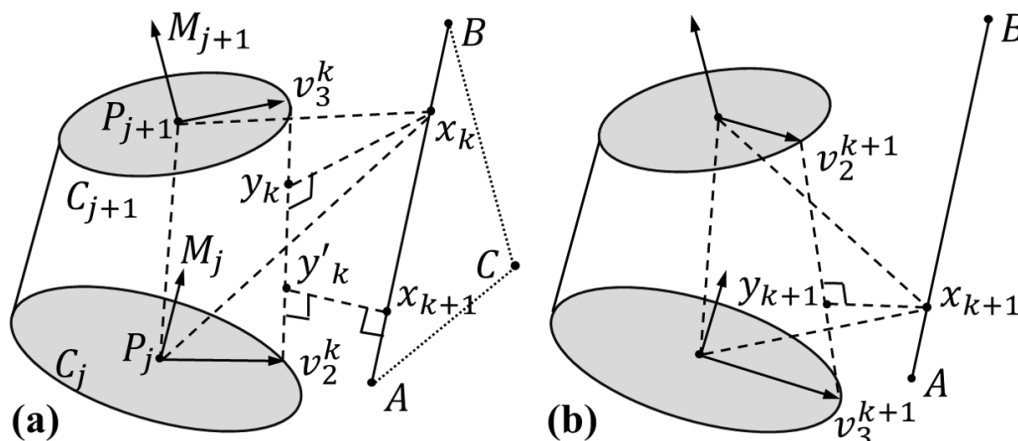


**Figure 3.5:** (a) Basic structure of a single segment enclosed by two adjacent circular contours. Mathematics variables introduced for geometric analysis; (b) New variables are estimated after the previous iterative result.

Triangular mesh is one of the most common representations of 3D irregular geometry in computer graphics and virtual reality [138]. The mesh could be either constructed by using robot sensors or based on the synthetic model. Many tessellation algorithms (e.g. [138]) have been proposed to efficiently transform the non-uniform 3D sensing data into triangle mesh, which comprises a large set of triangles with common edges and vertices. Collision occurs when any triangle is in contact with the robot segments, which implies that the shortest distance between the surround constraints and robot segment is zero ( $d = 0$ ).

The PQ between an enclosing segment and a triangle can be regarded as a 4-dimensional constrained optimization problem. To date, the optimal value can be achieved via an iterative numerical technique, which is at a higher computational expense. In this study, a new algorithm is presented to eliminate this barrier by regarding each edge of the triangle mesh as an independent entity. Thus, the estimation of edge-segment shortest distance will be conducted firstly; thereby the closest point of each triangle will be searched by evaluating its three edges. This method is computationally efficient compared to the traditional approach, which processes triangles independently. It dramatically reduces the computational workload in the way of averting the repetitive computation of edges shared by adjacent triangles. Besides, parallel computation with multiple independent threads on GPU can achieve significant acceleration. All these improvements implemented have led to the performance evaluation of a novel PQ algorithm and the exploration of its application.

### 3.3.3 Proximity Queries for Irregular Mesh Model

In order to realize the objectives stated in Section II, detailed PQ algorithm will be presented in this section. More specifically, it consists of the three steps: 1) analytical formulation of the edge-segment shortest distance; 2) approximation of its shortest distance; 3) identification of triangle-segment shortest distance.

#### 3.3.3.1 Analytical Formulation of Edge-Segment Point Pairs

To calculate the shortest distance between a triangle and segment, the primary step is to calculate the shortest distances between each edge of triangle and segment [139]. As an example,  $\vec{AB}$  is the edge of triangle  $\Delta ABC$  (Fig. 3.5), point  $x$  and point  $y$  are the parameterized points representing edge  $\vec{AB}$  and surface of segment  $\Omega_j$  respectively, which are defined as follows:

$$\begin{cases} x = A + \alpha \cdot \vec{AB} \\ y = (1 - \eta) \cdot C_j(\theta) + \eta \cdot C_{j+1}(\theta) \end{cases} \quad (3.2)$$

where parameters  $\alpha, \eta \in [0, 1]$ ,  $\theta \in [0, 2\pi)$ .

With these parameterizations, the problem is transformed into the searching for a closest point pair  $x_c y_c$  between edge  $\vec{AB}$  and segment  $\Omega_j$ , as to which the corresponding shortest distance can be expressed as  $d_c = \min\{|\vec{x}\vec{y}(\alpha, \eta, \theta)|\}$ . The closest point pair  $x_c y_c$  should meet the following three criteria in sense of geometrical analysis:

- i) Point  $y_c$  should lie on the cross section containing  $P_j, P_{j+1}, x_c$ ;
- ii) The closest point pair  $\vec{x}_c \vec{y}_c$  should be perpendicular to the edge  $\vec{AB}$ , which is  $\vec{x}_c \vec{y}_c \perp \vec{AB}$ ;
- iii) The closest point pair  $\vec{x}_c \vec{y}_c$  should also be perpendicular to segment edge  $\vec{v}_2 \vec{v}_3$ , which is  $\vec{x}_c \vec{y}_c \perp \vec{v}_2 \vec{v}_3$ .

Referred to the above criteria, the closest point set  $\vec{x}_c \vec{y}_c(\alpha, \eta, \theta)$  can be determined with



solution set  $(\alpha, \eta, \theta)$  of the formula below:

$$\begin{cases} \overrightarrow{x_c y_c} \times n_j = 0 \\ \overrightarrow{x_c y_c} \cdot \overrightarrow{AB} = 0 \\ \overrightarrow{x_c y_c} \cdot \overrightarrow{v_2 v_3} = 0 \end{cases} \quad (3.3)$$

where  $n_i$  is the normal of a plane containing points  $P_j, P_{j+1}, x_c$ , such that:

$$n_j = (x_c - P_j) \times (x_c - P_{j+1}) \quad (3.4)$$

By substitution of parameter vectors  $u(\eta)$ ,  $w(\theta)$  based on Eq. 3.2, Eq. 3.3 can be rearranged as follows:

$$\begin{cases} u(\eta)w(\theta)^T F_1 w(\theta) = \alpha \\ u(\eta)w(\theta)^T F_2 w(\theta) = 0 \\ u(\eta)w(\theta)^T F_3 w(\theta) = 0 \end{cases} \quad (3.5)$$

where coefficient matrix  $F_{1,2,3} \in \mathfrak{R}^{3 \times 3}$ , and parameter vectors  $u(\eta) = [1 \quad \eta]^T$ ,  $w(\theta) = [1 \quad \sin \theta \quad \cos \theta]^T$ .

Although we can simplify the triangular PQ into the shortest distance problem between the edge  $AB$  and contour segment  $\Omega_j$ , obtaining an analytical solution is still challenging [139]. In our case, the analytical formula (i.e. Eq. 3.3) is derived from a direct mathematical method and it can be regarded as a necessary reflection of the high geometrical complexity. In addition, this analytical formulation requires extensive computational burdens, making real-time calculation impossible. Instead, a novel algorithm costing light computational resources, but also with sufficient accuracy, might be the promising approach in searching for the closest point pair.

### 3.3.3.2 Optimization-based Closest Point Pair Estimation

Theoretically, an accurate distance  $d_1$  can be obtained by solution set  $(\alpha, \eta, \theta)$  in Eq. 3.3, but along with the expensive computation. This is a trade-off that acquiring approximated closest point pair is relatively practical, rather than aiming to solve a closed form solution of  $(\alpha, \eta, \theta)$ . By regarding the line as a cylinder of zero radius, then this problem is transformed into the case of calculation of the distance between two cylinders. Referring to the algorithm of cylinders intersection test proposed by Eberly *et al.* [139], it can be

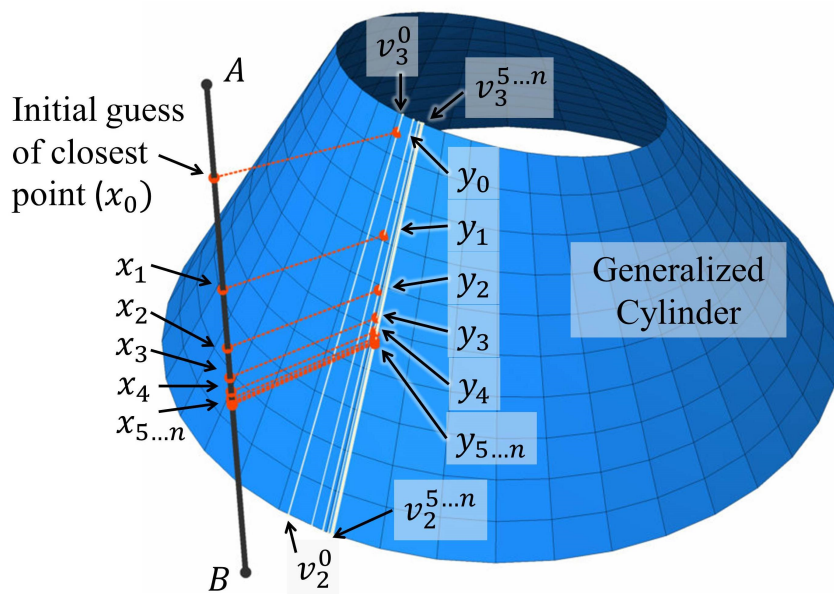


**Figure 3.6:** Example configuration showing the temporary closest point pairs of each step processed by the optimization-based estimation. This configuration can be considered as an more extreme case requiring for more number of steps to reach convergence.

deduced that the minimization cost function that searches the shortest distance between segment and point along the line is strictly convex. In addition, the objective function will have a global minimum that is either at the endpoints of line or the point in-between lines where its partial derivatives for each variable are zero or undefined. In the collision detecting system, it works almost exclusively with convex objects (e.g. cylinder) due to the fact that convex objects can force the algorithm to converge faster [140]. The properties of convexity and convergence guarantee the direction of the iterative method, which will be presented below, moving towards the closest pair as long as each step achieves point-pair with a shorter distance than the previous step. It is worth noting that the last two criteria can be used to evaluate the accuracy of this solution. Referred to Fig. 3.6, the proposed optimization-based method can be described as follows:

**Step 1:** Find an initial point  $x_0$  on edge  $\overrightarrow{AB}$ , which is the closest point to centerline  $\overrightarrow{P_j P_{j+1}}$ . This step provides an initial value of closest point, which only takes the distance between centerline  $\overrightarrow{P_j P_{j+1}}$  and edge  $\overrightarrow{AB}$  into account. However, due to the fact that  $\overrightarrow{AB}$  is not necessarily perpendicular to the centerline  $\overrightarrow{P_j P_{j+1}}$ , further steps will be provided.

**Step 2:** Referring to the methods proposed in [114], corresponding vertices  $v_2^0$  and  $v_3^0$  on the circle contours can be found, which lie on the plane containing points  $P_j, P_{j+1}, x_0$ . The segment edge  $\overrightarrow{v_2^0 v_3^0}$  contains the initial point  $y_0$  on the enclosing segment and the initial

distance is defined as  $d_0 = |\overrightarrow{x_0 y_0}|$ .

**Step 3:** Upon setting the initial guess, the iteration begins with finding the point  $x_{k+1}$  on edge  $\overrightarrow{AB}$  that is closest to segment edge  $\overrightarrow{v_2^k v_3^k}$ , where  $k$  is the index of iteration and  $k = 0, 1, 2, \dots$  (Fig. 3.5a). This step, in essence, applies the third criterion to the current value  $x_k$  and comes up with a closer point pair estimate  $\overrightarrow{x_{k+1} y_k}$ .

**Step 4:** Compute the corresponding closest point  $y_{k+1}$  and edge  $\overrightarrow{v_2^{k+1} v_3^{k+1}}$  on the enclosing segment by applying Kwok's PQ on  $x_{k+1}$  and the distance of this step is  $d_{k+1} = |\overrightarrow{x_{k+1} y_{k+1}}|$ . If  $x_{k+1}$  is found to locate inside the segment, return the shortest distance of the segment as zero ( $d_c = 0$ ). The first and third criteria are applied again in this step to give a new estimation.

**Step 5:** Test whether the resultant point pair  $\overrightarrow{x_{k+1} y_{k+1}}$  fulfills the criteria 2 and 3 for the closest point pair. In this step, two vectors are considered as perpendicular if the dot product is smaller than a threshold  $\varepsilon$ , where  $\varepsilon$  is a small positive number.

$$\begin{cases} |\overrightarrow{x_{k+1} y_{k+1}} \cdot \overrightarrow{AB}| < \varepsilon \\ |\overrightarrow{x_{k+1} y_{k+1}} \cdot \overrightarrow{v_2^{k+1} v_3^{k+1}}| < \varepsilon \end{cases} \quad (3.6)$$

If Eq. 3.6 is not satisfied, increase  $k$  by 1 and repeat Step 3 to 5 until the closest point pair is found. For GPU implementation, repeating these steps for a fixed iteration is more efficient than imposing an ending criterion. If Eq. 3.6 is satisfied, the shortest distance  $d_c$  is found by  $d_c = d_{k+1}$ .

Between the two edges  $\overrightarrow{AB}$  and  $\overrightarrow{v_2^{k+1} v_3^{k+1}}$ , point pair  $\overrightarrow{x_{k+1} y_k}$  is defined as the distance vector such that,

$$|\overrightarrow{x_{k+1} y_k}| \leq |\overrightarrow{x_k y_k}|, \text{ i.e. } d'_k \leq d_k \quad (3.7)$$

And considering the two points  $y'_k, y_{k+1}$  on segment surface, is defined as the distance

point pair between point  $\overrightarrow{x_{k+1}y_{k+1}}$  and segment  $\Omega_j$ . Thus,

$$|\overrightarrow{x_{k+1}y_{k+1}}| \leq |\overrightarrow{x_{k+1}y_k}| \quad (3.8)$$

The inequalities Eqs. 3.7 and 3.8 ensure that a vector with shorter distance will be found in each loop, i.e.  $d_{k+1} \leq d_k$ , i.e. straightly decreasing, in addition to the convexity of problem as mentioned above, the shortest distance will converge to global minimum after a certain number of iterations  $n$ .

$$d_c = \min\{d_k, k = 0, 1, 2, \dots, n\} \quad (3.9)$$

### 3.3.3.3 Identification of Shortest Distance

Upon computing the closest point pairs for each triangle edge, identification of the closest feature (vertex, edge, or face) on the triangle is of paramount importance. The traditional method (e.g. V-Clip [131]) operates iteratively by searching the closest points on the whole polyhedra, which is confined between convex shapes. The major disadvantage is its slow calculation speed for larger mesh and at the same time does not allow parallelization. Our identification method is realized based on Theorem 1, while the parallelization is allowed so as to increase its processing speed.

**Theorem 1:** Assume that  $F_X$  and  $F_Y$  is a pair of features from each of two disjoint convex polyhedra, containing a pair of closest points for the polyhedra. Let  $VR(F_X)$  and  $VR(F_Y)$  denote their Voronoi Regions,  $x \in F_X$  and  $y \in F_Y$  be the closest points between  $F_X$  and  $F_Y$ . If  $x \in VR(F_Y)$  and  $y \in VR(F_X)$ , then  $x$  and  $y$  are a globally closest pair of points between the polyhedra.

In the proposed PQ algorithm,  $F_X$  and  $F_Y$  represent the features (vertex, edge or surface) of triangle  $\Delta ABC$  and segment  $\Omega_j$  respectively. As shown in Fig. 3.7a, upon extracting a cross-sectional region confined by  $^jv_{i=1,2,3,4}$ , the closest feature  $F_Y$  (i.e. segment edge  $\overrightarrow{^jv_2^jv_3}$ ) is determined by such that the Voronoi Region  $VR(F_Y)$  always contains  $x$ . Thus  $x \in VR(F_Y)$  is always true by definition. Therefore, only the correlation between  $VR(F_X)$  and  $F_Y$  need to be evaluated in order to find out the closest feature  $F_X$ .

A triangle possesses 7 features with mutually exclusive Voronoi Regions: 3 vertices, 3 edges and 1 surface. As shown in Fig. 3.7b, Voronoi Regions  $VR_{III}$ ,  $VR_V$ ,  $VR_{VII}$  are for the

vertex features respectively,  $A, B, C$  are for the edge features  $\overrightarrow{AB}, \overrightarrow{AC}, \overrightarrow{BC}$  respectively and  $VR_I$  is for the face feature.

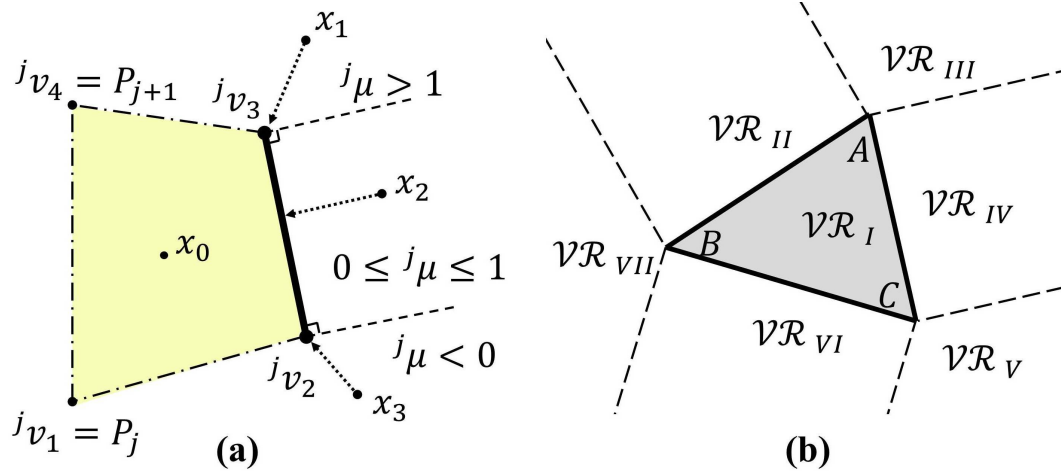


**Figure 3.7:** (a) Portion of cross-sectional region extracted from a single segment. It passes through the corresponding contour centers  $P_j$  and  $P_{j+1}$ . The potential closest points  $x_0...3$  always lay inside the Voronoi Region of the corresponding closest feature  $F_Y$ ; (b) Voronoi Regions of a triangle in 2D space.

To identify the closest feature, the boundary features of a triangle comprising 3 edges and 3 vertices except for the face, are considered. The corresponding shortest distance will then be computed, thus finding the closest one to the contour segment. The shortest distance of the 3 bounding edges ( $AB, AC, BC$ ) is calculated using the proposed PQ formulation in Section 3.3.3.2. This process naturally covers the PQ of vertex features as they are the endpoints of edges. Hence, the closest feature  $F_{Xmin}$  could be either laid on an edge or exactly at a vertex, depending on whether the resultant closest point is located at a vertex or on an edge on the triangle boundary. The closest feature will then be determined as the minimum one among the resultant shortest distances:

$$d_{\min} = \min\{d_{c,AB}, d_{c,BC}, d_{c,AC}\} \quad (3.10)$$

At this stage, the only remaining potential closest features on the triangle are  $F_{Xmin}$  and the face. Referring to Theorem 1, if the corresponding closest point on the segment side  $y_c$  lies within  $VR(F_{Xmin})$ , we can confirm that the  $F_{Xmin}$  is the closest feature to the segment. Otherwise, the closest point appears on the surface of the triangle. This situation is relatively rare because it only happens when the closest point on the segment side lies on its circular contours. In this case, the corresponding closest point can be estimated intuitively with the centroid of the closest points of the three edges.

### 3.3.4 Experimental Results

The overall performance of the proposed PQ algorithm was evaluated on two different types of processors: multi-core CPUs and GPUs. Their speed up and real-time response were investigated. The CPU-based PQs act as the baseline or reference for comparison with the implementation on GPUs. The CPU-based reference is also designed with detailed kernel source code (CUDA), and compiled using Visual Studio 2012 on an AMD Phenom™ II X4 955 Processor@3.20GHz. A standard GPU platform, nVidia GTX 770, is adopted, which contains 1536 CUDA cores.

#### 3.3.4.1 Fast Triangular Proximity Query

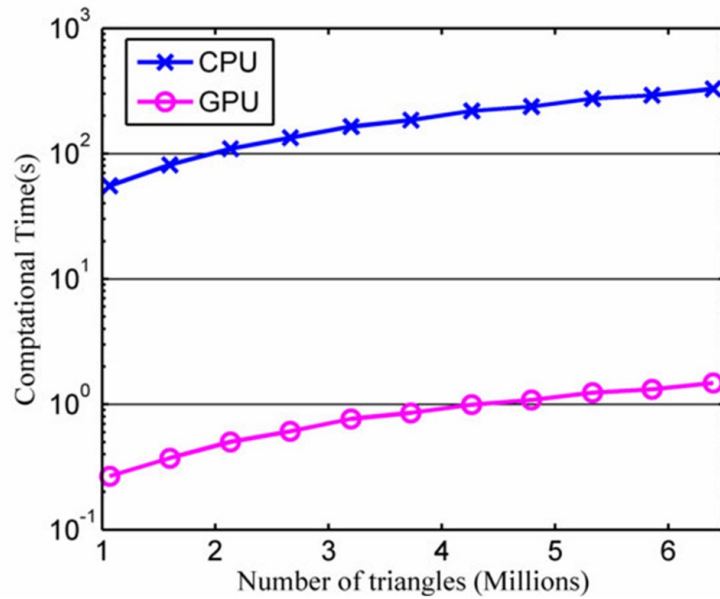
Modern GPUs normally have 10-100 times higher computation throughput in floating-point precision, compared to the modern CPUs. As shown in Fig. 3.8a, our GPU algorithm can achieve two orders of speedup, around 200 times faster than the single-core CPU; Thirty segments of general cylinders are involved, and it allows PQs on around 4M triangle meshes at the rate of >1Hz. It is worth noting that the GPU main memory bandwidth does not scale up accordingly and is only 5-10 times higher than CPUs. This limitation in GPU data transfer rate also account for the variation in speedup Fig. 3.8b. The speedup can be even increased with the number of triangular mesh because of its further efficient memory access.

In our GPU-based computational scheme, we propose to transfer mesh data into small local memory within each CUDA processor; therefore, only the triangle data are loaded from the main memory. This prevents the performance from degrading due to the insufficient bandwidth of the main memory access.

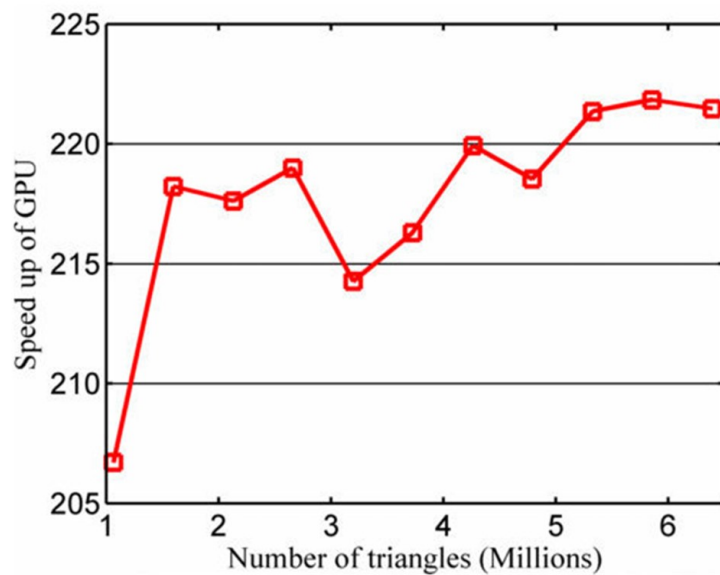
#### 3.3.4.2 Broad-phase Culling with Level of Detail Techniques

A broad phase technique based on mesh segmentation was employed. It can efficiently prune away unnecessary pair-wised PQ test in search of the shortest distance. Such technique further enhances the overall performance of the proposed PQ algorithm:

- i) A set of sub-meshes is created by bisecting the input mesh successively into smaller pieces, as shown in Fig. 3.9.



(a)



(b)

**Figure 3.8:** (a) Illustration of GPU and CPU computational performance of PQ process with 30 segments and millions of meshes; (b) Speedup of GPU-based PQ computation with respect to CPU

- ii) Each sub-mesh is simplified into a lower level-of-detail (LOD) version while preserving their geometric feature.
- iii) To cull out the closest sub-mesh to the contour segments, the PQ of every simplified sub-meshes are computed, which can be completed quickly because of the substantial reduction in number of mesh.

- iv) Finally, the exact closest point pair is determined by performing our proposed PQ only on the closest piece of mesh in high resolution.

The advantage of this technique is that it does not require a convex or bounding volume representation of the input mesh, resulting in high computational efficiency and easy implementation. The experimental result (Table 3.1) demonstrated that the culling technique can further speed up the overall PQ performance on both CPU and GPU processors by at least 70%.

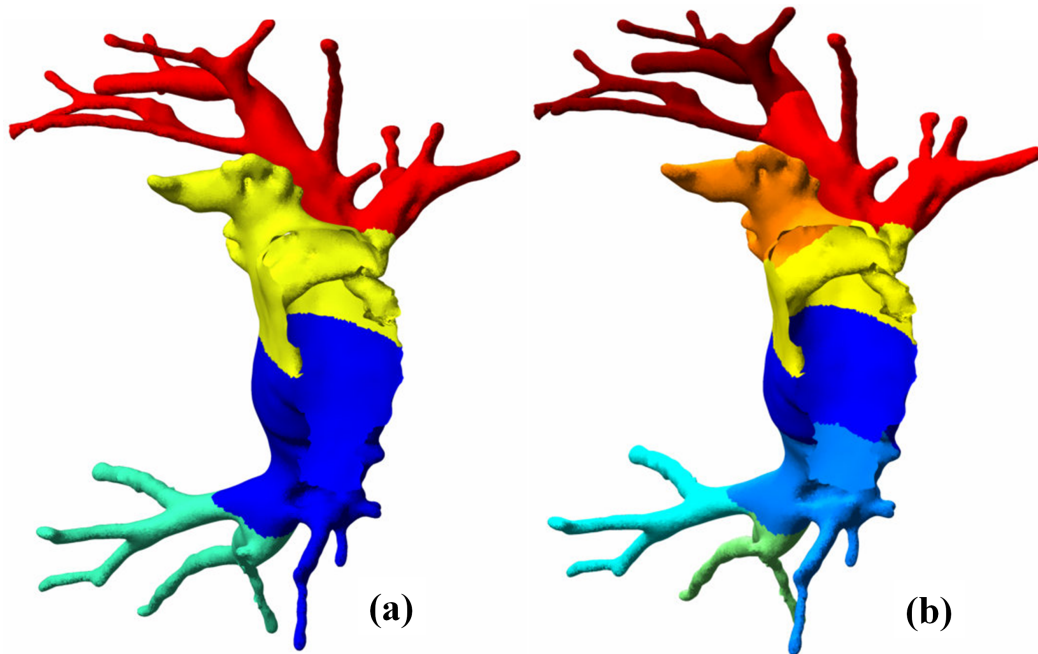


**Figure 3.9:** Segmented sub-mesh of the left atrium model with (a) 8 segments (b) 4 segments for broad-phase culling

**Table 3.1:** Computation time of PQs on 1 million of mesh with different levels of bisections culling.

Processor	Layer(s) of Bisection	Culling Time (s)	Narrow-phase Time (s)	Total Time (s)
CPU	Brute	-	46.04	46.04
	1	9.15	1.73	10.89
	2	9.22	0.70	9.9
	3	9.22	0.33	9.5
GPU	Brute	-	0.946	0.946
	1	0.193	0.035	0.227
	2	0.206	0.014	0.220
	3	0.213	0.006	0.219



### 3.3.5 Applications and Implementations

Four scenarios were simulated and designed according to practical robotic tasks, which involves different nature of mesh complexity and manipulation accuracy requirement. All simulated tasks provide sufficient information to analyze the efficiency and accuracy of the proposed PQ under the software framework of Robot Operating System (ROS).

#### 3.3.5.1 MRI-guided Catheter Navigation

Figure 3.10 shows the human left atrial model constructed by pre-operative cardiac MR images for cardiovascular electrophysiology (EP) intervention - a minimally-invasive surgical treatment of heart rhythm disorders [141]. This mesh surface model comprises 5,372 vertices, 31,974 edges and 10,658 triangular meshes, which is a part of the EP roadmap acting as the primary reference for electrophysiologist to maneuver the catheter tip to the lesion target for tissue ablation [142]. The EP catheter tip is fitted with 7 contour segments, and its position is measured and tracked continuously [143]. Its instantaneous PQ distances relative to the roadmap surface are indicated with the RGB color codes. Such PQ information can be foreseen to give strong hints for safe and precise catheter navigation since the robotic control of catheter for EP has already adopted in real clinical practice (e.g. Hansen Sensei<sup>®</sup> robotic catheter system). Given the EP roadmap modeled by the number of mesh below 10K, the PQ can be mainland at rate >1Hz; thereby, image-based haptic feedback can be made possible, and it could provide electrophysiologist with navigation guidance to access route to lesion regions safely and accurately [144].

#### 3.3.5.2 Collision Detection for Robot-assisted Laparoscopy

The applications of fast PQ processing could also be extended to robot-assisted laparoscopic surgery. As compared to open surgery, robot-assisted surgery can remarkably reduce the interventional invasiveness by teleoperating compact robotics arms inside the patient body via small incisions. However, such technique is very challenging as the surgeons have to perform precise and complicated manipulation inside the confined internal cavity of patients, while avoiding delicate tissue structure, such as nerve and vessels. Surgeons also lose the sense of touch due to the tele-operation of robot and can only rely on the stereo laparoscopic camera to acquire visual guidance. Previous work in Virtual Fixture (VF) techniques [145] have demonstrated that the real-time reconstruction

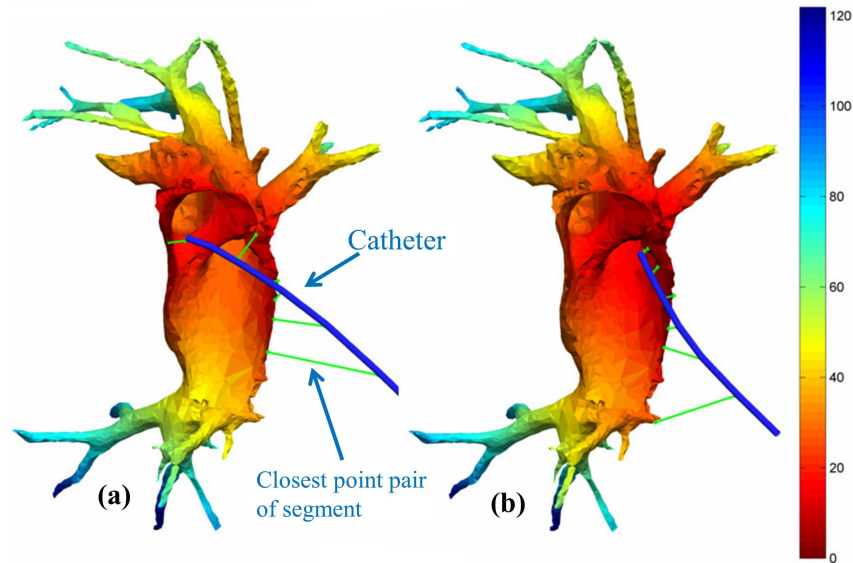


**Figure 3.10:** (a-b) Two catheter configurations with different degree of steering curvature. The catheter (with 7 segments) is advanced inside the left atrium model (with 10,658 mesh) for radiofrequency ablation during the cardiovascular electrophysiology procedure. The PQ sampling rate is maintained at rate of 1kHz.

of haptic feedback and force interaction is a viable way to enhance surgical performance. VF could also facilitate surgical safety and precision by providing haptic guidance based on the pre-defined trajectory or safe zone. To generate authentic and consistent force interactions, the collision detection in the surgical environment (i.e. instrument and tissue) must be calculated with a high updating rate ( $\sim 1\text{kHz}$ ).

This computational bottleneck can be resolved by the proposed high-performance PQ technique (Fig. 3.11). The stereo images acquired by the laparoscopic camera (as shown at the bottom of Fig. 3.11 in each time-lapse) enable real-time reconstruction of the internal cavity in the form of a 3D mesh. The reconstruction of the 3D geometry is achieved by triangulation techniques [146] in computer vision. To cope with the highly irregular and dynamic geometry, the dense triangular mesh ( $\approx 15\text{K}$  of meshes) is then processed with PQ. On the other hand, the configuration of surgical instrument are determined by the on-board encoder, which has a typical update rate of  $>1\text{kHz}$ . General cylinders with 7 segments are hence defined and updated in real-time to enclose the laparoscopic instrument similarly to Fig. 3.4 and Fig. 3.14. As a result, the PQ technique can perform real-time collision detection between the surgical instrument and the soft tissue anatomy.

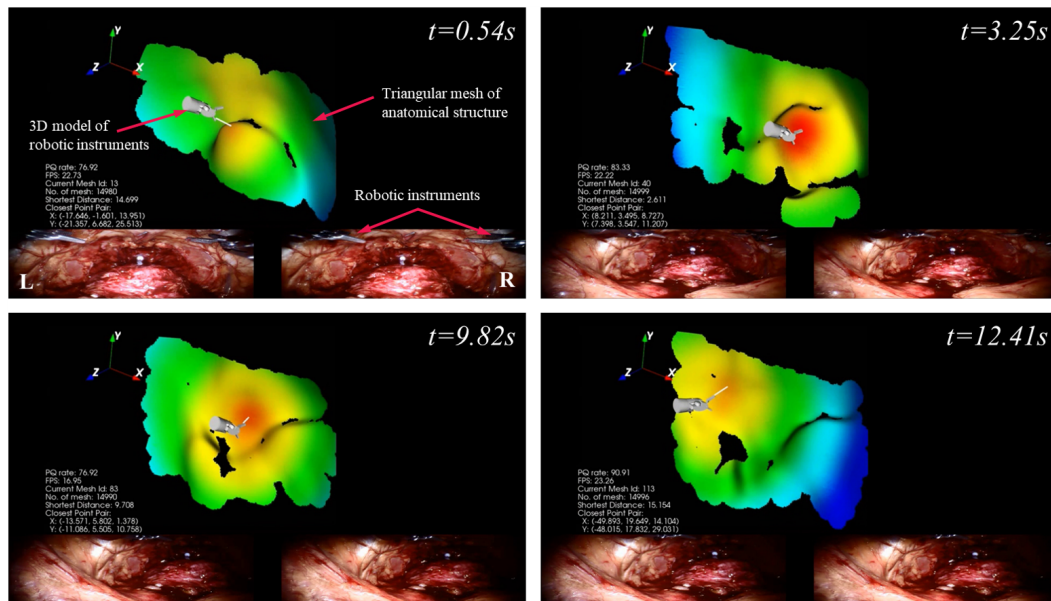


**Figure 3.11:** Time lapse illustration of the fast PQ computation between the surgical instrument and live anatomical structure during a robot-assisted minimally-invasive prostatectomy. The warm color on the mesh surface depicts the separation from the robot. The white line reveals the shortest distance.

### 3.3.5.3 Motion Planning for Anthropomorphic Manipulator

Fast PQ processing is a crucial technique for many interactive robotic tasks involving high degree-of-freedom (DoF) manipulation. A simulated manipulation scenario is illustrated in Fig. 3.12 carried out by an advanced humanoid robot, ATLAS (Boston Dynamics, MA, USA) [147]. The active sensory system, Light Detection and Ranging (LIDAR), mounted on its head, enables accurate geometry perception. It also facilitates high-quality 3D representation of the unstructured environment in the form of cloud points. The mesh surface (Fig. 3.12) is constructed online with fast tessellation of the point-cloud data. This is a subtask in the DARPA Challenge, which is required to accomplish autonomously with minimal human intervention. The anthropomorphic arm and hand are controlled to reach the valve wheel behind a thin wall. The warped surface throughout the hole is also detailed by the 4308 meshes. High-frequency PQ process is applied to deduce a collision-free trajectory in high-dimension joint space so that the hand posture can be optimized so as to turn the valve wheel behind the wall ergonomically.

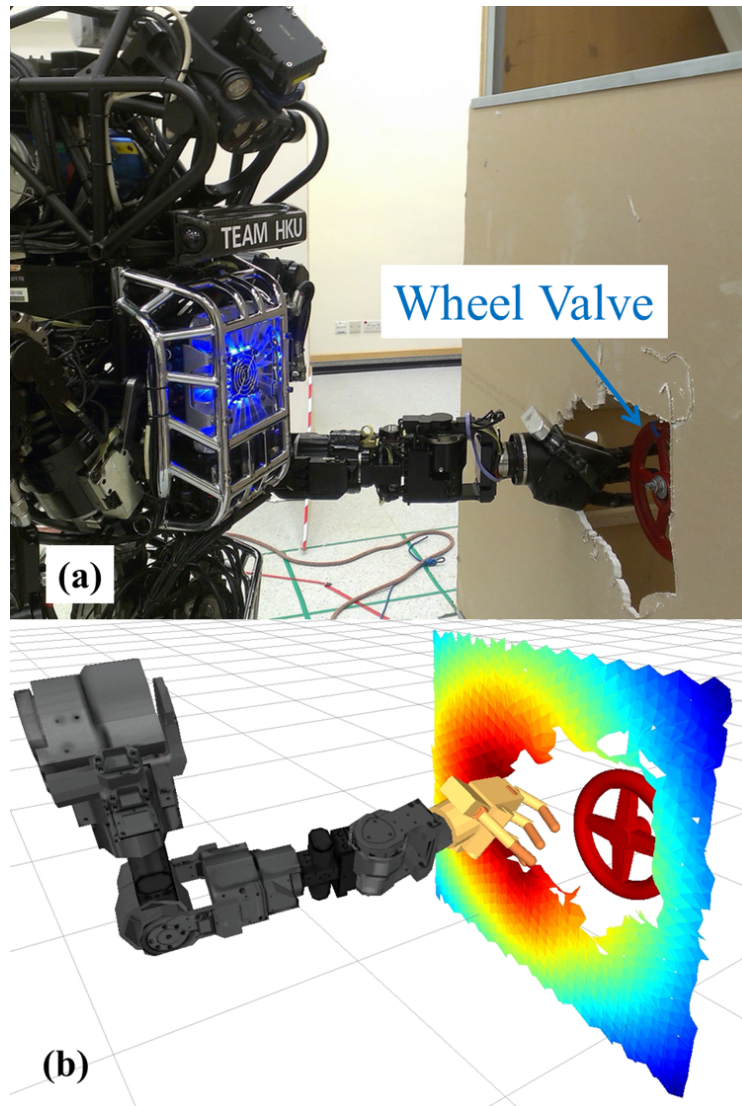


**Figure 3.12:** (a) ATLAS reaching the valve wheel through a hole created previously by the hand-held cutting tool; (b) PQ processed between the robot hand (with 39 segments) and the wall with hole (with 4,308 meshes). An optimal collision-free trajectory is estimated online with the aim to grasp the wheel. The warmer the colour on wall indicates, the closer distance to the robot arm and fingers is.

#### 3.3.5.4 Collision-free Trajectory Planning for Human-Robot Collaborative Tasks

Human-robot collaboration is an emerging paradigm in the latest manufacturing workflow. To achieve the optimal efficacy, human and robot have to coordinate seamlessly in close proximity, where intensive physical interactions are often inevitable. Real-time depth sensing units, such as stereo cameras or LIDAR are often utilized to monitor the human operators or any obstacles that can potentially enter the robot manipulation pathway. The sensed geometry is typically represented in the form of point cloud, from which a dense triangular mesh surface can be reconstructed. Due to the dynamic nature of human-robot

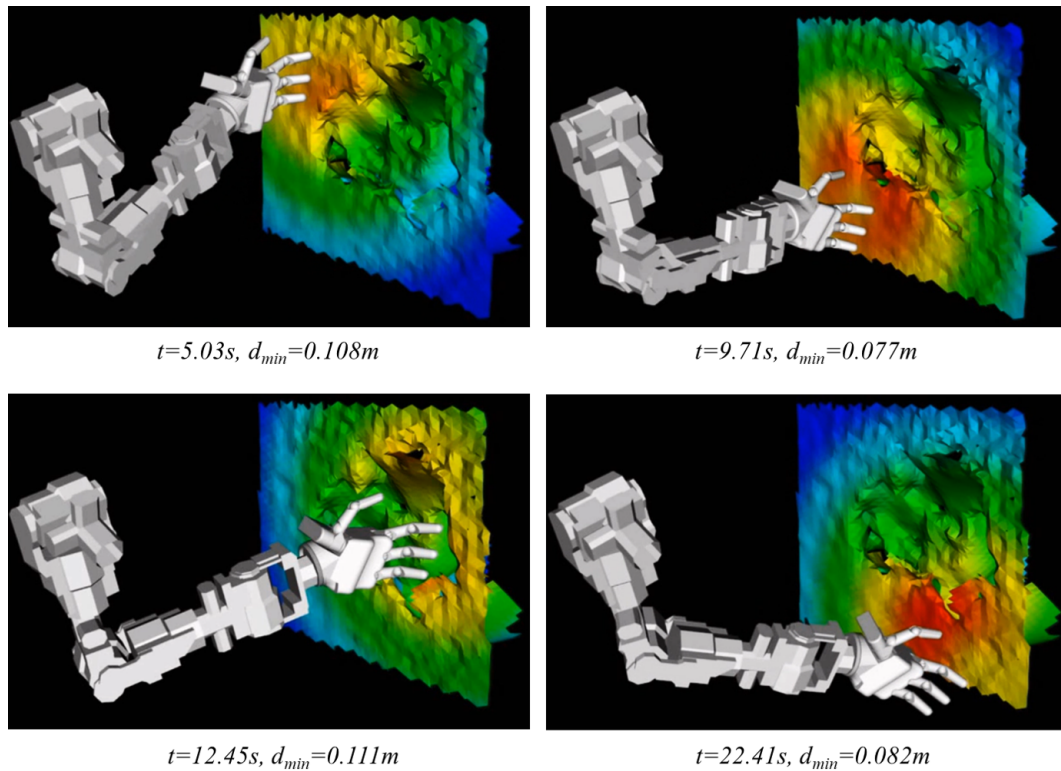


**Figure 3.13:** Color mesh illustrating the PQ computational result as overlaid on the 3D wall geometry. The updating frequency can be maintained above 30Hz throughout the entire manipulation with various configurations of the ATLAS robot arm.

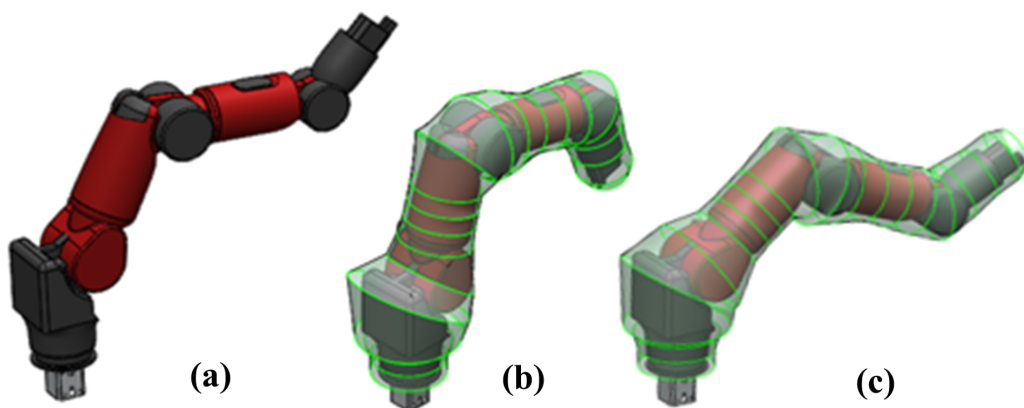


**Figure 3.14:** (a) CAD models of the Baxter robot arm; (b) Volumetric pathways comprising twenty segments (in green) tightly enclosing along the corresponding arm; (c) Circular contours attached flexibly along with their kinematic configurations updated.

collaborative environments, a point cloud sampling rate of  $>30\text{Hz}$  is often required to ensure safe operation. Such large volume of geometric data input necessitates fast PQ processing, so that a safe operating distance can be maintained between the robot and human operators. The PQ computation can become even more demanding if the robot has to re-calculate a viable manipulation trajectory under the dynamic geometric constraint, as a result of the rapid but unpredictable movement of human operators.

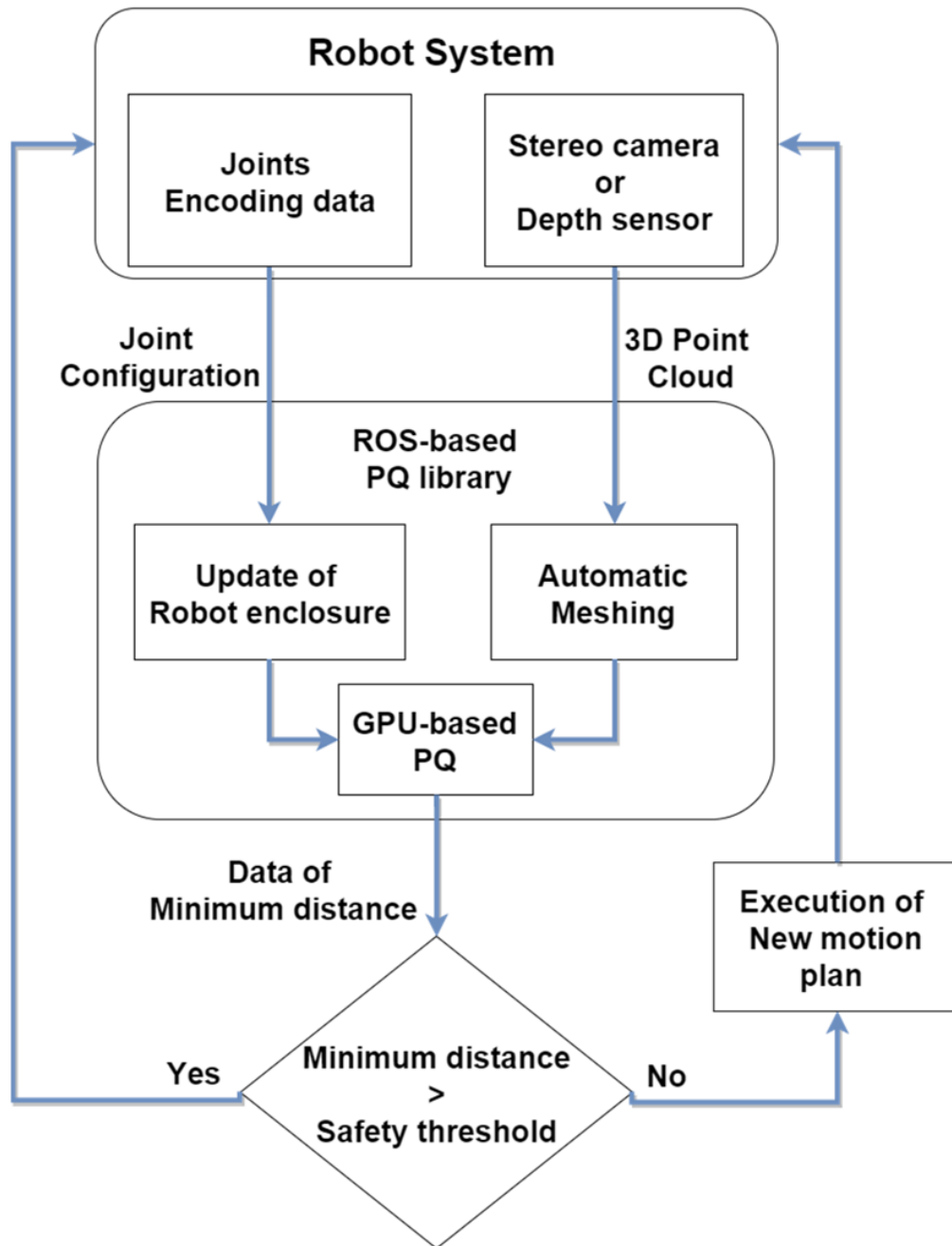


**Figure 3.15:** (a) Schematic diagram showing an example control workflow of using the proposed PQ for a human-robot collaborative task.

To resolve this issue, the proposed PQ technique has been implemented on the Robotics Operation System (ROS), which is a prevailing software framework for industrial robotics platform. Its features a standard communication protocol, enabling efficient exchange of data between various software libraries. As a result, the presented PQ process can be readily utilized by other motion planning libraries in ROS environments. Fig. 3.14 illustrates an industrial robotics platform (Baxter Robot, Rethink Robotics®) that is tightly enclosed by the proposed volumetric pathways under various configurations. The schematic diagram

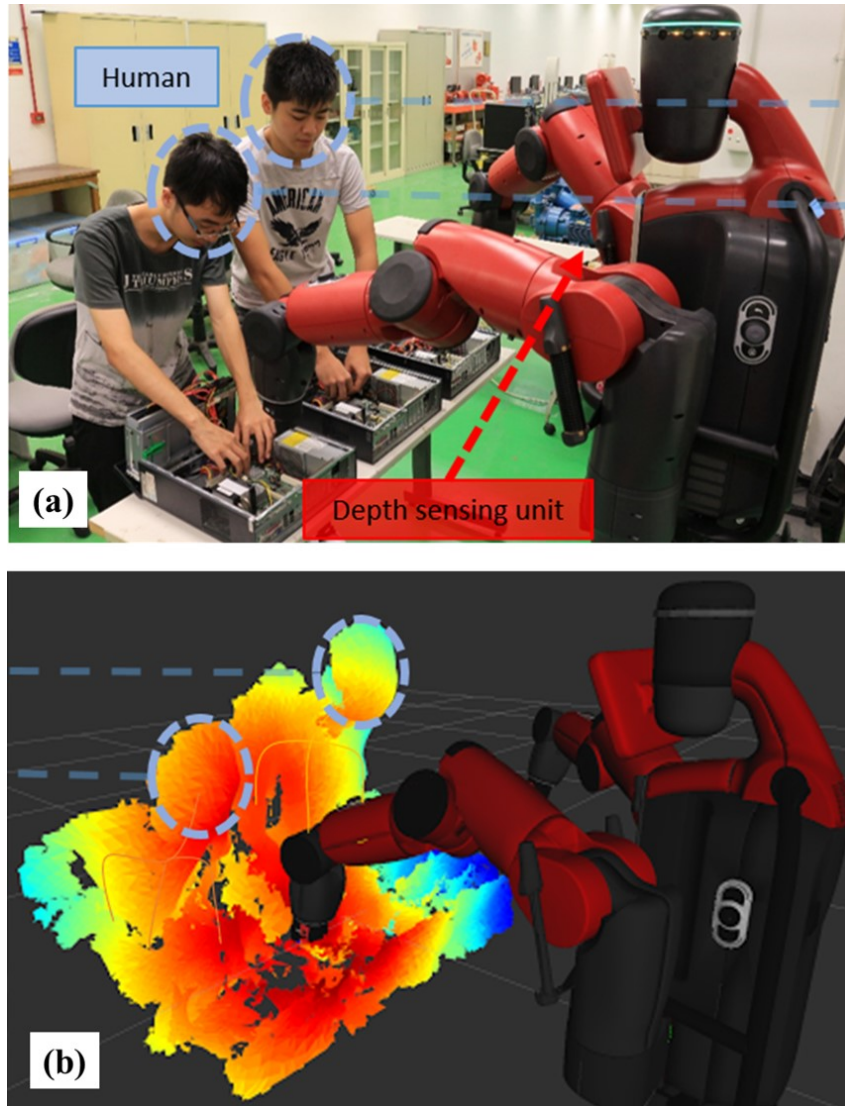


**Figure 3.16:** (a) Example industrial product assemble process that requires intimate human-robot collaborations. The Baxter industrial robot is integrated with depth sensing unit to identify humans and other objects within its workspace; (b) Graphic result of GPU-based PQ implemented on ROS. The warmer the color on the mesh surface, the closer the separation from the robot.

of the whole control workflow under ROS environment is also detailed in Fig. 3.15. The sensing data of robot joint sensors and depth sensing units are streamed into the GPU for real-time PQ processing. The computation result can be utilized to interfere with the control loop when necessary. The proposed workflow has been verified in a simulated human-robot collaborative assembly procedure. Fig. 3.16 It provides a real-time PQ result as a colored mesh and hence prevents collision between human and robot.

### 3.4 Discussion and Conclusion

This chapter summarize the key challenges and difficulties of computational-intensive tasks for intra-op image processing, namely *Intensity-based Registration* and *Proximity Query*. It is well recognized that the performance of many real-time applications, such as haptic rendering and intra-op roadmap update, is coupled with an increasing demand for fast and effective data processing.

Many deformable registration techniques, especially intensity-based methods like *DD* struggles in surgical scenario due to its computation intensiveness. In order to enable *DD* to be used intra-operatively, the computation time requirement should not interfere with the surgical rhythm. With our proposed GPU framework, the computation time is reduced by 60-fold, which sits well within the time constraints imposed by surgeries. The proposed framework implemented on GPUs can accomplish significant acceleration of computing gradient decomposition and convolution. Therefore, it could be applied, not only in *DD* approach, but also to any intensity based registration.

A versatile PQ formulation is proposed that the unstructured environment involved in robotic tasks can be flexibly represented by irregular triangular meshes, without having to preprocess the input geometric data. Moreover, the fitting of the contours along the robot kinematic chain needs only to be conducted once. No specific constraint is required for re-modeling the meshes, thus facilitating its use for generic geometric structures. The input geometric data is also not necessary to be temporal coherent. The number and configuration of meshes and contour segments can be varying time-by-time; therefore, the unstructured environment can be kept rapidly changing in terms of its morphology and topology. Although the BIG-O complexity of this PQ algorithm is proportional to the number of meshes and contour segments, its computation structure is highly parallel and anticipated to be further advanced with the trendy development of GPUs or FPGAs. The GPU-based PQ computation has been demonstrated to achieve >200 times speedup over single-core CPU. Two scenarios have also simulated for validating its practical values for real-time applications.



## Chapter 4

# MR Safe Actuation and Control of Robotic Catheter System

### 4.1 Introduction

In the review of [Chapter 2](#), I have highlighted the significant benefits of robot-assisted MRI-guided intervention as well as the advances of state-of-the-art intra-op MRI techniques. However, there is still no commercial robotic platform that can enter the mainstream of clinical practice in MRI-guided surgery. The soft tissue deformation, confined surgical site and convoluted entry pathway make MRI-guided intervention a challenging task even with the latest technology. Therefore, I have introduced high performance image registration and PQ in [Chapter 3](#) to realign the surgical roadmap to tissue movement, hence providing reliable image-guided navigation. Following that, this chapter will focus on the manipulation side in MIS. A miniturized and dexterous MR Safe robotic platform ([Fig. 4.3](#)) for catheter interventions will be proposed. It begins with outlining the major clinical motivations and concerns of MRI-guided catheterization. Detailed robot design features and hydraulic actuation mechanism are described ([Section 4.3](#)), followed by experimental evaluations ([Section 4.4](#)) of tele-manipulating standard cardiac catheter. I have also review some state-of-the-art techniques for MRI-guided intervention assisted by tele-operated robots ([Section 4.6](#)). Demonstration of the basic robot components and the integrated control interface for MRI guided EP are also highlighted.

## 4.2 Clinical Motivation

Heart rhythm disorder (also known as arrhythmia) is one of the most common cardiac diseases in the world, especially in developed countries. In the U.S. alone, more than 2.6 million people experience various categories of arrhythmia each year. Certain types of arrhythmias, such as ventricular tachycardia (VT) are particularly hazardous as they can cause sudden heart failure, which leads to more than half a million mortality a year in the US. And the numbers increase with the population ages. At least 80% of these deaths could be prevented through early diagnosis and treatments. Cardiac Electrophysiology (EP) Catheterization is known as an effective minimally invasive surgery that is attracting increased interest.

In general, catheterization involves dexterous manipulation of thin and flexible medical-grade instrument to pinpoint the target anatomy for biopsy, drug delivery or lesion ablation through the transluminal, intraluminal, intracavitary or intracranial surgical approach. Such surgical manipulation could be applied to cardiovascular intervention, prostate surgery, stereotactic neurosurgery or breast biopsy. Cardiovascular diseases, which remain the major cause of mortality in developed countries, particularly demand dexterous catheterization. Heart rhythm disorder (known as arrhythmia) is a typical example, to which cardiovascular electrophysiology (EP) is known as the effective surgical treatment [148, 149]. In the procedure, electrophysiologists insert a long catheter mostly from the femoral vein to the heart chamber, in which radiofrequency (RF) ablation is performed at the catheter tip in contact with lesion tissue to isolate the abnormal electrophysiological signals that cause arrhythmias.

Even with catheter navigation using a cardiac EP roadmap, manipulating the catheter to the desired location remains challenging due to the inconsistent control of a thin ( $\varnothing < 3\text{mm}$ ), long ( $\approx 1.5\text{m}$ ), flexible EP catheter within rapidly deforming cardiovascular tissue, such as the left ventricle (LV) and left atrium (LA). This challenge has drawn attention to the development of tele-operated robotic platforms, such as the well-known commercial platforms - Hansen Sensei™ X, Amigo Remote Cintratheter System, aiming at improving the dexterity and accuracy of catheter manipulation for intra-cardiac EP intervention.

Another challenge is that the catheter navigation can also be complicated by the lack of real-time and continuous updates of patient-specific cardiac EP roadmaps. The electrophysiologists may not feel sufficiently confident to perform effective RF ablation,

due to the possibly large misalignment (>5mm) of the actual position of catheter tip with respect to the roadmap or electro-anatomical (EA) map. This poses certain disadvantages in using the industry-leading EP robots, including Stereotaxis Niobe<sup>®</sup> even with highly steerable catheter tip driven by magnetic force.

Apart from dexterous maneuvering of cardiac catheters to the target tissues, both for electro-anatomical (EA) mapping (EP's diagnostic phase) and then RF ablation, the ability to intra-operatively assess lesion locations and their ablation progress is another very crucial factor to enhance the safety and efficacy of the EP procedure. Magnetic resonance imaging (MRI) is the unique image modality capable of offering excellent images contrast for cardiovascular soft tissue, forming a cardiac roadmap online in 3D. MRI-guided EP also avoids exposing patients and clinicians to harmful radiation as generated by X-ray and computed tomography (CT) in conventional EP procedure. Late gadolinium enhancement T2-weighted cardiac MRI [150] can also readily visualize the physiological change of tissues, and identify the scar or edema arising from successful or incomplete RF ablation. Many research groups (e.g. [151–154]) have already conducted numerous patient trials and demonstrated the significant clinical value with the use of intra-operative (intra-op) MRI for EP in clinical routine.

### 4.3 MR Safe Robotic Catheter based on Hydraulic Actuation

Forbidden use of electromagnet motor in MRI imposes a significant challenge to the design of robot actuation, in particular for catheter manipulation that involves precise coordination of 3 degrees of freedom (DoFs) at least. No ferromagnetic material could be involved. Electrically conductive materials would be adopted with caution, since the eddy currents may be induced and the magnetic field homogeneity would also be significantly disrupted. This section first briefly review the state-of-the-art MR Conditional actuation, followed by the proposed MR Safe hydraulic actuation and overall design of the MRI-guided catheter robot.

#### 4.3.1 State-of-the-art

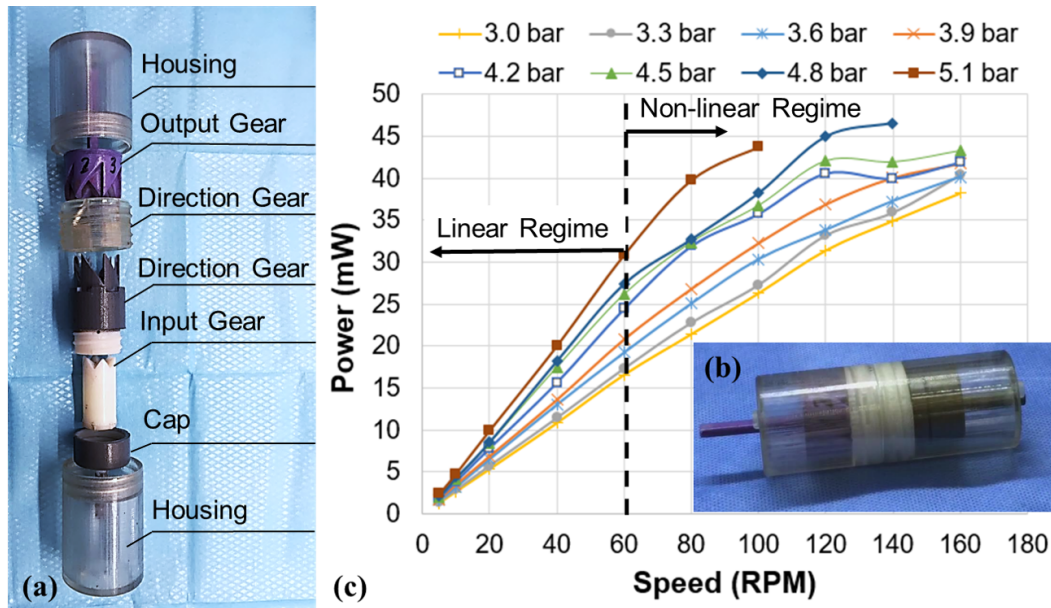
Piezoelectric and ultrasonic motors driven by oscillation of piezoelectric crystals facilitate the compact design and efficient power transfer. Both of them are driven by electric current. This is one of the most common actuation approaches adopted in MRI-guided

robots. As a core component of the robot, the motors will be placed close to the scanner. Thus the driving and encoding signals would inevitably induce electromagnetic interference (EMI) to MRI, deteriorating the image quality. In this case, complex EM-shielding is required to enclose the motors. It is technically difficult to filter the high-frequency control signals, but without affecting the motor operation and design compactness. To attenuate this interference, an advanced design on piezoelectric motor [33] has been proposed. It could significantly reduce the signal-to-noise ratio (SNR) loss to less than 15% by using high-frequency signal transmission. However, it is still very challenging to further enhancing the image quality, and safe distance of motor placement to the MR scanner will hamper its use in many clinical settings.

The drawbacks of piezoelectric/ultrasonic motors have naturally shifted the research focuses towards intrinsically MR-safe actuators driven by other energy sources, e.g. air or liquid flow. Pressurized air (at 0.2-0.4 MPa) supply is commonly available in hospital rooms, which could be considered as a handy energy resource for actuating the motors and guarantee zero EMI with the MRI. The first MR-safe pneumatic stepper motor was presented in [155]. It comprises 25 components and could provide high-torque rotation of maximum 650 mNm with 0.83 MPa input air pressure. However, its cost is relatively high due to the need of precise fabrication of parts with complex structure. In the previous work of [156] (Fig. 4.1), a compact, simple pneumatic motor has been developed. It consists of only seven components that are 3D-printed and solely made of MR-safe homogeneous materials. Compared to the hydraulic motors, the risk management of using pneumatic motors is easier, while the air is innocuous and leakage problem could be of less concern. Nonetheless, pneumatic motors are typically bulky and are not energy-efficient. Vibration and noise caused by high-frequency air dynamics are inappropriate in the clinical environment, which is still remained to be eliminated.

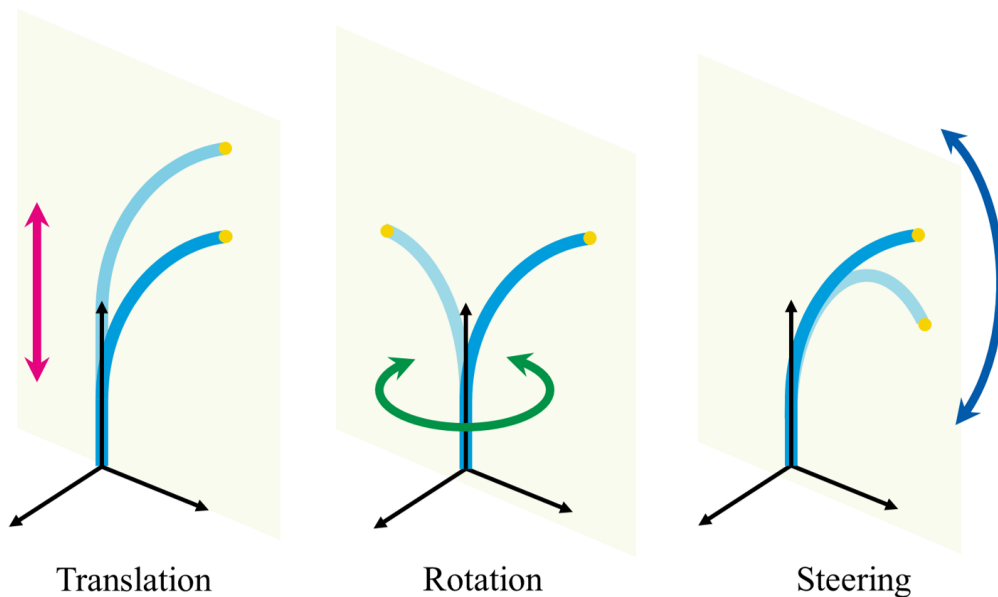
### 4.3.2 Hydraulic Actuation for Robotic Teleoperation

Fig. 4.3 illustrates the key components of the proposed MR Safe robotic manipulator. Such system has to comply with four major design requirements for clinical application: **R1**) the robot operation must not pose any hazard to the patient and to the MRI scanner, and does not adversely affect the quality of MR images; **R2**) the robot has to be compatible with clinically-used catheter and the corresponding 3D cardiovascular navigation system; **R3**) the robot can enable precise actuation with sufficient degrees of freedom (DoFs) to carry out intra-cardiac catheterization, comparable to manual control of the catheter (Fig. 4.2);



**Figure 4.1:** (a) Pneumatic motor composing of seven 3D-printed components; (b) Motor after handy assembly; (c) Linear correlation between power and speed holding below 60 rpm. High speed and power are achieved.

**R4)** the robot should be compact, light-weight and easy to sterilize.



**Figure 4.2:** Three basic manipulation DoFs of a catheter, namely translation, rotation and steering. All the DoFs have to be precisely controlled with sufficient range in order to perform an intra-cardiac ablation targeting task.

In MRI environments, electromagnetic (EM) and electrically conductive components have to be handled with caution. Any electric current would inevitably induce EM interference that disrupts the magnetic or gradient field homogeneity in MRI scanner, deteriorating the image quality. This poses a significant challenge to adopting EM motors

in actuation mechanism design, particularly for precise catheterization. A common approach is to isolate the motors with complex EM-shielding within the MRI room. However, it is still technically difficult to filter out high-frequency control signals without affecting motor operation and design compactness. Recently, an advanced design on piezoelectric motor has been shown to reduce signal-to-noise ratio (SNR) loss to less than 15% using high-frequency signal transmission [33]. To this end, we aim at developing intrinsically MR Safe and fluid-driven actuators, so that no EM material/power will exist in the MRI room. Previous examples are the MR Safe pneumatic stepper motor presented in [13, 29] and the MR Safe pneumatic needle-guide robot [157].

To address R1, master-slave hydraulic transmission is adopted in the design of actuation units (Fig. 4.4) to drive a catheter. In contrast to pneumatic actuation, hydraulic actuation uses incompressible fluid as working media, offering more steady transmission and quicker response. In the proposed robot, each master unit is actuated by an electric DC motor located in the control room. Each slave unit operates on the patient table near the MRI scanner. Such separation ensures negligible EM interference to the MR images, and allows the compact design of the slave units. During operation, each master unit drives the corresponding slave unit and subsequently the catheter, via two long pipelines ( $\approx 10\text{m}$  each) through the waveguide in-between the control room and the MRI room.

To achieve efficient transmission, rolling diaphragms [158] are employed to seal every master and slave actuation units (Fig. 4.4). Compared to the sealing approaches using O-ring, rolling diaphragms can offer effective sliding with negligible friction between the piston and the inner wall of the cylinder, thus reducing energy loss during actuation. This kind of elastomeric sealing is made of MR Safe, non-metallic material reinforced by fabric to withstand the high internal fluid pressure.

The slave actuation would be lagged behind the master input, for example, caused by the backlash between gears or long hydraulic transmission via flexible pipelines. This lagged phenomenon is known as hysteresis that may significantly affect the performance of the catheter robot. The gear backlash can be reduced by loading higher pressure inside the pipelines such that the pressurized fluid always pushes the pistons toward the gears, thereby keeping the teeth in contact (Fig. 4.4). The effects of preloading pressure on the robot's dynamic performance are experimentally analyzed in Section 4.4.

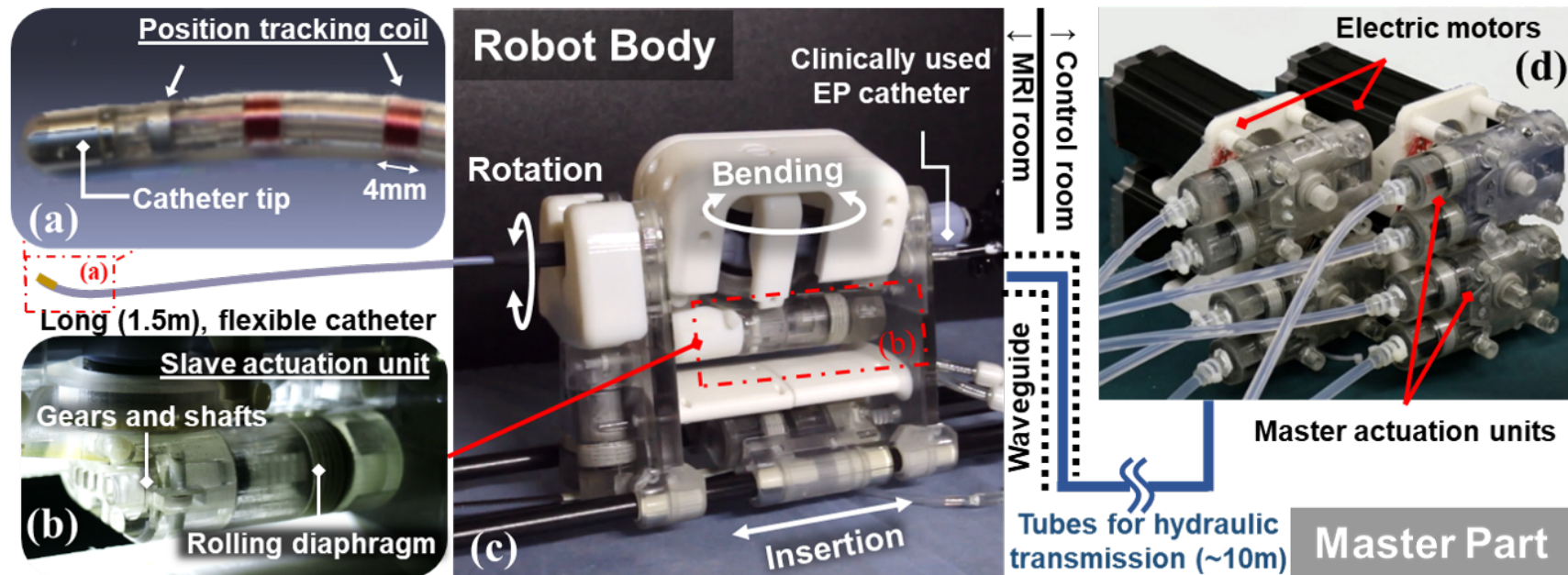


**Figure 4.3:** Overview of the MR Safe hydraulic catheter robotic manipulator showing the allocation of master-slave actuation in MRI room setting; (a) Two small active tracking coils wired along the catheter for real-time positional MR-tracking of its tip; (b) MR Safe robotic platform plugged-in with a standard EP catheter for RF ablation. The master-slave actuation units provide rotation, bending, coarse and fine insertion of the catheter; (c) Bending actuation unit that transmits the linear hydraulic actuation of rolling diaphragm into rotary motion. All hydraulic actuation units and the robot body are made of MR Safe materials; (d) Master electric motor units located in the control room serving as the source of hydraulics. The hydraulic fluid is transmitted to the slave catheter robot platform in MRI room via long ( $\approx 10\text{m}$ ) hydraulics pipelines. These hydraulics tubes can be channeled through the waveguide.

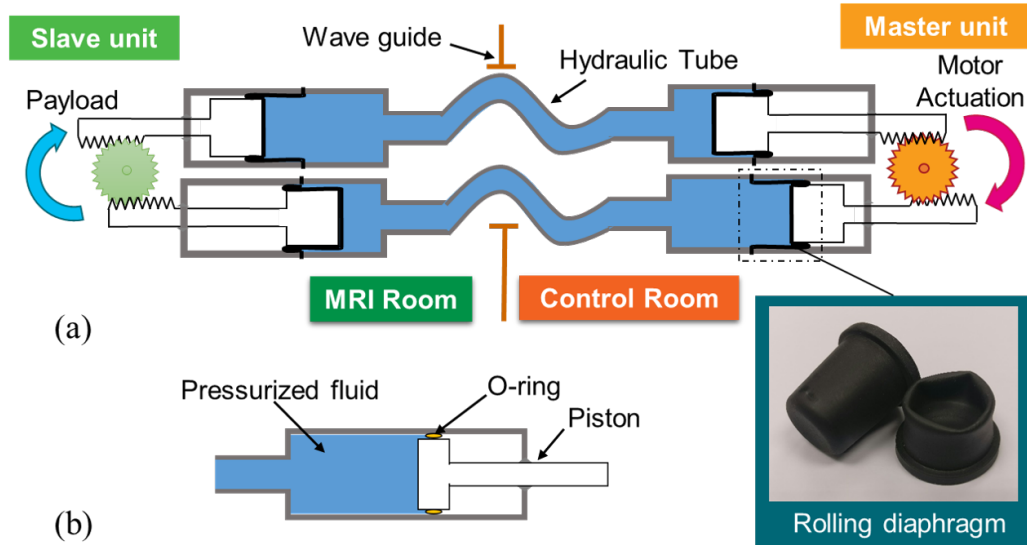


**Figure 4.4:** (a) Conceptual design of master-slave hydraulic transmission to ensure MR-compatibility of robot actuation. The contact between the gear teeth can be maintained by preloading fluid pressure, thus minimizing backlash. Rolling diaphragms are adopted to tightly sealed the pressurized fluid. (b) Conventional sealing using O-rings may induce significant sliding friction inside the cylinders.

### 4.3.3 Novel Design for MR Safe Robotic Catheter Manipulator

To address R3, the robot employs four pairs of the master-slave actuation units (Fig. 4.5), providing steering, rotation, coarse and fine translation of the catheter with sufficient motion ranges (Table 4.1). The coarse and fine translation DoFs enable, respectively, the longer journey navigation from vessels to the heart chambers, and the shorter range of dexterous tip movement inside the heart chambers for EA mapping and delicate RF ablation. Because the stroke lengths of the rolling diaphragms are limited, the ranges of motion at the rotation and the coarse translation DoFs are magnified using gearboxes at the corresponding slave units. The coarse translation DoF is belt-driven and shares the same moving axis with the fine translation DoF. The steering angle of the catheter tip depends on the choice of the catheter. For example, the Thermocool® Smarttouch™ Bi-Directional Catheter (Biosense Webster Inc.) can be steered up to 180° in two directions.

To address R2, the angular positions of the master gears can be precisely controlled (Table 4.1) using the motors' built-in proportional-integral-derivative (PID) controllers. Since pipeline diameter and length also contribute to the fluid dynamics [159], stiff pipelines made of nylon (Table 4.1) are employed to minimize the pipe deformation when subjected to transmission force, thereby maintaining high precision output at the slave gears.



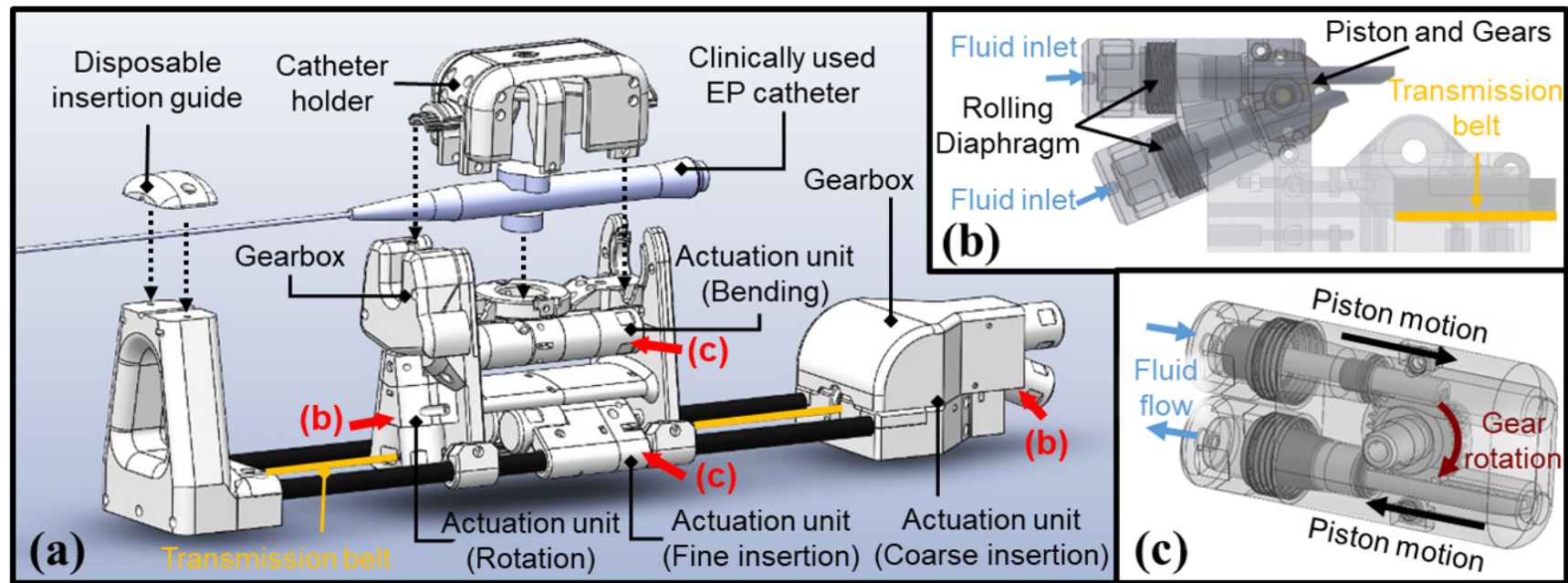


**Figure 4.5:** (a) Main components of the MR Safe robotic manipulator (the slave system) which operates in the MRI room. A clinically used EP catheter can be tightly mounted on a tailor-made catheter holder. (b) and (c): Actuation units providing steering, rotation, coarse and fine translation of the catheter.

**Table 4.1:** Specification of the MR Safe manipulator

<b>Size</b>	780 × 105 × 210 mm <sup>3</sup>
<b>Weight</b>	3.16kg (The whole slave body)
<b>Hydraulic pipelines</b>	Length: ≈10m Outer Diameter: 6mm Inner Diameter: 4mm Material: Nylon (DG-5431101) Manufacturer: Daoguan Inc.
<b>Transmission media</b>	Distill water (Pre-pressurized at ≤ 0.3 MPa) nominal
<b>Rolling diaphragms</b>	Diameter: 18mm Stroke length: 35mm Model no.: MCS2018M Manufacturer: FEFA Inc.
<b>Power source</b>	Four DC motors with 500 pulses encoder Maximum Torque: 278mNm Gear ratio: 14:1 Model no.: HFmotor-40150 Manufacturer: Chengdu Hangfa Hydraulic Engineering Co., Ltd
<b>Range of motion</b>	Steering: $-45^\circ \leq \theta_s \leq 45^\circ$ (0.063°) Rotation: $-360^\circ \leq \theta_r \leq 360^\circ$ (0.504°) Coarse Translation: $0\text{mm} \leq d_c \leq 200\text{mm}$ (0.115mm) Fine Translation: $0\text{mm} \leq d_f \leq 30\text{mm}$ (0.016mm) (Parentheses correspond to equivalent encoder resolution)

The modularized catheter holders (Fig. 4.5a) can be tailor-made for various kinds of steerable EP catheters (e.g. Biosense Webster Inc. or St. Jude Medical). It allows switching between different catheterization system simply by replacing the detachable catheter holders. A "plugging-in" mechanism is also designed to facilitate fast and reliable replacements. These catheter holders can be 3D-printed to account for future upgrades of any new catheter handle design.

To minimize the EM interference to the MR images, all the components of the slave system are made of MR Safe materials. Nonconducting, nonmetallic and nonmagnetic items may be determined to be MR Safe by providing scientifically based rationale rather than test data [160]. The main structural components are 3D-printed using acrylic compounds (VeroWhitePlus/VeroClear, Stratasys, USA). The key actuation components include gears made of nylon, a transmission belt made of rubber, and auxiliary parts made of polymers (e.g. Polyvinyl Chloride (PVC), Polyetherimide (PET)). This master-slave system has been tested to withstand rapid actuation (≤15Hz) under high fluid pressure

( $\leq 0.3\text{MPa}$ ). To address R4 regarding sterilization, this small-sized slave body can be enclosed by disposable surgical equipment drapes. The insertion guide (Fig. 4.5) made of low-cost acrylic compounds, is also disposable and can be sterilized beforehand.

## 4.4 Experimental Evaluation

To validate the robot performance for teleoperation under MR environments, we have conducted a series of experiments. An MRI-compatibility test is carried out to investigate the safety compliance and image interference imposed by the robot. The transmission performance of the master-slave hydraulic actuators is studied to validate its dynamic response for teleoperation. Finally, a lab-based simulated ablation task is performed on a left atrium (LA) phantom model to showcase its DoF and dexterity for achieving complicated manipulation.

### 4.4.1 MR-compatibility Test

The slave robotic manipulator placed in MRI room complies with the MR Safe classification of American Society for Testing and Materials (ASTM) standard F2503-13 [160], in which the robot comprises solely nonconducting, nonmetallic and nonmagnetic materials. For the safety concerns of experiment, some components were double-confirmed using metal/magnetic detectors before their integration. We simulated the basic operation for testing the compatibility with the MRI (Fig. 4.6a). The master system was actuated inside the control room inside a 1.5T MRI scanner (SIGNA, General Electric Company, USA). The slave system was placed adjacent to a standard MRI phantom (J8931, J.M. Specialty Parts, USA) filled with distilled water. The phantom was placed at the iso-center of the scanner, and then imaged to evaluate the potential EM interference generated by the slave robotic manipulator.

Fig. 4.6b depicts the resulting MR images of the phantom under four different conditions: i) Phantom: only the phantom alone was placed in the scanner; ii) Static: the robot introduced and remained power OFF; iii) Powered: the robot was kept still, but with the hydraulic and electric power ON in the control room; and iv) In motion: the robot was in operation, manipulating the EP catheter. Condition (i) serves as the baseline for evaluation. The EM-induced effects on the MR images were measured based on the changes in the signal-to-noise ratio (SNR)  $J = I/\sigma$ , where  $I$  is the mean intensity value of

a  $40 \times 40$  pixels region at the image center, and  $\sigma$  is the standard deviation of intensity value in a region of  $40 \times 40$  pixels at the lower right corner [161]. The MR images had maximum SNR loss less than 2% and had no observable image artifacts during operation.

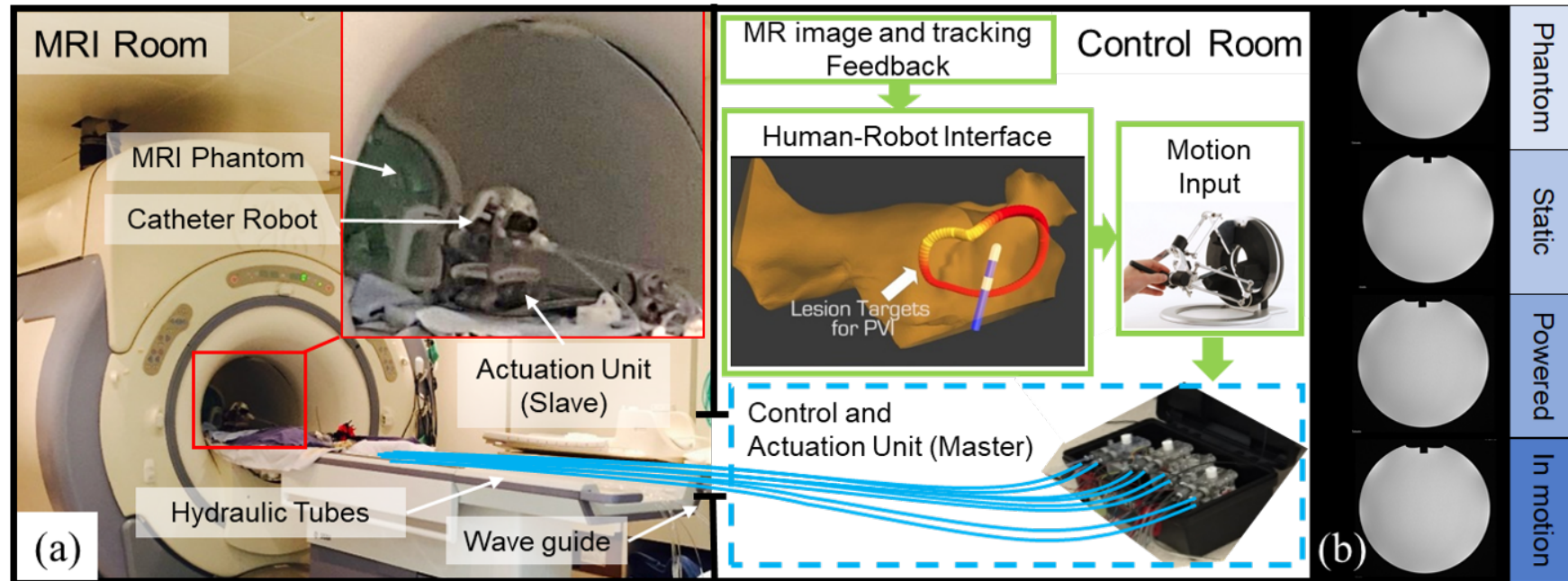


**Figure 4.6:** (a) Experimental setup of MR-compatibility test for the presented robot. Key components are connected between the MRI and the control rooms via the wave guide. The operator can tele-manipulate the catheter using the catheter navigation interface. (b) MR images of an MRI phantom placed aside the robot indicate the negligible EM interference in four different operating conditions.

## 4.4.2 Performance of Hydraulic Actuation

In the proposed master-slave actuators, the hydraulic transmission fluid was pre-pressurized in order to diminish the hysteresis due to gear backlash or the long ( $\approx 10\text{m}$ ) hydraulic transmission (Section 4.3.2). However, the excessive preload pressure also led to severe gear and pivot friction, which may in turn degrade the manipulation precision. In this section, we first evaluated the force transmission performance, and then analyzed the position tracking accuracy and the effects of preload fluid pressure on the hysteresis, as well as on the resultant dynamic performance.

### 4.4.2.1 Force Transmission

The force transmission performance of the master-slave actuator is evaluated with a free weight-lifting experiment. In this experiment, a rotary slave actuator depicted in Fig. 4.3 is coupled to a winch of 5cm radius. With the hydraulic fluid pre-loaded at 0.1MPa, the master-slave actuator is capable of lifting 3kg at a constant velocity of 10.01 cm/s, corresponding to an output torque of 1.47 Nm and net power of 2.93 W. The input torque at the motor axis on master side is also monitored by a torque sensor, which is used to estimate the hydraulic force transmission efficiency as 70%. Such force transmission performance is more than sufficient to steer the rotor on the standard catheter handle in full range, to roll the catheter ( $>360^\circ$ ), and also to push/pull the catheter ( $<230\text{mm}$ ) through the introducer sheath and the guiding tube.

In fact, the maximum torque of the present prototype is limited by the mechanical strength of the 3D printed components. In the real practice for human trials, the robot prototype ought to be fabricated with standard industrial machining procedures. Wider choices of MR Safe materials, such as Acetal (POM: Polyoxymethylene) or Nylon or any strong resilient plastic, will be used to comprise more robust structure for promising durability and enhanced actuation torque.

### 4.4.2.2 Hysteresis

Hysteresis is the primary concern for intra-cardiac intervention that requires accurate manipulation of the catheter with high resolution. The hysteresis of the pair of master-slave actuation units was measured and shown in Fig. 4.8. The translational

positions of the master and slave pistons were measured at different levels of preloaded fluid pressure inside the pipelines. The periodic motion of the master unit was controlled by the embedded PID positional controller at a frequency of 0.1Hz, where 70% of the stroke-length was covered. Fig. 4.7 depicts that the slave actuation unit could precisely follow a sinusoidal trajectory of the master unit, with a maximum absolute error of 0.67mm. The hysteresis was largely uniform throughout the whole range of motion, particularly at higher preloaded pressure. The hysteresis only slightly increase with the preloaded pressure, potentially due to the rise in static friction between the gears.

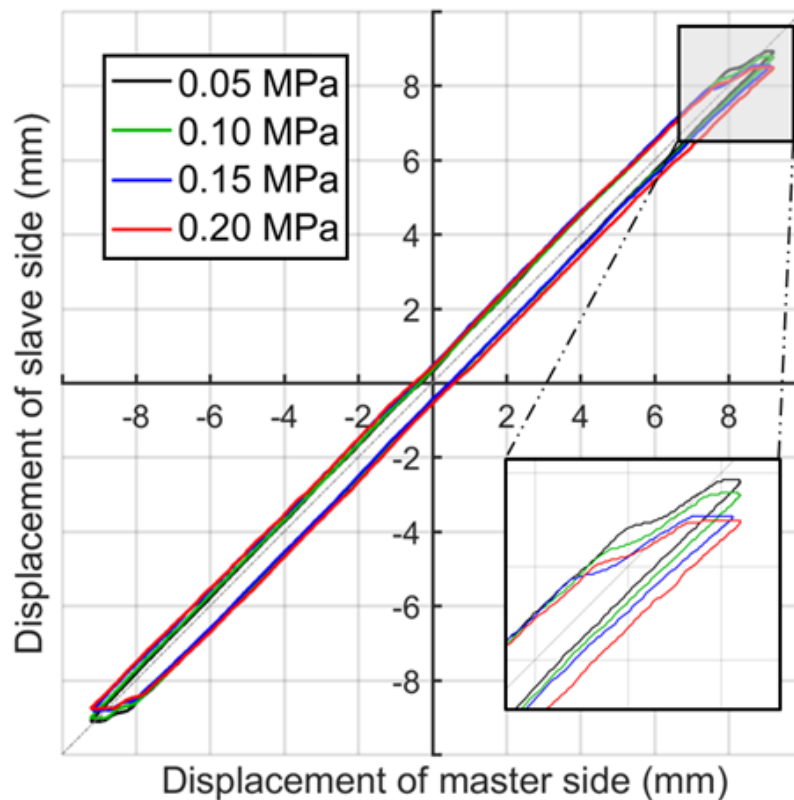


**Figure 4.7:** Hysteresis of the master-slave actuation unit at different preload fluid pressure. The average values of hysteresis were 0.88mm, 0.93mm, 1.02mm, 1.29mm for preloaded pressure 0.05 MPa, 0.1 MPa, 0.15 MPa and 0.2 MPa, respectively.

#### 4.4.2.3 Dynamic Response

The dynamic performance of the master-slave actuation units for different values of preloaded fluid pressure was investigated using a frequency response method. Given a sinusoidal torque input  $\tau = A \sin(\omega t)$  to the master gear, where  $\omega$  and  $t$  denote the frequency and time respectively, the torque at the slave gear was measured. The amplitude  $A$  was set to 0.1Nm, which is within the nominative operation range of the motor. Fig. 4.9

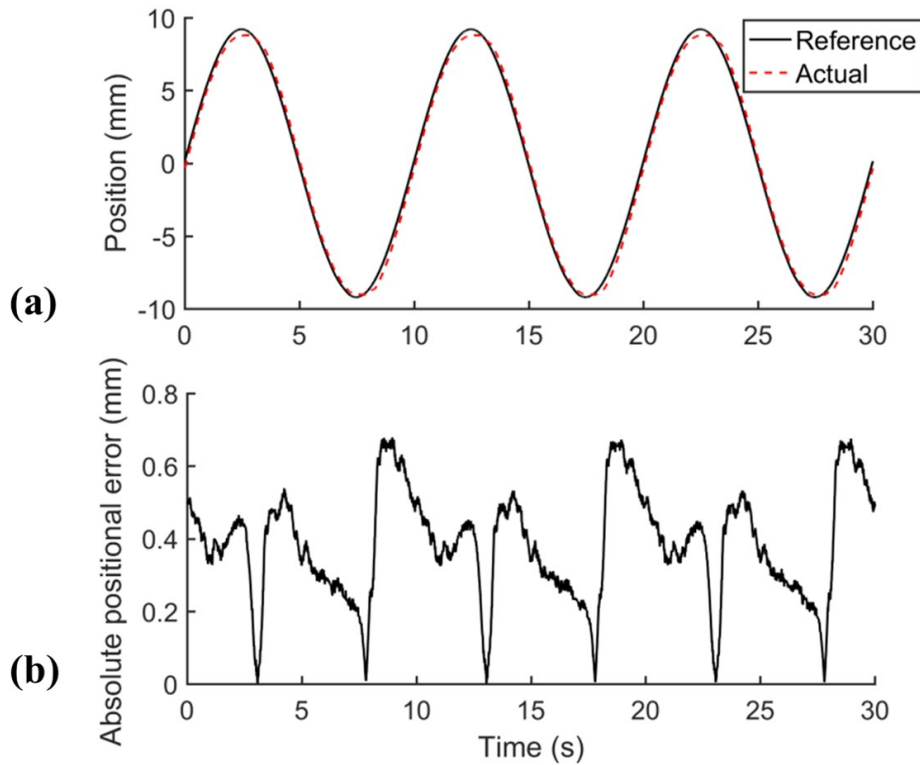


**Figure 4.8:** Periodic motion of master-slave actuation unit pre-loaded with 0.1 MPa of fluid pressure. The slave position (**a**, **dash line**) could precisely follow the sinusoidal reference trajectory (**a**, **concrete line**) of the master unit at 0.1 Hz. The absolute error (**b**) has a maximum of 0.67 mm.

depicts the Bode plot that characterizes the "magnification"  $M$  and the "phase-shift"  $\xi$  of the hydraulic transmission at steady state. Note that for a linear time invariant system, the frequency response at steady state becomes  $\tau_{ss} = MA \sin(\omega t + \xi)$ .

The magnitude plot indicates that the magnification increases with the preloaded fluid pressure. The magnification value peaks at around 5 Hz, which corresponds to the natural frequencies of the overall hydraulic transmission. We also found that the increase of the preloaded fluid pressure does not significantly affect the natural frequency.

The phase lag of the transmission was kept at around  $25^\circ$  for low actuation frequency ( $\leq 1$  Hz), and was not significantly affected by the variation of the preloaded fluid pressure. The transmission had small time delay: 45ms and 66ms at actuation frequency 1 Hz and 15 Hz, respectively, with preloaded fluid pressure 0.2 MPa. Such phase-shift and the natural frequency could result from the compliance of the 10m long nylon tubes, rolling diaphragms. However, the actual transmission performance also depends on the complicated fluid dynamics, it will require further investigations based on dynamic modelling techniques to explain for the frequency response.



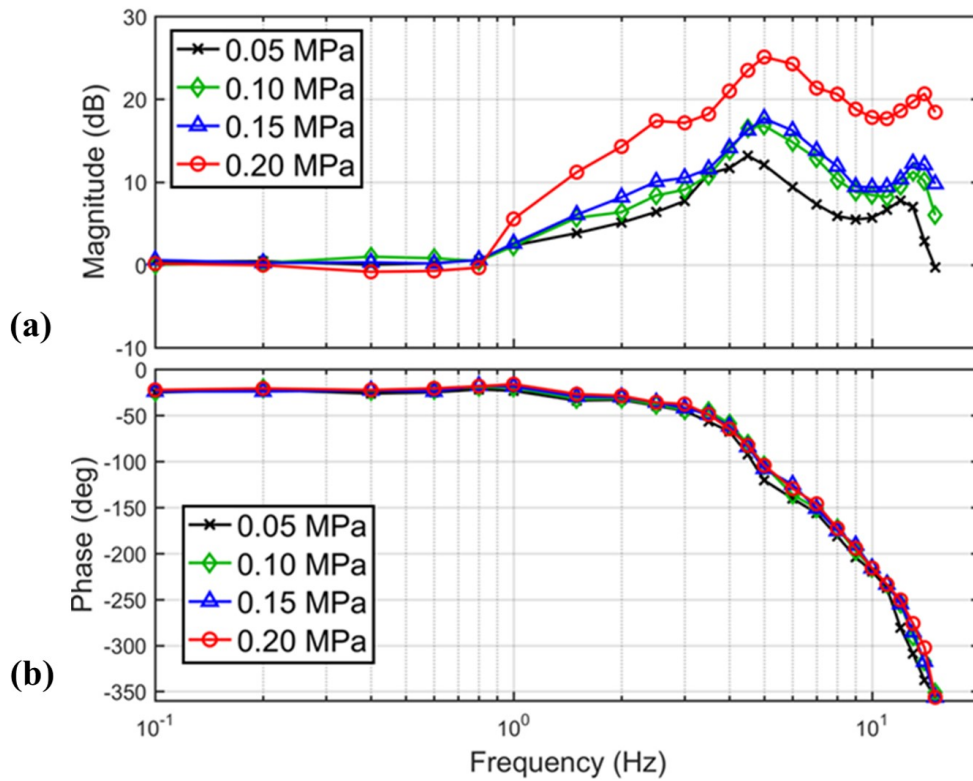


**Figure 4.9:** Bode plot showing torque transmission response of the master-slave hydraulic actuation unit at four different levels of preloaded fluid pressure. The magnitude (a) and phase shift (b) are shown. The data were collected from 10 cycles at the steady state.

In summary, the master-slave actuator had small (1.29 mm at 0.1 Hz) hysteresis and quick response (66 ms at 15 Hz), even at a high preloaded fluid pressure (0.2 MPa). Although the increase of the preloaded fluid pressure slightly increased the hysteresis (from 0.88 mm at 0.05 MPa to 1.29 mm at 0.2 MPa), it could attain effective force transmission as shown in the Bode plot (Fig. 4.9). As a result, it demonstrates that acceptable system delay could be maintained in a normative operating frequency for catheterization. Apart from the preloaded fluid pressure, fluid properties such as mass and viscosity would also affect the transmission. We employed distilled water as hydraulic fluid due to its ease of implementation and availability. The hydraulic pipelines length and diameter are also part of design considerations in regard to actuation dynamics. Previous analytical studies and experimental investigations [159] have suggested that the fluid friction can be reduced by using pipelines with a larger diameter, resulting in better system efficiency and smaller transmission phase lag; In addition, shorter pipelines are also preferable, which could reduce the transmission fluid inertia and also increase the transmission stiffness.

### 4.4.3 Catheter Manipulation for Cardiovascular Interventions

The robotic catheterization performance was validated by a simulated task of cardiac catheterization, namely pulmonary vein isolation (PVI), which is a treatment of atrial fibrillation. PVI requires RF ablation conducted inside the left atrium (LA). A typical task is to make lesion scars along the ostia of the left superior and inferior pulmonary veins. Such consistent scars would isolate the abnormal electrical signal originated from the arrhythmias, which causes the irregular heart motion [162].

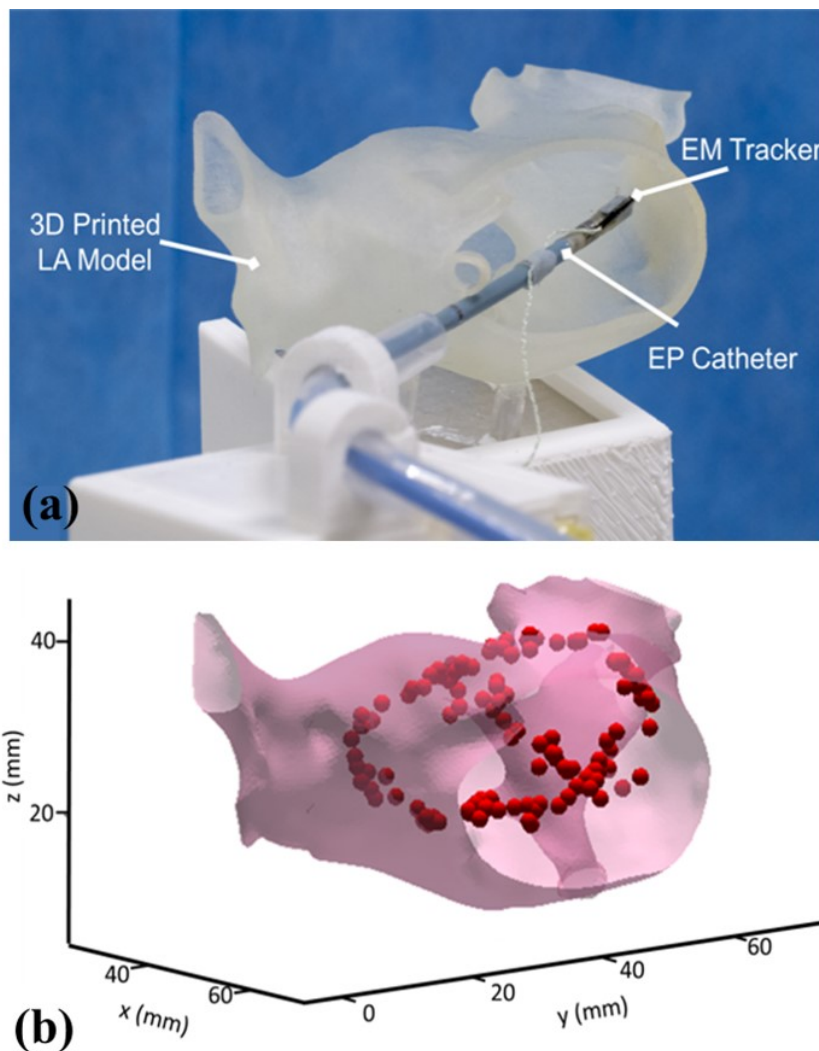


**Figure 4.10:** Experiment settings of the PVI task. (a) EP catheter tele-manipulated by the proposed robot to perform "ablation" on the left atrium (LA) phantom model; (b) Locations of the ablations (127 points) on the interior surface

In our lab-based validation, a standard clinically-used EP ablation catheter (Thermocool® Smarttouch™ Bi-Directional Catheter, Biosense Webster Inc.) was "plugged-in" to the slave robot. An EM positional sensor (NDI Medical Aurora) was

attached close to the catheter tip in order to track the 3-D tip positions in real-time. The phantom LA was a 3D-printed model made of soft material (AgilusClear, Stratasys Inc.) according to real anatomical data. In this task, the subject could tele-manipulate the catheter mounted the robot using a motion input device (Novint Falcon, NF1-L01-004). He/she was advised to press the foot pedal, then activate the "RF ablation", once being able to confirm the proper tip contact with the lesion targets prescribed on the virtual LA model. Note that the 3-D tracking coordinates, along with the virtual model, have to be well aligned with the actual LA phantom (Fig. 4.10a).

A reachability test was conducted with the aim to verify if the catheter tip driven by the presented robot is capable to reach or cover the region of interest along the ostia of the left superior and inferior pulmonary veins. Fig. 4.10b depicts the measured footprint of the catheter tip along the ostia, which are the ablation points confirmed by the operator during the tele-manipulation. Note that the robot catheterization precision should be taken into account, only if having detailed kinematic/dynamic study of the catheter itself. Such a study currently lies beyond the scope of this paper. In the real MRI-guided EP, such real-time 3-D tracking of the catheter can be achieved by MRI, also in the same image coordinate frame. Further details are discussed in Section 4.6.

## 4.5 Human-Robot Control Interface

A human-robot control interface is proposed to facilitate precise teleoperation of catheter. The interface integrates real-time MR-based positional feedback to enable closed-loop control of catheter teleoperation. This section will explore two mainstream control approaches, including conventional model-based method and also the newer data-driven model-free control techniques. The interface also offers visualization of the 3D electrophysiology (EP) roadmap in conjunction with the catheter tracking system. Thus the operator can tele-manipulate the catheter robot using a 3D motion input device.

### 4.5.1 Visual Guidance with Intra-operative MRI

Both the virtual catheter tip and the 3D EP roadmap constructed based on the pre-op MR images can be rendered in the navigation interface. Accurate alignment of the virtual catheter with the EP roadmap is attributed by the real-time and continuous MR-tracking of the catheter. Multi-modal visual guidance such as an endoscopic view from the point of the

catheter tip, can also be virtually generated, provided with the accurate alignment.

Intra-op imaging can be applied in conjunction with MR-tracking, such that the tracking is interleaved with the MR image sequence. This tracking involves measurement of both 3D position and orientation of the catheter tip. These data can be continuously streamed to the EP navigation system and the robot control interface [163]. Note that the entire MR-based catheter tracking takes place in the same MR imaging coordinate system.

Unlike conventional EP, our MR-based approach does not require external tracking reference, thereby avoiding potential disparity caused by relative registrations between tracking and imaging system. This enables rendering of the virtual endoscopic view from the viewpoint of the catheter tip [164]. Such virtual view facilitates fine placement of the catheter tip while approaching ablation targets registered on the roadmap (Fig. 4.6). Moreover, robotic control methods that account for the catheter's kinematics/dynamics [165] could also be applied to provide the operator with a consistent manipulation reference upon this 2D endoscopic view, as demonstrated in our attached video.

Two micro RF coils are incorporated into a clinically-use cardiac catheter, which can directly signal with the scanner via two pairs of coaxial cables connected to a custom-built receiver interface. A dedicated MR tracking sequence [35] could be applied to acquire the MR signals from the micro coils along the XYZ directions of the magnetic field gradient. To correct the inhomogeneities of the static magnetic field, both zero-phase-reference and Hadamard multiplexing methods could be employed. Such an MR sequence is able to achieve a spatial resolution up to  $0.6 \times 0.6 \times 0.6 \text{mm}^3$ , and a sampling rate of up to 40 Hz.

Such frequent and accurate localization of the micro coils catheter tip enables the estimation of both 3D position and orientation of the catheter tip. The MR-based tracking data can be continuously streamed into the navigation interface (e.g. EnSite VelocityTM, St. Jude Medical). The entire catheter localization takes place with the MR imaging coordinate system. Therefore, it does not require any external tracking reference, thereby avoiding potential disparity caused by relative registrations between tracking and imaging system. As a result, the tracked catheter tip position shares the same coordinate space with the MR images, facilitating precise placement of catheter tip at the ablation target registered on the roadmap. Moreover, it is clinically advantageous, while the MR-tracking can be applied in conjunction with the intra-op. imaging such that the tracking is interleaved with the MR image sequence. This enables the instantaneous visualization of the tissue edema or scars surrounding the catheter tip as the result of RF ablation [143].

### 4.5.1.1 Virtual Endoscopic View

As shown in Fig. 4.11(a), a virtual camera view (endoscopic view) is defined and attached to the catheter tip, of which the z-axis is aligned along the tip normal axis. The pose of the endoscopic frame could be sampled by the tracking system available in MRI-guided catheterization. In this work, we propose to correlate the catheter motion in endoscopic view with user's input motion. First, the transformation of the tip position from the Cartesian space to the X-Y coordinates with respect to (w.r.t) the 2D endoscopic view have to be derived. Incremental movement of the virtual camera at the catheter tip is denoted by  $\Delta p_w = [\Delta x_w \ \Delta y_w \ \Delta z_w]^T$  w.r.t the world coordinate (Cartesian space)  $\{W\}$ , while this movement w.r.t. the endoscopic coordinate  $\{C\}$  is denoted as  $\Delta p_c = [\Delta x_c \ \Delta y_c \ \Delta z_c]^T$ .  $\Delta z_c$  is the unit vector that aligns along the catheter tip normal orientation.

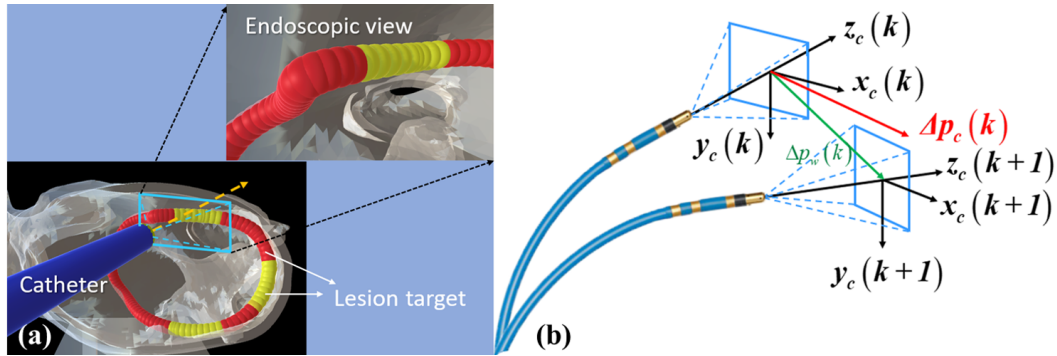


**Figure 4.11:** (a) Left atrial EP roadmap showing the virtual lesion targets defined close to the pulmonary vein ostia: Yellow for ablated regions; red for incomplete ones. The virtual endoscopic view is rendered from the catheter tip point of view. (b) Schematic diagram showing the movement of the catheter tip at time step  $k$  and step  $(k+1)$ , along with its endoscopic image plane.

To ensure the consistency of the steering direction of the catheter tip, the rolling of the camera along its z-axis is fixed during the transition. The rolling axis is defined by a unit vector  $z_c \in \mathfrak{R}^3$ . Thereby, the x- and y-axis of the camera frame, also act as the horizontal and vertical axes  $[\Delta x_c \ \Delta y_c]^T$  of its image plane. The  $3 \times 3$  rotation matrix  ${}^C_W R = [x_c \ y_c \ z_c]^T$  from the world  $\{W\}$  to camera  $\{C\}$  coordinate frame can be formed. Skipping the last row, the matrix becomes  ${}^C_W \hat{R} = [x_c \ y_c]^T$  with dimension of  $\mathfrak{R}^{2 \times 3}$ , which transforms the tip displacement relative to its image plane coordinate, i.e.  $\Delta p_c = {}^C_W R(\Delta p_w)$ .

### 4.5.2 Closed-loop Control for Catheter Manipulation

The control problem of robotic catheterization has attracted much attention in the field of research and commercial section. Traditional robotic control is based on the kinematic/dynamic model of the robot configuration and motion[94]. The distal bendable section of a catheter could be modeled as a continuum robot. Constant curvature (CC) approach is one of the most common methods for kinematic modeling of continuum structures [94]. CC models of catheters [95, 166] have simple formulations that facilitate implementation. Catheter deflection could also be predicted from actuation force using quasi-static force-deflection models based on beam theory[167]. Other approaches also include modeling the bendable sections as discretized rigid links with passive spherical joints, which has been demonstrated in 2D motion planning simulation [168]. However, external disturbance to the catheter, such as the pulsatile blood flow and contact with the cardiac chamber, can promptly deteriorate the reliability of these models in real-life applications. Furthermore, the accuracy of these kinematic/dynamic models strongly depends on proper selection of the structural parameters, but the search for these coefficients is often a heuristic process.

In contrast, model-free control methods avoid complicated system identification procedures for specific analytical models. The control mapping is solely sensory data. A PID controller for hybrid control of a 4-tendon catheter has been proposed in [169], where the actuation commands rely only on real-time position/force error feedback. Another representative model-free controller for a catheter prototype has been proposed in [170], which bases on real-time estimation of the Jacobian that relates sensory feedback at the catheter tip and the actuator command. Although these model-free approaches demonstrate promising control performance, they were validated with custom-made catheter prototypes that are not employed in current clinical practice. Therefore, the performance of model-based and model-free control methods in tele-operated robotic catheterization system still need further validation.

The validation of the MR Safe catheter robot and human-robot interface is presented in the following section. A control mapping for hand-to-eye coordination is implemented based on the virtual endoscopic view. Quantitative indices are designed to evaluate the performances of model-based and model-free methods on a static left-atrial ablation task. The model-based controller is designed based on the constant curvature kinematic model [95, 166]. The model-free controller utilizes position feedback to update the kinematic Jacobian [110]. Experimental evaluations were carried out using a standard clinically-used

catheter, which was tele-manipulated via an MR Safe robotic actuator (Fig. 4.3) under a virtual endoscopic guidance (Fig. 4.11). The major contributions are listed below:

- 1) Control mapping for hand-to-eye coordination based on the virtual endoscopic view utilizing model-based and model-free control methods (Sections 4.5.2.1 and 4.5.2.2);
- 2) Experimental validation platform for tele-operated robotic EP catheterization using a customized MR Safe robotic actuator (Section 4.5.3);
- 3) Performance evaluation and comparison of model-based and model-free control methods on an emulated ablation task carried out by ten subjects (Section 4.5.3.2).

#### 4.5.2.1 Model-based Control Approach

Model-based methods rely on the pre-established kinematic/dynamic model of the flexible catheter. Regarding the catheter distal section as continuum robot, constant curvature model [95, 166], beam model [167], n-rigid links model [168] were investigated in the previous work. Standard clinically-used steerable catheters could bend in two directions in the same plane by pulling tendons. The forward kinematic model of the clinically-used catheter based on D-H parameters has been established in [95]. This model is based on two assumptions, which are constant curvature and zero torsion. The equivalent model is briefly presented in Fig. 4.12.

As shown in Fig. 4.12(a), the catheter distal section has 3 DoFs: the axial translation denoted by  $d_i$ ; the bending angle denoted by  $\theta_b$ ; the rotation angle denoted by  $\theta_r$ . The movements of the catheter are driven by manipulating the catheter handle as shown in Fig. 4.12(b), where  $d$ ,  $\alpha$  and  $\phi$  represent the insertion distance, twisting angle of the knob and rotation angle of the handle respectively.

The axial translation  $d_i$  of the catheter is approximately equal to the insertion distance of the handle  $d$  ( $d \approx d_i$ ). The relation between the rotating angle of handle  $\alpha$  and tip  $\theta_r$  is given as  $\theta_r = K\alpha$ . The parameter  $K$  represents the torsional transmission effectiveness, which is taken as 1 in our experiment because of the low-friction between the catheter body and Polytetrafluoroethylene (PTFE) pipeline. Based on constant curvature assumption, the

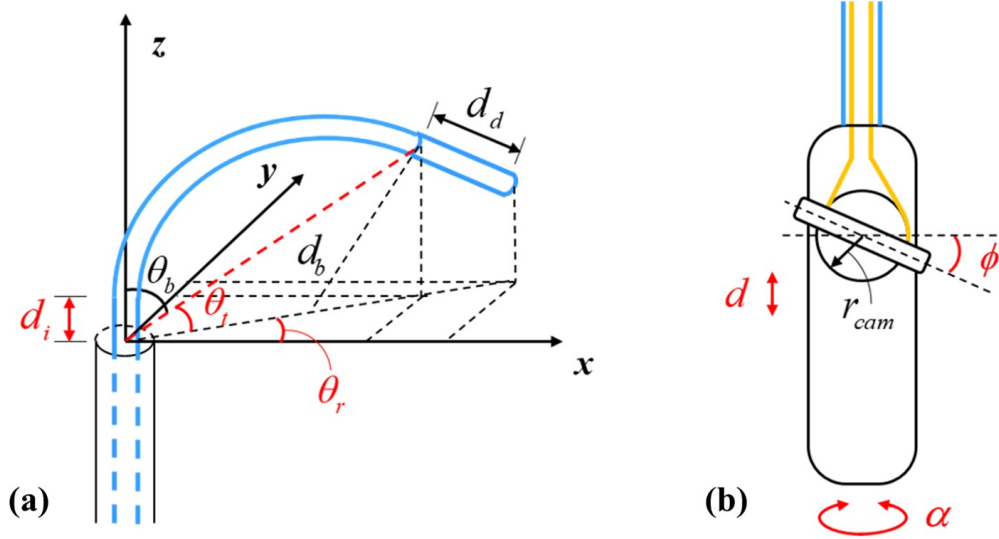


**Figure 4.12:** Schematic diagram of a typical catheter mechanism. (a) Constant curvature geometry of the distal section of the catheter. (b) Geometry of steering knob on the catheter handle indicated with its insertion distance  $d$ , twisting angle  $\phi$ , and rotating angle  $\alpha$ .

bending motion of the catheter tip is related to the knob twisting angle  $\phi$  by

$$\Delta R(\pi - 2\theta_t) = r_{cam}\phi(1 + k) \quad (4.1)$$

where  $\theta_t = \pi/2 - \theta_b$ ,  $\Delta R$  is the radius difference between inner and outer arcs of the bendable section,  $r_{cam}$  is the radius of the cam fixed with steering knob and  $k$  is the backlash factor to account for the tension-free wire displacement [166], which can be taken as 1 when both pull wires are well-tensioned.

Based on the coordinate system in Fig. 4.12, the position of end effector (catheter tip) can be calculated as below using  $d$ ,  $\phi$  and  $\alpha$

$$\mathbf{p} = \begin{bmatrix} c(K\alpha) \left( \frac{L}{M\phi} s^2(M\phi) + d_d s(2M\phi) \right) \\ s(K\alpha) \left( \frac{L}{M\phi} s^2(M\phi) + d_d s(2M\phi) \right) \\ d + \frac{L}{2M\phi} s(2M\phi) + d_d c(2M\phi) \end{bmatrix} \quad (4.2)$$

where  $M = \frac{r_{cam}(1+k)}{\Delta R}$ ,  $d_d$  is the length of the rigid distal section, and  $L$  is the length of the bending part of catheter. The symbol  $s(\cdot)$  and  $c(\cdot)$  are  $\sin(\cdot)$  and  $\cos(\cdot)$  respectively. The original and additional bending curve lengths are  $L_b$  and  $\Delta L$  respectively. As  $\Delta L$  is small compared to  $L_b$ , it could be ignored, that is

$$L = L_b + \Delta L = L_b + 2r_{cam}\theta_t \approx L_b \quad (4.3)$$



This catheter robotic manipulator can be described by a function of input variables relative to actuator  $\mathbf{q} = [\phi \ \alpha \ d]^T$  and the position of the catheter tip in the frame of camera view  $\{C\}$  is denoted as  $\mathbf{p}_c = [x_c \ y_c \ z_c]^T$ . The corresponding differential function could be represented as

$$\dot{\mathbf{p}}_c = \mathbf{J}\dot{\mathbf{q}} \quad (4.4)$$

where the Jacobian matrix  $\mathbf{J}$  could be calculated by differentiating the catheter tip position  $\mathbf{p}_w$  with respect to the input variable  $\mathbf{q}$ .  $\mathbf{p}_c$  and  $\mathbf{p}_w$  could be transformed using the rotation matrix  ${}^C_W\mathbf{R}$ .

With the Jacobian matrix of forward kinematics, we could establish its inverse kinematic function  $\dot{\mathbf{q}} = \mathbf{J}^{-1}\dot{\mathbf{p}}_c$ , which can be discretized to

$$\Delta\mathbf{q} = \mathbf{J}^{-1}\Delta\mathbf{p}_c \quad (4.5)$$

As this goal is to make the catheter tip motion and input motion synchronized,  $\Delta\mathbf{p}_c$  could be designed as the input read from the 3D motion input device, which is known in each step, and the inverse Jacobian matrix  $\mathbf{J}^{-1}$  could be calculated using the values in the last time step. With these two factors, the values of actuator variables  $\Delta\mathbf{q}$  could be obtained.

#### 4.5.2.2 Model-free Control Approach

The model-free control method implemented here is inspired by the optimal control method used in [110], but without the need of force sensor feedback. The Jacobian matrix is obtained and updated by the real-time data collected during the operation. After a quick initialization of the Jacobian matrix, the operator could control the robot with an updating mapping scheme. The main flow of this control is shown as below.

**Initialization of Jacobian Matrix** The 3 DoFs of the actuator for rotation, bending and insertion are independent to each other, therefore the initialization could be achieved by actuating the three motors in order with an incremental amount  $\Delta q_i$ ,  $i = 1, 2, 3$ , and measuring their corresponding displacements  $\Delta\mathbf{p}_{ci}$ . Then the initial Jacobian matrix could be constructed as  $\mathbf{J} = [\mathbf{J}_1 \ \mathbf{J}_2 \ \mathbf{J}_3]$ , where  $\mathbf{J}_i = \Delta\mathbf{p}_{ci}/\Delta q_i$ . A weighting matrix  $\mathbf{W}$  is designed as  $\mathbf{W} = \text{diag}(\|\mathbf{J}_1\|, \|\mathbf{J}_2\|, \|\mathbf{J}_3\|)$ . Therefore, the kinematic function (Eq. 4.4) could be represented as

$$\dot{\mathbf{p}}_c = \hat{\mathbf{J}}\mathbf{W}\dot{\mathbf{q}}, \quad \hat{\mathbf{J}} = \mathbf{J}\mathbf{W}^{-1} \quad (4.6)$$

which could be discretized as

$$\Delta \mathbf{p}_c = \widehat{\mathbf{J}} \mathbf{W} \Delta \mathbf{q} \quad (4.7)$$

**Update of Jacobian matrix** The online update relies on continuous estimation of the Jacobian, which is estimated by solving the following quadratic programming problem:

$$\begin{aligned} & \text{minimize} \quad \left\| \Delta \widehat{\mathbf{J}}(k) \right\| \\ & \text{subject to} \quad \Delta \mathbf{p}_c(k) = \widehat{\mathbf{J}}(k+1) \mathbf{W} \Delta \mathbf{q}(k), \widehat{\mathbf{J}}(k+1) = \widehat{\mathbf{J}}(k) + \Delta \widehat{\mathbf{J}}(k) \end{aligned} \quad (4.8)$$

where  $\Delta \widehat{\mathbf{J}}(k)$  is the variable to be optimized,  $\widehat{\mathbf{J}}(k)$  is the Jacobian matrix at time  $k$ ,  $\widehat{\mathbf{J}}(k+1)$  is the new Jacobian estimate at time  $k+1$ , and  $\{\Delta \mathbf{p}_c(k), \Delta \mathbf{q}(k)\}$  are displacements in camera view and output of actuator between the last time  $k$  and the present time  $k+1$ . We minimize the Frobenius norm ( $L_2$ -norm) of  $\Delta \widehat{\mathbf{J}}(k)$  for smooth transition of the column vectors of the Jacobian. After obtaining the latest Jacobian, the command to actuators could be calculated by

$$\Delta \mathbf{q}(k+1) = \left( \widehat{\mathbf{J}}(k+1) \mathbf{W} \right)^{-1} \Delta \mathbf{p}_c^*(k+1) \quad (4.9)$$

where  $\Delta \mathbf{p}_c^*(k+1)$  is the desired motion in camera view.

### 4.5.3 Experimental Results

This section describes the experimental results of the presented catheter control framework. Ten subjects were invited to a robot-assisted PVI task in an atrial phantom model. We chose PVI as a benchmarking task because of its prevalence in catheterization procedures used to treat atrial fibrillation (AF). Successful PVI requires effective ablation along the ostia of the left superior and inferior pulmonary veins, hence ceasing the electrical signals that cause AF. To targeting ablation lesion, the robot have to fully utilize all 3 DoFs to manipulate the catheter. All subjects had one trial on both model-based control and model-free control algorithms to enable compare and contrast on the performance indices. The virtual endoscopic view (Section 4.5.1.1) is also provided as the major visual cue.

#### 4.5.3.1 Experimental Setup

**Left Atrial Model** The 3D phantom model of left atrium (LA) (Fig. 4.13a) was obtained from an MRI scan and 3D-printed with soft material (AglusClear, Stratasys Inc.). The

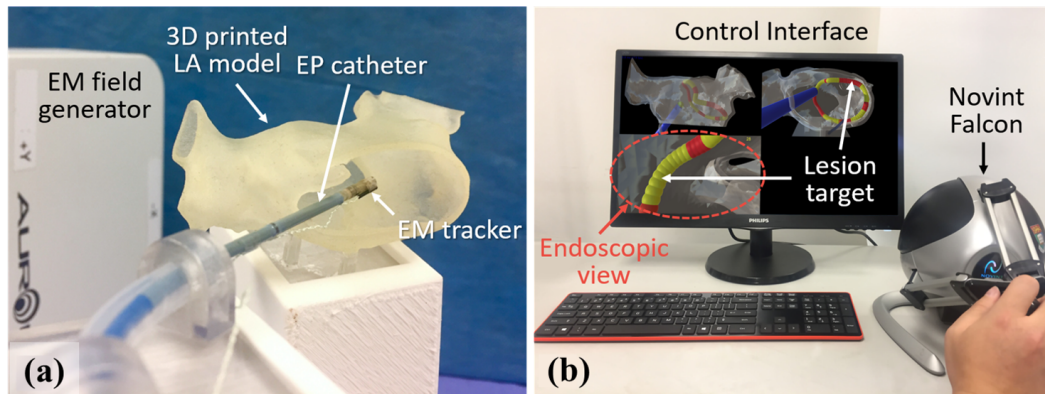


**Figure 4.13:** Experimental setup: (a) Left atrial phantom model and the EP ablation catheter. (b) Robot control interface providing the operator with simulated cardiac roadmap displayed in three different camera perspectives, including the virtual endoscopic view.

shore hardness of the material is A30-35 and the polymerized density is  $1.14\text{--}1.15\text{ g/cm}^3$ . The model comprises more than 5000 meshed, which is accurate and glossy enough to reproduce the geometry of real tissues.

To conduct RF ablation inside LA, catheter is inserted at femoral vein, through the inferior vena cava to the right atrium. After puncturing the atrial septum, it reaches LA for RF ablation [171]. In our experiment, a sheath (PTFE pipeline) is placed to form the pathway, guiding catheter towards LA phantom with similar entering direction and position to cardiovascular interventions.

**Position Tracking System** In the experiments, an electromagnetic (EM) tracking system (Aurora V3, Northern Digital Inc.) (Fig. 4.13a) is utilized to obtain the position and orientation of the catheter tip in world coordinate. This system allows the simultaneous tracking of multiple miniaturized sensor coils in five or six DoFs with sub-degree and sub-millimeter accuracy. In clinical practice, the MRI pulse tracking sequence design [172] can provide the MR-based active tracking system with high frequency (40 Hz) update.

**User Control Interface** The position and orientation of atrial phantom is registered to the Unity 3D environment before the test. The soft LA phantom was fixed on a rigid 3D-printed pedestal, on which six points were predefined for registration between EM coordinate and virtual environment. Once the transformation of reference points was established, the virtual LA in the interface could be registered to 3D-printed LA phantom. As described in Section 4.5.3.1, one 6-DoFs EM tracker (Aurora® #610029,

Northern Digital Inc.) is attached to the distal end of the catheter, to capture the position and orientation. Hence, the relative geometric configuration between atrium phantom and catheter could be measured in real-time for visualization and evaluation.

The human-robot control interface provides three virtual sub-views (Figure 4.13b), which includes two overall views from different visual angles and one endoscopic view, and all these three sub-views are available to the subjects during the subject test. The overall views can visualize the interaction between the inner cavity environment and catheter tip from the exterior position. The generation of endoscopic view (Fig. 4.11a) is introduced in Section 4.5.1.1.

The operator can control the catheter tip motion through a 3D haptic device (Novint Falcon Haptics Controller). An intuitive control can be achieved as the operator could readily perceive the spatial position using the endoscopic view while maneuvering the catheter tip inside the heart chamber. The input motion could be mapped to movement in endoscopic view, instead of Cartesian space, facilitating a more consistent hand-to-eye coordination.

#### 4.5.3.2 Subject Test

In our navigation interface, a 3D roadmap (Fig. 4.14) of “lesion” targets (in red) composed by 121 spheres reveal around the pulmonary vein ostium on the virtual LA model. The lesion targets are registered to the 3D-printed LA phantom together with its virtual model as mentioned in Section 4.5.3.1. The lesion targets are consistently aligned with the LA phantom, since the highly compliant catheter only imposed limited deformation ( $\leq 2\text{mm}$ ) on the LA phantom and even less on the “lesion” targets. This deformation caused by the catheter tip was insignificant to the resultant accuracy evaluation. When valid ablation (ablation duration and tip-to-target distance are satisfied) performs on the lesion targets, the color of target will turn yellow gradually, representing the corresponding section is successfully ablated. Experimental data, including 1) time, 2) 3D position of the catheter tip, 3) distances from the tip to all of the lesion targets, 4) status of ablation ON/OFF, and 5) ablation status of lesion target represented by values 0-50, are recorded at 20 Hz for offline analysis.

Ten subjects (age ranging from 20 to 30, 7 men and 3 women) were invited to participate in this experimental validation. As a within-subjects design, all the subjects performed

both catheter control methods, but in random order. This design can effectively reduce the error variance associated with individual differences, as each subject serves as his/her own standard of comparison [173]. The subjects have technical background but no experience in electrophysiology (EP) procedures. Before the test, cardiac EP catheterization surgery and the manipulation method of the experimental setup were introduced. Each of the subjects was required to perform RF ablation on pre-defined lesion targets within 3 minutes.

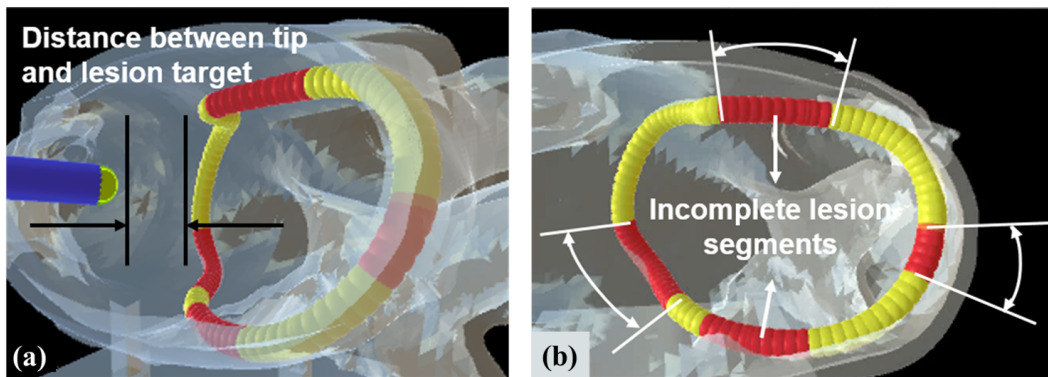


**Figure 4.14:** Two major performance indices, namely accuracy and efficiency defined based on (a) proximity distance measured from tip to lesion target around the pulmonary vein ostia and (b) total length of incomplete lesion segments (red).

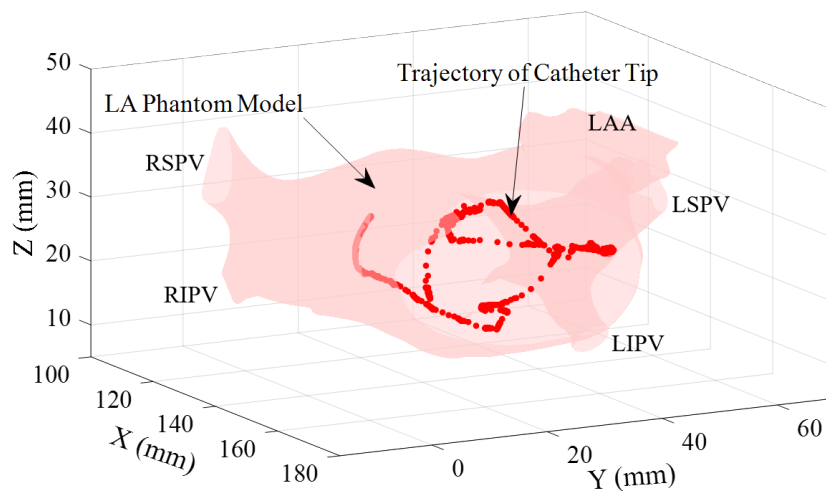


**Figure 4.15:** Trajectory of the catheter tip in the LA phantom model.

Accuracy and efficiency are of utmost importance to the clinical practice, thus which are defined for assessment in the task (Fig. 4.14). The accuracy could be assessed in terms of (1) the proximity distance measured from catheter tip to lesion target during the ablation, (2) number of times that ablation had been turned on, and (3) average ablation duration; and efficiency could be evaluated by (1) the missed proportion of lesion target segments and (2) the maximum number of continuously missed lesion targets, and (3) the total travel distance of the catheter tip. An example trajectory of catheter is shown in Fig. 4.15.

Table 4.2 shows the performance evaluation result of the subject test, where model-based and model-free control methods in robotic catheterization are compared for each index. Here, the improvement percentage is calculated by the increment of model-free method referring to the model-based method.

**Table 4.2:** Measured performance indices averaged across 10 subjects in performing the robotic catheterization of the phantom model

Model	Model-based		Model-free		Improvement
<b>Accuracy</b>	<b>Mean</b>	<b>STD</b>	<b>Mean</b>	<b>STD</b>	<b>% *p-val.</b>
Mean tip-to-target distance during ablation (mm)	6.94	1.34	5.61	1.31	19.1% *0.08
Mean times of ablation turning on (sec)	23.7	10.9	24.1	7.2	-1.88% *0.89
Ablation duration (sec)	1.49	0.36	1.76	0.48	-18.7% *0.07
<b>Efficiency</b>	<b>Mean</b>	<b>STD</b>	<b>Mean</b>	<b>STD</b>	<b>% *p-val.</b>
Mean proportion of missed targets (%)	51.9	14.7	33.3	11.9	35.8% *0.03
Maximum number of continuously missed targets	55.1	24.1	29.7	3.16	46.2% *0.01
Total travel distance (mm)	649	176	699	320	-7.65% *0.60

**Accuracy** The average distance between catheter tip to the closest lesion target during ablation of the model-free control method was 19.1% shorter than that of the model-based one, indicating the advantage of model-free control to approach static target. Model-based method had fewer times of ablation turned on and shorter ablation duration. The better accuracy of model-free control can be interpreted that the model-based method is analyzed by the inherent kinematic properties, without considering interactions between catheter and atrium model. But the EP intervention is inevitable on complicated interaction with endocardial environment. In comparison, the model-free control can adapt to the interaction by updating the inverse Jacobian, especially under the circumstance of soft contact with phantom.

**Efficiency** The model-free control method demonstrated a remarkable reduction in the missed lesion targets (35.8%), and the maximum number of continuous missed lesion target spheres (46.2%), both of which correspond to a low p-value ( $\leq 0.05$ ). For the total travel distance of the catheter tip during the task, the model-free method demonstrated

inferior improvement (-7.65%). This phenomenon indicates that the model-free method could provide faster and more sensitive response to the operator's input.

The proposed experimental validation platform, comprising an MR safe catheterization robot and a human-robot interface, could realize both model-based and model-free methods for catheter control. Subject test that emulates an ablation task is conducted to quantitatively evaluate the performance of both control methods. Quantitative evaluation of both methods are conducted via a subject test. Accuracy indices (e.g. mean of the closest distance between catheter tip and the closest target during ablation) and efficiency indices (e.g. proportion of missed lesion target) are adopted. It could be seen that model-free control method performed better than the model-based one in both aspects of accuracy (19.1% improvement in the tip-to-target ablation distance) and efficiency (35.8% reduction in the missed-target proportion and 46.2% reduction in the number of continuous missed targets).

## 4.6 Towards Clinical Validation of MRI-Guided and Robot-assisted Cardiac Electrophysiology

Apart from the robot hardware, accurate MR-based localization of the catheter, as well as high-performance image registration, are of paramount importance to realizing intra-op MRI-guided EP catheterization. In this section, MR-tracking and intra-operative image registration techniques are reviewed. We also discuss the prospective integration of these two components into a human-robot control interface, which will enable a closed-loop control of the proposed robot under MRI. [Fig. 4.16](#) illustrates this closed-loop architecture.

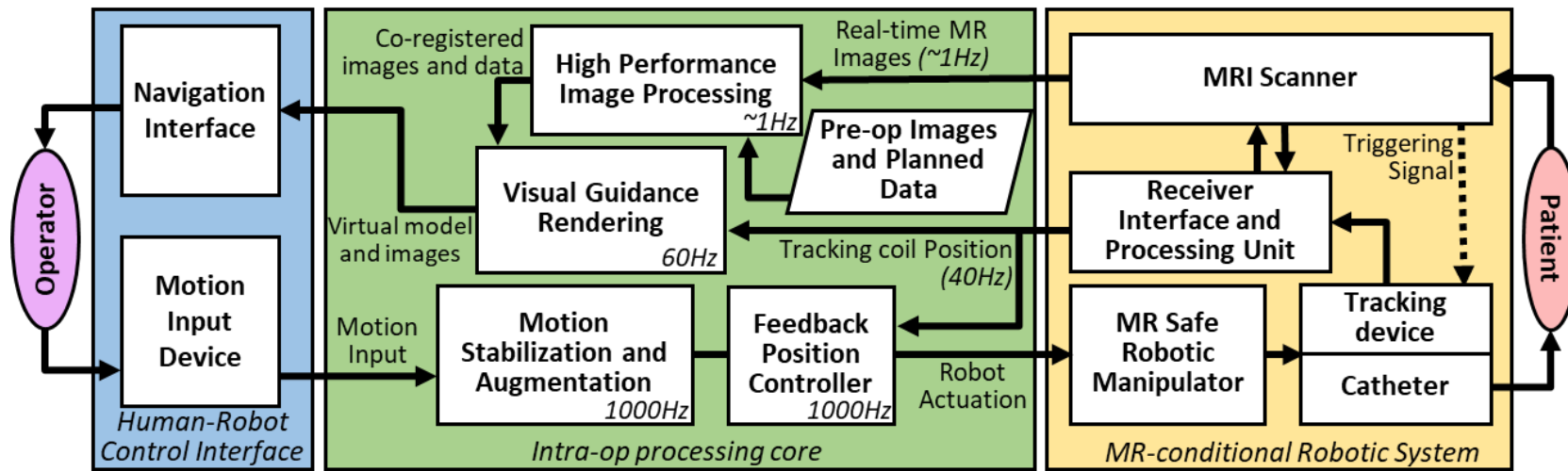


**Figure 4.16:** Schematic diagram of the MRI-guided robot-assisted catheterization. The operator can perform robotic EP catheterization in a closed-loop manner.



### 4.6.1 Real-time Tracking Techniques for MRI-guided Catheter

Tracking the catheter position is essential in many cardiac interventions. This positional feedback data will close the control loop of robotic navigation (Fig. 4.16). It also allows the operator to visualize the catheter configuration with respect to the cardiovascular roadmap constructed by the MR images. The three major categories of tracking technologies under MRI are presented in the following sections. Their pros and cons are also summarized in Table 4.3.

#### 4.6.1.1 Passive MR Fiducials/Markers

Two types of passive fiducials/marker, either encapsulating i) gadolinium-based MRI contrast agents, e.g. liquid with 4-6% gadolinic acid (Gd-DTPA), which could enhance MR

**Table 4.3:** Latest technologies for MRI-based positional tracking

	Operating principles	Advantages	Disadvantages
<b>Passive Tracking</b>	<ul style="list-style-type: none"> <li>Encapsulated -ve/+ve contrast agents causing MR signal void or T1 shortening.</li> <li>Encapsulated materials visible by non-proton multispectral</li> </ul>	<ul style="list-style-type: none"> <li>Simple and safe integration</li> <li>Capable of operating under different field strengths</li> </ul>	<ul style="list-style-type: none"> <li>Time consuming</li> <li>Tracking cannot be switched on/off</li> </ul>
<b>Active Tracking</b>	<ul style="list-style-type: none"> <li>Use image sequence to induce position-dependent MR gradient field within a volume of interest</li> <li>Detect the MR gradient field using micro coil/antenna in frequency domain</li> </ul>	<ul style="list-style-type: none"> <li>High spatial and temporal resolution of 3-D tracking information</li> <li>Easy to conduct automatic tracking and slice plane following</li> </ul>	<ul style="list-style-type: none"> <li>Potential risk of RF heating on wires connected to receiver</li> <li>Sophisticated tuning/matching the circuitry in the receiver interface required</li> </ul>
<b>Semi-active Tracking</b>	<ul style="list-style-type: none"> <li>Isolated LC circuit with photodiode/photoresistor connected in parallel is designed to resonate at MRI Larmor frequency</li> </ul>	<ul style="list-style-type: none"> <li>No electric wire connected with the scanner receiver</li> <li>Optically-controllable resonance behavior</li> </ul>	<ul style="list-style-type: none"> <li>Difficulty in assembly and miniaturization</li> <li>Sophisticated design of tracking sequence needed</li> </ul>

signal by shortening the T1-relaxation time, or **ii**) strongly paramagnetic material, e.g. dysprosium oxide, causing MR field inhomogeneity at the surrounding matter that can be visualized by delicate MR-triggering signal or sequence programmable in the MRI scan software. The corresponding 3D position of such markers is usually selected on the image domain. For automatic tracking, it requires complicated MR sequence as well as more computation time to process susceptibility artifacts in the high-resolution images for fast and accurate localization. An MR sequence, PRIDE [174], was an example proposed to acquire echo-phased projections in the three principal axes. It is capable of localizing the paramagnetic marker shortly at high frequency 20 ms (50 Hz), but within relatively large positional error of  $\leq 4.5\text{mm}$ . Tracking based on passive markers may also encounter difficulties in tracking multiple catheters that are in close proximity to each other. This can also be invalid while being out of the imaging site/slice, despite the uses of advanced image recognition techniques.

#### 4.6.1.2 Real-time Active Tracking Coil

MR-based tracking can be achieved by attaching two tiny solenoid coils (Fig. 4.3) close to the catheter tip, which are connected to a receiver electronic system via coaxial cables. This is a typical MR-active tracking setting, in which the coil can actively "pick up" the MR gradient field [175] along the three principal directions for localization. By matching/tuning the receiver's LC components for a specific MRI scanner, these coils can be highly sensitive to very local field inhomogeneity [176] without adversely affecting the image quality. To correct the inhomogeneities of the static magnetic field, both zero-phase-reference and Hadamard multiplexing methods could be employed. Such an MR sequence is able to achieve a spatial resolution up to  $(0.6 \times 0.6 \times 0.6\text{mm}^3)$  with fast sampling rate (40 Hz) [35].

Despite its promising spatial and temporal resolution, the main issue in active tracking is the heating issue due to the resonating radiofrequency (RF) waves; The standing wave also causes storage of electrical energy within the conducting structure that may cause potential safety hazards [177]. Besides, the integration of the tracking coil requires wiring and matching with the MRI scanner, and sophisticated assembling of small electronics components at the catheter tip, imposing further difficulties on further miniaturization of the tracking device.

### 4.6.1.3 Semi-active tracking

MR-*semi-active* tracking is a state-of-the-art approach, in which coils are integrated into small isolated LC circuits. These coils resonate with specific MR frequencies by means of wireless inductive coupling with the MRI system. There are no direct capacitive electrical connections with the MRI system. This avoids resonating RF waves along the coaxial cables connection, which can pose potential heating hazard in active tracking (Table 4.3). Using a properly programmed MR sequence that detunes/triggers the isolated resonant circuit, the semi-active device can be visualized in the MR images. To alter the RF resonant behaviour, an optical fibre could be connected to the circuit in order to illuminate a photodiode placed parallel to a coil, which could achieve real-time imaging (20fps) in an *in vivo* test [178]. Taking advantages from the wireless inductive coupling, semi-active devices avoid the potential development of standing waves along electrical connections found in active tracking. Nevertheless, the mechanical assembly and miniaturization of semi-active tracking devices are still challenging tasks [179].

MR-tracking also allows real-time visualization of the catheter configuration with respect to the EP roadmap constructed from the MR images. This could provide the operator with reliable navigation guidance and consistent motion reference to aim the catheter tip at the ablation lesions imaged and registered locally around the tip (Fig. 4.6). Such intra-operative visualization will involve fast image registration, which is described in the next section.

## 4.6.2 Fast Multi-phase Cardiac Image Registration

With zero EM interference accredited to the proposed MR Safe hydraulic actuators, fast MR images can be acquired in the region around the catheter tip being tracked. Thus, the post-ablation lesions (edema or scars) can be promptly visualized and selected on T2-weighted MR images. These physiological changes need to be instantly overlaid on the EP roadmap, allowing the electrophysiologist to determine whether the ablation is applied sufficiently to the lesions. However, such intra-op MR images are mostly obtained at different cardiac cycles from the pre-operative (pre-op) images that construct the EP roadmap. Non-rigid image registration is the prerequisite to continuously re-align the selected lesion on the EP roadmap (Fig. 4.17). Moreover, ECG-gated contact points collected during the EA mapping will have to be promptly co-registered to the roadmap based on the cardiac morphology. Therefore, fast and continuous co-registration between the pre- and intra-op images could

significantly smoothen the repeated workflow of RF ablation planning and catheterization. It also allows one to readily identify the locations of the next point collection regions, as well as the arrhythmia origins.

#### 4.6.2.1 Diffeomorphic Demons Approach

Feature-based image registration approaches relying on customized-feature detection or selection are investigated not to be clinically practical due to the susceptibility to artifacts in fast intra-op MR images. Such artifacts caused by turbulent blood flow or cardiac motion hamper the correct matching of landmarks between two sets of images. Much research effort has been focused on intensity-based approaches, given the advantage of its higher tolerance of MR image noise and artefact, compared to the feature-based methods. *Diffeomorphic demons* [112] is a typical intensity-based approach, however, which are

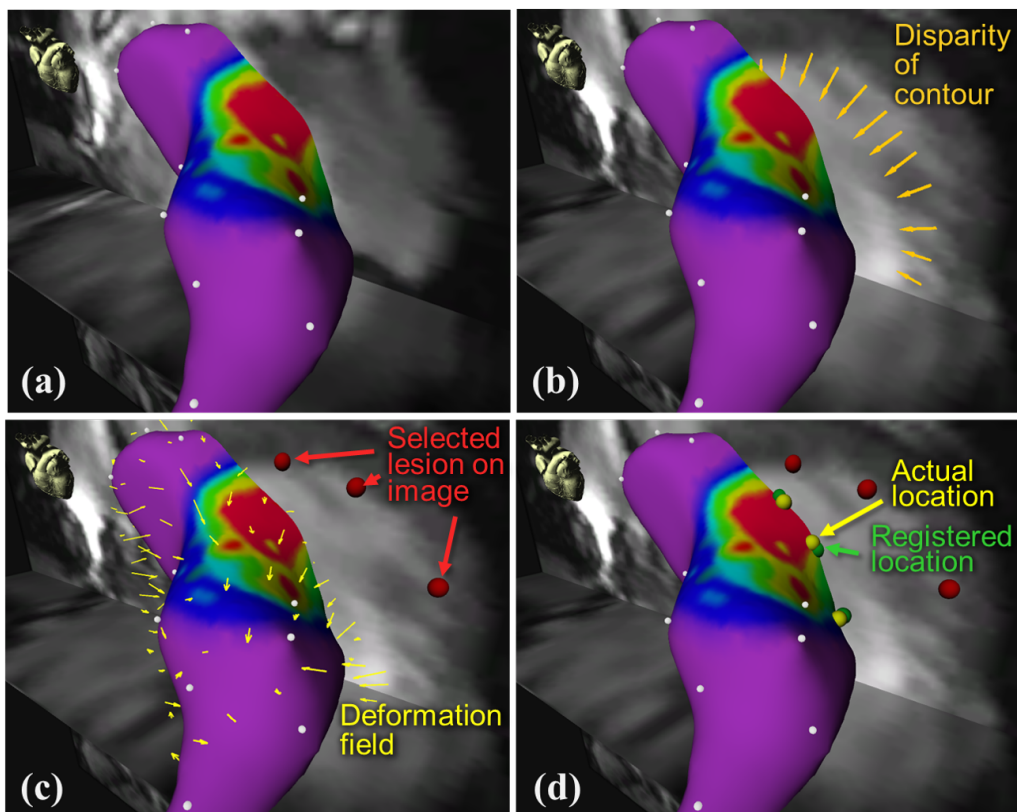


**Figure 4.17:** (a) 3-D EP roadmap of left ventricle segmented and rendered based on pre-op MR images; (b) Significant disparity (indicated by orange arrows) between the roadmap and intra-op images during the diastole; (c) Ablation landmarks selected on a slice of 2D intra-op MR images. Yellow flow arrows are shown as the deformation field estimated by the Demons-based registration method; (d) Landmarks re-aligned appropriately on the 3D roadmap based on the deformation field.

very computationally intensive because of the large amount of pixel/voxel gradient calculated to recover the change of image morphology. For example, our computer system currently takes 2 minutes and 30 seconds to process two sets of MR images with size of  $256 \times 256 \times 181$  pixels. Such prolonged computation time required to align the target lesions frequently with the roadmap will undoubtedly hinder the surgical workflow. Therefore, the conventional use of intensity-based registration is mostly applied only once after the EA mapping for improved integration between the EA map and the pre-op roadmap.

#### 4.6.2.2 Integration into Surgical Workflow

This section proposes a novel acceleration approach to resolve the computation bottleneck by using high-performance computing architectures [80, 143], such as graphical processing units (GPUs). It is based on the hypothesis that novel computing architecture featured with flexible and efficient memory access structures can enable online registration of the intra-operative images for clinical setting.

GPUs facilitate spatial parallelism by simultaneously sharing the computation load with thousands of its processing units under the "*Single Instruction, Multiple Data (SIMD)*" architecture. Vectorized data types (e.g. float4) by cascading multiple primitive data (e.g. 32-bit float) also allow full utilization of the memory bus in GPU, as well as batch processing of multiple data under a single instruction. However, as most intensity-based registration algorithm requires frequent access of nearby pixel value, such parallelized computation architecture will require a large memory throughput of the device, consequently result in a bottleneck on memory access as the computation scales up.

Reconfigurable computing technology, such as field-programmable gate arrays (FPGAs), can also be employed to accelerate image registration and related applications. FPGAs can resolve the computational bottleneck by employing temporal parallelism on top of spatial parallelism [180]. Computation can be done through a flexible computational pipeline, and the memory transfer between device memory and the processing units of FPGA can be minimized [80]. Furthermore, the bit-width of the data streams in FPGAs can be optimized based on trade-offs between computation speed and accuracy. As a result, co-registration between two sets of 3D images ( $192 \times 132 \times 300$  pixels) could be achieved within 1.1 seconds. Such rapid realignment of the intra-op image is crucial to achieving precise catheter manipulation in dynamic surgical scenarios. This fast MR

registration would offer effective visual guidance in the human-robot control interface (Fig. 4.6) that will be incorporated into our proposed robotic manipulator. Other robot motion planning tasks such as proximity query can also be accelerated by FPGAs [136].

## 4.7 Conclusion

The proposed MR Safe robotic manipulator is the first of its kind that offers sufficient DoFs to tele-manipulate a cardiac catheter under intra-op MRI guidance [181]. The robot fulfils the MR Safe standard (ASTM F2503-13), as it solely comprises of nonconductive, nonmetallic and nonmagnetic materials. Currently, there is no such commercial system that is MR compatible/conditional.

The proposed highly-efficient hydraulic transmission using rolling-diaphragm has been shown to have great potential for offering high-performance actuation under MRI without adversely affecting imaging quality. In a standard MR compatibility test under MRI environment [161], the SNR loss is found to be  $< 2\%$  even when the robot is operational (Section 4.4.1). This master-slave actuation system involves an advanced sealing method which has demonstrated its advantages in low-friction, quick-response and low-noise motion transmission. In a free weight-lifting experiment, the slave actuation unit can output torque up to 1.47Nm with a force transmission efficiency of 70% (Section 4.4.2.1). Such actuation torque can be transmitted from the control room into the MRI room via 10m long hydraulics pipelines that are channeled through the waveguide, while maintaining a small overall mechanical backlash of 0.88mm by applying appropriate hydraulic pressure at 0.05 MPa. The incompressibility of hydraulic fluid also results in stable and low-latency dynamic response ( $< 70\text{ms}$ ), even at high-frequency motion (15Hz) (Section 4.4.2.3). The proposed manipulator is capable of performing a simulated pulmonary vein isolation procedure, demonstrating its sufficient workspace and dexterity for EP catheterization.

Our ongoing work is to improve hydraulic actuation to offer a full range of catheter advancement along the vessels to the chamber. Furthermore, MR-tracking and intra-operative image registration techniques are also essential to realize MRI-guided EP catheterization. Advanced MR-tracking devices can be used to localize the catheter tip at high frequency (40Hz) and resolution ( $0.6 \times 0.6 \times 0.6\text{mm}^3$ ) in the image coordinates, thus enabling accurate alignment of catheter configuration with the roadmap. Fast image registration implemented on advanced GPU/FPGA-based architecture can rapidly

register/realign ( $\approx 1.1$ s) the lesions on the pre-op EP roadmap. The RF ablation progress can then be frequently monitored by the intra-op MR images. It avoids manual coordination of such lesions on the MR images which may not be consistent with the roadmap at different points of the cardiac cycle.

In summary, the advent of the proposed MRI-guided catheter robotic system will increase confidence to perform RF ablation completely, while improving the safety of catheter navigation. As a result, it may reduce nerve damage, esophageal fistula creation, pulmonary vein stenosis and stroke, as well as the chance of post-procedural disease recurrence (currently 30% in atrial fibrillation and 50% in ventricular tachycardia). This will contribute to justifying the use of MRI, while reducing the overall healthcare expenditure of the treatments.





## Chapter 5

# Soft Robot Design and Control for Flexible Access MRI-guided Surgery

### 5.1 Introduction

Bio-inspired robotic structures composed of soft actuation units have attracted increasing research interest. Taking advantage of its inherent compliance, soft robots can assure safe interaction with external environments, provided that precise and effective manipulation could be achieved. Many studies were successful in utilizing soft actuators [81], producing safe and compliant robots [182] that could be used in a range of fields like surgery and search and rescue [183]. STIFF-FLOP [24, 25] and Endotics [89, 90] were two pioneering examples of surgical robotic instruments made of soft materials and actuation. Furthermore, miniaturized soft robotic devices are particularly compatible to operate under MRI environments, because they mainly comprise polymers, soft and biocompatible materials, such as silicone-based elastomers. Soft robotic actuation, usually via elongate and expand of fluidic chamber with increase volume or pressure, is also inherently MR Safe and will not induce EM interference. However, design and control of soft robotics device of are well-known to be challenging due to the nonlinearity of hyper-elastic materials. Previous model-based control approaches often require simplified geometric assumptions on the soft manipulator, but which could be very inaccurate in the presence of unmodeled external interaction forces.

In this study, advanced finite element analysis (FEA) formulation was employed the

design optimization and miniaturization of soft robots. Not only can the FEA accurately predict the highly deformable behaviors, but it can also provide data for characterization of inverse kinematic relations. I also proposed a generic control framework based on nonparametric, online, as well as local training, in order to learn the inverse model directly, without prior knowledge of the robot's structural parameters. Detailed experimental evaluation were conducted on a soft robot prototype with control redundancy, performing trajectory tracking in dynamically constrained environments. Advanced element formulation of FEA was employed to initialize the control policy, hence eliminating the need for random exploration in the robot's workspace. The proposed control framework enabled a soft fluid-driven continuum robot to follow a 3D trajectory precisely, even under dynamic external disturbance. Such enhanced control accuracy and adaptability would facilitate effective endoscopic navigation in complex and changing environments. The major contributions of this work are:

- The first attempt to exploit online nonparametric local learning technique with the aim to directly approximate the inverse kinematics of a redundantly-actuated, fluid-driven endoscope prototype for soft robot control in 3-D space;
- Novel integration of FEA into the online learning method is implemented to initialize a reliable inverse model offline before deployment of the proposed controller in practical scenarios.;
- Experimental validation of the control performance and adaptability is conducted to demonstrate 3D trajectory tracking (mean error  $< 2.49^\circ$ ) of soft continuum robot even under dynamic external disturbance.

## 5.2 Clinical Motivation

Every year, head and neck cancers (HNCs) influence more than 4.6 million people in the world [184]. Being the 6<sup>th</sup> most popular cancer, also the 9<sup>th</sup> most common cause of cancer-related death, the actual case number of HNCs exhibit an ever-increasing trend [185]. Transoral surgery is known as an effective method to treat the HNCs on nasopharynx, oropharynx, larynx and hypopharynx regions, which can be accessed through the oral entry (Fig. 5.1). When compared to the other two approaches, namely radiotherapy and chemotherapy, transoral surgery offers the least toxicity and can reduce the long-term functional sequelae due to exposure of chemoradiation [186]. However, the

current practice of transoral surgery is susceptible to significant trauma due to the lack of dedicated techniques and instruments.

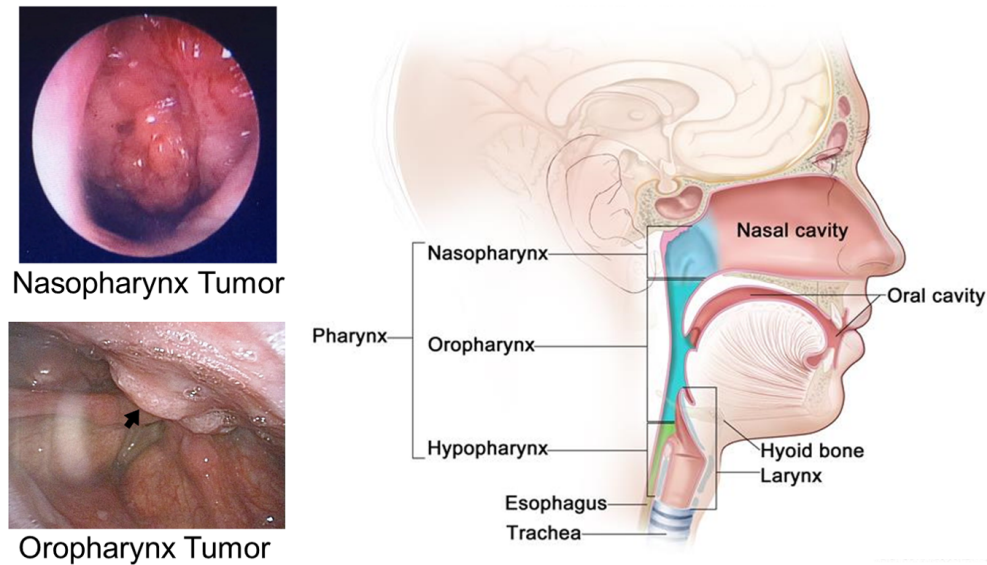


**Figure 5.1:** The head and neck anatomy denoted with the actual tumor mass from nasopharynx and oropharynx cavity. **Image Source:** [30, 31] and NIH National Cancer Institute

The advances in minimally invasive endoscope techniques have led to the introduction of transoral laser microsurgery (TLM) in the 1970s. Highly-concentrated laser beam can ablate the tumor lesions with minimized carbonization margin, hence preserving the integrity of functional anatomy [187]. Remarkable improvement in the local control rates of early laryngeal cancers was reported in many oncological studies [188–190], in which the vocal function can be preserved. In TLM, Carbon dioxide (CO<sub>2</sub>) laser beam with a wavelength of  $\approx 10,600$  nm is the most often-used ablation source. Depending on the tissue depth, it can modulate the output energy level from 0.1W to 100 W [185]. As a result, TLM outperforms the conventional electrocautery in favor of its precise penetration depth and hemostatic control [191]. The navigation mechanisms usually target the CO<sub>2</sub> laser by using a rigid optical system that comprises adjustable prisms/mirrors. However, when targeting the laser beam, it must be aligned perpendicularly to the tissue to attain the optimal clinical outcome. The rigid targeting mechanism makes it difficult at the supraglottic and oropharyngeal region, which involve frequent instrument adjustment to provide sufficient cutting effect and tumor exposure. To resolve this complication, flexible optic fibers were introduced to guide the laser beam. Such system can offer high-power, short wavelength tissue dissection, including thulium ( $\approx 2,013$  nm) and blue light ( $\approx 445$  nm) laser, as well as improved hemostasis function [191]. Clinical trials of these optical fiber-based laser dissection systems have been reported [192–194]. Yet, the long and flexible instruments still suffer inaccuracy and suboptimal manual control/manipulation,

which have led to the introduction of robot-assisted systems.

Currently, there are only a few FDA-approved robotic platforms capable of performing transoral surgery, e.g. Flex<sup>®</sup> Robotic System (Medrobotics, USA) [195] and da Vinci robot (Intuitive Surgical Inc., USA) [196]. As reported by several pilot studies [196, 197], transoral robotic surgery (TORS) integrated with flexible laser technology can improve accuracy, fine-tune cutting regions, mitigate postoperative pain and facilitate operational safety. However, the complex and confined environments of oral and nasopharyngeal (ONP) cavities makes maneuvering of the large robotic instruments a difficult task [185], particularly when resecting tumor located in deep region (5-10mm). This can be attributed to its close proximity to the delicate muscular and neurovascular anatomy which risks damaging the speech and swallowing function (Fig. 5.2). Even with the robot assistance, surgeons can only rely on their experience to estimate the laser penetration depth and avoid critical artery/nerve during the dissection. After the tumor resection, intra-op evaluation is a must to ensure complete removal of cancerous tissue through pathologic procedures, e.g. frozen section analysis (FSA) [198]. Such limitation is the primary motivation to develop new methods for real-time, frequent and in-situ tumor margin sampling.

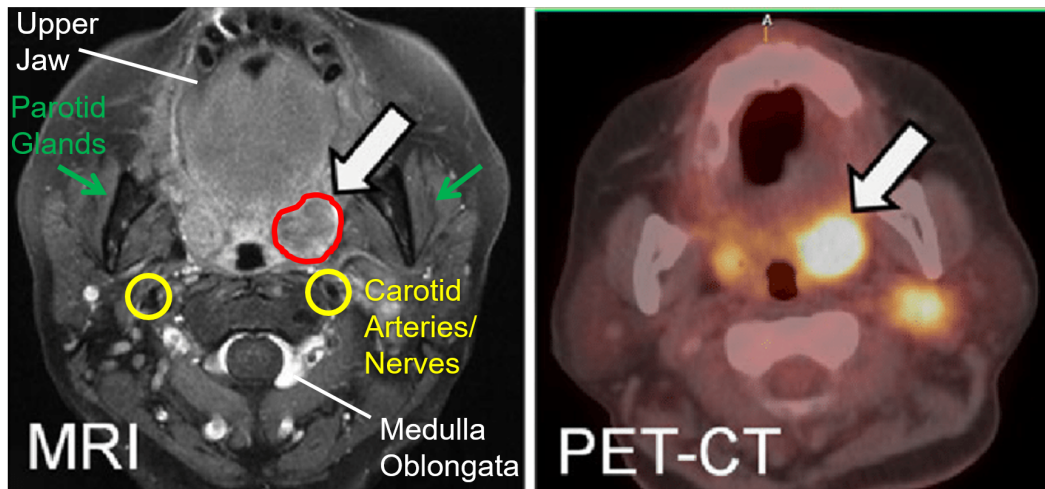


**Figure 5.2:** MR and PET-CT images of oropharyngeal cancer in axial plane. White arrow locates the primary tonsillar lesion. Yellow arrows indicate the critical neurovascular structures. Parotid glands are denoted by the green allows. **Image Source:** [32]

Magnetic resonance imaging (MRI) is advantageous in offering high contrast imaging of soft tissue in the oral and nasopharyngeal region. It gives rise to a 3D surgical roadmap to ease the pre-op planning which requires identifying early stage (T1/T2) carcinoma from the critical structures. Real-time MRI is also a novel technique to monitor the laser incision depth and ablation progress, which is achieved by observing the physiological changes of tissue resultant from complete or unsuccessful laser dissection/ablation. Furthermore, MRI

thermometry enables the inspection of small change in tissue temperature ( $<1^{\circ}\text{C}$ ). Such function MRI technique is widely employed in MRI-guided focused ultrasound procedures [199]. All in all, MRI guidance can monitor and access the 3D resection margin in an intra-op manner to ensure adequate resection margin and minimized damage to critical structures. This can potentially mitigate the demand for convention FSA, hence simplify the workflow and reduce the operation time.

To the best of our knowledge, there is still no mature MRI-guided robot-assisted platform that can manipulate and project a laser beam at lesion regions with intra-op image guidance. NeuroBlate<sup>®</sup> is a example of commercialize MRI-guided robotic system for neurosurgical laser ablation [200]. Although it can generate high-intensity thermal therapy with a rigid laser probe, it becomes effective only when positioned in contact with the target lesion. The system also involves complicated shielding to conceal the EM interference generated from the piezoelectric actuators. As a result, these constraints motivated the research and development for fluid-powered actuators which are intrinsically MR Safe [201]. A clinical study on an MRI-compatible pneumatic robot has been reported for transforaminal needle-based laser ablation using active cannula [59]. The robot is fixated to scanner gantry, right above the patient's torso. To reach the target area, the pre-curved tubes/needle are channeled with each other to alter the overall curvature and hence tip position. However, such pre-curved tube mechanism could only achieve limited dexterity, especially when manipulating inside the confine anatomical cavity. Soft robotic actuator driven by pressurized fluid can potentially resolve this constraint via deforming its morphology for navigation. This enabling technique has been successfully demonstrated in several soft robotic MIS systems, such as Endotics for colonoscopy [184, 202], and STIFF-FLOP soft robot for keyhole surgery [24, 25].

To achieve intra-op MRI-guided TLM, flexible manipulation and MRI compatibility are two necessary characteristics for the feasibility and effectiveness of the robotic system. However, none of those systems mentioned above platforms fulfill this requirement. Compact soft robotic actuator incorporated with model-free control algorithms may advocate new opportunities to accomplish intra-op MRI-guided TLM.

### 5.3 Soft Robotic Manipulator

This section describes the overall design and modelling of the proposed generic, fluidic-driven soft continuum robot for endoscopic applications (Fig. 5.3a). The soft robot

body is made of RTV (Room Temperature Vulcanization) silicone rubber. Robot actuation is achieved by elastic chambers, which are individually extendable/inflatable by pressurized fluid. To minimize the radial expansion without hindering the axial elongation, an appropriate constraint mechanism is the pre-requisite to generating effective bending under reasonable pressure/volume of fluid input [203]. This limitation in size and fluid pressure will be of importance in particular for the safe use of image-guided interventions inside patient's body.

### 5.3.1 Design of Hyper-elastic Actuator

As depicted in Fig. 5.3a, inextensible fibers (depicted in red) are employed to confine each inflatable chamber. With these individually wrapped fibers, the anisotropic expansion of inflatable chamber is enforced into radial bending direction. To enable effective endoscopic navigation, the three air chambers can be individually actuated by air or other fluid, facilitating a large panoramic workspace with a bending angle  $>150^\circ$  (Fig. 5.4). The

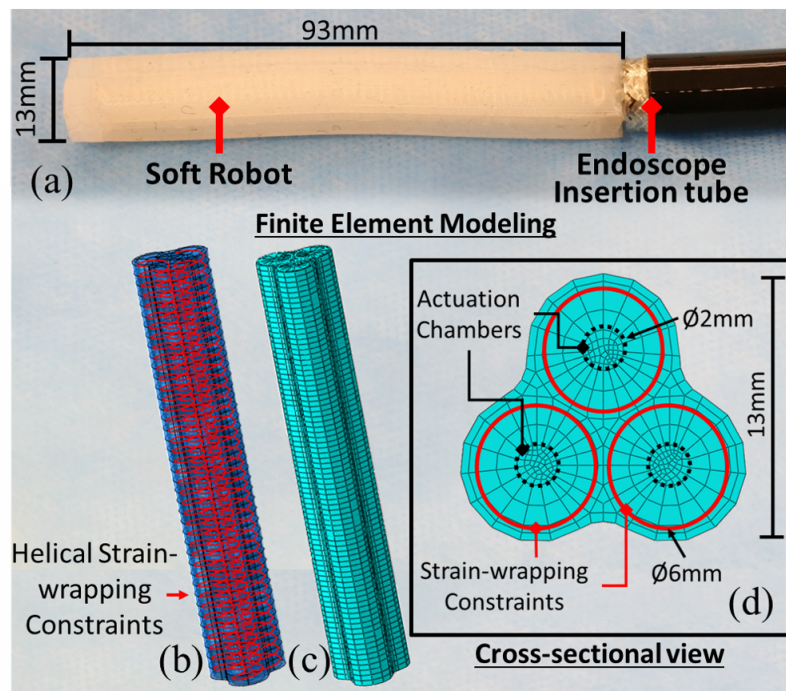


**Figure 5.3:** (a) Soft robotic endoscope prototype made of silicone rubber. The robot dimension is compatible with the insertion tube of conventional endoscope; (b) CAD/CAM model of the soft manipulator showing the simulated helical strain-wrapping constraints around its individual actuation chamber using linear truss, where the anisotropic expansion can be achieved; (c) Finite element model tessellated with 12,000 linear hexahedron elements. A total of 2,214 truss elements are defined to emulate the effect of strain-wrapping constraint; (d) Cross-sectional area tessellated by hexahedron meshing.

slender robot configuration with 13-mm outer diameter and 93-mm length are also compatible with conventional endoscopes, which is of importance to dexterous manipulation inside a confined trans-luminal workspace. The fabrication procedures are detailed in [Appendix B.2](#)

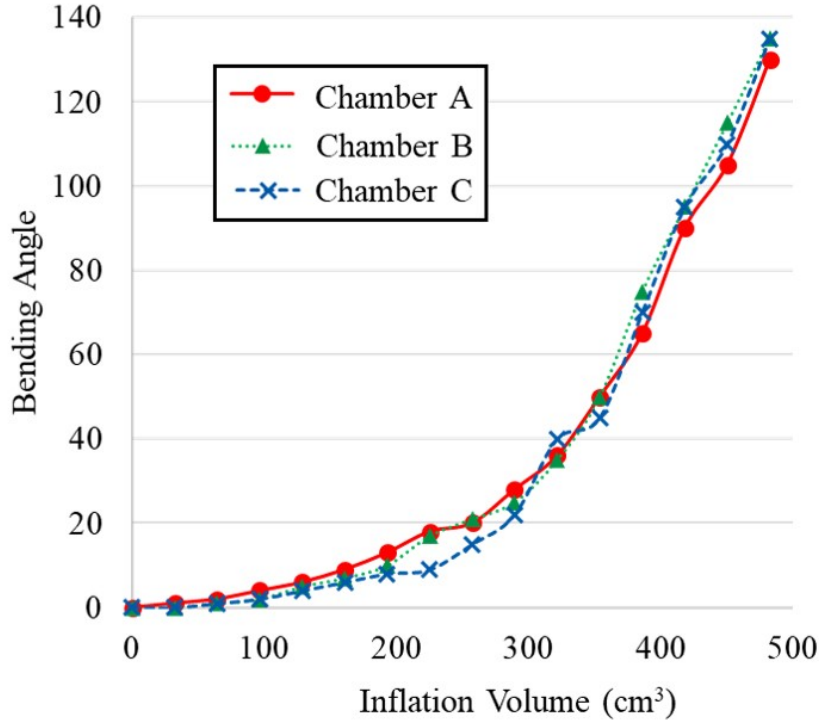


**Figure 5.4:** Bending angle of the soft actuator with individual fiber constraints under various inflation volume.

### 5.3.2 Kinematic Modeling with Finite Element Analysis

The FEA model of the robot is constructed using ABAQUS [204] to predict the robot kinematics and workspace. The RTV silicone rubber is considered as incompressible hyper-elastic material formulated by Odgen material model [205]. The strain energy density can be expressed in terms of the principal stretches where  $\lambda_j, j = 1, 2, 3$  as follows:

$$W(\lambda_1, \lambda_2, \lambda_3) = \sum_{p=1}^N \frac{\mu_p}{\alpha_p} \left( \lambda_1^{\alpha_p} + \lambda_2^{\alpha_p} + \lambda_3^{\alpha_p} - 3 \right). \quad (5.1)$$

$N, \alpha_p, \mu_p$  are material constants.

There are several considerations during the mesh tessellating process for FEA of the soft robotic manipulator. Silicone rubber exhibits negligible volume change under

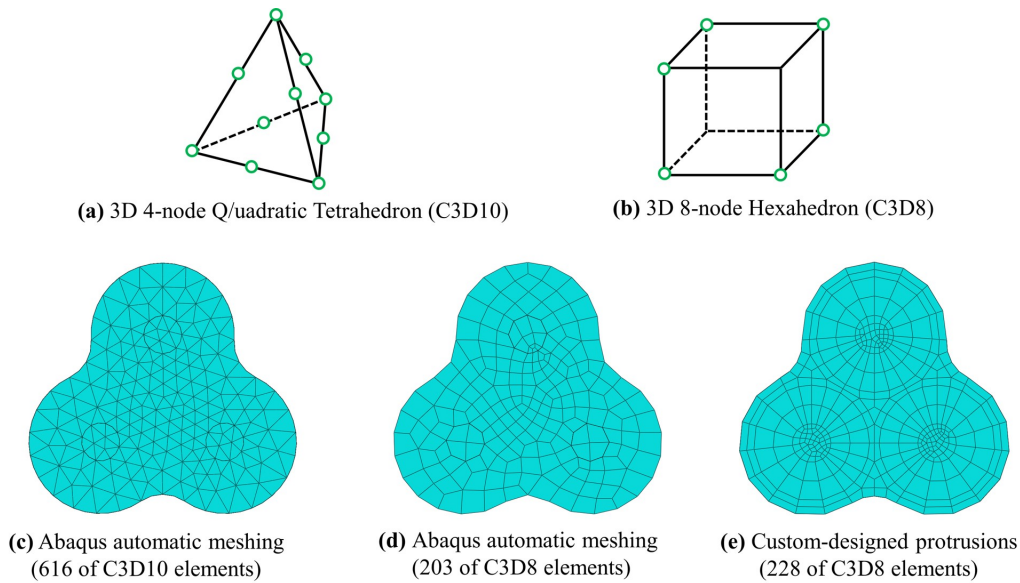


**Figure 5.5:** (a) Three dimensional quadratic tetrahedral elements with 10 nodes (C3D10); (b) Hexahedral elements with 8 nodes (C3D8); (c) Cross-section of the individually constrained soft robot FEA model tessellated by C3D10 elements. Automatic mesh generation function of Abaqus was employed; (d) Same soft robot FEA model tessellated by C3D8 elements using the Abaqus automatic mesh generation. Less elements (203) are required for hexahedral elements to fully cover the same cross-section as compared to tetrahedral elements (616). However, the automatic meshing quality is not satisfactory, the nodes distribution is highly irregular; (e) FEA model obtained by custom-designed protrusions. The overall meshing quality is restored while similar number of elements are employed.

hydrostatic compression and has a Poisson's ratio close to 0.5. Due to the incompressibility of silicone rubber and the large deformation nature of the simulation, the element formulation and the mesh quality pose a compelling effect on both the accuracy and convergence of the simulation. In incompressible material analyses, compressibility needs to be adequately enforced. However, excessive enforcement leads to the well-known dilatation locking under which the element assembly behaves as if it is locked. [206, 207] Mesh quality is also determinant to the accuracy, as distorted and slender elements are detrimental to the accuracy and may cause numerical problems. Therefore, hexahedral element (C3D8RH, Fig. 5.3c) based on u-p hybrid formulation with hourglass control [204] is chosen over the commonly used quadratic tetrahedral elements (Fig. 5.3d) in the FEA of our soft robotic manipulators. The C3D8RH element possesses eight displacement nodes and one interior pressure node. The combination of these displacement and pressure nodes are often close to optimal [207]. Moreover, its stiffness matrix is evaluated by reduced integration with hourglass control. [206] Such integration scheme improves, not only the element efficiency, but also the element accuracy under bending load. The element is widely used in incompressible material analyses. However, compared to tetrahedrons, automatic mesh generation of hexahedrons is relatively ineffective, resulting



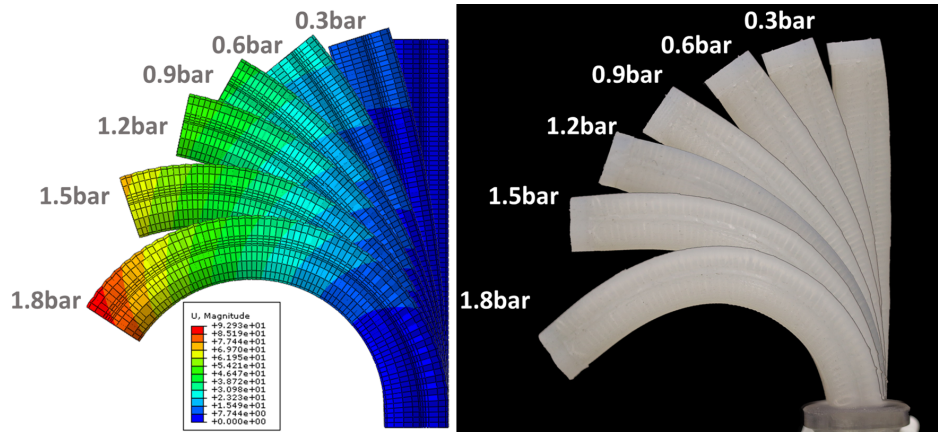


**Figure 5.6:** FEA models (Left) simulated with 7 levels of inflation pressure in a single chamber. Similar deformation characteristics are exhibited in actual configurations of the soft manipulator (Right) under the same corresponding pressure levels.

in poor tessellation quality (Fig. 5.5). To this end, the presented meshing has to be obtained by custom-designed protrusions, and all elements are right prisms initially. By restoring the mesh quality, the assemblage contains far fewer elements and is much more robust in convergence. It is because hexahedral elements can fill up the same volume with smaller number of elements, hence reducing the overall computational requirements.

FEA simulation was conducted to acquire the kinematic model of the individually constrained design at various inflation pressure. The presented manipulator model was tessellated with 12k linear hexahedral elements (C3D8RH, Fig. 5.3c). There were also 2,214 linear truss elements (T3D2) being placed along each actuation chamber in a layer-by-layer arrangement (Fig. 5.3b). Truss elements were used to model the helical strain-wrapping constraints that ensure the anisotropic expansion of the chambers upon a pressure actuation. Actuation and gravity loads were applied to the presented FEA model. The gradual change of the stress input, which is distributed across the surface mesh along the inner chamber surface, guarantees reliable convergence, giving rise to an equilibrium solution throughout all the time steps during the FEA. Quasi-static motion with negligible hysteresis can be achieved when the real robot prototype is manipulated while delicately regulating the inflation pressure into the chamber at high-resolution steps (0.04ml per incremental step). It is worth noting that deformation/bending of both the FEA-modelled manipulator and the actual one are very similar corresponding to the same levels of inflation pressure simulated, as shown in Fig. 5.6. Over 1,000 simulated motion samples were obtained using the FEA, covering the entire robot workspace (Fig. 5.7). All the computation was performed on a desktop PC equipped with Intel® Core™ i7-4790 CPU (4 GHz) and 16 GB of RAM. These simulated data are adopted to pre-train the online learning controller as described in the following sections.

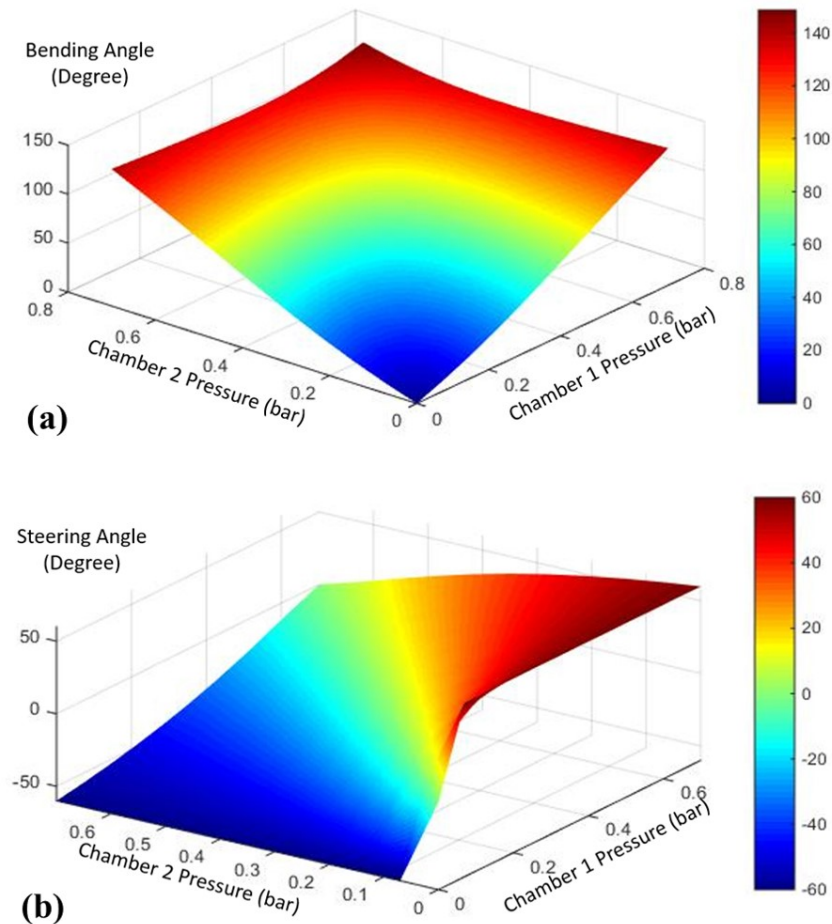


**Figure 5.7:** FEA results showing (a) correlation of the bending angle and (b) steering angle of the soft robot with pneumatic pressure (0-0.7 bar) applied on any two of the three actuation chambers.

## 5.4 FEA-based Kinematics Control for Image Space Navigation

This section demonstrates one of the proposed methods for soft robotic control, namely the image-based kinematics control. This approach enables targeting of the tele-operated soft manipulator to follow a pre-defined trajectory on the intracavity surface under human supervision. Such a task is admissible to various robotic applications. For examples, surgical procedures that require precise targeting of high-power laser to perform tissue ablation or cutting; Full inspection of an intracavity space using endoscopic camera view through a desired pathway. The control mapping, usually represented by a Jacobian matrix, is established directly based on the image-based coordinate of the endoscopic camera attached to the tip of soft robot.

### 5.4.1 Characterization of Robot Kinematics

Finite element analysis was employed to characterize the robot configuration when chambers are actuated by pressurized fluid. A set of inflation pressure combination  $U = \{\mathbf{u}_1, \mathbf{u}_2, \dots, \mathbf{u}_M\}$ ,  $\mathbf{u}_i \in \mathbb{R}^N$  is constructed by sampling from the feasible actuation space, where  $N$  is the number of inflatable chambers and  $M$  is the total number of simulations performed. This sampling interval could be a flexible function depending on the kinematic complexity and significance of the neighbor region. These sets of pressure input are then applied as distributed load on the robot FEA model to simulate the corresponding deformation. For our soft robotic manipulator (Fig. 5.3a), a total number of over 1,000 simulations are performed to find out the deformation characteristics as shown in Fig. 5.8. We define the discrete mapping between actuation input and resultant end-effector position as a set of discrete mapping pairs:  $F := \{({}^w\mathbf{x}_1, \mathbf{u}_1), ({}^w\mathbf{x}_2, \mathbf{u}_2), \dots, ({}^w\mathbf{x}_M, \mathbf{u}_M)\}$ , where  ${}^w\mathbf{x}_i = [\mathbf{p}_i, \mathbf{n}_i]^T \in \mathbb{R}^6$  is the 6D position and orientation of manipulator end-effector after inflation and the super-script refers to world coordinate.

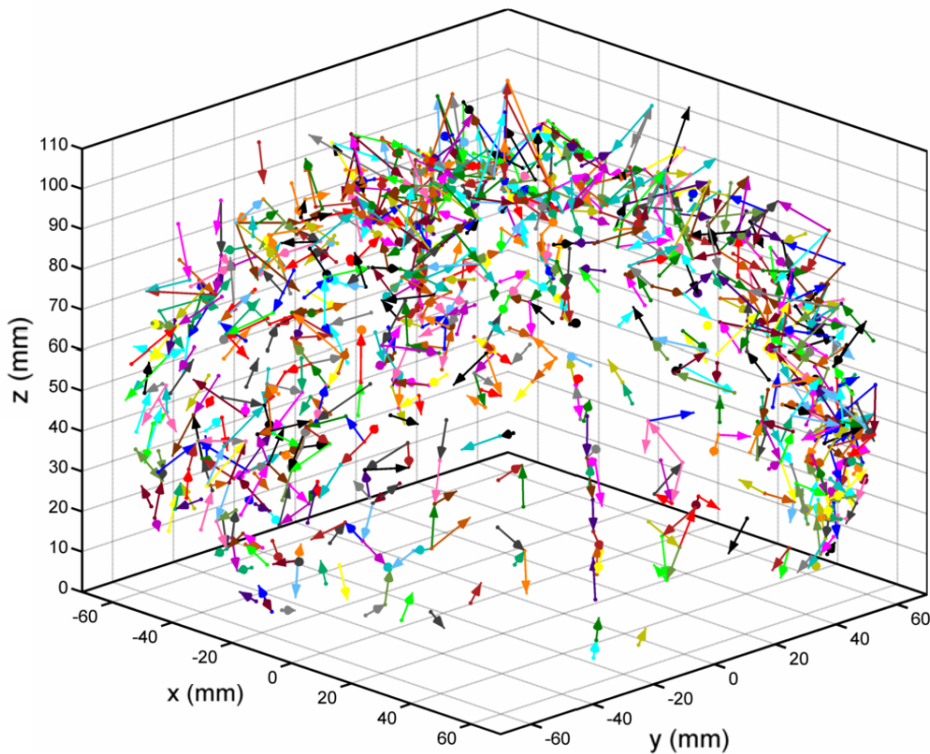


**Figure 5.8:** FEA-simulated kinematics data covering the entire workspace of the soft robot. The arrows illustrate the predicted movement of the robot tip when an arbitrary pressure change  $\Delta\mathbf{u}_k$  is applied. These data enable pre-training of a reasonable initial control policy before the online learning begins, without the need for undesired random movement (babbling).

To navigate the targeting point  ${}^w\mathbf{s}_i \in \mathbb{R}^3$  of end-effector smoothly on the intracavity task space  $S$ , all of the deformation mapping are transformed into the task space  $S$  (Fig. 5.9). This is done by finding the intersection between the principle axis of manipulator end-effector and the intracavity surface  $S$ .

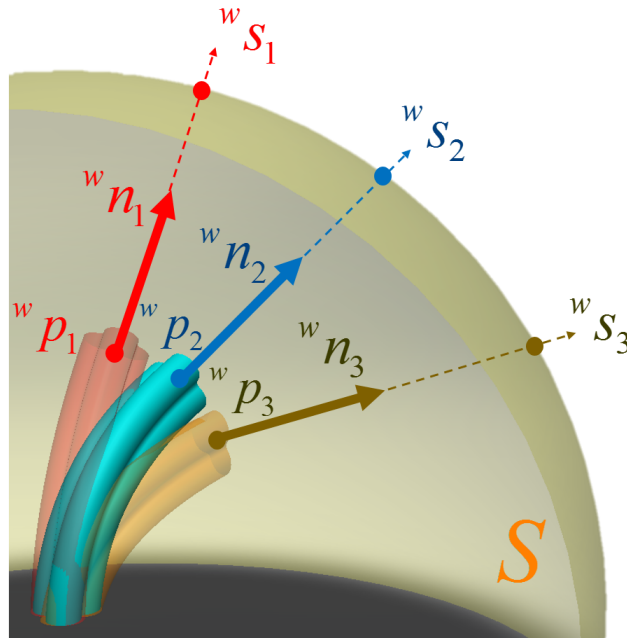


**Figure 5.9:** Soft robot configurations under various inflation pressure simulated by FEA. The corresponding targeting point  ${}^w\mathbf{s}_i$  on intracavity surface  $S$  (yellow) is the extension of the manipulator end-effector at  ${}^w\mathbf{p}_i$  along the normal  ${}^w\mathbf{n}_i$ .

#### 5.4.2 Local Linearization of Kinematics Model

To provide intuitive human-robot interaction during navigation, we have established a reliable visual guidance that accommodate visual-motor re-alignment. It is achieved by attaching a "virtual camera coordinate"  $L$  at the end-effector coordinate with its principle axis aligned with its  $Z$ -axis (Fig. 5.10). A virtual camera view is then rendered to visualize the pre-defined trajectory and intracavity surface in the image coordinate. This visual guidance realign the visual-motor mapping of Jacobian matrix and hence enhance the hand-eye coordinate of operators. As they are allowed to issue desired incremental end-effector motion in the planar image coordinate, which simplifies the control complexity by reducing the required control input into a two dimensional vector  $\Delta\mathbf{y} \in \mathbb{R}^2$  in image plane.

The kinematics model of the soft manipulator with respect to the camera coordinate is identified by best fitting a linear function to the neighbour discrete kinematics mapping pairs

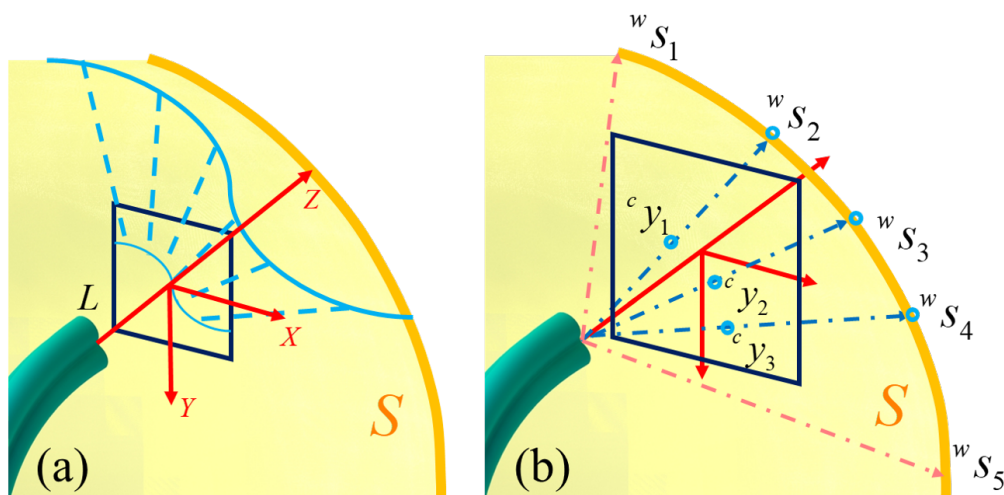


**Figure 5.10:** (a) Illustration of the "virtual camera view" provided to the operators during tele-operative navigation. The Jacobian matrix of motion mapping is estimated w.r.t. this image coordinate, hence aligned with the visual guidance. (b) Neighbor targeting points ( ${}^w s_2, {}^w s_3, {}^w s_4$ ) projected from intracavity surface  $S$  (yellow) to the camera coordinate  $L$  (red) as  ${}^c y_i$ . These points are used for local kinematics linearization. Others targeting points ( ${}^w s_1, {}^w s_5$ ) are neglect as they are out of the kinematics FOV.

$F$  pre-computed by FEA simulation. Following the concept of virtual camera coordinate, a mapping pair  $F_i$  is considered as viable neighbourhood and selected for linear fitting only if it lies within a kinematics field of view (FOV) of the camera coordinate  $L$  (Fig. 5.10). This FOV is not to be confused with the visualization rendering FOV of the virtual camera visual guidance, where the kinematics FOV is chosen to accommodate a locally viable kinematics model.

As illustrated in Fig. 5.10, assuming that a mapping sample point  $F_j({}^w \mathbf{x}_j, \mathbf{u}_j) \in F$  lay within the kinematics FOV of the current camera coordinate  $L$ ,  ${}^w \mathbf{x}_j$  is projected on the image plane of  $L$  as  ${}^c \mathbf{y}_j = [d_x, d_y]^T \in \mathbb{R}^2$ . A set of local kinematics mapping  $H = \{({}^c \mathbf{y}_j, \Delta \mathbf{u}_j)\}, j = 1, \dots, h, h > n$  can hence be obtained by projecting all neighbour  ${}^w s_j$  on the image plane and differencing the control pressure  ${}^c \mathbf{u}_j$  with current pressure, where  $\Delta \mathbf{u}_j = \mathbf{u}_j - \mathbf{u}_{current}$ . One can imagine this kinematics mapping as the end-effector displacement  ${}^c \Delta \mathbf{y}_j$  in image coordinate  $L$  corresponding to the change of actuation pressure  $\Delta \mathbf{u}_j$ . The linear kinematics model can be formulated as a Jacobian matrix that linearly map the actuation input to targeting point displacement  ${}^c \Delta \mathbf{y}$  w.r.t. the origin of image plane:

$${}^c \Delta \mathbf{y} = J \Delta \mathbf{u} \quad (5.2)$$

Each row of the Jacobian matrix is found by least square fitting method as formulated

below at every control iteration.

$$\min_{J_1} \frac{1}{2} \left\| \begin{bmatrix} \Delta \mathbf{u}_0^T \\ \Delta \mathbf{u}_1^T \\ \vdots \\ \mathbf{u}_h^T \end{bmatrix} J_1^T - \begin{bmatrix} \Delta \mathbf{d}_{x1} \\ \Delta \mathbf{d}_{x2} \\ \vdots \\ \Delta \mathbf{d}_{xh} \end{bmatrix} \right\|_2^2 \quad (5.3)$$

and

$$\min_{J_2} \frac{1}{2} \left\| \begin{bmatrix} \Delta \mathbf{u}_0^T \\ \Delta \mathbf{u}_1^T \\ \vdots \\ \Delta \mathbf{u}_h^T \end{bmatrix} J_2^T - \begin{bmatrix} \Delta \mathbf{d}_{y1} \\ \Delta \mathbf{d}_{y2} \\ \vdots \\ \Delta \mathbf{d}_{yh} \end{bmatrix} \right\|_2^2 \quad (5.4)$$

where  $J = \begin{bmatrix} J_1 \\ J_2 \end{bmatrix}$ ,  $J_i \in \mathbb{R}^{1 \times n}$  and  $\|\cdot\|_2$  is the L-2 norm operator for vector.

### 5.4.3 Optimization-based Inverse Kinematics Solver

With the estimated Jacobian matrix, it is possible to resolve the inverse kinematics for the required actuation  $\Delta \mathbf{u}$  to attain the desired image plane displacement  ${}^c\Delta \mathbf{y}$  as specified by the operator. However, such system of linear equations might not have a close form solution due to the fact that Jacobian matrix does not have full rank in general. For the case of our soft manipulator, three chambers can be actuated to achieve two dimensional desired motion in image coordinate, which give infinitely many solutions. This under-defined equation system also yield additional flexibility to select preferable robot behavior, such as minimizing the actuation effort or total inflation pressure to enhance robot stability.

This inverse kinematics problem is formulated as a constrained optimization problem

to search for the most appropriate actuation. The cost function is defined as the sum of actuation pressure change in order to minimize the resultant pressure of each chamber to avoid fatigue of elastomer due to high inflation pressure and expansion:

$$\min_{\mathbf{u}} \sum_m \Delta \mathbf{u}_i \quad (5.5)$$

subject to:

$$J\Delta \mathbf{u} = {}^c \Delta \mathbf{y}_{desired} \quad (5.6)$$

$$\mathbf{u}_{current} + \Delta \mathbf{u} \geq 0 \quad (5.7)$$

$$\mathbf{u}_{current} + \Delta \mathbf{u} \leq \mathbf{u}_{max} \quad (5.8)$$

The linear kinematics model using Jacobian matrix is defined as a part of the constraint in this optimization problem. Other constraints include limiting the inflation pressure above zero, because negative pressure is not allowed in our volumetric control. The pressure change is also constrained to prevent individual chamber from over inflation. Similar constraints may also apply to other actuation mechanism, such as tendon-driven actuators. This constrained convex optimization is resolved efficiently using interior point method in each control iteration. The optimal solution will be used to update the actuation input of soft robot.

$$\mathbf{u}[k+1] = \mathbf{u}[k] + \Delta \mathbf{u} \quad (5.9)$$

#### 5.4.4 Experiments Results

A robot identical to the design shown in Fig. 5.3 was made using Ecoflex 0050 (Smooth-on inc.) to verify the control algorithm. The soft manipulation tentacle was actuated by three separable power-screw fluidic cylinders with volumetric control. Block diagram of the overall control system, including human-machine interface, processing core and soft robotic manipulation system, is illustrated in Fig. 5.11. A volumetric control system was implemented for the setup. During the experiment, the particular combination of pressures of three separate chambers were actuated and the manipulator was driven to the designated position. The soft robot manipulator was controlled via a FEA-based control system to perform trajectory following task.

#### 5.4.4.1 Experimental Setup

To fabricate the soft manipulator, three individual actuation chambers, with 4mm internal diameter and 8mm outer diameter, were molded separately. Kevlar strings were wrapped in single helical structure and used as strain-wrapping constraints. Three wrapped chambers were glued into a single soft manipulator by a secondary molding layer of Ecoflex 0050. The soft manipulator was actuated via pneumatic volumetric control system.

Before operation, data were collected from real experiment to train the system. The data contain the mapping between the chambers' pressure and the position and orientation of the end-effector, which were recorded by an electro-magnetic (EM) tracking coil mounted on the top of soft robot manipulator. After the system training, the current position of the soft manipulator end-effector was recorded and used for the Jacobian Estimation and to provide a visual feedback to the operator. By inputting a target position, difference between the desired and current position can be calculated and then the change in pressure for the actuation chambers can be estimated by an optimization-based inverse kinematics solver to actuate the end-effector.

The soft robotic manipulator was placed inside a transparent spherical shell with 30cm diameter so as to stimulate a 3D workspace. A pre-defined trajectory was registered using with an EM tracking probe, and stored as a tracking target for the manipulator as shown in [Fig. 5.12](#). Throughout the experiment, the trajectory of figure-eight shape is separated into a series of points, continuously updated as target positions of the manipulator. The end-effector is then led by the trajectory for a certain amount of loops. By comparing the target trajectory with the end effector position and orientation measured by EM Tracking system, the accuracy and stability of the control scheme can be evaluated.



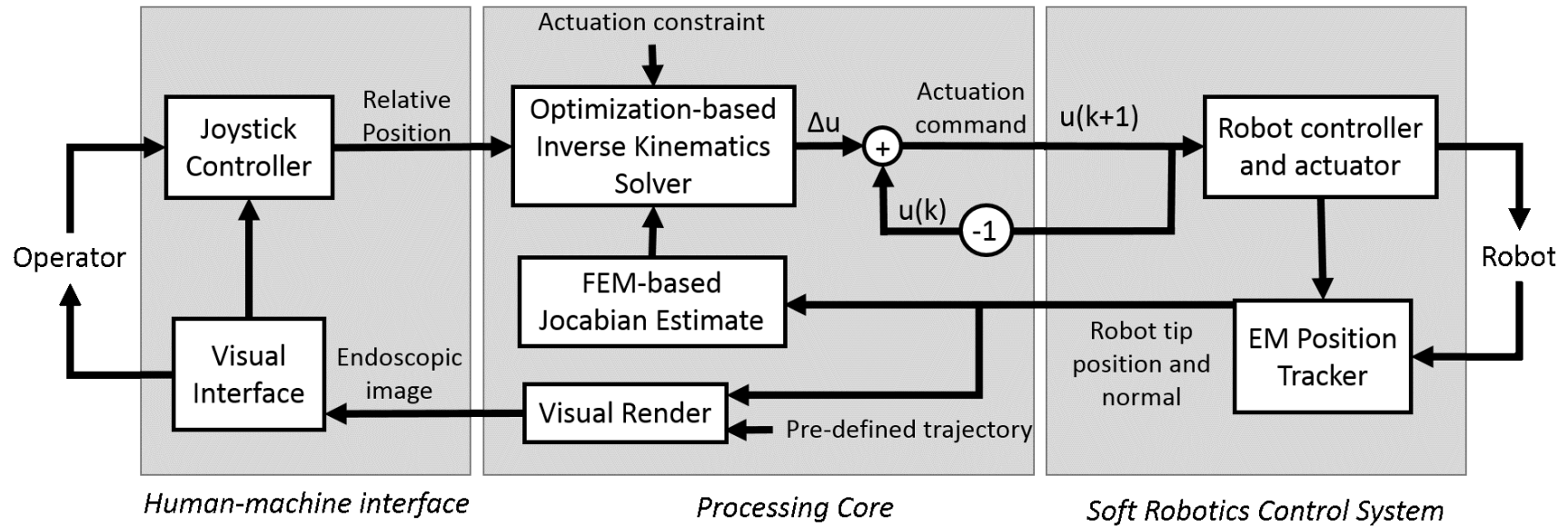


**Figure 5.11:** System architecture of the experimental setup illustrating the interconnection of the primary components: the human-machine interface, the process core that implement our proposed soft robot control framework and the robot control system.

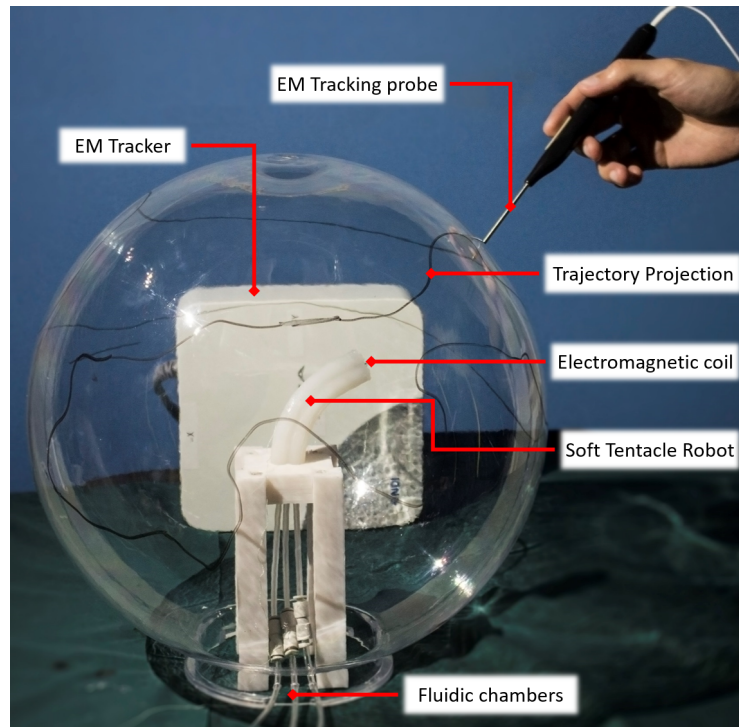


**Figure 5.12:** The desired trajectory is pre-registered on the intracavity surface (transparent sphere shell) by using EM position tracking system. The soft manipulator is controlled by operator's joystick input to trace the trajectory in virtual camera perspective. The position of the end-effector is also monitored by the same EM system throughout the experiment to validate the trajectory tracking accuracy of the proposed control framework.

#### 5.4.4.2 Performance Evaluation

Results of FEA simulation showing the bending angles and steering angles upon inflation is presented in Fig. 5.7. The comparison of simulation results and the real model is also presented in Fig. 5.6. As mentioned in the Section 5.4.1, the actuation effect of each individual chamber is complementary to the combined effect of other two. As the model is rotationally symmetric, sample points for kinematic estimation in the whole paranoiac workspace can be collected by FE simulation of inflating two actuation chambers only.

The reference and resultant trajectory are presented in Fig. 5.13. We define the result trajectory as the intersection point between the virtual camera principle axis and the spherical intracavity workspace. Tracking error is defined as the distance between the pointing position and the designated position on the reference trajectory. As shown in Fig. 5.14, the tracking error has a maximum of  $\pm 10\text{mm}$ , and the standard deviation of the error is below 6mm. The small error indicates that the FEA based control framework can be used to reliably estimate the Jacobian, based on the optimization-based inverse

kinematics estimation.

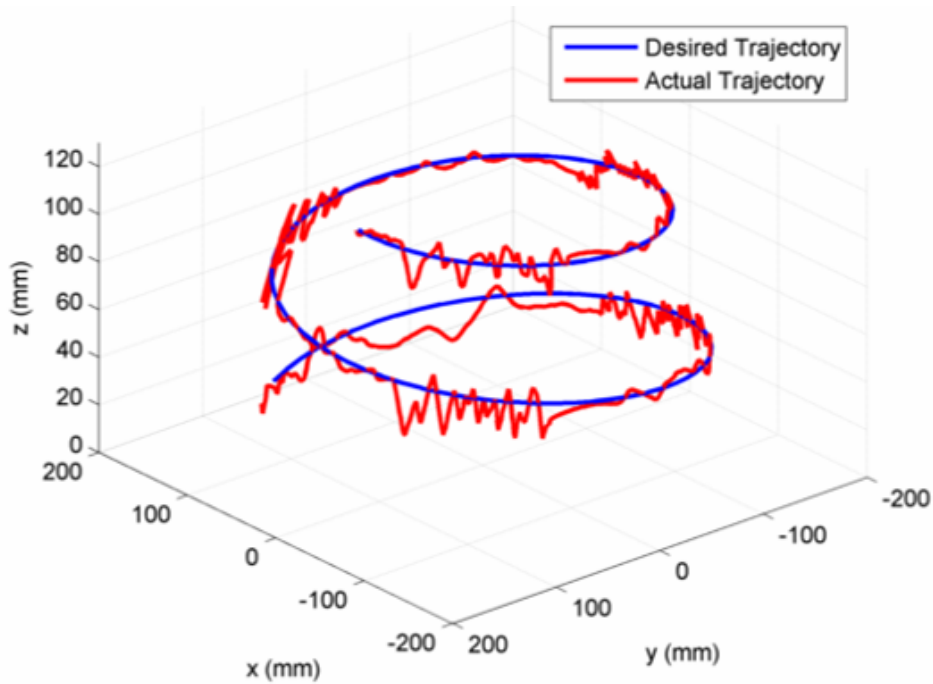


**Figure 5.13:** Results from the trajectory tracking experiment. Blue line represents the pre-defined target trajectory. Red line represents the resultant trajectory of the targeting point of manipulator end-effector projected on the spherical intercavity surface.

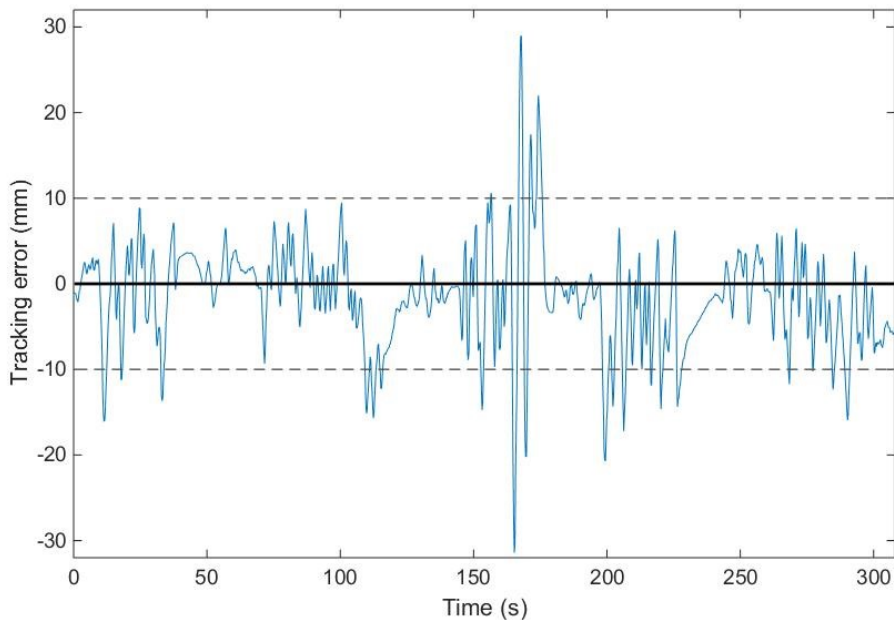


**Figure 5.14:** Absolute error of the tracking result in millimeters.

In this work, a virtual camera is adopted for the ease of user's control. By adopting the virtual camera guidance, which also act as an motion input in virtual image coordinate, the system can help users to perceive 3D geometry in an intuitive manner. Instead of requiring

the user to map motion input to movement, the virtual camera can help users to give control commands based on the 2D image plane. The concept of reduced dimensionality using the image coordinate can also be applied on soft robotics with more complex structures and/or with multiple segments. Theoretically, the FEA-based control can be used to control all kinds of soft robotics when sufficient data points is collected.

The current FEA-based control framework is largely limited by its computational requirement. Several techniques were employed in an attempt to reduce the computation. The current control framework attempted to make use of pre-computed FEA results to obtain the kinematics of the robot. Quasi-static simulations and reduced integration is adopted to further mitigate the computational bottleneck. However, with the current control framework, additional terms have to be included into the optimization model in order to deal with the robot's dynamics. For example, external contact and disturbance. Current control model have also neglected the effect of hysteresis of soft-bodied manipulator. Explicit FEA could be a solution for the dynamics problem as it can effectively simulate dynamics problem, but performing explicit FEA for the control framework will require additional computation power.

This work has opened a new perspective to make use of FEA for controlling a soft robot with hyper-elastic properties. The time-to-time estimation of robot Jacobian could be altered by the pre-computed results of FEA. Experimental validation has been realized with our fabricated soft continuum robot, showing the promising path following via the proposed human-control interface.

## 5.5 Nonparametric Online Learning for Soft Robot Control

Gradual, smooth regulation of the fluidic flow rate allows steady bending of the presented soft manipulator. It also allows rapid reaching of fluid pressure equilibrium, minimizing the residual motion generated during such fluidic actuation. During endoscopic navigation within small and confined spaces (e.g. duodenum), such quasi-static motion characteristic [168] can facilitate effective, precise targeting of the endoscopic camera or interventional tools (e.g., biopsy forceps or brush cytology) at the surgical regions of interest, thereby avoiding inadvertent damage to delicate tissue and potential discomfort to the patient.

### 5.5.1 Characterization of Robot Motion Transition

To mathematically describe the motion transition of the soft robot, let  $\mathbf{u}_k \in U$  be the fluid pressure (at equilibrium) in the actuation chambers at time step  $k$  where  $U$  denotes the control space. Let  $\boldsymbol{\theta}_k$  be the state of the robot when the chambers are filled with the pressure of  $\mathbf{u}_k$  at equilibrium. This state corresponds to the distal tip position  $\mathbf{p} \in \mathfrak{R}^3$  and orientation normal  $\mathbf{n} \in \mathfrak{R}^3$  in the Cartesian space (Fig. 5.15), which are collectively represented by  $\mathbf{x}_k = [\mathbf{p}, \mathbf{n}]^T \in \mathfrak{R}^6$ . The forward transition model of the soft robot can be described by the following equation system:

$$\begin{aligned}\boldsymbol{\theta}_{k+1} &= f(\boldsymbol{\theta}_k, \Delta \mathbf{u}_k) \\ \mathbf{x}_k &= h(\boldsymbol{\theta}_k)\end{aligned}\tag{5.10}$$

where  $\Delta \mathbf{u}_k = \mathbf{u}_{k+1} - \mathbf{u}_k$  is the difference of the fluid pressure. The motion transition function  $f$  is a continuous mapping that depends on the current state of the robot  $\boldsymbol{\theta}_k$ . Compared to rigid-link robots where the robot state can be well-defined by joint kinematics, it is difficult to describe the exact state of the soft robot. For example, model-based approaches approximate this robot state based on PCC [26, 92, 94, 96–101] and non-PCC [102–106] constraints. The nonlinear function transforms robot state  $\boldsymbol{\theta}_k$  to Cartesian representation  $\mathbf{x}_k$ .

Typical endoscopic navigation requires delicate articulation of the distal tip so as to provide accurate positioning and easy access to the soft tissue lesion. A micro-camera at the soft robot tip provides forward vision. Therefore, the operator can aim the distal tip at a lesion target on the luminal wall so as to guide the interventional instruments to deploy from the tip via the biopsy channel. This tele-manipulated endoscopic navigation gives rise to a robot task space coordinate  $\mathbf{s}_k$  defined by its viewing direction (i.e., pitch and yaw angle). The system equation in Eq. 5.10 can hence be extended to an actuation to task space mapping  $f_s$  as follow:

$$\mathbf{s}_{k+1} = f_s(\boldsymbol{\theta}_k, \Delta \mathbf{u}_k)\tag{5.11}$$

where  $\mathbf{s}_{k+1} = \mathbf{s}_k + \Delta \mathbf{s}_k$  is the task space coordinate at time step  $k + 1$  after the change in fluid pressure  $\Delta \mathbf{u}_k$  is applied.

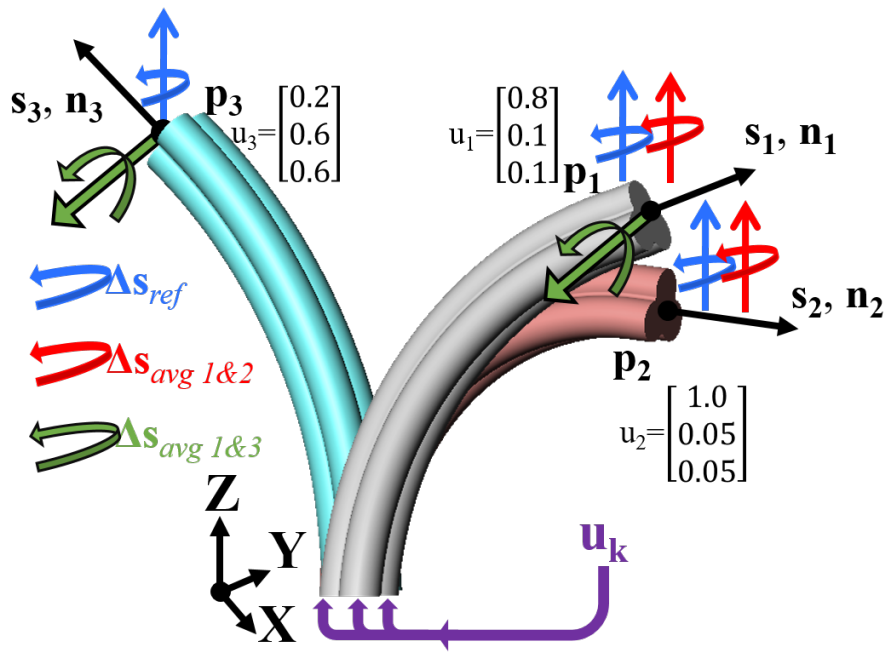


**Figure 5.15:** Three robot configurations illustrating the example of localized inverse models. Assume that their tip directions  $s_i$  will undergo the same rotation  $\Delta s_{ref}$  (blue arrow) with the proper pressure changes  $\Delta u_i$  applied, where  $i = 1 \dots 3$ . (a) In the case of configurations 1 and 2, the average of their control inputs  $\Delta u_1$  and  $\Delta u_2$  would still lead to a consistent  $\Delta s_{avg}$  (red arrow); (b) While two configurations, such as 1 and 3, are vastly different, this average of inputs  $\Delta u_1$  and  $\Delta u_3$  may lead to two dramatically different rotations  $\Delta s_{avg}$ , leading to undesired movement. Therefore, learning the inverse model directly with a global function approximator may lead to invalid solutions and unstable robot performance.

### 5.5.2 Inverse Problem for Online Learning Task Space Control

Our control objective is to enable the operator to control the displacement of the robot directly in the task space coordinate  $\Delta s_k^*$  (i.e., the desired change in the robot tip orientation) with the use of a motion input device. The superscript “\*” denotes the desired motion specified by the users or other reference input. Thus, the controller is designed to approximate the inverse of the motion transition  $f_s$  in Eq. 5.11, i.e.  $\Delta u_k = \tilde{\Phi}(\Delta s_k^*, \theta_k)$ , in order to estimate the required change in control input  $\Delta u_k$  (as seen in Fig. 5.16). The inverse motion transition model  $\tilde{\Phi}$  heavily depends on the current robot state  $\theta_k$ . However, the exact state cannot be directly measured due to its hyper-flexibility and the interactions with enclosed workspace inside a patient’s cavity. We sought to adopt the task space coordinates  $s$  which would offer the updated clues about the current robot state. This approach is also of practical interest because these measurements are readily available in our control system. The task space coordinate  $s$  can be tracked using advanced positional

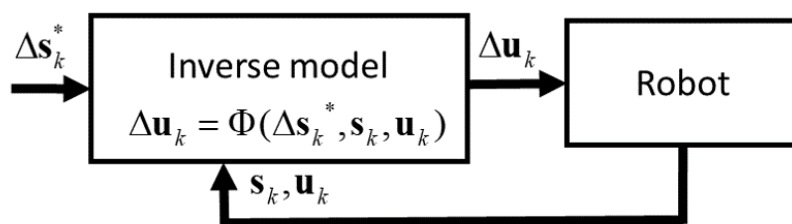


**Figure 5.16:** Schematic diagram of the robot control routine. The measured value of task space coordinate  $\mathbf{s}_k$  and actuation input  $\mathbf{u}_k$  provide localized information for the inverse estimation.

tracking systems. For example, electromagnetic tracking systems are commonly used in medical application to provide sub-millimetre-level tracking [208, 209]. Together with the actuators input  $\mathbf{u}_k$ , these online acquired data are presented to the learning algorithms to update the inverse mapping during robot run-time.

$$\Delta \mathbf{u}_k = \Phi(\Delta \mathbf{s}_k^*, \mathbf{s}_k, \mathbf{u}_k) \quad (5.12)$$

Note that  $\Phi$  is the approximation of the true inverse mapping  $\tilde{\Phi}$ . If the dimensionality of the task space is smaller than that of the control space, theoretically there exists an infinite number of solutions  $\Delta \mathbf{u}_k$  of that result in the same task space displacement  $\Delta \mathbf{s}_k$ . This leads to the *ill-posed* problem in learning the inverse mapping  $\Phi$ .

### 5.5.3 Inverse Model Learning with Multiple Local Controllers

Nonparametric local learning techniques have been applied to learn the ill-posed inverse problem, aiming to control redundantly actuated robots [107, 210, 211]. Referring to Peters *et al.* [212], the inverse model of a rigid link robot can be learnt using spatially localized nonparametric learning techniques, given that the robot state is well-defined by the joint kinematics. Here, the spatial localization refers to the robot state  $\boldsymbol{\theta}_k$ . Such localization scheme is motivated by the hypothesis that the inverse problem would be well-defined locally [212]. It is because nonparametric learning techniques essentially average out the sampled data. Model learning based on nonconvex training datasets would give invalid solutions [212]. However, in the vicinity of  $(\mathbf{s}, \mathbf{u})$ , the average of would be consistent with the average of  $\Delta \mathbf{u}$  the task space displacement  $\Delta \mathbf{s}$  (Fig. 5.15). Therefore, in a local region of a given  $(\mathbf{s}, \mathbf{u})$ , the training dataset  $\{\Delta \mathbf{u}, \Delta \mathbf{s}, \mathbf{s}, \mathbf{u}\}$  would become a convex set. This enables learning of the inverse mapping in the vicinity of  $(\mathbf{s}, \mathbf{u})$  (Fig. 5.15). We approximate the local inverse mapping from the desired task space displacement to the

actuation command as follows:

$$\Delta \mathbf{u}_k = \Phi^i(\Delta \mathbf{s}_k^*, \mathbf{s}_k, \mathbf{u}_k) = [\Delta \mathbf{s}_k^*]^T \boldsymbol{\beta}^i \quad (5.13)$$

where  $\boldsymbol{\beta}^i$  is the parameter of the local inverse model. Each mapping serves as a local controller. Compared to [212], we do not include an intercept/bias term, since the change of actuation command  $\Delta \mathbf{u}$  should have zero mean. The computation of  $\boldsymbol{\beta}^i$  will be explained in the later context.

#### 5.5.4 Online Learning of the Global Controller

To approximate the global inverse mapping, we employ a linear combination of the locally learned mapping [213]:

$$\Delta \mathbf{u}_k = \frac{\sum_{i=1}^n w^i(\mathbf{s}_k, \mathbf{u}_k) \Phi^i(\Delta \mathbf{s}_k^*, \mathbf{s}_k, \mathbf{u}_k)}{\sum_{i=1}^n w^i(\mathbf{s}_k, \mathbf{u}_k)} = \frac{\sum_{i=1}^n w^i(\mathbf{s}_k, \mathbf{u}_k) [\Delta \mathbf{s}_k^*]^T \boldsymbol{\beta}^i}{\sum_{i=1}^n w^i(\mathbf{s}_k, \mathbf{u}_k)} \quad (5.14)$$

This controller architecture allows straightforward, one-iteration computation in each time step, in contrast to indirect modeling approaches [110]. The number of local models  $n$  and the weight  $w^i(\mathbf{s}_k, \mathbf{u}_k)$ , as well as the local controllers  $\Phi^i(\Delta \mathbf{s}_k^*, \mathbf{s}_k, \mathbf{u}_k)$  can be obtained in an online manner.

For this purpose, the local forward model is “learnt” using Locally Weighted Projection Regression (LWPR) [214] which offers piecewise linear function approximation, while simultaneously determines the appropriate local region of each linear model. Each local forward model performs a linear mapping as:

$$\Delta \mathbf{s}_k = f_s^i(\mathbf{s}_k, \mathbf{u}_k, \Delta \mathbf{u}_k) = [\Delta \mathbf{u}_k]^T \hat{\boldsymbol{\beta}}^i \quad (5.15)$$

where  $\hat{\boldsymbol{\beta}}^i$  denotes the corresponding parameter. Each local region, namely the receptive field (RF), is shaped based on the membership function:

$$w^i(\mathbf{s}_k, \mathbf{u}_k) = \exp \left( -0.5 \left( \begin{bmatrix} \mathbf{s}_k \\ \mathbf{u}_k \end{bmatrix} - \mathbf{c}^i \right)^T \mathbf{D}^i \left( \begin{bmatrix} \mathbf{s}_k \\ \mathbf{u}_k \end{bmatrix} - \mathbf{c}^i \right) \right) \quad (5.16)$$

centered at  $\mathbf{c}^i$ , where  $\mathbf{D}^i$  is the distance metric. Each membership function weights the corresponding locally learned inverse model in the controller Eq. 5.15. One advantage of LWPR is that it can automatically spawn new linear models and the corresponding RF



when new data laid outside all existing RF is presented. Meanwhile, the center  $\mathbf{c}^i$  of RF is determined by the input space of new data through the incremental learning, so as the total number of local regions  $n$  (Fig. 5.17). Each newly spawned RF is initialized with a diagonal distance metric  $\mathbf{D}_i$  value. This  $\mathbf{D}_i$  value will be updated throughout the incremental learning process to improve the overall regression accuracy and convergence rate. To prevent overfitting and allocation of too many numbers of RFs  $n$ , a smaller initial  $\mathbf{D}_i$  value is preferred (i.e. larger receptive fields). Cross-validation is also employed in determining the initial  $\mathbf{D}_i$ , which is of important to ensure that the forward model can be accurately reflected by the piece-wise linear regression.

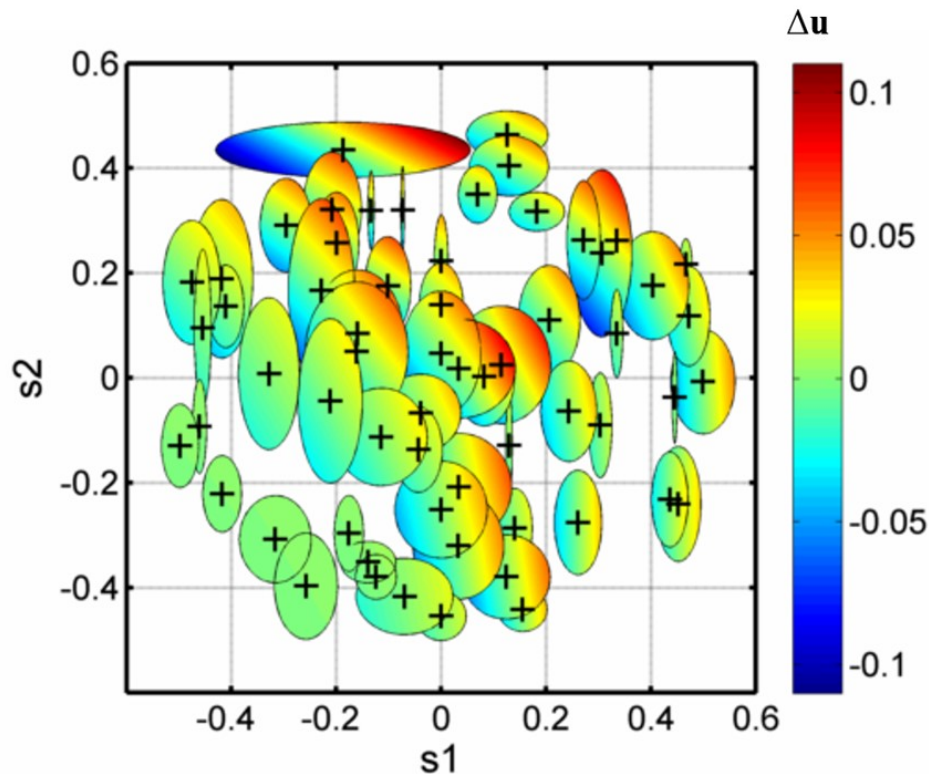


**Figure 5.17:** Example set of localized linear controllers that approximate the nonlinear inverse mapping  $\Phi$  of a 1-D actuation  $\Delta \mathbf{u}$ . The valid region of each spatially localized controller is centered at  $\mathbf{c}_i$  (denoted by plus sign), with their range parameterized by  $\mathbf{D}_i$  (colored ellipse) in the robot state space. The warm color depicts the actuation  $\Delta \mathbf{u}$  predicted by the linear control law  $\beta_i$ , in order to achieve a particular movement  $\Delta \mathbf{s}^*$  in task space.

Despite the fact that each RF could fulfill the local convexity requirement, due to the redundancy in the robotic system, the solutions of the local controllers (Eq. 5.13) could be inconsistent with the desired solutions [212]. Therefore, two approaches, namely i) data pre-process scheme and ii) constrained optimization, are proposed to modify the training dataset such that the underlying inverse model is approximately a one-to-one mapping.

### 5.5.4.1 Pre-processing of Training Dataset with Redundancy

The one-to-one mapping of the training dataset  $\mathbf{Q} := \{\Delta\mathbf{u}_i, \Delta\mathbf{s}_i, \mathbf{s}_i, \mathbf{u}_i\}_{i=1}^N$  can be enforced by a data pre-processing scheme, which only picks out a subset of data  $\mathbf{R}$  that does not contain redundancy. The pseudocode of the pre-processing scheme is outlined in [Algorithm 5.1](#). One simple heuristic is to freeze one of the actuation chambers so that only two chambers are responsible for the motion on the task space. This can be done by only selecting samples where at least one of its components in the change of actuation vector  $\Delta\mathbf{u}_i$  is equal to zero ([Algorithm 5.1](#), Line 4). In addition, the inverse solution should also avoid inflating all three chambers simultaneously, because it will further elongate the whole manipulator so that more pressured fluid must be inflated to achieve the same bending effect. Such requirement is imposed on Line 5 of [Algorithm 5.1](#) that choose data comprised of at least one or more zero components in the inflation volume vector  $\mathbf{u}_i + \Delta\mathbf{u}_i$ .

---

**Algorithm 5.1** Pseudocode of the training dataset pre-processing scheme. Input variable  $\mathbf{Q}$  denotes the arbitrary training dataset obtained from experiment, and output variable  $\mathbf{R}$  refers to the pre-processed training dataset.

---

```

1  Input: array of  $N$  training dataset  $\mathbf{Q} := \{\Delta\mathbf{s}_i, \mathbf{s}_i, \mathbf{u}_i, \Delta\mathbf{u}_i\}_{i=1}^N$ 
2   $\mathbf{R} := \text{empty\_array}()$ 
3  for  $i = 1, \dots, N$  do
4    if  $\text{contain\_zero}(\Delta\mathbf{u}_i)$ 
5      AND  $\text{contain\_zero}(\mathbf{u}_i + \Delta\mathbf{u}_i) \rightarrow \text{True}$  then
6         $\text{append}(\mathbf{R}, \mathbf{Q}_i)$ 
7  Output: array of training dataset  $\mathbf{R}$  without redundancy

```

---

### 5.5.4.2 Constrained Optimization to Resolve Redundancy

Although the data redundancy problem could be resolved by the abovementioned data pre-processing scheme so that it only produces one particular solution, it lacks the generality and is difficult to apply in high dimensional systems [107]. Therefore, a constrained optimization approach that reshape the local inverse models is employed, enforcing the local controllers to provide consistent solutions from infinite possibilities in the null space of the control space. The optimization problem is defined as follows:

$$\min_{\Delta\mathbf{u}} C_k(\Delta\mathbf{u}_k) = (\Delta\mathbf{u}_k - \Delta\mathbf{u}_{0,k})^T \mathbf{N}(\Delta\mathbf{u}_k - \Delta\mathbf{u}_{0,k}) \quad (5.17)$$

subject to  $\Delta\mathbf{u}_k = \Phi(\Delta\mathbf{s}_k^*, \mathbf{s}_k, \mathbf{u}_k)$

where the cost function  $C_k$  represents the user-defined optimality scaled by a diagonal matrix  $\mathbf{N}$ .  $\Delta \mathbf{u}_{0,k} = \mathbf{v}(\mathbf{s}_k, \mathbf{u}_k)$  is the user-defined null space behavior. One example of null space behavior could be minimizing the elongation of the robot, which results in smaller bending radius to facilitate dexterous motion inside enclosed cavity. Finally, the optimization constraint  $\Delta \mathbf{u}_k = \Phi(\Delta \mathbf{s}_k^*, \mathbf{s}_k, \mathbf{u}_k)$  ensures the correctness of the inverse solution.

The constrained optimization problem can be solved by introducing a reward function Eq. 5.18 and a cost function Eq. 5.19:

$$r(\mathbf{u}_k) = \sigma_i \exp(-0.5\sigma_i^2 C_k) \quad (5.18)$$

$$E_i = \sum_{k=1}^N r(\mathbf{u}_k) w^i(\mathbf{s}_k, \mathbf{u}_k) (\Delta \mathbf{u}_k - [\Delta \mathbf{s}_k^T] \boldsymbol{\beta}^i)^2 \quad (5.19)$$

The reward function  $r(\mathbf{u}_k)$  is scaled by the mean cost  $\sigma_i$  to improve the learning efficiency [212]:

$$\sigma_i^2 = \frac{\sum_{h=1}^k w^i(\mathbf{s}_h, \mathbf{u}_h) C_h}{\sum_{h=1}^k w^i(\mathbf{s}_h, \mathbf{u}_h)} \quad (5.20)$$

The cost function is then minimized by means of reward-weighted regression, where each local model needed to be updated:

$$\boldsymbol{\beta}_{k+1}^i = (\mathbf{X}^T \mathbf{W}^i \mathbf{X})^{-1} \mathbf{X}^T \mathbf{W}^i \mathbf{Y} \quad (5.21)$$

where  $\mathbf{W}^i = \text{diag}(r(\mathbf{u}_1)w_1^i, \dots, r(\mathbf{u}_k)w_k^i)$ ,  $\mathbf{X} = [\Delta \mathbf{s}_k^*]$  and  $\mathbf{Y} = [\Delta \mathbf{u}_k]$  are the training datasets. The overall procedures of the learning-based controller are summarized in Algorithm 5.2.

**Algorithm 5.2** Nonparametric online learning of inverse mapping.

- 
- 1 **for each new input data sample:**  $[\Delta \mathbf{s}_k^*, \mathbf{s}_k, \mathbf{u}_k, \Delta \mathbf{u}_k]$
  - 2     Add  $(\mathbf{s}_k, \mathbf{u}_k, \Delta \mathbf{u}_k) \rightarrow \Delta \mathbf{s}_k^*$  to the forward model LWPR.
  - 3     Update the current number of models  $n$  and localization of the forward models  $w^i(\mathbf{s}, \mathbf{u})$  for all input data  
   Compute desired null-space behavior
  - 4      $\Delta \mathbf{u}_{0,k} = \nu(\mathbf{s}_k, \mathbf{u}_k)$ .  
   Compute costs  $C_k = (\Delta \mathbf{u}_{1,k})^T \mathbf{N} \Delta \mathbf{u}_{1,k}$ , where
  - 5      $\Delta \mathbf{u}_{1,k} = \Delta \mathbf{u}_k - \Delta \mathbf{u}_{0,k}$
  - 6     **for each model**  $i = 1, 2, \dots, K, n$   
   Update the mean cost:
  - 7     
$$\sigma_i^2 = \sum_{h=1}^k w^i(\mathbf{s}_h, \mathbf{u}_h) C_h / \sum_{h=1}^k w^i(\mathbf{s}_h, \mathbf{u}_h)$$
  
   Compute reward:
  - 8      $r(\Delta \mathbf{u}_k) = \sigma_i \exp(-0.5 \sigma_i^2 C_k)$   
   Solve the following reward-weighted regression problem with step 10-13:
  - 9     
$$E_i = \sum_{k=1}^N r(\mathbf{u}_k) w^i(\mathbf{s}_k, \mathbf{u}_k) (\Delta \mathbf{u}_k - [\Delta \mathbf{s}_k^T] \boldsymbol{\beta}^i)^2$$
  
   Add new data point to the weighted regression:
  - 10      $\mathbf{X}_k = [\Delta \mathbf{s}_k^*]$
  - 11      $\mathbf{Y}_k = [\Delta \mathbf{u}_k]$
  - 12      $\mathbf{W}^i = \text{diag}(r(\mathbf{u}_1) w_1^i, \dots, r(\mathbf{u}_k) w_k^i)$
  - 13     Update the weighted regression of inverse mapping model  
   
$$\boldsymbol{\beta}_{k+1}^i = (\mathbf{X}^T \mathbf{W}^i \mathbf{X})^{-1} \mathbf{X}^T \mathbf{W}^i \mathbf{Y}$$
  - 14     end
  - 15 end
-

### 5.5.5 Experimental Results

The proposed control framework is implemented on a custom-made soft robot to investigate its performance and behavior under external dynamic constraints. We have also attempted to utilize FEA to simulate robot motion data for pre-training of an initial control policy. This can avoid the need for random exploration of its robot workspace to initialize online learning functions. Such exploration is usually time-consuming, and may not be practical, particularly for single-use purposes in surgical applications. Accuracy and stability of the proposed controller are examined via path following under various constrained environments. The interaction force with the external constraint is also measured throughout the experiments. The control block diagram of the overall robotic system, including the processing core and actuation system, is illustrated in [Fig. 5.18](#).

#### 5.5.5.1 Initialization of Online Learning by FEA-based Model

Proper initialization of pre-training data is essential to many online learning techniques. These preceding data are dedicated to pre-training an initial control policy before the online learning begins. It is usually acquired by driving the robot with random input. Instead, we proposed to incorporate FEA, by which the robot deformation can be simulated with a hyper-elastic computation model. This simulation can generate comprehensive pre-training samples that cover the entire robot workspace at a high resolution, facilitating offline pre-training of the learning-based controller ([Fig. 5.8](#)).

#### 5.5.5.2 Experimental Setup

To evaluate the proposed control performance, three motorized pneumatic units are employed to actuate the presented soft manipulator incorporated with our close-loop control testing platform ([Fig. 5.18](#)). Each unit consists of a pneumatic cylinder coupled to a precise stepper motor through a leadscrew transmission. This facilitates accurate regulation of the air flow. Our soft robotic manipulator can be fully articulated in a dome-shaped workspace with a maximum curve angle of  $>150^\circ$  in all directions.

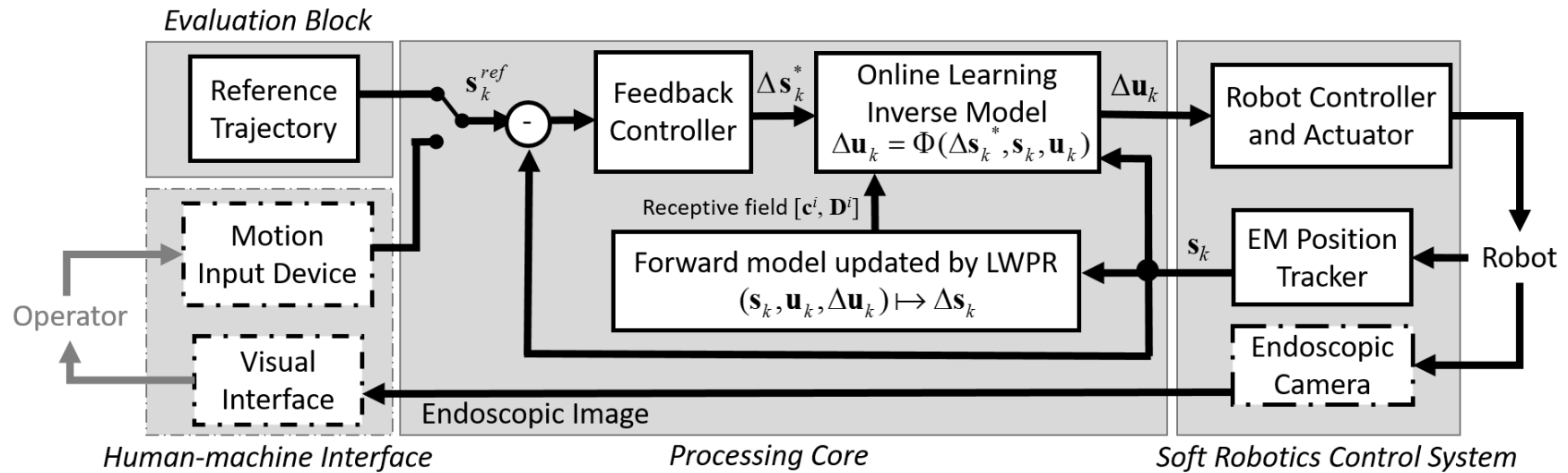


**Figure 5.18:** System architecture of the proposed control framework depicting interconnection of the key components. The processing core is responsible for fast computation of inverse solution. The inverse model is also updated continuously by incorporating the online data in real time. The operator can specify the reference input  $\mathbf{s}_k^{ref}$  via a motion input device for effective endoscopic navigation. In our experiments, this input is replaced by a pre-defined reference trajectory to evaluate the online learning performance of the inverse mapping.

An electromagnetic (EM) tracking system (NDI Medical Aurora) is employed to close the robot control loop by the continuous positional data feedback (Fig. 5.19a). This tracking system is commonly available in many image-guided intervention systems. It can track of the position and orientation of tiny EM coils in real time with RMS accuracy of 0.7mm and 0.2° at 40Hz. A tiny tracking coil is embedded at the robot distal tip. Online updating (at 20Hz) of the inverse mapping estimation  $\Delta \mathbf{u}_k = \Phi(\Delta \mathbf{s}_k^*, \mathbf{s}_k, \mathbf{u}_k)$  by the local learning algorithm is achieved, where  $\mathbf{s}_k$  is measured tip direction. The positional data is also recorded throughout the robot task so as to evaluate the overall control performance. The entire control framework is implemented in the MATLAB environment. The open source library of LWPR [215] is employed to incrementally learn the robot forward model, which determines the valid linearization of each local controllers.

A series of path following tasks is performed under various constraints scenarios to investigate how the online learning control approach reacts to such unknown interactions. At the beginning, the robot is allowed to move freely in its workspace without any interference. This serves as the control experiment to establish the baseline of controller performance. Subsequently, the robot is gently pushed by a plastic rod in order to simulate an unknown, dynamic interaction with the robot manipulation (Fig. 5.19b). The rod is actuated by a high precision stepping motor to generate repeatable contact with the robot body; meanwhile, the contact force is monitored by a force/torque sensor (ATI Industrial Automation: F/T Nano17). The tracking error is defined as the shortest distance between the robot targeting direction and the desired trajectory.

### 5.5.5.3 Performance Evaluation

To realize accurate navigation under unknown constraints, the inverse model is adapted in the proposed learning-based controller, which has to be updated online based on the newly acquired motion data. In this study, we compared three types of data sources for the inverse models training:

- i) Pre-trained by FEA data without using online data;
- ii) Initialized by random exploration with online learning data; and
- iii) Pre-trained by the FEA data, and then updated by online data.

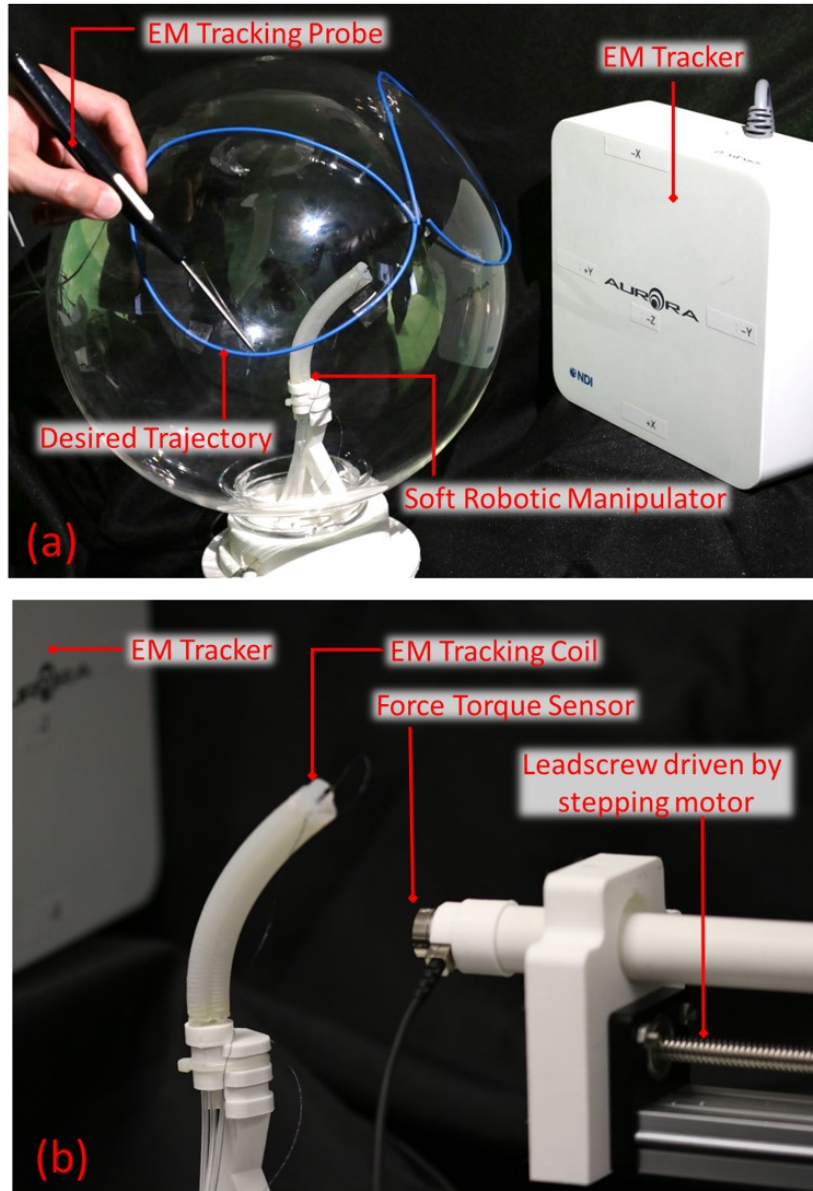


**Figure 5.19:** (a) Registration process of the predefined trajectory using an EM position tracking system. Blue line on the transparent sphere illustrates the tracking trajectory on the task space; (b) Soft manipulator is commanded to follow the desired trajectory automatically. Its end-effector position is also measured by the tracking system to close the feedback loop under online learning control policy. Plastic rod actuated by a stepping motor pushes against the soft robot, generating the external constraints. The contact force is monitored by a force/torque sensor.



These online-updated inverse models are evaluated for resolved motion rate control [216] to track a pre-defined trajectory. Thus, the desired task space displacement  $\Delta \mathbf{s}_k^*$  that tracks the reference input is obtained as follow:

$$\Delta \mathbf{s}_k^* = \Delta \mathbf{s}_k^{ref} + \mathbf{K}_p^{ref} (\mathbf{s}_k^{ref} - \mathbf{s}_k) \quad (5.22)$$

where  $\Delta \mathbf{s}_k^{ref}$  and  $\mathbf{s}_k^{ref}$  are the reference task space displacements and coordinates generated from interpolating a pre-defined trajectory. Note that the reference input can be replaced by manual control in actual endoscopic navigation scenario. We employed the same proportional–derivative (PD) gain  $\mathbf{K}_p^{ref} = \mathbf{I}$  for all three settings to perform tracking along a reference trajectory. Thus, the actuation input  $\Delta \mathbf{u}_k$  is estimated by the online learning inverse model as depicted Eq. 5.13.

To enforce the consistency of inverse mapping among all localized linear controllers, a standard null space behavior  $[\Delta \mathbf{u}_{0,k} = \mathbf{v}(\mathbf{s}_k, \mathbf{u}_k)]$  is defined. This gives rise to an immediate reward function  $r(\Delta \mathbf{u}_k)$  to weigh the training data that best imitates the desired null space behavior (Eq. 5.18). For the presented soft robot, we first choose a rest configuration to be  $\mathbf{u}_{rest} = [0, 0, 0]^T$ , which can minimize the overall inflation pressure as well as the elongation of the manipulator. Then the robot is attracted towards to the rest configuration with a loose attractor function  $\Delta \mathbf{u}_{0,k} = -\mathbf{K}_p(\mathbf{u}_k - \mathbf{u}_{rest})$ , where  $\mathbf{K}_p = 0.2\mathbf{I}$ . We defined an identity matrix  $\mathbf{N} = \mathbf{I}$  as all three inflatable actuators of the robot are identical and should contribute the same in achieving the desired null space behavior.

It is also necessary to normalize the training dataset into the same scale component-wise so that the LWPR can learn the data variance properly. Min-max normalization is a simple but effective technique commonly used [217]:

$$\hat{q}_i = \frac{q_i - \min(q_i)}{\max(q_i) - \min(q_i)} \quad (5.23)$$

However, the statistical  $\max(q_i)$  and  $\min(q_i)$  values would be sensitive to outliers; therefore, we define the min-max values according to the physical constraints of data, including the typical robot workspace and the maximum volume of the cylinder unit.

**Pre-trained by FEA without Using Online Data** In this setting, both the forward model and control policy are pre-trained solely by the FEA simulated data (Section 5.5.5.1). The online data was not taken account in this setting. This acts as a control experiment to

depict the actual influence of the external interactions. In the unconstrained experiment (Fig. 5.21a), it was observed that the controller could roughly follow the trajectory with a relatively large tracking error of  $\pm 1.79^\circ$  and a maximum error of  $\pm 4.64^\circ$ . Despite the considerable discrepancy between the FEA-simulated and the actual configuration, this experiment still demonstrates that the FEA data is capable of pre-training a reasonable inverse model for rough path following.

In the later constrained experiment (Fig. 5.22a), the robot maintained tracking of the trajectory with similar accuracy at the beginning. When the external interaction is engaged at the moment of 25 second, the robot was pushed further away from the desired trajectory, resulting in an increased mean tracking error  $\pm 4.64^\circ$  and a maximum error of  $\pm 14^\circ$  (Table 5.2). This indicates that the feedback controller cannot fully compensate the significant motion bias that is induced by the external disturbance. In the case of a conventional rigid-linked robot, this kind of error due to the interaction with the constraint is often considered as a perturbation. The error can hence be compensated by increasing the feedback control gain, given that the inverse model is readily available from the kinematics chain. However, such approach is not directly applicable to a soft robot due to their mechanical compliance that inevitably induces much larger positioning errors. In addition, the interaction force may also alter the force equilibrium of the robot and therefore, substantially degrading the reliability of the predetermined inverse model. The following experiments demonstrate how the proposed online algorithm can accommodate the influence of constrained environment, which is particularly demanding for the control of soft robots.

**Online Learning Initialized by Random Exploration** The random exploration of robot workspace is a typical approach [110] to initialize a data-driven controller before its actual deployment. This kind of arbitrary movement is necessary to provide preceding data for setting up a learning model. It involves tracking 50 random input pressure waypoints  $\mathbf{u}_k$  with a PD feedback controller. The deliberately-tuned PD gains can cause poor tracking of the random waypoints. Such babbling movement (green path in Fig. 5.21b & Fig. 5.22b) can facilitate faster learning rate as the robot sweep throughout a wider neighboring workspace. Pre-training with the exploration data resulted in a forward LWPR model with approximately 110 receptive fields (Fig. 5.20), which define the linearization for the piecewise linear inverse model in advance to actual deployment of the online learning.

Upon exploration, the online learning controller could follow the desired trajectory with an average error of  $\pm 1.13^\circ$  in the first cycle under the constraint-free environment

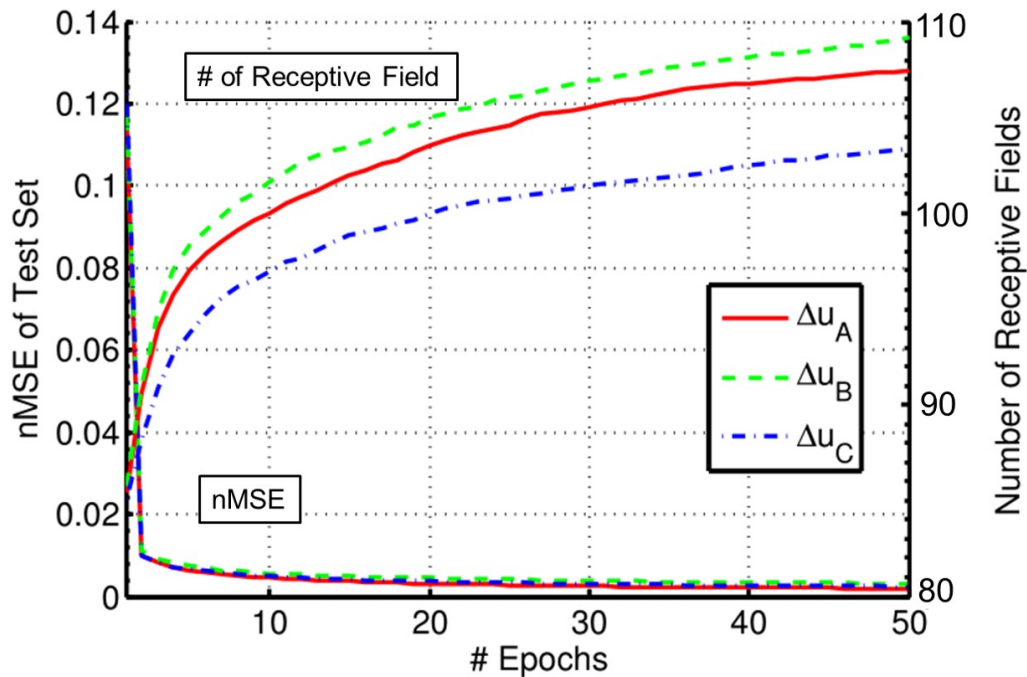


**Figure 5.20:** Learning curve of the nonparametric method approximating the inverse motion transition model  $\Delta \mathbf{u} = \Phi(\Delta \mathbf{s}^*, \mathbf{s}, \mathbf{u})$  for each of the three soft actuators A, B and C. Nonparametric method offers fast learning convergence as shown by the test error curve (nMSE) that rapidly descent within the first few epochs. The number of localized model and the complementary receptive fields increase over training epochs to achieve more accurate approximation of the inverse model.

(Fig. 5.21b). The error was found to be significantly lower than the inverse model pre-trained by FEA simulated data. It is reasonable because the actual robot data was used. After a few cycles, the tracking error further decayed to an average of  $\pm 0.87^\circ$  and maximum of  $\pm 1.92^\circ$ , as having the online learning controller adapted with the trajectory.

Next, the feasibility of online inverse model adaptation was validated by engaging external force interactions (Fig. 5.22b). The online learning controller can compensate the bias, and hence minimize the error down to an average of  $\pm 2.35^\circ$  within 5 seconds upon contact with the constraint. The external constraint is moved away after 30 seconds of contact. It is also worth noting that the controller could quickly update the inverse mapping online and follow the trajectory will high accuracy. No control instability is observed throughout the experiment. The pure online learning approach achieves the highest average accuracy among all settings, both for constrained and unconstrained scenarios (Table 5.1 & Table 5.2). However, the need for initialization by “babbling motion” (green path in Fig. 5.21b & Fig. 5.22b) should be avoided in clinical scenarios to prevent unnecessary interactions with patient anatomy.

**Online learning Pre-trained by FEA Data** To alleviate the need for random exploration, we attempted to pre-train the controller with FEA data and then update the inverse model by online learning. This approach combines the advantages of the both aforementioned settings, in which the inverse model can be initialized with FEA data. The robot can immediately begin navigation using this pre-trained model, without the need of the initialization through undesired babbling movement. The subsequent manipulation data are also acquired to incrementally train a more precise inverse model, so as to adapt to external interactions. This feature is demonstrated in Fig. 5.21c, in which the robot is allowed to move freely.

Although the robot begins with a relatively large tracking error of average  $\pm 2.21^\circ$  and maximum of  $\pm 7.49^\circ$  in the first cycle, the error is quickly compensated by the online learning and converged to an average of  $\pm 0.90^\circ$  and maximum of  $\pm 2.80^\circ$ . This tracking result is compared with the other two approaches in Table 5.1. In the first cycle, the combined approach exhibit tracking error close to pre-training with FEA only (Avg.  $\pm 2.21^\circ$  vs  $\pm 1.79^\circ$ ), because both inverse models are initialized with less accurate FEA data. The learning technique then correct the inverse model with online data, so that the tracking error decrease rapidly and become comparable with the pure online approach (Avg.  $\pm 0.90^\circ$  vs  $\pm 0.87^\circ$ ). This shows that the combined approach can initialize a reasonable learning-based controller with less accurate but analytically valid FEA data, then further refine the inverse model while performing the tracking task. Although the resultant tracking accuracy is not the best among the three approaches, note that the combined approach does not required random exploration (green path in Fig. 5.21b & Fig. 5.22b) to obtain pre-training data. Random exploration is an undesirable step to initialize an online learning model because it could be time consuming to collect data that cover the entire robot workspace with sufficient density. The data collection process also potentially cause damage to the robot body or the environments when performed under unknown constrained space.

This combined approach is also capable of adapting to the unknown external interaction (Fig. 5.22c). The inverse model can quickly adapt the inverse mapping upon contact with the external interaction at 36s. It continues to follow the trajectory with a small mean absolute error of  $\pm 2.49^\circ$ . The controller also remains stable and re-adapts after the removal of the constraints. Referring to Section 5.5.3, we presented the challenge in learning an inverse model spatially localized by the unmeasurable robot state  $\theta_k$ , as well as how this robot state can be retrieved indirectly from sensory measurements. These trajectory tracking experiments have shown that the inverse model could be successfully

learnt by continuous updates of both the task space coordinate  $\mathbf{s}_k$  and control input  $\mathbf{u}_k$ . Both are set as the localization parameters required in the inverse model. Therefore, the robot state  $\boldsymbol{\theta}_k$  could be estimated sustainably by the learning algorithm. These 3-6D positional data updates are clinically practical. The comparable position tracking techniques designed for image-guided interventions are also under active research [218], one of which would be MRI-guided endoscopic retrograde cholangio-pancreatography (ERCP).

**Table 5.1:** Trajectory tracking performance under freely moveable environment

Training Mode	Mean Abs. Error		Max. Abs. Error		Error SD $\sigma$	
	First Cycle	After	First Cycle	After	First Cycle	After
Pre-trained by FEA only	$\pm 1.79^\circ$	$\pm 1.82^\circ$	$\pm 6.96^\circ$	$\pm 6.56^\circ$	$1.71^\circ$	$1.66^\circ$
Pure Online Learning	$\pm 1.13^\circ$	$\pm 0.87^\circ$	$\pm 4.24^\circ$	$\pm 1.92^\circ$	$0.86^\circ$	$0.45^\circ$
Combined	$\pm 2.21^\circ$	$\pm 0.90^\circ$	$\pm 7.49^\circ$	$\pm 2.80^\circ$	$1.81^\circ$	$0.65^\circ$

**Table 5.2:** Trajectory tracking performance under constrained environment

Training Mode	Mean Abs. Error	Max. Abs. Error	Error SD $\sigma$	Mean Contact Force	Max. Contact Force
Pre-trained by FEA only	$\pm 4.64^\circ$	$\pm 14.00^\circ$	$3.20^\circ$	$0.77\text{N}$	$1.06\text{N}$
Pure Online Learning	$\pm 2.35^\circ$	$\pm 18.38^\circ$	$2.47^\circ$	$0.78\text{N}$	$0.97\text{N}$
Combined	$\pm 2.49^\circ$	$\pm 11.03^\circ$	$1.74^\circ$	$0.80\text{N}$	$0.96\text{N}$

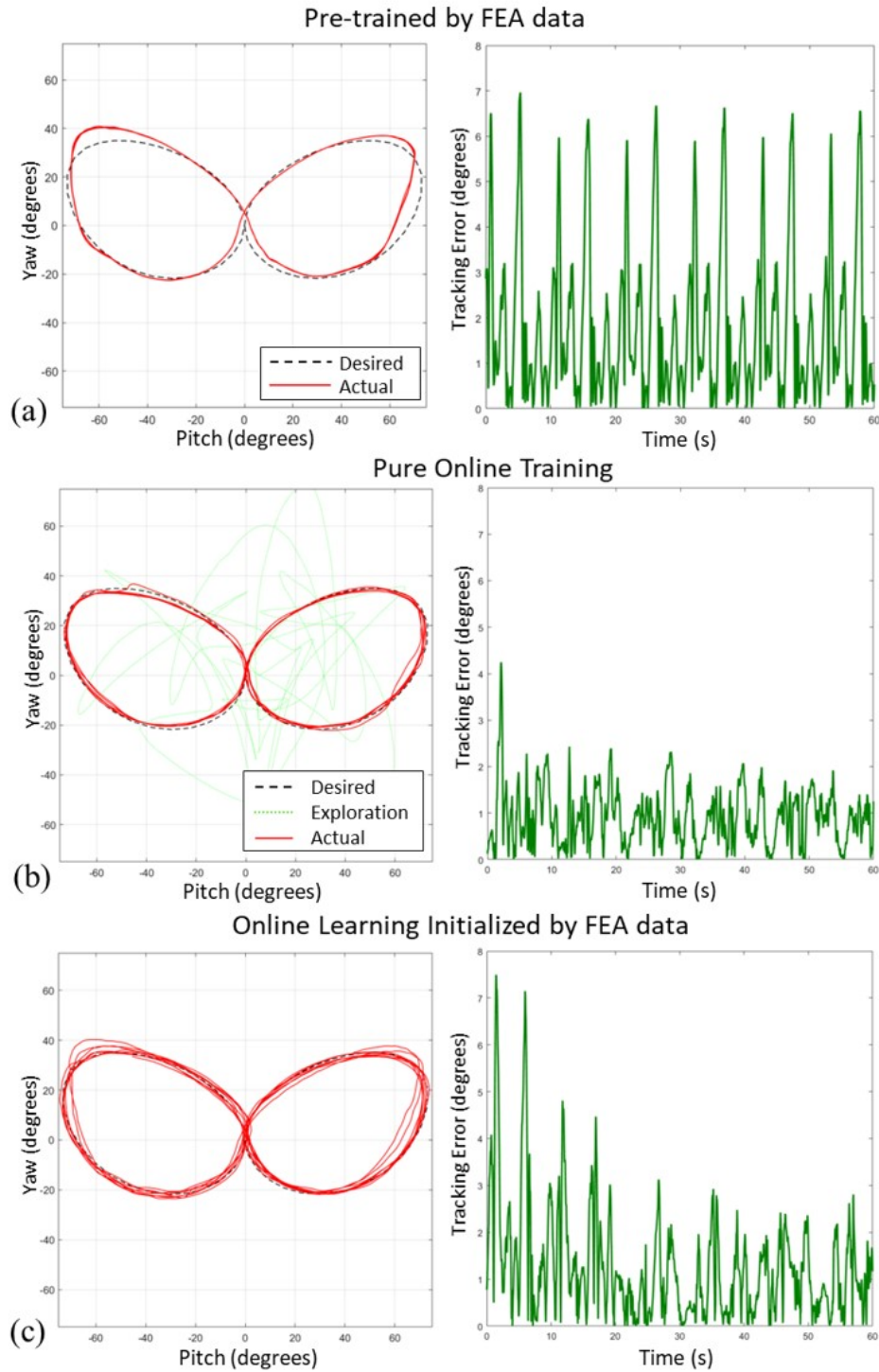


**Figure 5.21:** Plot of (Left) tracked trajectory and (Right) corresponding tracking error in time domain. In the control experiment, the robot is allowed to move freely without any constraint. Control performance of the online learning controllers trained by three different data source is validated: (a) Pre-trained by FEA without using online data; (b) Pure online learning initialized by random exploration; (c) Pre-trained by FEA data and updated by online data. The online learning initialized by FEA data approach (c) combines the advantage of (a) and (b), in which random exploration (Green path in (b)) is not required, but its tracking error converge to similar accuracy as in pure online learning.

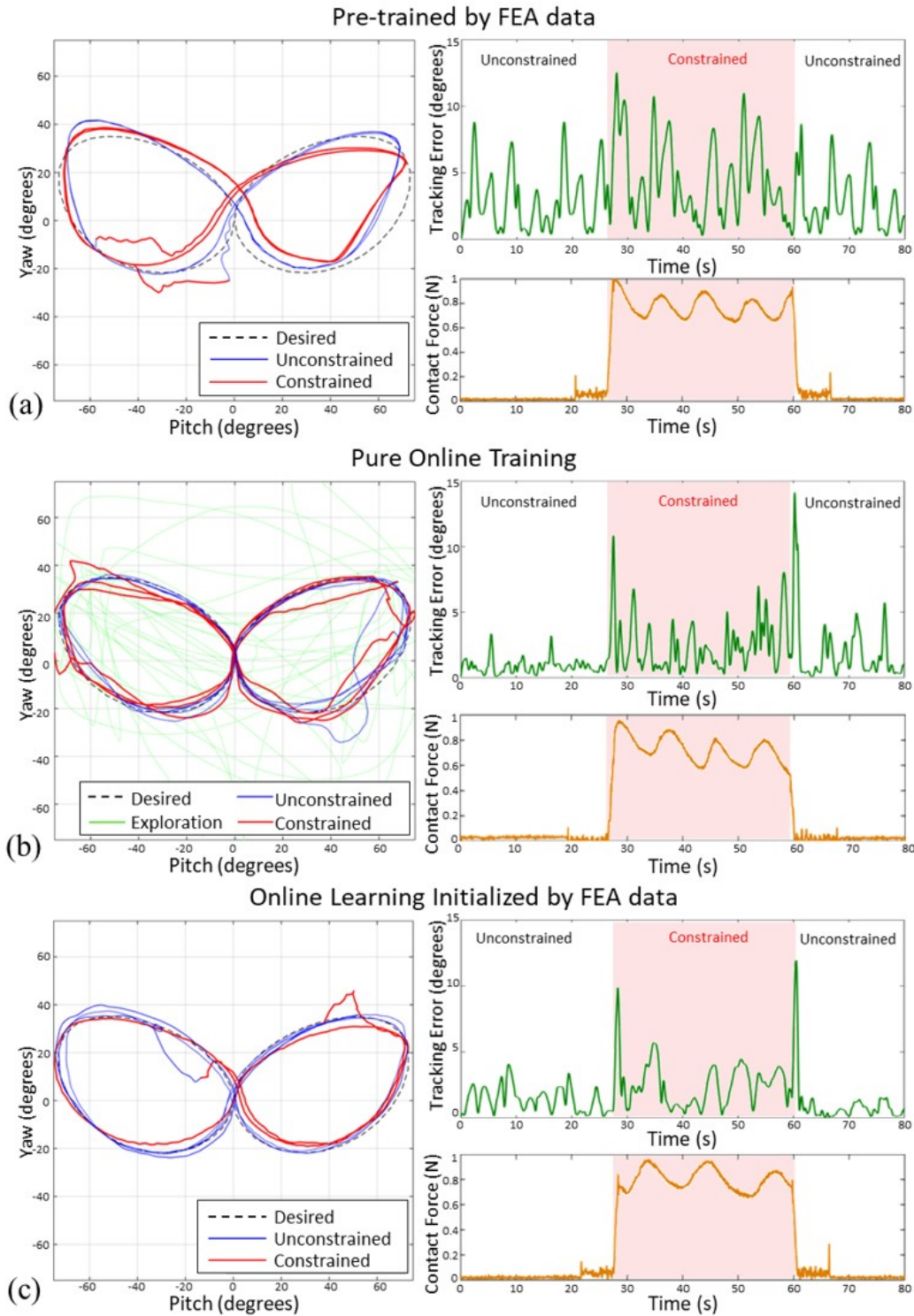


**Figure 5.22:** Plot of (Left) tracked trajectory and (Right) corresponding tracking error in time domain under external interactions. Control performance is validated in the three different conditions as in Fig. 5.21. It can be observed that the online learning for (b) and (c) is capable of compensating the external interaction with the tracking error reduced, as compared to the controller without using online data (a).

## 5.6 Conclusion

We have proposed a model-free control framework which adopts an online nonparametric local learning technique for manipulation of a redundantly-actuated, fluid-driven soft continuum robot in the presence of a dynamic external disturbance. Nonparametric techniques are capable of constructing highly nonlinear functions by measurement data solely, which is particularly suitable for characterization of hyper-elastic robot structure. To accommodate the flexibility of soft robot body, we approximate the global inverse kinematics by a linear combination of many locally learnt inverse kinematic models. Our model-free controller employs this global approximation, where the behavior of the redundant actuator can be optimized by a user-defined criterion, and simultaneously fulfilling the control objective defined in task space coordinates. In addition, the controller is adaptive to changes in the environment, where each local model can be updated online independently according to newly acquired data. This equips the robot with the ability to maintain control accuracy under external dynamic disturbance. Our work is the first attempt of implementing such direct inverse modeling using online nonparametric learning technique to control a redundantly-actuated soft continuum robot.

We have also incorporated FEA into the learning control framework for proper initialization of the robot inverse model. It enables precise prediction of the hyper-elastic robot deformation under various actuation pressure, without the need for the over-simplified analytical model. It can also offer adequate sample data covering the entire workspace at high resolution. This avoids the need of time-consuming random exploration to initialize the learning model, which may not be practical in many surgical applications. The proposed controller can hence be initialized offline using FEA simulated data, ready for endoscopic navigation procedure.

The proposed novel control framework has been experimentally validated. In the constrained experiment, after FEA-based initialization of the controller, the endoscope prototype could follow a 3-D trajectory with an accuracy of mean  $\pm 2.21^\circ$  and max.  $\pm 7.49^\circ$ , and attained the almost the same tracking accuracy (mean  $\pm 2.49^\circ$  and max.  $\pm 11.03^\circ$ ) after 5 seconds upon the addition/removal of external disturbance (max. 1N). This is also the first demonstration of realizing model-free close-loop control of a fluid-driven soft continuum in 3-D task space even under dynamic external disturbance.



## Chapter 6

# Conclusions and Future Work

### 6.1 Achievements of this Thesis

The latest technological advancement in intra-operative MRI-guided surgery allows for safer and less invasive procedures, consistent surgical outcome and reduced post-procedural. To fully leverage these advantages, surgical interventions will require significant improvement in accessibility, accuracy and manipulation dexterity, which is made possible with high-performance computing to process pre-op and intra-op images, as well as new continuum robot design and control dedicated for MRI environment. It is expected that the introduction of continuum articulated robots will bring a profound contribution to the upcoming trend of MRI-guided interventions. The techniques and design scheme proposed in this thesis are meant to facilitate enhanced teleoperation of continuum surgical robot, enabling improved accuracy, dexterity and safety of MRI-guided intervention for complex procedures.

The major contribution of the thesis can be summarized by the objectives as described in [Chapter 1](#):

- *Real-time Proximity Queries (PQ) processing*: Based on the highly parallelized architecture of Graphical Processing Unit (GPU), the proposed PQ algorithm has demonstrated significant improvement of the computation performance, which is >200 times faster than single-core CPU. It enables real-time computation of the relative configurations or potential collision between the robotic body and surgical

environments. While the algorithm is designed to work on parallel processors, the computation framework is readily scalable to resolve large-scale problems. Furthermore, no convexity assumption or bounding volumes are required because the General Cylinder (GC) constraint can readily fit the robot kinematics chain and movement. The PQ calculation can also directly take triangular mesh as input, which is the most general form of representation for 3D environments, without any pre-processing. This addresses the *Objective 1* of the thesis.

- *Fast Non-rigid Image Registration:* The proposed algorithm has demonstrated significant acceleration of the deformable registration using advanced computing architecture. It has been successfully adapted to a GPU-based framework, in which 3D images are divided into smaller segments and hence can be pre-fetched into the local memory (or shared memory in CUDA). In general, local memory is  $\approx 20\times$  faster than global memory. Such memory organization paradigm enabling fast access to adjacent pixel values and as a result improve the overall computation time by  $\approx 60\times$  when compared to single-threaded CPU. Input image sets with different scanning directions are readily compatible with the framework. This work can enable accurate alignment of pre-op data (e.g. planned trajectory, tumour margins) with the exact anatomical model in real time, providing augmented visualization of significant tissue changes in an automatic manner. Presently, such re-alignment have to be performed mentally by surgeons based on their subjective geometric perception. This address the *Objective 2* of the thesis.
- *Integrated Robotic Catheter Platform under MRI:* A novel MRI-guided robotic platform for catheterization is constructed with solely MR Safe materials. Hydraulic transmission with water is adopted to guarantee minimized imaging interference with the MRI. It has been shown that the robot can provide steering, rolling, translation and fine advancement of a catheter. To achieve effective manipulation, the actuators are designed to eliminate backlash effect and rolling diaphragms are employed to reduce friction. Real-time, intra-operative visualization and position feedback can also be incorporated for navigation. A real-time 3D cardiac roadmap can be constructed and updated base on intra-operative MR images. It has been demonstrated that a micro coil can be attached to the catheter tip, offering real-time ( $> 30$  Hz), low latency ( $<3$ ms) and accurate (fine spatial resolution  $0.6 \times 0.6 \times 0.6\text{mm}^3$ ) position tracking. The position feedback enables a virtual camera attached to the tip of the catheter to provide a virtual view for navigation. It is the first robotic systems for image-guided robot-assisted catheterization that integrates intra-operative MRI, real-time visual and position feedback and

visual-motor alignment. This also addresses *Objective 3* of the thesis.

- *Model-free Control for Catheter Robot*: The proposed model-free robotic catheter platform can enhance the targeting accuracy and reduce manipulation time, when compared to the prior-art model-based method. Users can manipulate the catheter by providing their desired displacement in the virtual view via a motion input device. The achievement has been validated with subject tests, in which an emulated ablation task is performed a high-fidelity phantom model, the proposed catheter robotics system. It can be attributed to the capability of model-free control in adapting to the confined environment of the heart chamber, while alleviating the visual motor-misalignment. This also addresses *Objective 4* of the thesis.
- *Soft Robotic Manipulator Design Scheme based on Finite Element Analysis (FEA)*: The hyperelastic FEA models for an individually constrained soft robots are established and validated. This computational model adopts customized hexahedral meshing to alleviate the dilatation locking effect, thus achieving enhanced mathematical stability and prediction accuracy even for large deformation model. The proposed FEA model enables efficient design optimization for the soft robot geometry, resulting in a new soft actuator that has high stiffness and capable of withstanding high inflation pressure (8bar). This address the *Objective 5* of the thesis.
- *Online Learning for Soft Robot Control*: The proposed online nonparametric local learning can directly approximate the inverse kinematics (IK) of a redundantly actuated flexible manipulator. The control framework can successfully accommodate the change in IK due to unknown external disturbance, by updating the model with robot motion data acquired online. To further enhance the training efficiency, FEA technique is incorporated to offer simulation data to initialize the learning model before deployment of the proposed controller. Precise control and rapid adaptability are demonstrated in a 3D trajectory tracking task, even under dynamic external disturbance. This address the *Objective 6* of the thesis.

## 6.2 Ongoing Research and Future Directions

To fully exploit the potential clinical impact of the proposed work in this thesis, many technical challenges have to be addressed. In [Chapter 3](#), further validation of the



GPU-based non-rigid image registration framework will need to be conducted with clinically-used navigation systems, e.g. for cardiac electrophysiology (EP). However, it could be a challenging task for main-stream MRI system because most of their computers are not equipped with GPU, not to mention that integration of third-party software is often prohibited. To this end, a software interface that can directly interface with an MRI (e.g. HeartVista [219]) shall be incorporated, so that the real-time images, upon acquisition, can be immediately streamed into a GPU-enabled computation platform. This will also enable real-time update of the 3D roadmap for navigation using intra-operative images.

On the technical aspect, the GPU-based acceleration technique is also compatible to many advanced image registration schemes that is based on the diffeomorphic log-demons algorithm. For example, spherical demons [220], spectral log-demons [221], adaptive demons [222], and many other improved demons-based approaches [223–225]. However, there is a lack of open-sourced GPU support for advanced demons-based algorithms. In this regard, the software package of the presented implementation of diffeomorphic log-demons will be open-sourced for the research community. As many advanced intensity-based image registration algorithms shares similar workflow (e.g. diffeomorphic field mapping) with the proposed implementation of algorithm, the established acceleration schemes can be easily translatable. This optimized implementation can also enable the use of the diffeomorphic log-demons algorithm in many time-critical applications. To further enhance the usage in the clinical research community, it will also require an implementation of software packages that are compatible to the Insight Segmentation and Registration Toolkit (ITK) which is an open software platform widely-use in medical imaging research. Thus, it is expected that the open implementation on GPU can encourage fellow researchers to improve the algorithms without concerns on computation performances.

Further acceleration of the Demon registration and PQ is also possible by leveraging the flexible computational architecture of Field Programmable Gate Array (FPGA) FPGA is specialized hardware originally being designed for developing electronic circuitry in a highly flexible manner. Recent development of HPC FPGA leverages their reconfigurable datapath to enable many novel computational schemes that is not possible for conventional computing platform. Mixed precision technology [126] is one of the example approaches, which enables trade-off between performance and precision by customized datapath with various bit-width. For the PQ process, that is We will also investigate how this PQ algorithm can take further advantage of exploiting mixed precision technologies with larger single-precision floating point unit (FPU) resources on FPGAs. For the PQ process,

the computation between far separated objects can go through a datapath with lower bit-width, thus attain lower resolution but higher throughput.

For the MR Safe catheter robotic platform presented in **Chapter 4**, the key ongoing work is to improve hydraulic actuation to offer a full range of catheter advancement along the vessels to the heart chamber. This is made possible through the new design of the hydraulic motor that integrates  $\geq 3$  of rolling-diaphragm cylinders. Due to the fact that the rolling-diaphragm cylinder can only offer push motion, a new crankshaft mechanism similar to that of the automotive engine shall be adopted to enable bi-directional and continuous actuator output. Furthermore, force control on each piston is also necessary to ensure a smooth and stable output torque. When combined MR Safe force sensing, such as FBG strain sensor, this will offer new potential to implement computed-torque control on the hydraulic motor, thus enable high performance and dynamic manipulation task. To further validate the practical application of the proposed robotic platform, *in vivo* experiments on animal subjects will need to be conducted under the interventional MRI environment. Besides, the proposed technique for MRI-guided interventions, including the real-time image registration, hydraulic actuation and MR-based tracking are all readily applicable to many other surgeries, such as stereotactic neurosurgery, breast biopsy or prostate interventions.

In **Chapter 5**, the current form of the learning-based control method is first designed for a single segment manipulator. As for the future work, it is possible to extend the framework to address soft manipulation with multi-segment [226]. As a cascade of multiple actuation modules, it provides enhanced manipulation flexibility for interventional tools, facilitating more complicated operations in confined space. In this case, a generic optimization function will be developed to resolve the null-space control of hyper-redundant robot [227]. Further characterization of such multi-segment soft manipulators will be investigated. To address its hyper-redundancy, it will also require additional sensory systems or algorithms to parameterize the possible motion transition of robot configuration, thus estimating the inverse model for the higher DoF robot. Another aspect of future work will focus on resolving the computational bottleneck of hyper-elastic FEA through the implementation of high-performance computing (HPC) architecture. This will incorporate not only parallel, but also reconfigurable computing features (found in FPGA), in order to pinpoint the complexity with regard to large memory access inevitably induced by numerous boundary problems. Such computation could be incorporated into a separated feedforward control loop running at relatively low frequency. It is anticipated that this prospective online FEA could give strong cues in regards to any interaction with

the external disturbance. Sensor is also another key element to the feedback control of soft robot. The current EM-based position tracking requires an external EM field generator with large footprint and an environment free from EM interference and metallic materials in order to function properly. As a result, these requirements hinder its usage in many practical applications. To further validate the proposed control scheme, the EM-based tracking will need to be replaced by self-contained sensing modality. Image-based feedback is a natural choice because the tip-mounted camera is often available in many applications of soft manipulators, e.g. endoscopy. Thus, the robot motion can be estimated by computer vision techniques like optical flow. Strain-based sensors, such as bending sensors or Fiber Bragg gratings (FBG) are also viable choices, because they can be embedded into the soft robot body and measure the exact robot configurations. This feature is crucial to more sophisticated dynamics control.

Currently, there is no existing commercial robotic platform that is MR Safe, that is also integrated with flexible manipulators and real-time MR image processing. This thesis represents a new benchmark in these three major aspects, which could accelerate the developing trend of MRI-guided assisted robotic systems, opening a new dimension for many existing image-guided procedures. It is expected that the emergence of the proposed MRI-guided robotic framework will facilitate safer, more precise and effective interventional approaches. This will decrease the chances of post-procedural disease recurrence, currently 30% in atrial fibrillation (AF) and 50% in ventricular tachycardia (VT), which could compensate for the cost of using MRI, and significantly reduce the overall healthcare expenditure on arrhythmia treatment. A new line of study will be developed attracting other researchers to push the envelope of robot-assisted interventions, particularly those using MRI on rapidly deformable tissues.

# References

- [1] R. González, “MRI and MRA of ischemic stroke,” in *Primer on Cerebrovascular Diseases (Second Edition)*, pp. 695–702, Elsevier, 2017.
- [2] P. Gimenez, N. Bugescu, J. Black, R. Hancock, K. Pugh, M. Nagamine, E. Kutner, P. Mazaika, R. Hendren, B. McCandliss, *et al.*, “Neuroimaging correlates of handwriting quality as children learn to read and write,” *Frontiers in human neuroscience*, vol. 8, p. 155, 2014.
- [3] V. Seifert and C. Senft, “Utilization of low-field intraoperative mri in glioma surgery: An overview,” 2016. [Online]. Available: <https://radiologykey.com/utilization-of-low-field-intraoperative-mri-in-glioma-surgery-an-overview/> [Accessed: Feb 2019].
- [4] The Ferenc Jolesz National Center for Image Guided Therapy, Department of Radiology, Brigham and Women’s Hospital, Harvard Medical School, “Amigo,” *Harvard University*, 2019. [Online]. Available: <https://ncigt.org/amigo> [Accessed: Feb 2019].
- [5] K. Masamune, E. Kobayashi, Y. Masutani, M. Suzuki, T. Dohi, H. Iseki, and K. Takakura, “Development of an mri-compatible needle insertion manipulator for stereotactic neurosurgery,” *Journal of Image Guided Surgery: Official Journal of the International Society for Computer Aided Surgery (ISCAS)*, vol. 1, no. 4, pp. 242–248, 1995.
- [6] N. Miyata, E. Kobayashi, D. Kim, K. Masamune, I. Sakuma, N. Yahagi, T. Tsuji, H. Inada, T. Dohi, H. Iseki, *et al.*, “Micro-grasping forceps manipulator for mr-guided neurosurgery,” in *International Conference on Medical Image Computing and Computer-Assisted Intervention*, pp. 107–113, Springer, 2002.
- [7] G. R. Sutherland, P. B. McBeth, and D. F. Louw, “Neuroarm: an mr compatible robot for microsurgery,” in *International congress series*, vol. 1256, pp. 504–508, Elsevier, 2003.

- [8] G. Li, H. Su, G. A. Cole, W. Shang, K. Harrington, A. Camilo, J. G. Pilitsis, and G. S. Fischer, "Robotic system for mri-guided stereotactic neurosurgery," *IEEE transactions on bio-medical engineering*, vol. 62, no. 4, p. 1077, 2015.
- [9] D. Stoianovici, C. Jun, S. Lim, P. Li, D. Petrisor, S. Fricke, K. Sharma, and K. Cleary, "Multi-imager compatible, mr safe, remote center of motion needle-guide robot," *IEEE Transactions on Biomedical Engineering*, vol. 65, no. 1, pp. 165–177, 2018.
- [10] D. B. Comber, J. E. Slightam, V. R. Gervasi, J. S. Neimat, and E. J. Barth, "Design, additive manufacture, and control of a pneumatic mr-compatible needle driver," *IEEE Transactions on Robotics*, vol. 32, no. 1, pp. 138–149, 2016.
- [11] R. C. Susil, A. Krieger, J. A. Derbyshire, A. Tanacs, L. L. Whitcomb, G. Fichtinger, and E. Atalar, "System for mr image-guided prostate interventions: canine study," *Radiology*, vol. 228, no. 3, pp. 886–894, 2003.
- [12] D. Stoianovici, D. Song, D. Petrisor, D. Ursu, D. Mazilu, M. Mutener, M. Schar, and A. Patriciu, "'mri stealth" robot for prostate interventions," *Minimally Invasive Therapy & Allied Technologies*, vol. 16, no. 4, pp. 241–248, 2007.
- [13] D. Stoianovici, A. Patriciu, D. Petrisor, D. Mazilu, and L. Kavoussi, "A new type of motor: pneumatic step motor," *IEEE/ASME Transactions On Mechatronics*, vol. 12, no. 1, pp. 98–106, 2007.
- [14] H. Su, M. Zervas, G. A. Cole, C. Furlong, and G. S. Fischer, "Real-time mri-guided needle placement robot with integrated fiber optic force sensing," in *Robotics and Automation (ICRA), 2011 IEEE International Conference on*, pp. 1583–1588, IEEE, 2011.
- [15] S.-E. Song, J. Tokuda, K. Tuncali, C. M. Tempany, E. Zhang, and N. Hata, "Development and preliminary evaluation of a motorized needle guide template for mri-guided targeted prostate biopsy," *IEEE Transactions on Biomedical Engineering*, vol. 60, no. 11, pp. 3019–3027, 2013.
- [16] S.-E. Song, K. Tuncali, J. Tokuda, A. Fedorov, T. Penzkofer, F. Fennessy, C. Tempany, K. Yoshimitsu, J. Magill, and N. Hata, "Workflow assessment of 3t mri-guided transperineal targeted prostate biopsy using a robotic needle guidance," in *Medical Imaging 2014: Image-Guided Procedures, Robotic Interventions, and Modeling*, vol. 9036, p. 903612, International Society for Optics and Photonics, 2014.
- [17] B. T. Larson, A. G. Erdman, N. V. Tsekos, E. Yacoub, P. V. Tsekos, and I. G. Koutlas, "Design of an mri-compatible robotic stereotactic device for minimally invasive



- interventions in the breast,” *Journal of Biomechanical Engineering*, vol. 126, no. 4, pp. 458–465, 2004.
- [18] D. Navarro-Alarcon, S. Singh, T. Zhang, H. L. Chung, K. W. Ng, M. K. Chow, and Y. Liu, “Developing a compact robotic needle driver for mri-guided breast biopsy in tight environments,” *IEEE Robotics and Automation Letters*, vol. 2, no. 3, pp. 1648–1655, 2017.
- [19] B. Yang, S. Roys, U.-X. Tan, M. Philip, H. Richard, R. P. Gullapalli, and J. P. Desai, “Design, development, and evaluation of a master–slave surgical system for breast biopsy under continuous mri,” *The International journal of robotics research*, vol. 33, no. 4, pp. 616–630, 2014.
- [20] V. Groenhuis, F. J. Sipel, M. K. Welleweerd, J. Veltman, and S. Stramigioli, “Sunram 5: An mr safe robotic system for breast biopsy,” in *Hamlyn Symposium on Medical Robotics: Pioneering the next generation of medical robotics*, 2018.
- [21] N. Archip, O. Clatz, S. Whalen, D. Kacher, A. Fedorov, A. Kot, N. Chrisochoides, F. Jolesz, A. Golby, P. M. Black, *et al.*, “Non-rigid alignment of pre-operative mri, fmri, and dt-mri with intra-operative mri for enhanced visualization and navigation in image-guided neurosurgery,” *Neuroimage*, vol. 35, no. 2, pp. 609–624, 2007.
- [22] K. Suzumori, S. Iikura, and H. Tanaka, “Development of flexible microactuator and its applications to robotic mechanisms,” in *IEEE International Conference on Robotics and Automation (ICRA)*, pp. 1622–1627, 1991.
- [23] R. F. Shepherd, F. Ilievski, W. Choi, S. A. Morin, A. A. Stokes, A. D. Mazzeo, X. Chen, M. Wang, and G. M. Whitesides, “Multigait soft robot,” *Proceedings of the national academy of sciences*, vol. 108, no. 51, pp. 20400–20403, 2011.
- [24] M. Cianchetti, T. Ranzani, G. Gerboni, T. Nanayakkara, K. Althoefer, P. Dasgupta, and A. Menciassi, “Soft robotics technologies to address shortcomings in today’s minimally invasive surgery: the STIFF-FLOP approach,” *Soft Robotics*, vol. 1, no. 2, pp. 122–131, 2014.
- [25] J. Fras, J. Czarnowski, M. Macias, J. Glowka, M. Cianchetti, and A. Menciassi, “New STIFF-FLOP module construction idea for improved actuation and sensing,” in *IEEE International Conference on Robotics and Automation (ICRA)*, pp. 2901–2906, 2015.
- [26] D. B. Camarillo, C. F. Milne, C. R. Carlson, M. R. Zinn, and J. K. Salisbury, “Mechanics modeling of tendon-driven continuum manipulators,” *IEEE Transactions on Robotics*, vol. 24, no. 6, pp. 1262–1273, 2008.

- [27] D. C. Rucker and R. J. Webster III, "Statics and dynamics of continuum robots with general tendon routing and external loading," *IEEE Transactions on Robotics*, vol. 27, no. 6, pp. 1033–1044, 2011.
- [28] T. Zheng, D. T. Branson, R. Kang, M. Cianchetti, E. Guglielmino, M. Follador, G. A. Medrano-Cerda, I. S. Godage, and D. G. Caldwell, "Dynamic continuum arm model for use with underwater robotic manipulators inspired by octopus vulgaris," in *Robotics and Automation (ICRA), 2012 IEEE International Conference on*, pp. 5289–5294, IEEE, 2012.
- [29] Y. Chen, K.-W. Kwok, and Z. T. H. Tse, "An MR-conditional high-torque pneumatic stepper motor for MRI-guided and robot-assisted intervention," *Annals of biomedical engineering*, vol. 42, no. 9, pp. 1823–1833, 2014.
- [30] M. I. S. Ibrahim, A. H. A. Alwi, A. Mohamad, and N. M. Lazim, "Dural metastasis of nasopharyngeal carcinoma: A case report," *Egyptian Journal of Ear, Nose, Throat and Allied Sciences*, vol. 18, no. 3, pp. 325–327, 2017.
- [31] K. Honda, R. Asato, J. Tsuji, T. Kanda, Y. Watanabe, Y. Mori, and T. Tsujimura, "Pyogenic spondylodiscitis after transoral surgery for oropharyngeal cancer," *Auris Nasus Larynx*, vol. 40, no. 3, pp. 320–322, 2013.
- [32] M. Kikuchi, S. Shinohara, Y. Nakamoto, Y. Usami, K. Fujiwara, T. Adachi, S.-y. Hori, Y. Tona, H. Yamazaki, Y. Imai, *et al.*, "Sequential fdg-pet/ct after neoadjuvant chemotherapy is a predictor of histopathologic response in patients with head and neck squamous cell carcinoma," *Molecular Imaging and Biology*, vol. 13, no. 2, pp. 368–377, 2011.
- [33] H. Su, W. Shang, G. Cole, G. Li, K. Harrington, A. Camilo, J. Tokuda, C. M. Tempny, N. Hata, and G. S. Fischer, "Piezoelectrically actuated robotic system for MRI-guided prostate percutaneous therapy," *IEEE/ASME Transactions on Mechatronics*, vol. 20, no. 4, pp. 1920–1932, 2015.
- [34] N. V. Navkar, Z. Deng, D. J. Shah, and N. V. Tsekos, "A framework for integrating real-time MRI with robot control: application to simulated transapical cardiac interventions," *IEEE Transactions on Biomedical Engineering*, vol. 60, no. 4, pp. 1023–1033, 2013.
- [35] W. Wang, C. L. Dumoulin, A. N. Viswanathan, Z. T. H. Tse, A. Mehrtash, W. Loew, I. Norton, J. Tokuda, R. T. Seethamraju, and T. Kapur, "Real-time active MR-tracking of metallic stylets in MR-guided radiation therapy," *Magnetic resonance in medicine*, vol. 73, no. 5, pp. 1803–1811, 2015.

- [36] C. L. Dumoulin and H. Hart Jr, "Magnetic resonance angiography.," *Radiology*, vol. 161, no. 3, pp. 717–720, 1986.
- [37] P. M. Black, T. Moriarty, E. Alexander, P. Stieg, E. J. Woodard, P. L. Gleason, C. H. Martin, R. Kikinis, R. B. Schwartz, and F. A. Jolesz, "Development and implementation of intraoperative magnetic resonance imaging and its neurosurgical applications," *Neurosurgery*, vol. 41, no. 4, pp. 831–845, 1997.
- [38] K. D. Blumberg, J. B. Catalano, J. M. Cotler, and R. A. Balderston, "The pullout strength of titanium alloy mri-compatible and stainless steel mri-incompatible gardner-wells tongs.," *Spine*, vol. 18, no. 13, pp. 1895–1896, 1993.
- [39] R. Gassert, E. Burdet, and K. Chinzei, "Mri-compatible robotics," *IEEE Engineering in Medicine and Biology Magazine*, vol. 27, no. 3, pp. 12–14, 2008.
- [40] D. Stoianovici, C. Kim, G. Srimathveeravalli, P. Sebrecht, D. Petrisor, J. Coleman, S. B. Solomon, and H. Hricak, "Mri-safe robot for endorectal prostate biopsy," *IEEE/ASME Transactions on Mechatronics*, vol. 19, no. 4, pp. 1289–1299, 2014.
- [41] S. Hao, A. Camilo, G. A. Cole, H. Nobuhiko, C. M. Tempany, and G. S. Fischer, "High-field mri-compatible needle placement robot for prostate interventions," *Studies in health technology and informatics*, vol. 163, p. 623, 2011.
- [42] G. S. Fischer, G. Cole, and H. Su, "Approaches to creating and controlling motion in mri," in *Engineering in Medicine and Biology Society, EMBC, 2011 Annual International Conference of the IEEE*, pp. 6687–6690, IEEE, 2011.
- [43] D. Stoianovici, "Multi-imager compatible actuation principles in surgical robotics," *The International Journal of Medical Robotics and Computer Assisted Surgery*, vol. 1, no. 2, pp. 86–100, 2005.
- [44] D. Beyersdorff, A. Winkel, B. Hamm, S. Lenk, S. A. Loening, and M. Taupitz, "Mr imaging-guided prostate biopsy with a closed mr unit at 1.5 t: initial results," *Radiology*, vol. 234, no. 2, pp. 576–581, 2005.
- [45] R. C. Susil, C. Ménard, A. Krieger, J. A. Coleman, K. Camphausen, P. Choyke, G. Fichtinger, L. L. Whitcomb, C. N. Coleman, and E. Atalar, "Transrectal prostate biopsy and fiducial marker placement in a standard 1.5 t magnetic resonance imaging scanner," *The Journal of urology*, vol. 175, no. 1, pp. 113–120, 2006.
- [46] J. Cepek, B. A. Chronik, U. Lindner, J. Trachtenberg, S. R. Davidson, J. Bax, and A. Fenster, "A system for mri-guided transperineal delivery of needles to the prostate for focal therapy," *Medical physics*, vol. 40, no. 1, 2013.

- [47] R. A. Vega, K. L. Holloway, and P. S. Larson, “Image-guided deep brain stimulation,” *Neurosurgery Clinics*, vol. 25, no. 1, pp. 159–172, 2014.
- [48] C. Nimsky, O. Ganslandt, P. Hastreiter, and R. Fahlbusch, “Intraoperative compensation for brain shift,” *Surgical neurology*, vol. 56, no. 6, pp. 357–364, 2001.
- [49] K. Chinzei, N. Hata, F. A. Jolesz, and R. Kikinis, “Mr compatible surgical assist robot: System integration and preliminary feasibility study,” in *International Conference on Medical Image Computing and Computer-Assisted Intervention*, pp. 921–930, Springer, 2000.
- [50] Y. Koseki, R. Kikinis, F. A. Jolesz, and K. Chinzei, “Precise evaluation of positioning repeatability of mr-compatible manipulator inside mri,” in *International Conference on Medical Image Computing and Computer-Assisted Intervention*, pp. 192–199, Springer, 2004.
- [51] D. F. Louw, T. Fielding, P. B. McBeth, D. Gregoris, P. Newhook, and G. R. Sutherland, “Surgical robotics: a review and neurosurgical prototype development,” *Neurosurgery*, vol. 54, no. 3, pp. 525–537, 2004.
- [52] J. W. Motkoski and G. R. Sutherland, “Why robots entered neurosurgery,” in *Experimental Neurosurgery in Animal Models*, pp. 85–105, Springer, 2016.
- [53] G. R. Sutherland, Y. Maddahi, L. S. Gan, S. Lama, and K. Zareinia, “Robotics in the neurosurgical treatment of glioma,” *Surgical neurology international*, vol. 6, no. Suppl 1, p. S1, 2015.
- [54] C. J. Nycz, R. Gondokaryono, P. Carvalho, N. Patel, M. Wartenberg, J. G. Pilitsis, and G. S. Fischer, “Mechanical validation of an mri compatible stereotactic neurosurgery robot in preparation for pre-clinical trials,” in *Intelligent Robots and Systems (IROS), 2017 IEEE/RSJ International Conference on*, pp. 1677–1684, IEEE, 2017.
- [55] M. Ho, Y. Kim, S. S. Cheng, R. Gullapalli, and J. P. Desai, “Design, development, and evaluation of an mri-guided sma spring-actuated neurosurgical robot,” *The International journal of robotics research*, vol. 34, no. 8, pp. 1147–1163, 2015.
- [56] Y. Kim, S. S. Cheng, M. Diakite, R. P. Gullapalli, J. M. Simard, and J. P. Desai, “Toward the development of a flexible mesoscale mri-compatible neurosurgical continuum robot,” *IEEE Transactions on Robotics*, vol. 33, no. 6, pp. 1386–1397, 2017.
- [57] S. S. Cheng, Y. Kim, and J. P. Desai, “New actuation mechanism for actively cooled sma springs in a neurosurgical robot,” *IEEE Trans. Robot.*, vol. 33, no. 4, pp. 986–993, 2017.

- [58] C. Raoufi, A. A. Goldenberg, and W. Kucharczyk, "Design and control of a novel hydraulically/pneumatically actuated robotic system for mri-guided neurosurgery," *Journal of Biomedical Science and Engineering*, vol. 1, no. 01, p. 68, 2008.
- [59] D. B. Comber, E. B. Pitt, H. B. Gilbert, M. W. Powelson, E. Matijevich, J. S. Neimat, R. J. Webster III, and E. J. Barth, "Optimization of curvilinear needle trajectories for transforaminal hippocampotomy," *Operative Neurosurgery*, vol. 13, no. 1, pp. 15–22, 2016.
- [60] R. L. Siegel, K. D. Miller, and A. Jemal, "Cancer statistics, 2017," *CA: a cancer journal for clinicians*, vol. 67, no. 1, pp. 7–30, 2017.
- [61] J. Naitoh, R. L. Zeiner, and J. B. Dekernion, "Diagnosis and treatment of prostate cancer.," *American family physician*, vol. 57, no. 7, pp. 1531–9, 1998.
- [62] K. K. Yu and H. Hricak, "Imaging prostate cancer.," *Radiologic Clinics of North America*, vol. 38, no. 1, pp. 59–85, 2000.
- [63] M. Norberg, L. Egevad, L. Holmberg, P. Sparen, B. Norlen, and C. Busch, "The sextant protocol for ultrasound-guided core biopsies of the prostate underestimates the presence of cancer," *Urology*, vol. 50, no. 4, pp. 562–566, 1997.
- [64] M. K. Terris, "Sensitivity and specificity of sextant biopsies in the detection of prostate cancer: preliminary report," *Urology*, vol. 54, no. 3, pp. 486–489, 1999.
- [65] A. Krieger, R. C. Susil, C. Ménard, J. A. Coleman, G. Fichtinger, E. Atalar, and L. L. Whitcomb, "Design of a novel mri compatible manipulator for image guided prostate interventions," *IEEE TRANSACTIONS ON BIOMEDICAL ENGINEERING*, vol. 52, no. 2, 2005.
- [66] D. Stoianovici, C. Kim, D. Petrisor, C. Jun, S. Lim, M. W. Ball, A. Ross, K. J. Macura, and M. E. Allaf, "Mr safe robot, fda clearance, safety and feasibility of prostate biopsy clinical trial," *IEEE/ASME Transactions on Mechatronics*, vol. 22, no. 1, pp. 115–126, 2017.
- [67] M. R. Van den Bosch, M. R. Moman, M. Van Vulpen, J. J. Battermann, E. Duiveman, L. J. van Schelven, H. de Leeuw, J. J. Lagendijk, and M. A. Moerland, "Mri-guided robotic system for transperineal prostate interventions: proof of principle," *Physics in Medicine & Biology*, vol. 55, no. 5, p. N133, 2010.
- [68] D. Yakar, M. G. Schouten, D. G. Bosboom, J. O. Barentsz, T. W. Scheenen, and J. J. Fütterer, "Feasibility of a pneumatically actuated mr-compatible robot for transrectal prostate biopsy guidance," *Radiology*, vol. 260, no. 1, pp. 241–247, 2011.

- [69] S. Zangos, A. Melzer, K. Eichler, C. Sadighi, A. Thalhammer, B. Bodelle, R. Wolf, T. Gruber-Rouh, D. Proschek, R. Hammerstingl, *et al.*, “Mr-compatible assistance system for biopsy in a high-field-strength system: initial results in patients with suspicious prostate lesions,” *Radiology*, vol. 259, no. 3, pp. 903–910, 2011.
- [70] H. Su, W. Shang, G. Cole, G. Li, K. Harrington, A. Camilo, J. Tokuda, C. M. Tempany, N. Hata, and G. S. Fischer, “Piezoelectrically actuated robotic system for mri-guided prostate percutaneous therapy,” *IEEE/ASME Transactions on Mechatronics*, vol. 20, no. 4, pp. 1920–1932, 2015.
- [71] J. Ferlay, I. Soerjomataram, M. Ervik, R. Dikshit, S. Eser, C. Mathers, M. Rebelo, D. Parkin, D. Forman, and F. Bray, “Globocan 2012 v1. 0, cancer incidence and mortality worldwide: Iarc cancerbase no. 11. lyon, france: International agency for research on cancer; 2013,” 2015.
- [72] W. Kaiser and E. Zeitler, “Mr imaging of the breast: fast imaging sequences with and without gd-dtpa. preliminary observations.,” *Radiology*, vol. 170, no. 3, pp. 681–686, 1989.
- [73] E. R. Price, “Magnetic resonance imaging-guided biopsy of the breast: Fundamentals and finer points,” *Magnetic Resonance Imaging Clinics*, vol. 21, no. 3, pp. 571–581, 2013.
- [74] M.-C. Chevrier, J. David, M. El Khoury, L. Lalonde, M. Labelle, and I. Trop, “Breast biopsies under magnetic resonance imaging guidance: challenges of an essential but imperfect technique,” *Current problems in diagnostic radiology*, vol. 45, no. 3, pp. 193–204, 2016.
- [75] W. A. Kaiser, H. Fischer, J. Vagner, and M. Selig, “Robotic system for biopsy and therapy of breast lesions in a high-field whole-body magnetic resonance tomography unit,” *Investigative Radiology*, vol. 35, no. 8, pp. 513–519, 2000.
- [76] S. O. Pfeleiderer, C. Marx, J. Vagner, R.-P. Franke, J. R. Reichenbach, and W. A. Kaiser, “Magnetic resonance-guided large-core breast biopsy inside a 1.5-t magnetic resonance scanner using an automatic system: in vitro experiments and preliminary clinical experience in four patients,” *Investigative radiology*, vol. 40, no. 7, pp. 458–463, 2005.
- [77] R. Kokes, K. Lister, R. Gullapalli, B. Zhang, A. MacMillan, H. Richard, and J. P. Desai, “Towards a teleoperated needle driver robot with haptic feedback for rfa of breast tumors under continuous mri,” *Medical image analysis*, vol. 13, no. 3, pp. 445–455, 2009.

- [78] V. Groenhuis, F. J. Siepel, J. Veltman, J. K. van Zandwijk, and S. Stramigioli, “Stormram 4: An mr safe robotic system for breast biopsy,” *Annals of biomedical engineering*, pp. 1–11, 2018.
- [79] J. P. Thirion, “Image matching as a diffusion process: an analogy with Maxwell’s demons,” *Medical Image Analysis*, vol. 2, no. 3, pp. 243–260, 1998.
- [80] K. W. Kwok, G. C. T. Chow, T. C. P. Chau, Y. Chen, S. H. Zhang, W. Luk, E. J. Schmidt, and Z. Tse, “FPGA-based acceleration of MRI registration: an enabling technique for improving MRI-guided cardiac therapy,” *Journal of Cardiovascular Magnetic Resonance*, vol. 16(Suppl 1):W11, 2014.
- [81] D. Trivedi, C. D. Rahn, W. M. Kier, and I. D. Walker, “Soft robotics: Biological inspiration, state of the art, and future research,” *Applied Bionics and Biomechanics*, vol. 5, no. 3, pp. 99–117, 2008.
- [82] S. Mao, E. Dong, H. Jin, M. Xu, S. Zhang, J. Yang, and K. H. Low, “Gait study and pattern generation of a starfish-like soft robot with flexible rays actuated by SMAs,” *Journal of Bionic Engineering*, vol. 11, no. 3, pp. 400–411, 2014.
- [83] S. Sareh, A. Jiang, A. Faragasso, Y. Noh, T. Nanayakkara, P. Dasgupta, L. D. Seneviratne, H. A. Wurdemann, and K. Althoefer, “Bio-inspired tactile sensor sleeve for surgical soft manipulators,” in *IEEE International Conference on Robotics and Automation (ICRA)*, pp. 1454–1459, 2014.
- [84] L. Wang and F. Iida, “Deformation in soft-matter robotics,” *IEEE Robotics and Automation Magazine*, vol. 22, no. 3, pp. 125–139, 2015.
- [85] W. McMahan, V. Chitrakaran, M. Csencsits, D. Dawson, I. D. Walker, B. A. Jones, M. Pritts, D. Dienno, M. Grissom, and C. D. Rahn, “Field trials and testing of the OctArm continuum manipulator,” in *IEEE International Conference on Robotics and Automation (ICRA)*, pp. 2336–2341, 2006.
- [86] G. Runge, T. Preller, S. Zellmer, S. Blankemeyer, M. Kreuz, G. Garnweitner, and A. Raatz, “SpineMan: Design of a soft robotic spine-like manipulator for safe human-robot interaction,” in *IEEE/RSJ International Conference on Intelligent Robots and Systems (IROS)*, pp. 1103–1110, IEEE, 2015.
- [87] F. Maghooa, A. Stilli, Y. Noh, K. Althoefer, and H. A. Wurdemann, “Tendon and pressure actuation for a bio-inspired manipulator based on an antagonistic principle,” in *IEEE International Conference on Robotics and Automation (ICRA)*, pp. 2556–2561, IEEE, 2015.

- [88] V. Lohsiriwat, "Colonoscopic perforation: Incidence, risk factors, management and outcome," *World Journal of Gastroenterology*, vol. 16, no. 4, p. 425, 2010.
- [89] E. Tumino, R. Sacco, M. Bertini, M. Bertoni, G. Parisi, and A. Capria, "Endotics system vs colonoscopy for the detection of polyps," *World J Gastroenterol*, vol. 16, no. 43, pp. 5452–5456, 2010.
- [90] F. Cosentino, E. Tumino, G. R. Passoni, E. Morandi, and A. Capria, "Functional evaluation of the endotics system, a new disposable self-propelled robotic colonoscope: in vitro tests and clinical trial," *The International journal of artificial organs*, vol. 32, no. 8, pp. 517–527, 2009.
- [91] J. Pfeffer, R. Grinshpon, D. Rex, B. Levin, T. Rösch, N. Arber, and Z. Halpern, "The Aer-O-Scope: proof of the concept of a pneumatic, skill-independent, self-propelling, self-navigating colonoscope in a pig model," *Endoscopy*, vol. 38, no. 02, pp. 144–148, 2006.
- [92] B. Jones and I. D. Walker, "Kinematics for multisection continuum robots," *IEEE Transactions on Robotics*, vol. 22, no. 1, pp. 43–55, 2006.
- [93] M. Mahvash and P. E. Dupont, "Stiffness control of surgical continuum manipulators," *IEEE Transactions on Robotics*, vol. 27, no. 2, pp. 334–345, 2011.
- [94] R. J. Webster III and B. A. Jones, "Design and kinematic modeling of constant curvature continuum robots: A review," *The International Journal of Robotics Research*, 2010.
- [95] Y. Ganji and F. Janabi-Sharifi, "Catheter kinematics for intracardiac navigation," *IEEE Transactions on Biomedical Engineering*, vol. 56, no. 3, pp. 621–632, 2009.
- [96] B. A. Jones and I. D. Walker, "A new approach to Jacobian formulation for a class of multi-section continuum robots," in *IEEE International Conference on Robotics and Automation (ICRA)*, pp. 3268–3273, 2005.
- [97] R. J. Webster III, J. P. Swensen, J. M. Romano, and N. J. Cowan, "Closed-form differential kinematics for concentric-tube continuum robots with application to visual servoing," *Experimental Robotics: The Eleventh International Symposium*, pp. 485–494, 2009.
- [98] S. Neppalli, M. A. Csencsits, B. A. Jones, and I. D. Walker, "Closed-form inverse kinematics for continuum manipulators," *Advanced Robotics*, vol. 23, no. 15, pp. 2077–2091, 2009.



- [99] A. D. Marchese, K. Komorowski, C. D. Onal, and D. Rus, “Design and control of a soft and continuously deformable 2d robotic manipulation system,” in *IEEE International Conference on Robotics and Automation (ICRA)*, pp. 2189–2196, 2014.
- [100] A. D. Marchese, R. Tedrake, and D. Rus, “Dynamics and trajectory optimization for a soft spatial fluidic elastomer manipulator,” *The International Journal of Robotics Research*, vol. 35, no. 8, pp. 1000–1019, 2016.
- [101] H. Wang, W. Chen, X. Yu, T. Deng, X. Wang, and R. Pfeifer, “Visual servo control of cable-driven soft robotic manipulator,” in *IEEE/RSJ International Conference on Intelligent Robots and Systems (IROS)*, pp. 57–62, 2013.
- [102] G. S. Chirikjian, “Hyper-redundant manipulator dynamics: A continuum approximation,” *J. Adv. Robot.*, vol. 9, no. 3, pp. 217–243, 1995.
- [103] R. Kang, D. T. Branson, T. Zheng, E. Guglielmino, and D. G. Caldwell, “Design, modeling and control of a pneumatically actuated manipulator inspired by biological continuum structures,” *Bioinspiration and Biomimetics*, vol. 8, p. 36008, 2013.
- [104] Y. Yekutieli, R. Sagiv-Zohar, R. Aharonov, Y. Engel, B. Hochner, and T. Flash, “Dynamic model of the octopus arm. I. biomechanics of the octopus reaching movement,” *J. Neurophysiol.*, vol. 94, no. 2, pp. 1443–1458, 2005.
- [105] M. Giorelli, F. Renda, M. Calisti, A. Arienti, G. Ferri, and C. Laschi, “A two dimensional inverse kinetics model of a cable driven manipulator inspired by the octopus arm,” in *IEEE International Conference on Robotics and Automation (ICRA)*, pp. 3819–3824, 2012.
- [106] F. Renda, M. Giorelli, M. Calisti, M. Cianchetti, and C. Laschi, “Dynamic model of a multibending soft robot arm driven by cables,” *IEEE Transactions on Robotics*, vol. 30, no. 5, pp. 1109–1122, 2014.
- [107] D. Nguyen-Tuong and J. Peters, “Model learning for robot control: a survey,” *Cognitive processing*, vol. 12, no. 4, pp. 319–340, 2011.
- [108] D. Braganza, D. M. Dawson, I. D. Walker, and N. Nath, “A neural network controller for continuum robots,” *IEEE Transactions on Robotics*, vol. 23, no. 6, pp. 1270–1277, 2007.
- [109] M. Giorelli, F. Renda, M. Calisti, A. Arienti, G. Ferri, and C. Laschi, “Neural Network and Jacobian Method for Solving the Inverse Statics of a Cable-Driven Soft Arm With Nonconstant Curvature,” *IEEE Transactions on Robotics*, vol. 31, no. 4, pp. 823–834, 2015.

- [110] M. C. Yip and D. B. Camarillo, “Model-less feedback control of continuum manipulators in unknown environments,” *IEEE Transactions on Robotics*, vol. 30, no. 4, pp. 880–889, 2014.
- [111] P. Muyan-Ozcelik, J. D. Owens, J. Xia, and S. S. Samant, “Fast deformable registration on the GPU: A CUDA implementation of demons,” in *International Conference on Computational Sciences and Its Applications (ICCSA)*, pp. 223–233, IEEE, 2008.
- [112] T. Vercauteren, X. Pennec, A. Perchant, and N. Ayache, “Diffeomorphic demons: Efficient non-parametric image registration,” *Neuroimage*, vol. 45, no. 1, pp. S61–S72, 2009.
- [113] S. J. Harris, M. Jakopec, R. D. Hibberd, J. Cobb, and B. L. Davies, “Interactive pre-operative selection of cutting constraints, and interactive force controlled knee surgery by a surgical robot,” in *International Conference on Medical Image Computing and Computer-Assisted Intervention*, pp. 996–1006, Springer, 1998.
- [114] K. W. Kwok, K. H. Tsoi, V. Vitiello, J. Clark, G. C. T. Chow, W. Luk, and G. Z. Yang, “Dimensionality Reduction in Controlling Articulated Snake Robot for Endoscopy Under Dynamic Active Constraints,” *IEEE Transactions on Robotics*, vol. 29, no. 1, pp. 15–31, 2013.
- [115] K. Cleary and T. M. Peters, “Image-Guided Interventions: Technology Review and Clinical Applications,” *Annual Review of Biomedical Engineering*, vol. 12, no. 1, pp. 119–142, 2010.
- [116] G. Xuejun, P. Hubert, L. Yun, C. Richard, Y. Deshan, C. Dongju, C. Edward, M. Amitava, G. Thomas, and B. J. Steve, “Implementation and evaluation of various demons deformable image registration algorithms on a GPU,” *Physics in Medicine and Biology*, vol. 55, no. 1, p. 207, 2010.
- [117] V. Narasiman, M. Shebanow, C. J. Lee, R. Miftakhutdinov, O. Mutlu, and Y. N. Patt, “Improving gpu performance via large warps and two-level warp scheduling,” in *Proceedings of the 44th Annual IEEE/ACM International Symposium on Microarchitecture*, pp. 308–317, ACM, 2011.
- [118] J. C. Thibault and I. Senocak, “Accelerating incompressible flow computations with a pthreads-cuda implementation on small-footprint multi-gpu platforms,” *The Journal of Supercomputing*, vol. 59, no. 2, pp. 693–719, 2012.

- [119] N. Chakraborty, J. Peng, S. Akella, and J. Mitchell, "Proximity Queries between Convex Objects: An Interior Point Approach for Implicit Surfaces," in *IEEE International Conference on Robotics and Automation*, pp. 1910–1916.
- [120] J. Pan, L. Zhang, and D. Manocha, "Collision-free and Smooth Trajectory Computation in Cluttered Environments," *International Journal of Robotics Research*, vol. 31, no. 10, pp. 1155–1175, 2012.
- [121] M. Li and R. H. Taylor, "Spatial motion constraints in medical robot using virtual fixtures generated by anatomy," in *IEEE International Conference on Robotics and Automation*, vol. 2, pp. 1270–1275.
- [122] M. Li, M. Ishii, and R. H. Taylor, "Spatial motion constraints using virtual fixtures generated by anatomy," *IEEE Trans. on Robotics*, vol. 23, no. 1, pp. 4–19, 2007.
- [123] B. Davies, M. Jakopc, S. J. Harris, F. R. Y. Baena, A. Barrett, A. Evangelidis, P. Gomes, J. Henckel, and J. Cobb, "Active-constraint robotics for surgery," *Proceedings of the IEEE*, vol. 94, no. 9, pp. 1696–1704, 2006.
- [124] K. W. Kwok, V. Vitiello, and G. Z. Yang, "Control of Articulated Snake Robot under Dynamic Active Constraints," *Medical Image Computing and Computer-Assisted Intervention - Miccai 2010, Pt Iii*, vol. 6363, pp. 229–236, 2010.
- [125] X. Zhang and Y. J. Kim, "Interactive Collision Detection for Deformable Models Using Streaming AABBs," *IEEE Trans. on Visualization and Computer Graphics*, vol. 13, no. 2, pp. 318–329, 2007.
- [126] G. C. T. Chow, K. W. Kwok, W. Luk, and P. Leong, "Mixed Precision Comparison in Reconfigurable Systems," in *IEEE International Symposium on Field-Programmable Custom Computing Machines*, pp. 17–24.
- [127] A. Escande, S. Miossec, and A. Kheddar, "Continuous gradient proximity distance for humanoids free-collision optimized-postures," in *IEEE-RAS International Conference on Humanoid Robots*, pp. 188–195.
- [128] C. L. Bajaj and T. K. Dey, "Convex Decomposition of Polyhedra and Robustness," *SIAM Journal on Computing*, vol. 21, no. 2, pp. 339–364, 1992.
- [129] M. C. Lin and J. F. Canny, "A fast algorithm for incremental distance calculation," in *IEEE International Conference on Robotics and Automation*, pp. 1008–1014.
- [130] J. F. Canny and M. C. Lin, "An opportunistic global path planner," in *IEEE International Conference on Robotics and Automation*, vol. 3, pp. 1554–1559.

- [131] B. Mirtich, "V-Clip: Fast and robust polyhedral collision detection," *ACM Trans. on Graphics*, vol. 17, no. 3, pp. 177–208, 1998.
- [132] E. Gilert, D. Johnson, and S. S. Keerthi, "A fast procedure for computing the distance between complex objects in three dimensional space," *IEEE Journal of Robotics and Automation*, vol. 4, no. 2, pp. 193–203, 1988.
- [133] S. Cameron, "A Comparison of Two Fast Algorithms for Computing the Distance between Convex Polyhedra," *IEEE Trans. on Robotics*, vol. 13, no. 6, pp. 915–920, 1997.
- [134] N. Chakraborty, J. Peng, S. Akella, and J. E. Mitchell, "Proximity Queries Between Convex Objects: An Interior Point Approach for Implicit Surfaces," *IEEE Trans. on Robotics*, vol. 24, no. 1, pp. 211–220, 2008.
- [135] R. H. Byrd, M. E. Hribar, and J. Nocedal, "An Interior Point Algorithm for Large Scale Nonlinear Programming," *SIAM Journal on Optimization*, vol. 9, no. 4, pp. 35–59, 1999.
- [136] T. C. P. Chau, K. W. Kwok, G. C. T. Chow, K. H. Tsoi, K. H. Lee, Z. Tse, P. Y. K. Cheung, and W. Luk, "Acceleration of real-time Proximity Query for dynamic active constraints," in *Field-Programmable Technology (FPT), 2013 International Conference on*, pp. 206–213.
- [137] K. W. Kwok, G. P. Mylonas, L. W. Sun, M. Lerotic, J. Clark, T. Athanasiou, A. Darzi, and G. Z. Yang, "Dynamic Active Constraints for Hyper-Redundant Flexible Robots," *Medical Image Computing and Computer-Assisted Intervention - Miccai 2009, Pt I, Proceedings*, vol. 5761, pp. 410–417, 2009.
- [138] S. Ilic and P. Fua, "Implicit meshes for surface reconstruction," *IEEE Trans on Pattern Analysis and Machine Intelligence*, vol. 28, no. 2, pp. 328–333, 2006.
- [139] D. Eberly, "Intersection of cylinders," 2010.
- [140] C. Fares and Y. Hamam, "Collision detection for rigid bodies: A state of the art review," *GraphiCon 2005*, 2005.
- [141] Y. Chen, K. W. Kwok, J. Ge, Y. Hu, M. Fok, K. R. Nilsson, and Z. T. H. Tse, "Augmented Reality for Improving Catheterization in MRI-guided Cardiac Electrophysiology," *Journal of Medical Devices - Transactions of the ASME*, vol. 8, no. 2, p. 20917, 2014.
- [142] Y. Chen, J. Ge, K. W. Kwok, K. R. Nilsson, F. Fok, and Z. Tse, "MRI-conditional catheter sensor for contact force and temperature monitoring during cardiac

- electrophysiological procedures,” *Journal of Cardiovascular Magnetic Resonance*, vol. 16(Suppl 1):P150, 2014.
- [143] K. W. Kwok, K. H. Lee, Y. Chen, W. Wang, Y. Hu, G. C. T. Chow, S. H. Zhang, W. G. Stevenson, R. Y. Kwong, W. Luk, E. J. Schmidt, and Z. T. H. Tse, “Interfacing Fast Multi-phase Cardiac Image Registration with MRI-based Catheter Tracking for MRI-guided Electrophysiological Ablative Procedures,” *Circulation*, vol. 130, A18568, 2014.
- [144] K. W. Kwok, Y. Chen, T. C. P. Chau, W. Luk, K. Nilsson, E. J. Schmidt, and Z. Tse, “MRI-based visual and haptic catheter feedback: simulating a novel system’s contribution to efficient and safe MRI-guided cardiac electrophysiology procedures,” *Journal of Cardiovascular Magnetic Resonance*, vol. 16, no. Suppl 1, p. O50, 2014.
- [145] G. P. Mylonas, K.-W. Kwok, D. R. James, D. Leff, F. Orihuela-Espina, A. Darzi, and G.-Z. Yang, “Gaze-contingent motor channelling, haptic constraints and associated cognitive demand for robotic mis,” *Medical image analysis*, vol. 16, no. 3, pp. 612–631, 2012.
- [146] R. I. Hartley and P. Sturm, “Triangulation,” *Computer vision and image understanding*, vol. 68, no. 2, pp. 146–157, 1997.
- [147] K. H. Lee and W. S. Newman, “Natural admittance control of an electro-hydraulic humanoid robot,” in *IEEE International Conference on Robotics and Biomimetics (ROBIO)*, pp. 1100–1105, IEEE, 2014.
- [148] F. Morady, “Radio-frequency ablation as treatment for cardiac arrhythmias,” *New England Journal of Medicine*, vol. 340, no. 7, pp. 534–544, 1999.
- [149] M. Haïssaguerre, P. Jaïs, D. C. Shah, A. Takahashi, M. Hocini, G. Quiniou, S. Garrigue, A. Le Mouroux, P. Le Métayer, and J. Clémenty, “Spontaneous Initiation of Atrial Fibrillation by Ectopic Beats Originating in the Pulmonary Veins,” *New England Journal of Medicine*, vol. 339, no. 10, pp. 659–666, 1998.
- [150] E. J. Schmidt, R. P. Mallozzi, A. Thiagalingam, G. Holmvang, A. D’Avila, R. Guhde, R. R. Darrow, G. Slavin, M. Fung, and J. Dando, “Electro-Anatomical Mapping and Radio-Frequency Ablation of Porcine Left Atria and Atrio-Ventricular Nodes using Magnetic Resonance Catheter Tracking,” *Circulation: Arrhythmia and Electrophysiology*, p. CIRCEP. 109.882472, 2009.
- [151] R. Razavi, D. L. G. Hill, S. F. Keevil, M. E. Miquel, V. Muthurangu, S. Hegde, K. Rhode, M. Barnett, J. van Vaals, and D. J. Hawkes, “Cardiac catheterisation

- guided by MRI in children and adults with congenital heart disease,” *The Lancet*, vol. 362, no. 9399, pp. 1877–1882, 2003.
- [152] R. C. Susil, C. J. Yeung, H. R. Halperin, A. C. Lardo, and E. Atalar, “Multifunctional interventional devices for MRI: a combined electrophysiology/MRI catheter,” *Magnetic resonance in medicine*, vol. 47, no. 3, pp. 594–600, 2002.
- [153] S. R. Dukkipati, R. Mallozzi, E. J. Schmidt, G. Holmvang, A. D’Avila, R. Guhde, R. D. Darrow, G. Slavin, M. Fung, and Z. Malchano, “Electroanatomic mapping of the left ventricle in a porcine model of chronic myocardial infarction with magnetic resonance-based catheter tracking,” *Circulation*, vol. 118, no. 8, pp. 853–862, 2008.
- [154] A. N. Raval, P. V. Karmarkar, M. A. Guttman, C. Ozturk, R. DeSilva, R. J. Aviles, V. J. Wright, W. H. Schenke, E. Atalar, and E. R. McVeigh, “Real-time MRI guided atrial septal puncture and balloon septostomy in swine,” *Catheterization and cardiovascular interventions*, vol. 67, no. 4, pp. 637–643, 2006.
- [155] D. Stoianovici, A. Patriciu, D. Petrisor, D. Mazilu, and L. Kavoussi, “A new type of motor: Pneumatic step motor,” *IEEE/ASME Transactions on Mechatronics*, vol. 12, no. 1, pp. 98–106, 2007.
- [156] Z. Guo, T. Lun, Y. Chen, H. Su, D. Chan, and K. Kwok, “Novel design of an MR-safe pneumatic stepper motor for MRI-guided robotic interventions,” in *Proceedings of The Hamlyn Symposium on Medical Robotics*, p. 50, 2016.
- [157] D. Stoianovici, C. Jun, S. Lim, P. Li, D. Petrisor, S. Fricke, K. Sharma, and K. Cleary, “Multi-Imager Compatible, MR Safe, Remote Center of Motion Needle-Guide Robot,” *IEEE Transactions on Biomedical Engineering*, 2017.
- [158] J. P. Whitney, M. F. Glisson, E. L. Brockmeyer, and J. K. Hodgins, “A low-friction passive fluid transmission and fluid-tendon soft actuator,” in *IEEE/RSJ International Conference on Intelligent Robots and Systems*, pp. 2801–2808, IEEE, 2014.
- [159] G. Ganesh, R. Gassert, E. Burdet, and H. Bleuler, “Dynamics and control of an MRI compatible master-slave system with hydrostatic transmission,” in *IEEE International Conference on Robotics and Automation*, vol. 2, pp. 1288–1294, IEEE, 2004.
- [160] W. C. ASTM International PA, “ASTM F2503-13, Standard Practice for Marking Medical Devices and Other Items for Safety in the Magnetic Resonance Environment, ASTM International, West Conshohocken, PA.”

- [161] K. Chinzei, R. Kikinis, and F. A. Jolesz, “MR compatibility of mechatronic devices: design criteria,” in *International Conference on Medical Image Computing and Computer-Assisted Intervention*, pp. 1020–1030, Springer, 1999.
- [162] H. Oral, C. Scharf, A. Chugh, B. Hall, P. Cheung, E. Good, S. Veerareddy, F. Pelosi, and F. Morady, “Catheter ablation for paroxysmal atrial fibrillation,” *Circulation*, vol. 108, no. 19, pp. 2355–2360, 2003.
- [163] Y. Feng, Z. Guo, Z. Dong, X.-Y. Zhou, K.-W. Kwok, S. Ernst, and S.-L. Lee, “An efficient cardiac mapping strategy for radiofrequency catheter ablation with active learning,” *International Journal of Computer Assisted Radiology and Surgery*, vol. 12, no. 7, pp. 1199–1207, 2017.
- [164] Y. Chen, K.-W. Kwok, J. Ge, Y. Hu, M. Fok, K. Ronald Nilsson, and Z. T. Ho Tse, “Augmented Reality for Improving Catheterization in Magnetic Resonance Imaging-Guided Cardiac Electrophysiology Therapy1,” *Journal of Medical Devices*, vol. 8, no. 2, pp. 20912–20917, 2014.
- [165] C. L. Cheung, K. H. Lee, Z. Guo, Z. Dong, C. W. M. Leong, A. P. W. Lee, K. W. Kwok, and Y. Chen, “Kinematic-model-free positional control for robot-assisted cardiac catheterization,” in *Proceedings of The Hamlyn Symposium on Medical Robotics*, p. 80, 2016.
- [166] Y. Ganji and F. Janabi-Sharifi, “Kinematic characterization of a cardiac ablation catheter,” in *Intelligent Robots and Systems, 2007. IROS 2007. IEEE/RSJ International Conference on*, pp. 1876–1881, IEEE, 2007.
- [167] T. Liu and M. C. Çavuşoğlu, “Three dimensional modeling of an mri actuated steerable catheter system,” in *Robotics and Automation (ICRA), 2014 IEEE International Conference on*, pp. 4393–4398, IEEE, 2014.
- [168] T. Greigarn and M. C. Cavusoglu, “Task-space motion planning of MRI-actuated catheters for catheter ablation of atrial fibrillation,” in *IEEE/RSJ International Conference on Intelligent Robots and Systems (IROS)*, pp. 3476–3482, IEEE, 2014.
- [169] J. Back, L. Lindenroth, K. Rhode, and H. Liu, “Model-free position control for cardiac ablation catheter steering using electromagnetic position tracking and tension feedback,” *Frontiers in Robotics and AI*, vol. 4, p. 17, 2017.
- [170] M. C. Yip and D. B. Camarillo, “Model-less hybrid position/force control: A minimalist approach for continuum manipulators in unknown, constrained environments.,” *IEEE Robotics and Automation Letters*, vol. 1, no. 2, pp. 844–851, 2016.

- [171] M. Kern, *The Cardiac Catheterization Handbook*. Mosby, 2003.
- [172] W. Wang, C. L. Dumoulin, A. N. Viswanathan, Z. T. Tse, A. Mehrtash, W. Loew, I. Norton, J. Tokuda, R. T. Seethamraju, T. Kapur, *et al.*, “Real-time active mr-tracking of metallic stylets in mr-guided radiation therapy,” *Magnetic resonance in medicine*, vol. 73, no. 5, pp. 1803–1811, 2015.
- [173] R. Hoyle, *Statistical strategies for small sample research*. Sage Publications, 1999.
- [174] S. Patil, O. Bieri, P. Jhooti, and K. Scheffler, “Automatic slice positioning (ASP) for passive real-time tracking of interventional devices using projection-reconstruction imaging with echo-dephasing (PRIDE),” *Magnetic resonance in medicine*, vol. 62, no. 4, pp. 935–942, 2009.
- [175] J. L. Duerk, E. Y. Wong, and J. S. Lewin, “A brief review of hardware for catheter tracking in magnetic resonance imaging,” *Magnetic Resonance Materials in Physics, Biology and Medicine*, vol. 13, no. 3, p. 199, 2002.
- [176] A. Glowinski, G. Adam, A. Bücke, J. Neuerburg, J. J. van Vaals, and R. W. Günther, “Catheter visualization using locally induced, actively controlled field inhomogeneities,” *Magnetic resonance in medicine*, vol. 38, no. 2, pp. 253–258, 1997.
- [177] M. K. Konings, L. W. Bartels, H. F. Smits, and C. J. Bakker, “Heating around intravascular guidewires by resonating rf waves,” *Journal of Magnetic Resonance Imaging*, vol. 12, no. 1, pp. 79–85, 2000.
- [178] S. Weiss, T. Kuehne, F. Brinkert, G. Krombach, M. Katoh, T. Schaeffter, R. W. Guenther, and A. Buecker, “In vivo safe catheter visualization and slice tracking using an optically detunable resonant marker,” *Magnetic resonance in medicine*, vol. 52, no. 4, pp. 860–868, 2004.
- [179] F. Galassi, D. Brujic, M. Rea, N. Lambert, N. Desouza, and M. Ristic, “Fast and accurate localization of multiple rf markers for tracking in mri-guided interventions,” *Magnetic Resonance Materials in Physics, Biology and Medicine*, vol. 28, no. 1, pp. 33–48, 2015.
- [180] W. Atabany and P. Degenaar, “A Spatiotemporal Parallel Image Processing on FPGA for Augmented Vision System,” in *Advances in Computer and Information Sciences and Engineering*, pp. 558–561, Springer, 2008.
- [181] Z. Guo, Z. Dong, K.-H. Lee, D. K. C. Fu, and K.-W. Kwok, “Robotic Catheter System for MRI-guided Cardiovascular Interventions,” 2016.



- [182] K. Suzumori, "Elastic materials producing compliant robots," *Robotics and Autonomous systems*, vol. 18, no. 1-2, pp. 135–140, 1996.
- [183] H. Tsukagoshi, A. Kitagawa, and M. Segawa, "Active hose: An artificial elephant's nose with maneuverability for rescue operation," in *Robotics and Automation, 2001. Proceedings 2001 ICRA. IEEE International Conference on*, vol. 3, pp. 2454–2459, IEEE, 2001.
- [184] T. Vos, R. M. Barber, B. Bell, A. Bertozzi-Villa, S. Biryukov, I. Bolliger, F. Charlson, A. Davis, L. Degenhardt, D. Dicker, *et al.*, "Global, regional, and national incidence, prevalence, and years lived with disability for 301 acute and chronic diseases and injuries in 188 countries, 1990–2013: a systematic analysis for the global burden of disease study 2013," *The Lancet*, vol. 386, no. 9995, pp. 743–800, 2015.
- [185] H.-H. Liu, L.-J. Li, B. Shi, C.-W. Xu, and E. Luo, "Robotic surgical systems in maxillofacial surgery: a review," *International journal of oral science*, vol. 9, no. 2, p. 63, 2017.
- [186] J. Attra and N. Kokot, "Transoral robotic surgery and lasers," in *Biomedical Optics in Otorhinolaryngology*, pp. 183–201, Springer, 2016.
- [187] C. Arens, "Transoral treatment strategies for head and neck tumors," *GMS current topics in otorhinolaryngology, head and neck surgery*, vol. 11, 2012.
- [188] M. K. Bhayani, "A shifting paradigm for patients with head and neck cancer: transoral robotic surgery (tORS)," *the surgeon*, vol. 2, pp. 4–5, 2010.
- [189] D. G. Grant, M. L. Hinni, J. R. Salassa, W. C. Perry, R. E. Hayden, and J. D. Casler, "Oropharyngeal cancer: a case for single modality treatment with transoral laser microsurgery," *Archives of Otolaryngology–Head & Neck Surgery*, vol. 135, no. 12, pp. 1225–1230, 2009.
- [190] W. Steiner, O. Fierek, P. Ambrosch, C. P. Hommerich, and M. Kron, "Transoral laser microsurgery for squamous cell carcinoma of the base of the tongue," *Archives of Otolaryngology–Head & Neck Surgery*, vol. 129, no. 1, pp. 36–43, 2003.
- [191] J. A. Burns, J. B. Kobler, J. T. Heaton, G. Lopez-Guerra, R. R. Anderson, and S. M. Zeitels, "Thermal damage during thulium laser dissection of laryngeal soft tissue is reduced with air cooling: ex vivo calf model study," *Annals of Otolaryngology, Rhinology & Laryngology*, vol. 116, no. 11, pp. 853–857, 2007.
- [192] S. M. Zeitels, J. A. Burns, L. M. Akst, R. E. Hillman, M. S. Broadhurst, and R. R. Anderson, "Office-based and microlaryngeal applications of a fiber-based thulium

- laser,” *Annals of Otolaryngology, Rhinology & Laryngology*, vol. 115, no. 12, pp. 891–896, 2006.
- [193] S. Ayari-Khalfallah, C. Fuchsmann, and P. Froehlich, “Thulium laser in airway diseases in children,” *Current opinion in otolaryngology & head and neck surgery*, vol. 16, no. 1, pp. 55–59, 2008.
- [194] E. Passacantilli, M. Antonelli, A. D’Amico, C. P. Delfinis, G. Anichini, J. Lenzi, and A. Santoro, “Neurosurgical applications of the 2- $\mu$ m thulium laser: histological evaluation of meningiomas in comparison to bipolar forceps and an ultrasonic aspirator,” *Photomedicine and laser surgery*, vol. 30, no. 5, pp. 286–292, 2012.
- [195] J. D. Richmon, “Transoral palate-sparing nasopharyngectomy with the flex ® system: Preclinical study,” *The Laryngoscope*, vol. 125, no. 2, pp. 318–322, 2015.
- [196] K. M. Van Abel, E. J. Moore, M. L. Carlson, J. A. Davidson, J. J. Garcia, S. M. Olsen, and K. D. Olsen, “Transoral robotic surgery using the thulium: Yag laser: a prospective study,” *Archives of Otolaryngology–Head & Neck Surgery*, vol. 138, no. 2, pp. 158–166, 2012.
- [197] M. Benazzo, P. Canzi, and A. Occhini, “Transoral robotic surgery with laser for head and neck cancers: a feasibility study,” *ORL*, vol. 74, no. 3, pp. 124–128, 2012.
- [198] S. M. Olson, M. Hussaini, and J. S. Lewis Jr, “Frozen section analysis of margins for head and neck tumor resections: reduction of sampling errors with a third histologic level,” *Modern Pathology*, vol. 24, no. 5, p. 665, 2011.
- [199] M. Marx, P. Ghanouni, and K. Butts Pauly, “Specialized volumetric thermometry for improved guidance of MRgFUS in brain,” *Magnetic resonance in medicine*, vol. 78, no. 2, pp. 508–517, 2017.
- [200] A. E. Sloan, M. S. Ahluwalia, J. Valerio-Pascua, S. Manjila, M. G. Torchia, S. E. Jones, J. L. Sunshine, M. Phillips, M. A. Griswold, M. Clampitt, *et al.*, “Results of the neuroplate system first-in-humans phase i clinical trial for recurrent glioblastoma,” *Journal of neurosurgery*, vol. 118, no. 6, pp. 1202–1219, 2013.
- [201] P. Vartholomeos, L. Qin, and P. E. Dupont, “Mri-powered actuators for robotic interventions,” in *Intelligent Robots and Systems (IROS), 2011 IEEE/RSJ International Conference on*, pp. 4508–4515, IEEE, 2011.
- [202] E. Tumino, R. Sacco, M. Bertini, M. Bertoni, G. Parisi, and A. Capria, “Endotics system vs colonoscopy for the detection of polyps,” *World Journal of Gastroenterology: WJG*, vol. 16, no. 43, p. 5452, 2010.

- [203] A. A. M. Faudzi, M. R. M. Razif, I. N. A. M. Nordin, K. Suzumori, S. Wakimoto, and D. Hirooka, "Development of bending soft actuator with different braided angles," in *IEEE/ASME International Conference on Advanced Intelligent Mechatronics*, pp. 1093–1098, 2012.
- [204] D. S. Simulia, "ABAQUS 6.13 User's Manual," *Dassault Systems, Providence, RI*, 2013.
- [205] Y. Bacsar and M. Itskov, "Finite element formulation of the Ogden material model with application to rubber-like shells," *International Journal for Numerical Methods in Engineering*, vol. 42, no. 7, pp. 1279–1305, 1998.
- [206] O. C. Zienkiewicz, R. L. Taylor, O. C. Zienkiewicz, and R. L. Taylor, *The finite element method*, vol. 36. McGraw-hill London, 1977.
- [207] T. J. R. Hughes, *The finite element method: linear static and dynamic finite element analysis*. Courier Corporation, 2012.
- [208] S. Y. Ko, L. Frasson, and F. R. y Baena, "Closed-loop planar motion control of a steerable probe with a programmable bevel inspired by nature," *IEEE Transactions on Robotics*, vol. 27, no. 5, pp. 970–983, 2011.
- [209] R. Xu, A. Asadian, A. S. Naidu, and R. V. Patel, "Position control of concentric-tube continuum robots using a modified Jacobian-based approach," in *IEEE International Conference on Robotics and Automation (ICRA)*, pp. 5813–5818, IEEE, 2013.
- [210] C. Hartmann, J. Boedecker, O. Obst, S. Ikemoto, and M. Asada, "Real-Time Inverse Dynamics Learning for Musculoskeletal Robots based on Echo State Gaussian Process Regression," in *Robotics: Science and Systems*, 2013.
- [211] O. Sigaud, C. Salaün, and V. Padois, "On-line regression algorithms for learning mechanical models of robots: a survey," *Robotics and Autonomous Systems*, vol. 59, no. 12, pp. 1115–1129, 2011.
- [212] J. Peters and S. Schaal, "Learning to control in operational space," *The International Journal of Robotics Research*, vol. 27, no. 2, pp. 197–212, 2008.
- [213] S. Schaal, C. G. Atkeson, and S. Vijayakumar, "Scalable techniques from nonparametric statistics for real time robot learning," *Applied Intelligence*, vol. 17, no. 1, pp. 49–60, 2002.
- [214] S. Vijayakumar, A. D'souza, and S. Schaal, "Incremental online learning in high dimensions," *Neural computation*, vol. 17, no. 12, pp. 2602–2634, 2005.

- [215] S. Klanke, S. Vijayakumar, and S. Schaal, “A library for locally weighted projection regression,” *Journal of Machine Learning Research*, vol. 9, no. Apr, pp. 623–626, 2008.
- [216] D. E. Whitney, “Resolved Motion Rate Control of Manipulators and Human Prostheses,” *IEEE Transactions on Man-Machine Systems*, vol. 10, no. 2, pp. 47–53, 1969.
- [217] A. Jain, K. Nandakumar, and A. Ross, “Score normalization in multimodal biometric systems,” *Pattern recognition*, vol. 38, no. 12, pp. 2270–2285, 2005.
- [218] Y. Chen, W. Wang, E. J. Schmidt, K. W. Kwok, A. N. Viswanathan, R. Cormack, and Z. T. H. Tse, “Design and Fabrication of MR-Tracked Metallic Stylet for Gynecologic Brachytherapy,” *IEEE/ASME Transactions on Mechatronics*, vol. PP, no. 99, p. 1, 2015.
- [219] “Heartvista,” *Heartvista Inc.* 2019. [Online]. Available <https://www.heartvista.ai/> [Accessed Jan 2019].
- [220] B. T. Yeo, M. R. Sabuncu, T. Vercauteren, N. Ayache, B. Fischl, and P. Golland, “Spherical demons: fast diffeomorphic landmark-free surface registration,” *IEEE transactions on medical imaging*, vol. 29, no. 3, pp. 650–668, 2010.
- [221] H. Lombaert, L. Grady, X. Pennec, N. Ayache, and F. Chriet, “Spectral log-demons: diffeomorphic image registration with very large deformations,” *International journal of computer vision*, vol. 107, no. 3, pp. 254–271, 2014.
- [222] L. Zhao and K. Jia, “Deep adaptive log-demons: diffeomorphic image registration with very large deformations,” *Computational and mathematical methods in medicine*, vol. 2015, 2015.
- [223] L. Zhang and Y. Wen, “Log-demons with driving force for large deformation image registration,” in *Neural Networks (IJCNN), 2016 International Joint Conference on*, pp. 3052–3059, IEEE, 2016.
- [224] H. Lu, M. Reyes, A. Šerifović, S. Weber, Y. Sakurai, H. Yamagata, and P. C. Cattin, “Multi-modal diffeomorphic demons registration based on point-wise mutual information,” in *Biomedical Imaging: From Nano to Macro, 2010 IEEE International Symposium on*, pp. 372–375, IEEE, 2010.
- [225] S. Nithianathan, S. Schafer, D. J. Mirota, J. W. Stayman, W. Zbijewski, D. D. Reh, G. L. Gallia, and J. H. Siewerdsen, “Extra-dimensional demons: A method for incorporating missing tissue in deformable image registration,” *Medical physics*, vol. 39, no. 9, pp. 5718–5731, 2012.

- [226] S. M. H. Sadati, Y. Noh, S. E. Naghibi, A. Kaspar, and T. Nanayakkara, *Stiffness Control of Soft Robotic Manipulator for Minimally Invasive Surgery (MIS) Using Scale Jamming*, pp. 141–151. Springer, 2015.
- [227] K. W. Kwok, K. H. Tsoi, V. Vitiello, J. Clark, G. C. T. Chow, W. Luk, and G.-Z. Yang, “Dimensionality reduction in controlling articulated snake robot for endoscopy under dynamic active constraints,” *IEEE Transactions on Robotics*, vol. 29, no. 1, pp. 15–31, 2013.
- [228] H.-S. Yoon and B.-J. Yi, “A 4-dof flexible continuum robot using a spring backbone,” in *Mechatronics and Automation, 2009. ICMA 2009. International Conference on*, pp. 1249–1254, IEEE, 2009.
- [229] D.-G. Choi, B.-J. Yi, and W.-K. Kim, “Design of a spring backbone micro endoscope,” in *Intelligent Robots and Systems, 2007. IROS 2007. IEEE/RSJ International Conference on*, pp. 1815–1821, IEEE, 2007.
- [230] C. Lekakou, Y. Elsayed, T. Geng, and C. M. Saaj, “Skins and sleeves for soft robotics: inspiration from nature and architecture,” *Advanced Engineering Materials*, vol. 17, no. 8, pp. 1180–1188, 2015.
- [231] M. Cianchetti, T. Ranzani, G. Gerboni, I. De Falco, C. Laschi, and A. Menciassi, “Stiff-flop surgical manipulator: mechanical design and experimental characterization of the single module,” in *Intelligent Robots and Systems (IROS), 2013 IEEE/RSJ International Conference on*, pp. 3576–3581, IEEE, 2013.



# Appendix A

## Overview of the MR Safe Catheter Robot Control System

### A.1 System Architecture

The section provides detailed implementation of the electronic and computational system for the MR Safe catheter robot control. The overall schematic diagram is illustrated in [Fig. A.1](#). This system comprises of a central PC that acts as the main processor to handle high-level computational tasks, including: **i)** Reception and filtering of user input control signal and positional sensor feedback; **ii)** Processing of the catheter feedback control methods and instantiation of motor command; **iii)** 3D rendering of visual guidance inside the navigation interface.

Low-level computational tasks, especially those related to motor control, are off-loaded to microcontrollers (PIC chipKIT™ uC32™, [Fig. A.2a](#)). The control of stepper motor ([Fig. A.2b](#)) involves many repetitive and high frequency instructions which must be executed at exact time point. Generation of stepping motor pulse, which can go up to 1kHz is a typical example. While normal PC is not equipped with real-time computing hardware, microcontrollers are commonly employed as hardware extension to resolve the demand. It act as a slave unit to precisely process the high-level motor control command sent from the PC. The communication protocol is explained in the following section.

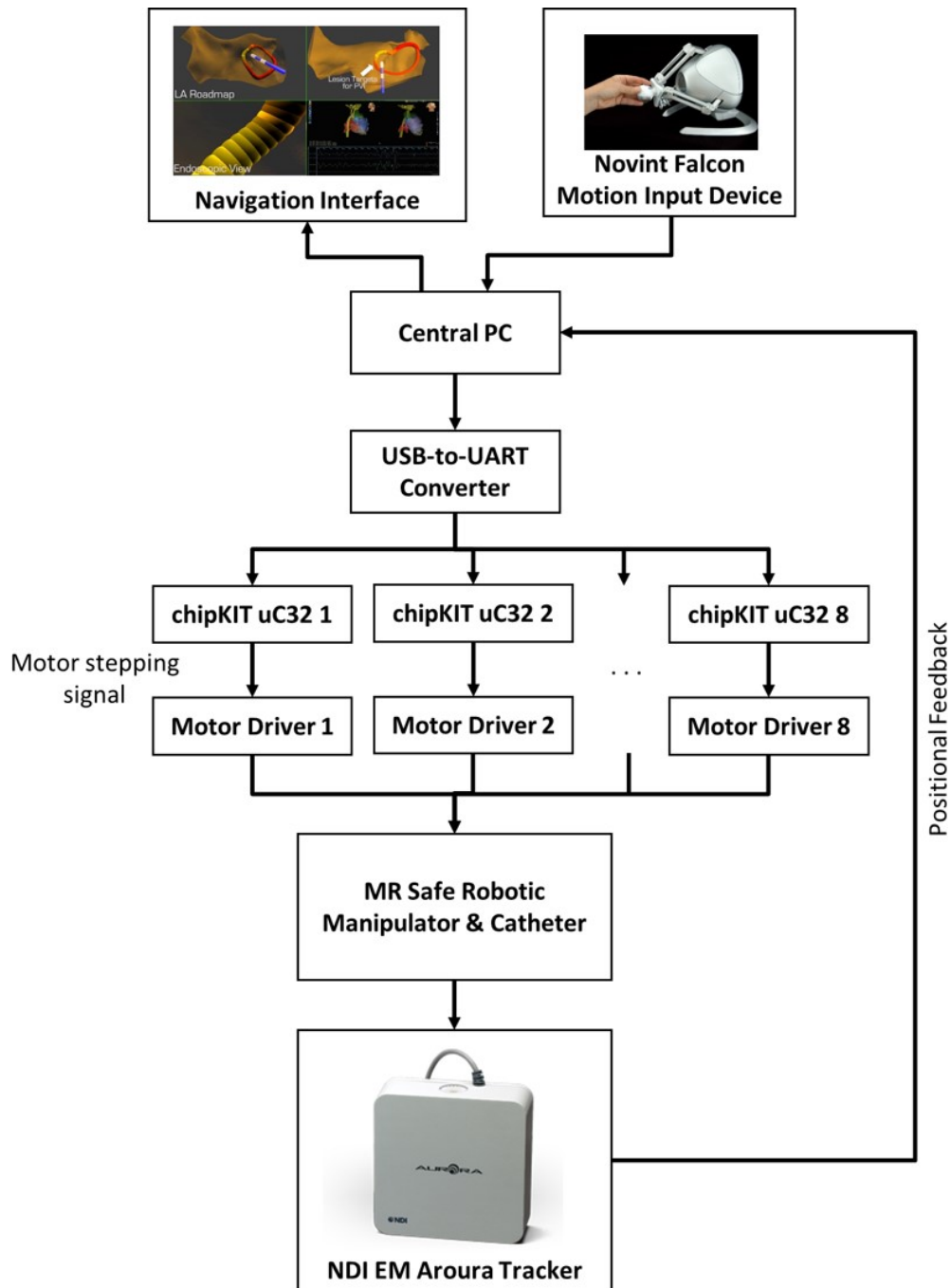


**Figure A.1:** Schematic diagram of the catheter robot control electronic system. The low-level tasks related to motor control (e.g. step counting and pulse generation) are off loaded to the PIC chipKIT™ uC32™ microcontrollers. Each motor is equipped with its dedicated microcontroller to ensure consistent generation of high frequency motor stepping pulse. Such design paradigm also favour system scalability for others potential applications.



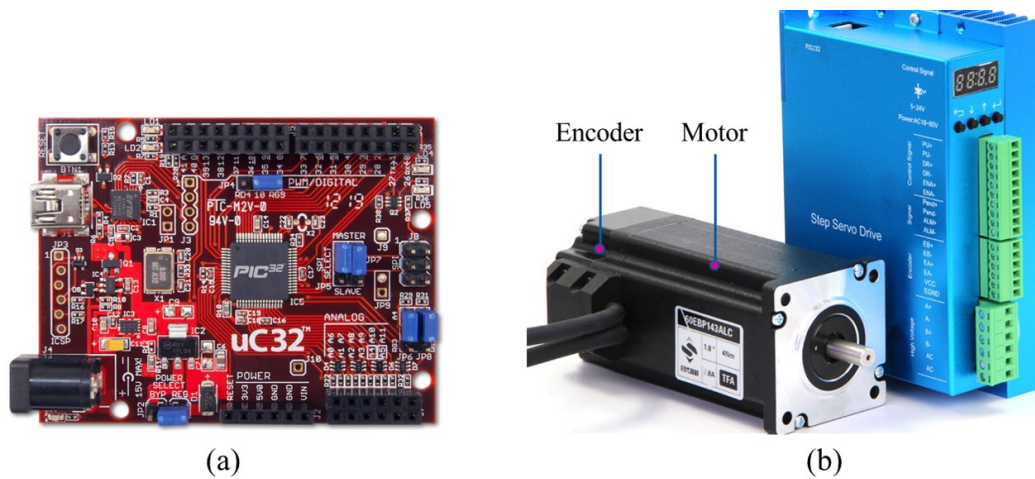


**Figure A.2:** (a) PIC chipKIT™ uC32™ microcontrollers with 32-bit MIPS processor core running at 80MHz; (b) High power stepper motor and driver set with a maximum output torque of 4Nm. The proximal end of motor shaft is connected to an encoder to measure the exact motor rotation. It allows compensation of skipping step and hence robust motor positioning.

## A.2 Communication Protocol

The communication interface between the central PC and the microcontrollers is achieved via a custom-designed protocol (Tables A.1 and A.2). The protocol features dedicated command code and data packet framework. To prevent transmission error due to external EM interference, CRC-16 check sum is employed to cross-check the validity of transmitted messages. This allows the operator to control the electric motor and hence the MR Safe transmission units.

Start of Message	Check Sum Range		Check Sum (CS)	End of Message
	Payload			
0x0F 0x0C	Message ID	Message Body	2 Byte	0x0E 0X0B
	1 Byte	Up to 20 Byte		

**Table A.1:** Communication protocol of motor control command and response between the central PC and microcontroller for motor control

Message ID	Message Type
0x01	Acknowledge of Message
0x02	Recognized of Message
0x03	Check sum error
0x04	Command Accomplished
0x05	Error occur when carrying out the command
0x06	Change motor duty cycle
0x07	Force Stop
...	...

**Table A.2:** Sample message type of the communication protocol

## Appendix B

# Technical Details of Soft Robotics Actuator

### B.1 Pneumatic Static Mixing Dispenser for Silicone Rubber Molding

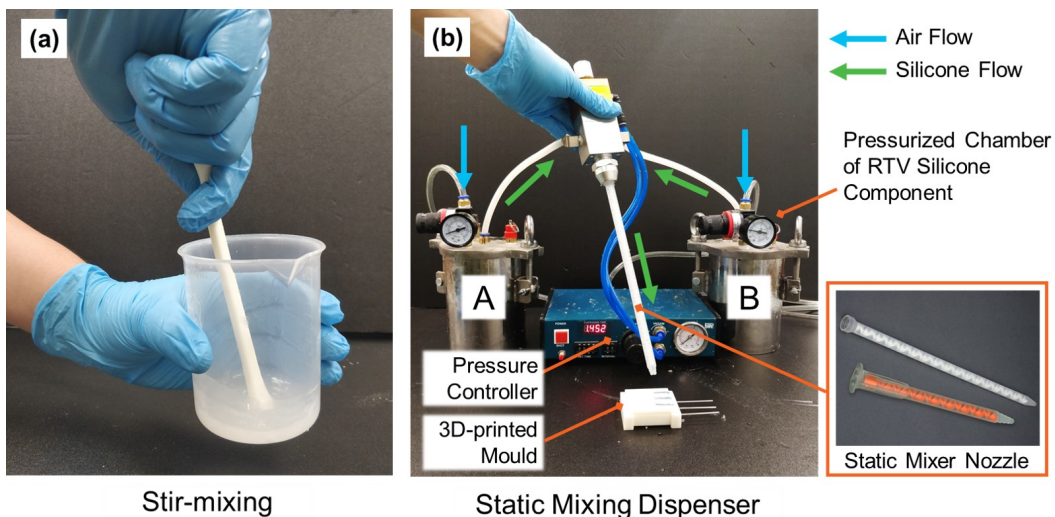


**Figure B.1:** (a) Typical stir-mixing of 2-components RTV Silicone Rubber. The mixing process will induce a significant amount of micro-bubbles in the silicone fluid mixture, deteriorating the outcome quality of workpiece; (b) Pneumatic mixing and dispenser system for silicone fluid. The 2 components of silicone fluid are first de-gassed and then pumped out of the chamber by pressured air. The AB components are forced through the sealed static mixer nozzle and hence thoroughly combined. This approach could prevent the formation of micro-bubbles during the mixing process.

The casting process of RTV silicone rubber involves the mixing of two fluidic components (A+B) in order to trigger vulcanization. Stir-mixing (Fig. B.1a) with rod and beaker is a common way to thoroughly combine the two fluidic components, but this process inevitably introduce air bubbles into the highly viscous mixed fluid. These air bubbles compromise the resultant tensile strength, or even appear as cracks after curing. De-airing with vacuum is required to remove the entrained air bubbles from the mixed silicone, but it also reduce the work time before the silicone cure up. To resolve this issue, static mixing dispenser, which is usually employed in industrial adhesive disposition is utilized to dispense the silicone fluid (Fig. B.1b). The AB components are vacuum de-aired separately in dedicated chambers. During dispensing, air pressure is applied to push the fluid through a static mixer nozzle, efficiently mixes the two components of silicone. When a smooth flow is established, there will be no air in the mixer nozzle.

## B.2 Individually Constrained Design

The section describe the detailed fabrication process of the individually constrained soft robotic actuator. The fabrication process involves three major phases:

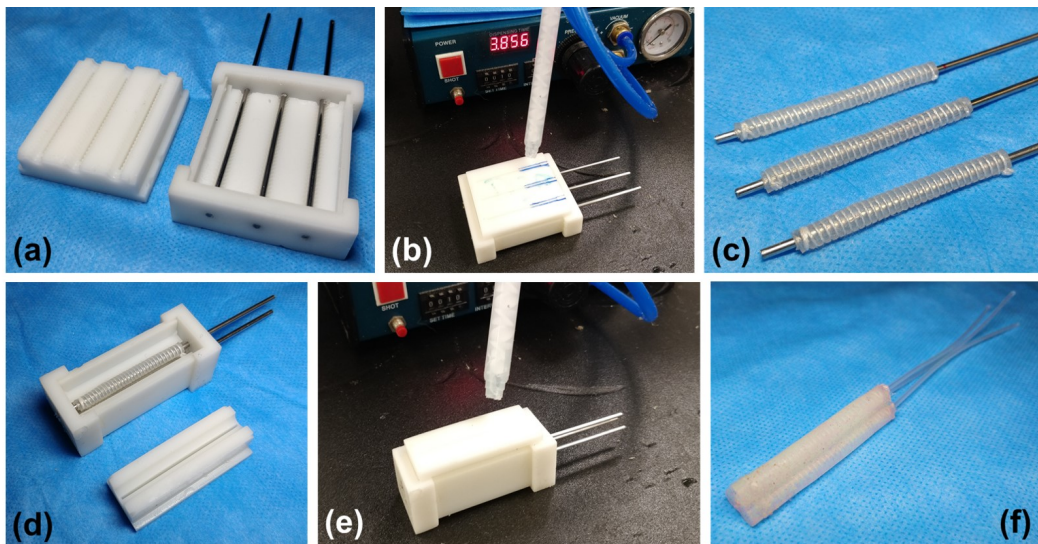


**Figure B.2:** Fabrication procedure of the individually constrained soft robotic actuator. (a) Assembly of 3D-printed mold for inner chamber walls; (b) Deposition of RTV silicone with automatic mixing dispenser; (c) Wrapping of fiber constraints to the inner chamber walls; (d) Assembly of inner chamber wall with the mold of outer wall; (e) Deposition of RTV silicone to form outer wall; (f) Demolding, trimming and addition of silicone tubes to attain final product.

**Phase 1:** Three cylindrical actuation chambers made of RTV silicone are cast separately with 3D-printed molds (Fig. B.2a-b). The inner mold is made of stainless steel rods instead of 3D-printer materials, so that straight act as the inner mold, provide sufficient strength for demolding. It is worth noting that the stainless steel rods are fixated at both ends, allowing accurate, parallel alignment of the long inner hole inside each inflatable chambers. In contrast, the convention one-end fixation design often result in cropped chambers. Although the two-end fixation will lead to a through-hole in each chambers, these small holes ( $\varnothing 2\text{mm}$ ) can be easily sealed with silicone adhesive.

**Phase 2:** Kevlar strings are wrapped densely in single helical structure with a pitch of 1mm along each soft chamber (Fig. B.2c). This fiber constrained structure is first proposed by Suzumori *et al.* [22, 203], in which the helical constraint layer enforces axial anisotropic expansion of inflatable chambers, so as to generate an effective bending moment when subject to pressure input. Tiny rifts is created on the outer layer of the soft chambers to hoist the fiber constraint in place.

**Phase 3:** Additional layer of silicone are cast to house the three inflatable chambers into one. (Fig. B.2d-e) This could fix the strings against their dislocation, even after numerous trials of bending actuation. The curing processing can be accelerated with oven. Finally, inflatable chamber is attached with silicone tube to allow fluid to be inflated. (Fig. B.2f).

## B.3 Overall Constrained Design

### B.3.1 Mechanical Structure

We have explored the use of an overall fiber constraint to confine the expansion of all inflatable chambers (Fig. B.3). In this approach, only one single, circular constraining mesh layer is wrapped on the circumference of actuator, so that the inflatable chambers is no more limited to cylindrical shape as in the individual constraint approach. It opens a great room to optimize the cross-sectional geometrical design, in order to accomodate various functional requirements and the enhance actuation performance. For incidence, the inflable chambers can be morphed into fan shape and hence accomodating an instrutment channel at the center (Fig. B.3c), which it is of importance to many endoscopic applications. Instrutment channel can creates the passage for many functional

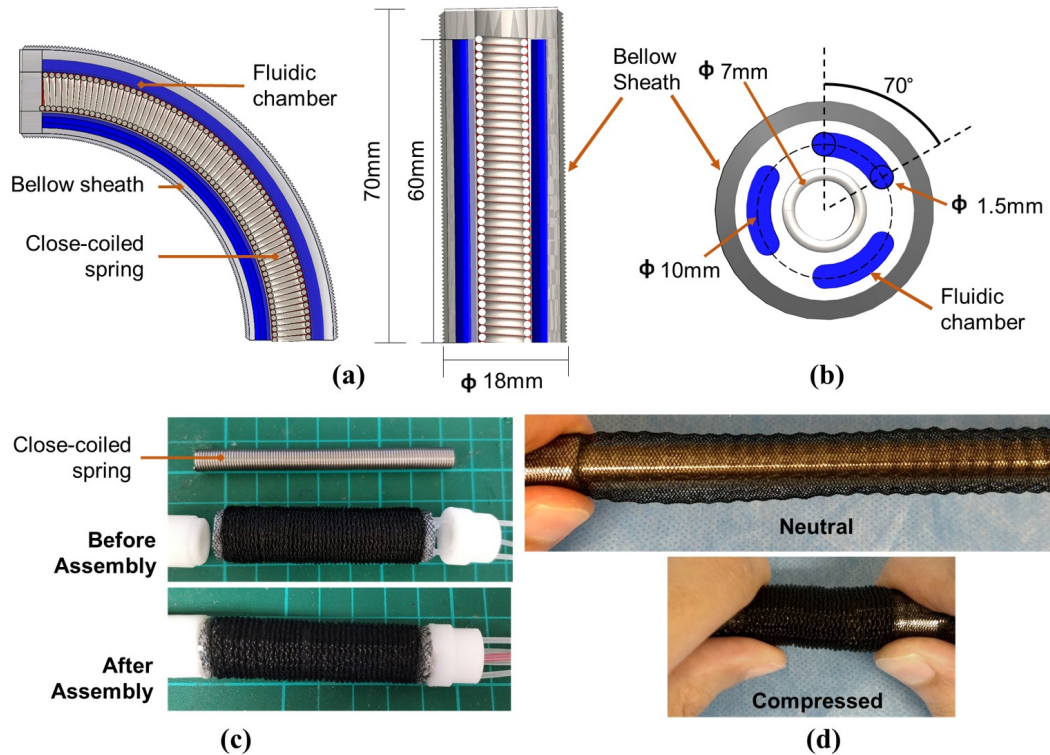


**Figure B.3:** (a) CAD/CAM model of the soft actuator internal structure with overall constraint. The air chamber can expand when being pressurized. Both the bellow sheath and close-coiled spring act as physical constraint of the air chambers, forcing them to expand in axial direction, which leads to bending motion; (b) Illustration of the cross-sectional design and dimensions; (c) Soft robotic actuator with overall constraints; (d) The bellow sheath constraint obtained by compressing a braided fiber mesh. The constraint sheath with bellow structure restricts radial expansion of the actuator during chamber inflation but allows elongation to permit bending.

components, such as camera, illumination, biopsy gripper or snare. To protect the integrity of the channel, closed-coil spring is employed to resist the chamber internal expansion toward centripetal direction. The close-coiled spring also possess the ability to augment the effective stiffness of the robot actuator, so that the robot can move against the environment interactions. (Fig. B.4)

However, the use of overall constraint often leads to a more complicated design process, because the expansion of chambers is now coupled in-between. The expansion of a chamber will remarkably distort the overall cross-section geometry, enlarging the chamber cross-sectional area, as well as compressing other chambers (Fig. B.5). Although the increase in chamber cross-section area gives rise to a larger bending force, it also adversely affect the robot control precision. These trade-off and potential design optimization will be further studies using FEA method in Appendix B.3.2

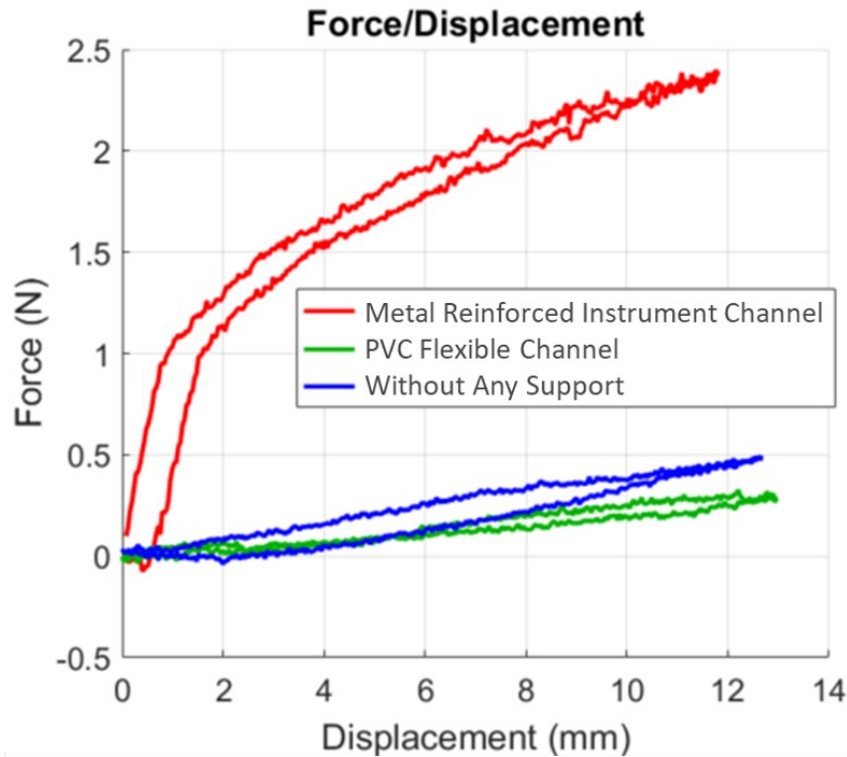


**Figure B.4:** Experimental result of the actuator stiffness analysis. The robot stiffness is measured by pushing its tip in lateral direction with a stepping motor. The contact force is measured by an industrial grade-force sensor. The soft actuation integrated with metal spring reinforce exhibit a significant improvement in stiffness, facilitate high actuation force and fast dynamic response.

### B.3.2 Design Optimization with Finite Element Analysis

To search for an optimal geometrical design, the FEA model of the soft robot with overall constraint design is constructed. We aim to study the internal chamber deformation when being pressurized and its relation to the overall bending motion. Same elastic material model and simulation conditions are adopted as in [Section 5.3.2](#). The actuator CAD/CAM model is tessellated with a custom-designed mesh ([Fig. 5.5g](#)) and protruded along the axial direction. The design optimization has to fulfil the following outcomes:

- i) Preserve the integrity of instrument channel even under large bending and high inflation pressure;
- ii) Maximize the bending force/angle with minimal inflation pressure; and
- iii) Even distribution of stress/strain in silicone material over the pressurized process.

For endoscopic applications of soft manipulator, instrument channel serves the purpose

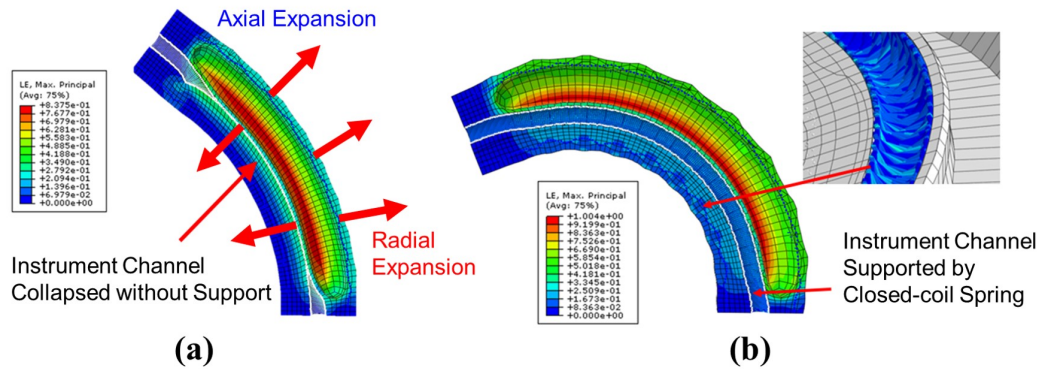


**Figure B.5:** (a) FEA simulation result of an overall constrained soft actuation when one chamber is pressurized. Without any support, the instrument channel will collapse due to the internal expansion of fluidic chamber, hindering the movement of any instrument passing-through; (b) Closed-coil spring is integrated as a central channel to reinforce the integrity of the instrument channel, acting against the internal expansion pressure.

of allowing direct passage of interventional components, including endoscopic camera, fluidic channels for insufflation/irrigation, biopsy forceps and also laser fiber for ablation. The channel should allow bending but prevent compression in order to protect the enclosed components. The FEA simulation (Fig. B.5a) has shown that, without any support, the instrument channel is prompt to collapse due to the radial expansion of inflatable chambers. Therefore, a closed-coil spring is integrated, acting as the "outer shell" of the instrument channel, providing structural support against the chamber pressure (Fig. B.5b).

The concentration of stress is another design concerns that must be considered with FEA. High stress/strain beyond the limit of silicone rubber may lead to tearing or rupture of the inflatable chamber. With FEA simulation (Fig. B.6), we discovered that chamfered corners and proper increase of outer layer thickness can reduce the occurrence of stress concentration. As a result, the final design of soft manipulator can withstand a high inflation pressure up to 8 bar.



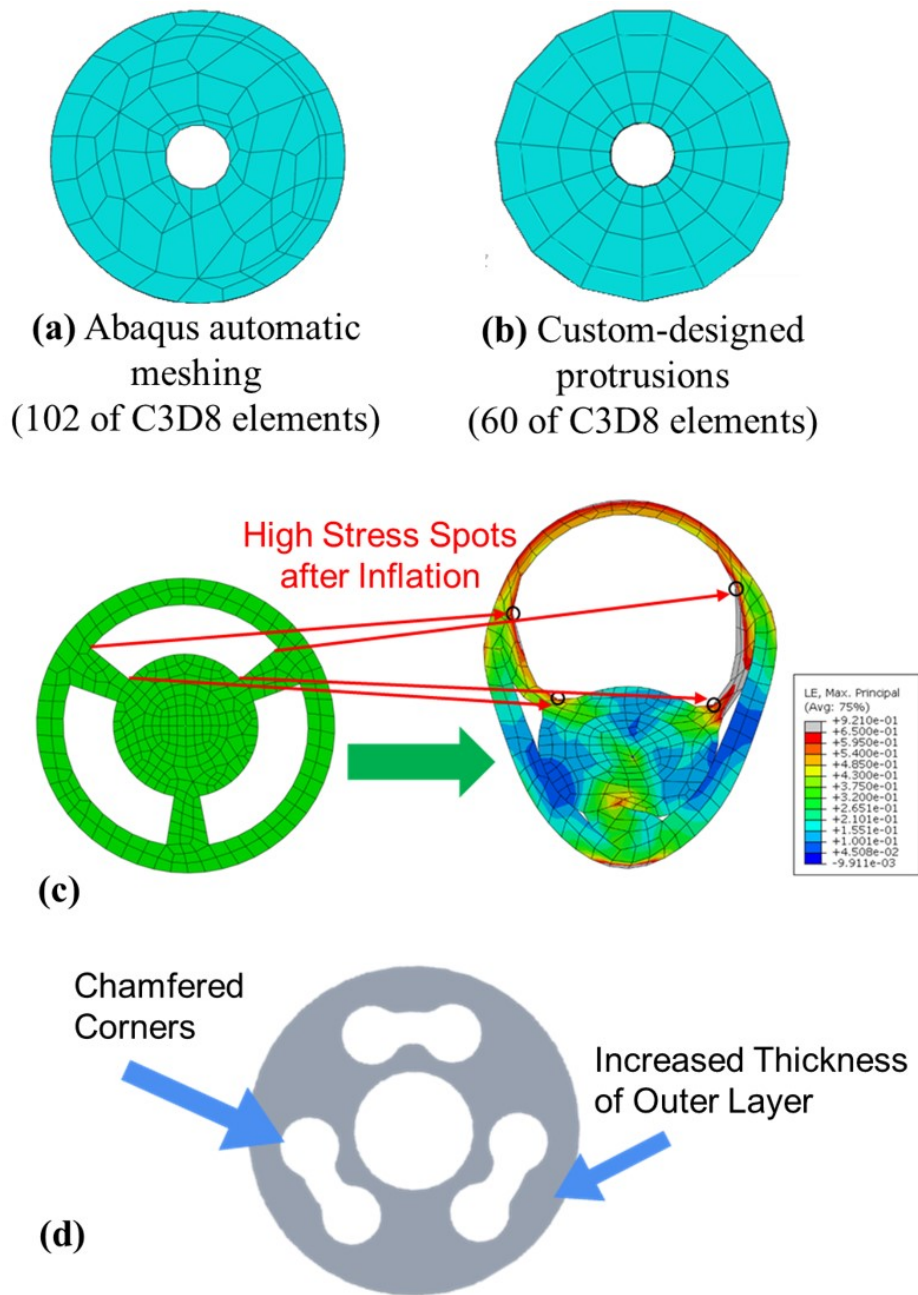


**Figure B.6:** (a) FEA model of the overall constrained soft actuation generated by Abaqus automatic meshing of C3D8; (b) Same robot FEA obtained by a well-structured manual mesh design; (c) FEA plot showing the high strain areas (red area) was observed at the corner and the outer surface of the bendable section, when one actuation chambers was inflated; (d) Revised cross-section design of the bendable section. The high strain areas found in previous FEA plot were reinforced with chamfered corners and thicker outer wall.

### B.3.3 Fabrication

Springs are a basic and common component of a mechanical system, allowing a wide selection of materials, dimensions and pre-tensioning. In previous studies, helical metallic springs have demonstrated excellent flexibility and back-drivability when incorporated with cable-driven continuum robots [228]. Open-coiled springs (like those seen in car suspension) are often employed as the backbone of continuum robots, which can attain effective bending and shortening when pulled by cables [229]. However, open-coil springs are not favorable for soft-bodied actuators due to the large gaps between coils, which can cause local ballooning during inflation, ultimately resulting in premature bursting [230].

In this study, a closed-coil spring, or so-called tension spring is selected as the backbone element as opposed to its open-coiled counterpart. Closed-coil springs can achieve a comparable amount of bending curvature to that of open-coil springs while having much smaller inter-coil gaps. They also possess a pre-compression is superimposed with the linear elastic force seen in normal springs, providing a bilinear force-displacement behavior. Physically, the spring does not open until the pre-stress force is overcome. By integrating a closed-coil spring into our actuator design, the pre-compression gives rise a significant antagonistic restoring force that can passively enhance the dynamic response of the soft continuum robot. Moreover, the centrally-placed spring can sustain the high compressive force produced radially by the inflated soft actuator body, allowing critical components like sensors, wires or tubes to pass through it freely. In our study, a range of closed-coil tension springs made of spring steel (GB/T 1222-2007) are used to reinforce the soft continuum actuators. The fabrication process of the overa consists of four major steps:

1. Molding of the soft body;
2. Attachment of the crimped sheath;
3. Insertion of the closed coil spring;
4. Encapsulation of the entire system.

The soft body of the hybrid actuator is of tentacle-inspired design, with three parallel fluidic chambers spaced  $120^\circ$  apart that allow omni-directional bending [231]. The soft body was molded with silicone (Dragon skin 20, Ecoflex, Smooth on Inc) in an FDM 3D printed mold. (Fig. B.7a) In addition to the three fluidic chambers, a central channel was

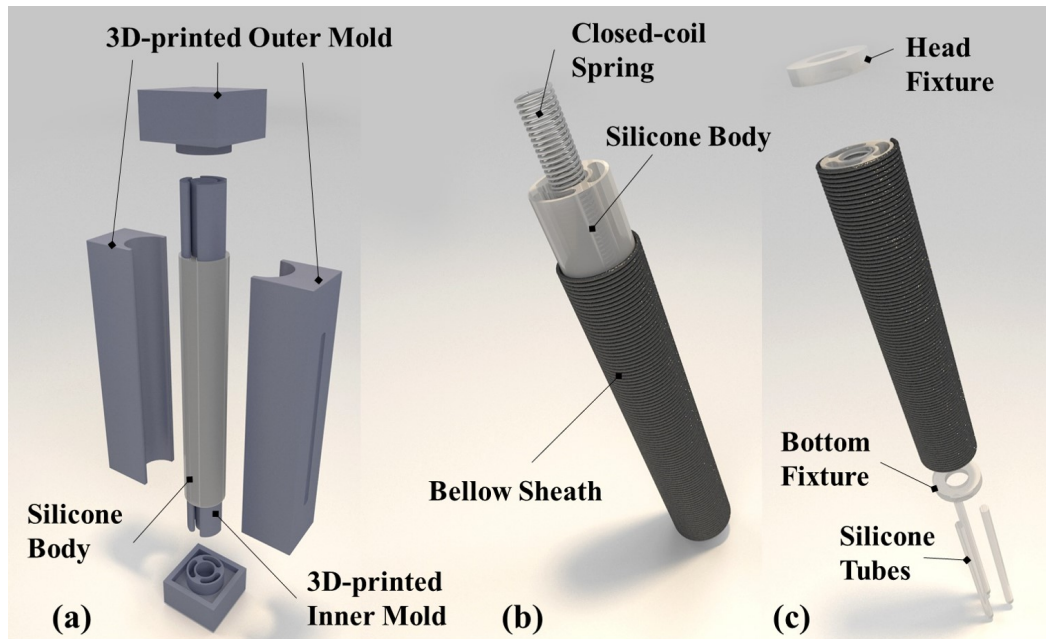


**Figure B.7:** (a) Fabrication procedure of the soft robotic actuator with overall constrained design. The soft body is molded with silicone rubber in 3D-printed mold. The cross-sectional geometry of the inflatable chamber shape is determined by the inner mold; (b) Exploded-view drawing of the actuation with closed-coil spring backbone, soft body and bellow sheath. The combined effect of these components allows much higher actuation pressures without rupture or bulging, while also enhancing the actuator's stiffness with the closed-coil spring; (c) Final assembly of the actuator. Two rigid fixtures are adhered to both ends, connecting silicone tubes and reinforcing the sealing at the typically weak end connections of soft actuators.

left to allow integration of the spring reinforcement. To enable pneumatic transmission, silicone tubes were connected to one end of each fluidic chamber. A bellow sheath was slipped onto the soft body to limit radial expansion while allowing linear extension of the body. (Fig. B.7b) Bellow sheath allows the actuator to be inflated to a pressure up to 8 bar. Afterwards, the closed-coil spring with outer diameter matching the inner channel diameter was cut to a suitable length (70mm) and then inserted through the center channel of the soft body until 3-4mm protruded from both ends of the body. To fix the spring backbone into place, a top and bottom cap was 3D printed (Objet Connex 500) and mounted to the exposed spring ends. The head cap and bottom cap were designed with a groove with diameter close to the outer diameter of springs for better adhesion when mating. After that, the soft actuator was pulled and elongated to the length of the springs and was fixed to the end caps together with the spring end using adhesive as shown in (Fig. B.7c).